Multilayer Mirrors for Attosecond Pulses in the Water Window Spectral Range

Alexander Guggenmos

SIGILL·UNIVERSITAT·LUDOVIC·MAXIM

München 2015

Multilayer Mirrors for Attosecond Pulses in the Water Window Spectral Range

Alexander Guggenmos

Dissertation
an der Fakultät für Physik
der Ludwig–Maximilians–Universität
München

vorgelegt von
Alexander Guggenmos
aus Hausham

München, den 14. Oktober 2015

Erstgutachter: Prof. Dr. Ulf Kleineberg
Zweitgutachter: Priv.-Doz. Dr. Bert Nickel
Tag der mündlichen Prüfung: 03. Dezember 2015

To Erika, Lisa, Leoni, Lilly

Contents

List of Figures

List of Tables

Publications by the author

Articles in journals

- J. Schmidt, A. Guggenmos, M. Hofstetter, S. H. Chew, and U. Kleineberg, “Generation of circularly polarized high harmonic radiation using a transmission multilayer quarter waveplate,” *Optics Express* (in press).

- A. Guggenmos, M. Jobst, M. Ossiander, S. Radünz, J. Riemensberger, M. Schäffer, A. Akil, C. Jakubeit, P. Böhm, S. Noever, B. Nickel, R. Kienberger, and U. Kleineberg, “Chromium/scandium multilayer mirrors for isolated attosecond pulses at 145 eV,” *Optics Letters* 40(12), 2846–2849 (2015).

- M. Zürch, J. Rothhardt, S. Hädrich, S. Demmler, M. Krebs, J. Limpert, A. Tünnermann, A. Guggenmos, U. Kleineberg, and C. Spielmann, “Real-time and Sub-wavelength Ultrafast Coherent Diffraction Imaging in the Extreme Ultraviolet,” *Scientific Reports* 4, 7356 (2014).

- A. Guggenmos, S. Radünz, R. Rauhut, M. Hofstetter, S. Venkatesan, A. Wochnik, E. M. Gullikson, S. Fischer, B. Nickel, C. Scheu, and U. Kleineberg, “Ion polished Cr/Sc attosecond multilayer mirrors for high water window reflectivity,” *Optics Express* 22(22), 26526–26536 (2014).

- A. Guggenmos, R. Rauhut, M. Hofstetter, S. Hertrich, B. Nickel, J. Schmidt, E. M. Gullikson, M. Seibald, W. Schnick, and U. Kleineberg, “Aperiodic CrSc multilayer mirrors for attosecond water window pulses,” *Optics Express* 21(19), 21728–21740 (2013).

- S. H. Chew, F. Süßmann, C. Späth, A. Wirth, J. Schmidt, S. Zherebtsov, A. Guggenmos, A. Oelsner, N. Weber, J. Kapaldo, A. Gliserin, M. I. Stockman, M. F. Kling, and U. Kleineberg, “Time-of-flight-photoelectron emission microscopy on plasmonic structures using attosecond extreme ultraviolet pulses,” *Applied Physics Letters* 100, 051904 (2012).

- M. Hofstetter, A. Aquila, M. Schultze, A. Guggenmos, S. Yang, E. Gullikson, M. Huth, B. Nickel, J. Gagnon, V. S. Yakovlev, E. Goulielmakis, F. Krausz, and U. Kleineberg, “Lanthanum-molybdenum multilayer mirrors for attosecond pulses between 80 and 130 eV,” *New Journal of Physics* 13, 063038 (2011).

- M. Hofstetter, M. Schultze, M. Fieß, B. Dennhardt, A. Guggenmos, J. Gagnon, V. Yakovlev, E. Goulielmakis, R. Kienberger, E. M. Gullikson, F. Krausz, and U. Kleineberg, “Attosecond dispersion control by extreme ultraviolet multilayer mirrors,” *Optics Express* 19(3), 1767–1776 (2011).

- G. P. Acuna, F. F. Buersgens, C. Lang, M. Handloser, A. Guggenmos, and R. Kersting “Interdigitated terahertz emitters,” *Electonics Letters* 44(3), 229–230 (2008).

Articles in proceedings

- A. Guggenmos, S. Radünz, R. Rauhut, M. Hofstetter, S. Venkatesan, A. Wochnik, C. Scheu, E. Gullikson, S. Fischer, B. Nickel, U. Kleineberg, "Attosecond broadband multilayer mirrors for the water window spectral range," *Proc. SPIE 9207, Advances in X-Ray/EUV Optics and Components IX*, 92070L (2014).

- A. Guggenmos, M. Hofstetter, R. Rauhut, C. Späth, S. Hertrich, B. Nickel, S. Yang, E. M. Gullikson, J. Schmidt, M. Seibald, W. Schnick, F. Krausz, and U. Kleineberg, "Broadband multilayer mirror and diffractive optics for attosecond pulse shaping in the 280-500 eV photon energy range," *EPJ Web of Conferences* 41, 01011 (2013).

- A. Guggenmos, M. Hofstetter, R. Rauhut, B. Nickel, E. Gullikson, U. Kleineberg, "Aperiodic multilayer mirrors for attosecond soft x-ray pulses," *Proc. SPIE 8502, Advances in X-Ray/EUV Optics and Components VII*, 850204 (2012).

Books

- S. H. Chew, K. Pearce, C. Späth, A. Guggenmos, J. Schmidt, F. Süßmann, M. F. Kling, U. Kleineberg, E. Mårsell, C. L. Arnold, E. Lorek, P. Rudawski, C. Guo, M. Miranda, F. Ardana, J. Mauritsson, A. L'Huillier, and A. Mikkelsen, "Imaging Localized Surface Plasmons by Femtosecond to Attosecond Time-Resolved Photoelectron Emission Microscopy - "ATTO-PEEM"," in *Attosecond Nanophysics: From Basic Science to Applications* (Wiley Verlag, Edts.: Peter Hommelhoff and Matthias Kling, 2015).

- A. Guggenmos, "Der Hybride Terahertz-Emitter: Designkonzepte für eine hohe Emission und Herstellung mittels Lithografie," (Akademische Verlagsgemeinschaft München, 2010).

Conference paper

- A. Guggenmos, J. Schmidt, S. Heinrich, B. Nickel, F. Krausz, and U. Kleineberg, "Multilayer Mirrors for VUV-XUV Attosecond Pump-Probe Experiments," *Optical Society of America: Frontiers in Optics*, FM3A.3 (2015).

- M. Zürch, J. Rothhardt, S. Hädrich, S. Demmler, M. Krebs, J. Limpert, A. Tünnermann, A. Guggenmos, U. Kleineberg, and C. Spielmann, "Approaching the Abbe Limit in the Extreme Ultraviolet: Ultrafast Imaging Using a Compact High Average Power High Harmonic Source," *Optical Society of America: Frontiers in Optics*, FTh3A.6 (2015).

- M. Zürch, J. Rothhardt, S. Hädrich, S. Demmler, M. Krebs, J. Limpert, A. Tünnermann, A. Guggenmos, U. Kleineberg, and C. Spielmann, "Coherent ultrafast diffraction imaging at the Abbe limit using a compact high average power high harmonic source," *CLEO/Europe EQEC*, CF-8.1 (2015).

- A. Guggenmos, S. Radünz, R. Rauhut, S. Venkatesan, A. Wochnik, C. Scheu, E. Gullikson, S. Fischer, B. Nickel, F. Krausz, and U. Kleineberg, "Optimizing broadband attosecond Cr/Sc water window multilayer mirrors," *Optical Society of America: Frontiers in Optics*, FTh1G.6 (2014).

- S. Karsch, J. Wenz, K. Khrennikov, M. Heigoldt, A. Popp, A. Buck, J. Xu, L. Veisz, S.-W. Chou, A. Maier, N. Kajumba, T. Seggebrock, F. Grüner, A. Guggenmos, U. Kleineberg, S. Schleede, M. Bech, P. Thibault, and F. Pfeiffer, "X-ray Generation by Relativistic Laser-Accelerated Electrons," *Optical Society of America: CLEO - Science and Innovations*, JTh3L (2014).

- A. Moulet, J. B. Bertrand, A. Jain, M. Garg, T. T. Luu, A. Guggenmos, S. Pabst, F. Krausz, and E. Goulielmakis, "Attosecond Pump-Probe Measurement of an Auger Decay," *Optical Society of America: International Conference on Ultrafast Phenomena XIX*, 10.Thu.B (2014).

- M. Zürch, J. Rothhardt, S. Hädrich, S. Demmler, M. Krebs, J. Limpert, A. Tünnermann, A. Guggenmos, U. Kleineberg, and C. Spielmann, "Coherent Imaging with a Narrow-band High Average Power XUV Source," *Optical Society of America: High Intensity Lasers and High Field Phenomena*, HTu3C.4 (2014).

- E. M. Bothschafter, A. Sommer, W. Schweinberger, M. Jobst, T. Latka, C. Jakubeit, A. Guggenmos, V. Yakovlev, R. Kienberger, M. Schultze, and F. Krausz, "Sub-Cycle Strong-Field Induced Modification of the Optical Properties of SiO2," *Optical Society of America: QELS Fundamental Science*, QTh4D.1 (2013).

- M. Hofstetter, M. Schultze, M. Fieß, A. Guggenmos, J. Gagnon, E. Magerl, E. Bothschafter, V. S. Yakovlev, E. Goulielmakis, R. Ernstorfer, R. Kienberger, E. M. Gullikson, F. Krausz, and U. Kleineberg, "First attosecond pulse control by multilayer mirrors above 100 eV photon energy," *Optical Society of America: International Conference on Ultrafast Phenomena XVII*, PDP8 (2010).

Zusammenfassung

Der junge Bereich der Attosekundenphysik beabsichtigt die zeitliche Erforschung und letztendlich die Kontrolle von Elektronendynamiken in Materie (Atome, Moleküle oder Festkörper) auf ihrer wahren Zeitskala, der zeitliche Bereich der Attosekunden (10^{-18} s). Kürzliche experimentelle Beispiele sind die Charakterisierung der zeitlichen Verzögerung bei der Photoionisation von Kernelektronen in Neonatomen oder die Photoemissionsverzögerung zwischen Valenz- und Kernzuständen von Magnesium. Solche Experimente basieren auf der Erzeugung von Attosekundenpulsen im extremen ultravioletten bis weichen Röntgenbereich, über hoher harmonischen Erzeugung in Gasen, was heutzutage ein bewährtes Verfahren ist und durch verbesserte Lasersysteme zu immer höheren Photonenenergien getrieben wird. Irgendwann wird der wichtige Spektralbereich im Wasserfenster mit ausreichenden Photonenzahlen erreicht werden. Dies wird die Attosekundenphysik auf biologisches Gewebe erweitern, was bahnbrechende Ergebnisse auf dem Gebiet der Biophysik ermöglichen könnte. Neben der Quellenentwicklung besteht ein starker Bedarf an entsprechender Optikentwicklung um Attosekundenpulse zu kontrollieren. Multilagenspiegel sind Schlüsselkomponenten in der Attosekundenphysik, welche beispielsweise das Maßschneidern von Attosekundenpulsparametern ermöglichen. Diese Arbeit widmet sich dem Design, der präzisen Herstellung und der Charakterisierung von periodischen als auch aperiodischen Multilagenspiegeln, hauptsächlich aus Chrom (Cr) und Scandium (Sc) Schichten. Die extrem genaue Kontrolle des Ionenstrahlbeschichtungsprozesses ermöglichte die Realisierung der ersten frequenzmodulierten Multilagenspiegel für das Wasserfenster mit genauer Phasenkontrolle, welche zur Pulskompression (τ=69 as) verwendet werden können. Der Reflexionsgrad der Spiegel wurde durch polieren der Zwischenschichten mit Ionenstrahlen wesentlich verbessert, was beispielsweise zu einem Reflexionshöchswert (21% an der Sc L_3-Kante) unter normalem Einfallswinkel führte, einer der höchsten gemessenen Werte für einen reinen Cr/Sc Spiegel. Ein Transmissionsmultilagensystem wurde entworfen, hergestellt und charakterisiert um linear polarisierte Attosekundenpulse in elliptisch polarisierte Pulse umzuwandeln, was die Untersuchung von ferromagnetischen Materialien oder chiralen Molekülen mit hoher Zeitauflösung ermöglicht. Weiterhin wurden verschiedene Multilagenspiegel verwendet um Strahlung von einer Laserplasma getriebenen Undulatorquelle spektral zu selektieren, was beispielsweise die Isolierung und Charakterisierung von Femtosekundenpulsen im Wasserfenster nahe 300 eV ermöglichte. Die höchste je gemessene Photonenenergie von solch einer Quelle. Die Attosekundenzeitskala war durch die Verwendung von optimierten Multilagenspiegel, zur Erzeugung von isolierten Attosekundenpulsen im weichen Röntgenbereich bei 145 eV, erreichbar. Die bis jetzt höchste Zentralenergie für charakterisierte Attosekundenpulse.

Die Ergebnisse dieser Arbeit erweitern die Kontrolle von Attosekundenpulsen mit Multilagenoptiken auf höhere Photonenenergien (ins Wasserfenster), auf eine bessere Pulsdispersionskontrolle (für kürzere Pulse) und auf Polarisationskontrolle. Dies wird den Weg für völlig neue Experimente in der Attosekundenphysik ebnen.

Abstract

The emerging field of attosecond physics aims for the temporal investigation and eventually the control of electron dynamics in matter (atoms, molecules or solids) on its genuine time scale, the temporal range of attoseconds (10^{-18} s). Recent experimental examples are the characterization of the photoionization time delays of core electrons in neon atoms or the photoemission time delay between valence and core states of magnesium. Such experiments are based on the generation of attosecond pulses in the extreme ultraviolet to soft x-ray range by high harmonic generation in gases, which is nowadays a well established method and is constantly pushed toward ever higher photon energies by improved laser systems. It will eventually reach the important water window spectral range with adequate photon numbers in the foreseen future. This will extend attosecond physics to biological specimens and may facilitate groundbreaking results in the field of biophysics. Besides the source development, there is a strong demand for corresponding optics development to steer and control attosecond pulses. Multilayer mirrors are key components in attosecond physics with a high degree of freedom, facilitating e.g. the tailoring of attosecond pulse parameters. In this thesis, the design, the accurate nano-fabrication and the characterization of periodic (regular layers) as well as aperiodic (irregular stack design) multilayer mirrors, mainly based on chromium (Cr) and scandium (Sc) layers, is presented. The extremely precise control of the ion beam deposition process enabled the realization of the first chirped multilayer mirrors for the water window with a precise phase control, which can be used for pulse compression (τ=69 as). The mirror's reflectivity performance was additionally improved by ion beam polishing of the interfaces, resulting e.g. in a peak normal incidence reflectivity (21% at the Sc L_3-edge) which is among the highest measured reflectivities of a pure Cr/Sc multilayer mirror. A transmission multilayer quarter wave retarder has been designed, fabricated and characterized to transform linearly polarized attosecond pulses to elliptically polarized pulses, which could allow for the investigation of ferromagnetic materials or chiral molecules with a high temporal resolution. Furthermore, different multilayer mirrors have been applied to spectrally select and shape radiation from a laser-plasma driven undulator source, which enabled e.g. the successful isolation and characterization of femtosecond pulses in the water window close to 300 eV, the highest measured photon energy from such a source so far. Finally, the attosecond timescale was accessible utilizing optimized multilayer mirrors for the generation of isolated attosecond pulses in the soft x-ray range at 145 eV, up to now the highest central energy for characterized (by attosecond electron streaking) table-top attosecond pulses.

With the results presented in this thesis, the control of attosecond pulses by multilayer optics has been extended to higher photon energies (into the water window), to a better pulse dispersion control (for shorter pulses) and polarization control. This will pave the way for entirely new experiments in attosecond physics in the near future.

Chapter 1

Introduction: Attosecond physics on the way from the extreme ultraviolet to the soft x-ray water window spectral range

Multilayer optics are key components in attosecond science and advanced laser sources all around the world. Their spectral field of advanced applications nowadays ranges from the IR, for example as stretcher and compressor components in CPA systems [1], across the extreme ultraviolet XUV range, as a control element in attosecond science [2], up to the soft/hard x-ray regime, as a focusing [3] or monochromatizing [4] element. The described spectral ranges, together with the corresponding photon energies and wavelengths, are illustrated in figure 1.1. This broad field of applications is attributed to their consecutive development which started already in the 1950s/60s [6, 7]. Multilayer mirrors are used as beam steering elements, for focusing or can be

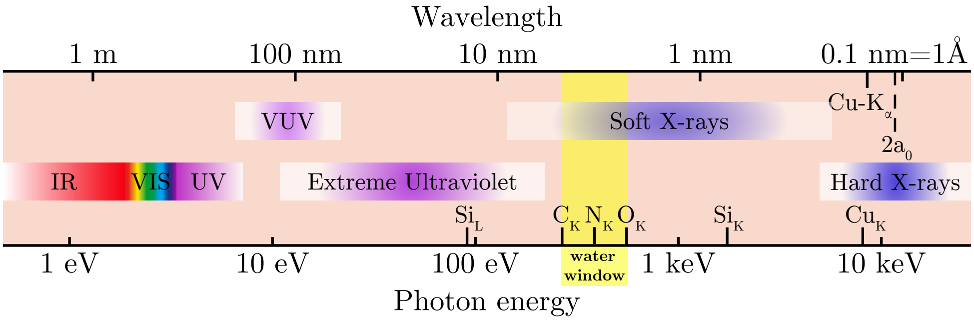

Figure 1.1: The electromagnetic spectrum from IR to hard x-rays. The upper axis shows the wavelength and the lower axis the corresponding photon energy. The spectral range of the water window, defined by the K-shell absorption edges of carbon (C) and oxygen (O), is highlighted (figure adapted from [5]).

used in their advanced application pulse shaping. Multilayer mirrors allow for a high degree of freedom, in terms of spectrally shaping and controlling the spectral phase upon reflection, which becomes more important the shorter the pulses are. The shortest flashes of light are nowadays generated and used in attosecond (1 as=10^{-18} s) physics [8]. Due to bandwidth and electric field requirements, attosecond science takes place in the XUV/soft x-ray range. These high energy regions are of great interest as e.g. inner shell electrons are strongly bound within an atom at these energy scales and their transitions happen on the few fs down to the as time scale. Attosecond physics aims the time resolved investigation of electron dynamics in matter with a never before achieved temporal resolution utilizing, for example, isolated attosecond pulses in pump-probe experiments [9]. This physical field investigates fundamental theories of electron processes like charge transport [10], photoionization [11], nanoplasmonic field oscillations [12] or even cascaded atomic Auger decay [13]. This fundamental research paves the way toward an ever deeper understanding of electron dynamics and finally ends up in their control [14]. With improved laser sources [15] and optics [16] the accessible energy range was pushed to ever higher energies over the past few years, nowadays facilitating attosecond physics at the intersection to the soft x-ray range [17]. A further extension of the energy range to the water window spectral range will pave the way toward attosecond physics on biological specimens. The water window spectral range is defined between the K-shell absorption edges of carbon (284.2 eV) and oxygen (543.1 eV). Its location in the electromagnetic spectrum is highlighted in figure 1.1. The water window serves as an almost perfect spectral range for the investigation of biological processes as the carbon or nitrogen atoms of a cell tissue are highly absorbent, while their natural aqueous environment is transparent in comparison. Figure 1.2 illustrates the importance of this spectral range due to the different penetration distances of x-rays and electrons dependent on their energy. In the 400–500 eV range carbon-rich protein has a far shorter penetration distance than water, thus providing natural contrast of biological material in 10 µm of water, the thickness of a typical cell [5]. Figure 1.2 also shows the big advantage of x-rays in comparison to electrons, since their penetration distance is larger and a higher contrast can be achieved. Thus, much thicker samples can be imaged in-vivo whereas in electron microscopy samples are usually dehydrated and have to be thin (but electrons exhibit a shorter *de Broglie* wavelength and consequently a higher spatial resolution). All these properties make the water window an attractive region for soft x-ray microscopy, which is already possible today [19], or in the near future for time resolved attosecond pump-probe spectroscopy. Every attosecond pump-probe spectroscopy experiment requires tailored pulses being synchronized in central energy and dispersion, in addition to a certain spectral or temporal resolution appropriate to investigate the underlying process of interest. This asks for sophisticated attosecond optics which are mainly multilayer mirrors. It has been mentioned that multilayer mirrors are key components in attosecond science due to their pulse shaping and focusing properties which have been used in attosecond experiments from the very beginning, the first characterization of isolated attosecond

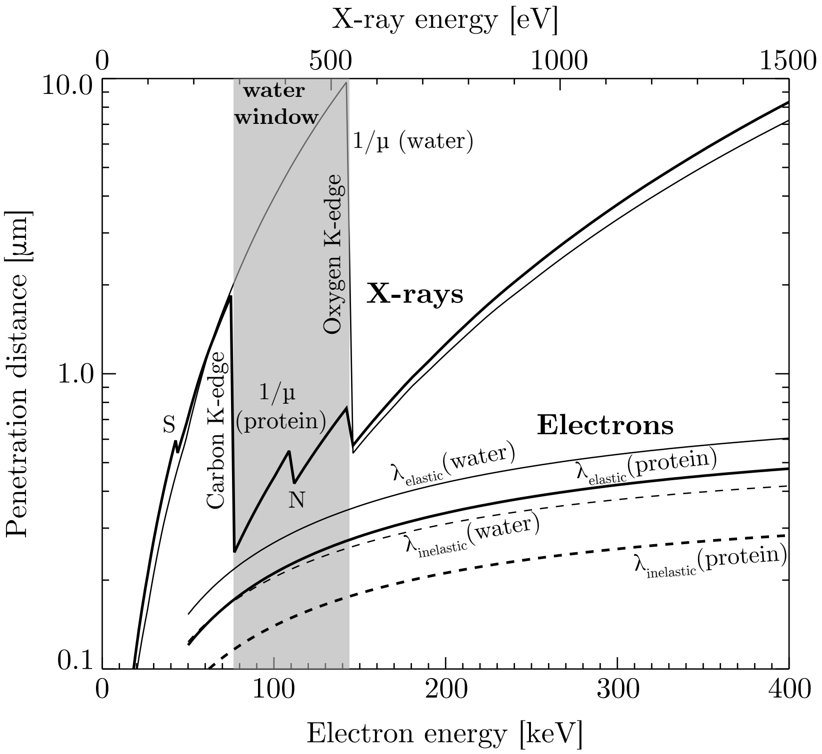

Figure 1.2: Penetration distance in the water window range. Penetration distances in water and protein for electrons and x-rays dependent on their energy. For electrons, the mean free paths λ for elastic and inelastic scattering are shown. The gray area shows the water window range (figure taken/adapted from [18]).

pulses (τ=650 as) in 2001 [20]. The importance of multilayer mirrors increases with the extension of attosecond science to the water window as a higher photon energy puts stringent demands on their realization. This thesis presents the realization, optimization and characterization of the first attosecond multilayer mirrors in the water window and shifts the state-of-the-art optics technology below 120 eV to a three times higher energy regime. Their application by the first characterization of water window pulses from a laser-plasma driven undulator, in addition to the first characterization of isolated attosecond pulses at the up till now highest table-top soft x-ray photon energy at 145 eV, prove their implementation. Attosecond physics is thus on the way toward the soft x-ray water window spectral range.

Chapter 2

Theoretical background

2.1 XUV/soft x-ray sources

There has been a growing interest in applications utilizing ultrafast XUV/x-ray pulses during the past decades. It is prompted by the perspective of getting new physical insights on dynamics in atoms, molecules or solid surfaces. There are various sources generating radiation in this spectral range like electron-impact [21], Cherenkov [22], laser produced plasma (LPP) [23] or the famous synchrotron [24]. Indeed the following sections will focus on three prominent techniques with the potential for a coherent table-top source size combined with a high brightness.

2.1.1 Laser Wakefield Acceleration

Electron acceleration by laser-driven plasma waves is capable of producing ultra-relativistic, quasi-monoenergetic electron bunches, with orders of magnitude higher accelerating gradients and much shorter electron pulses than state-of-the-art RF accelerators [25, 26]. The concept of a laser wakefield accelerator (LWFA) is based on ultrashort few-cycle laser pulses with intensities up to the petawatt range that are focused into a gas target [27, 28]. The concept is illustrated in figure 2.1. The atoms of the gas are ionized by the laser which additionally excites a plasma wave. This plasma wave trails the laser pulse at its group velocity and generates an electric field, the so-called wakefield. This field can be more than three orders of magnitude larger than in conventional accelerators ranging up to the GV/m range. A high laser intensity allows for the plasma wave to break, which results in trapped electrons surfing these accelerating fields. Thus the electrons reach relativistic energies within distances of only a few millimeters compared to tenth of meters at RF accelerators [30]. The pulse duration of these electron bunches is in the 10 fs regime with charges of several hundred pC [31]. This large amount of charge in ultrashort electron bunches results in extremely high peak currents, a key prerequisite for the realization of a table-top FEL [32] which is described next.

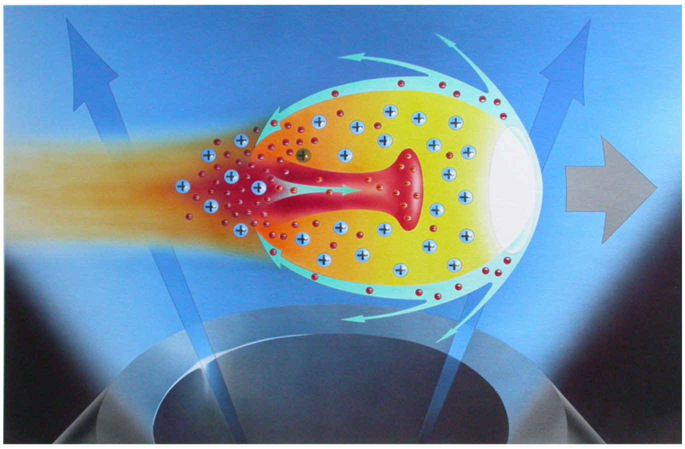

Figure 2.1: Laser wakefield acceleration. The laser pulse (white) propagates (gray arrow) through the gas flowing out of the nozzle (blue arrows). The gas is immediately ionized and the laser expels most of the electrons (red) transversely, while the ions (light blue) stay at their position during the transit of the laser. The electrons move around the bubble (turquoise trajectories) to the point of trajectory crossing, where the electron density is high. Some electrons are injected into the bubble to be accelerated (figure and caption taken from [29]).

2.1.2 Table-top FEL

A free electron laser (FEL) is considered to be the next generation in the evolution of radiation sources. While large facilities are already in operation (LCLS, FLASH), the realization of small powerful table-top systems is still on the status of investigation but first steps are demonstrated [33]. The electrons from the LWFA exit the plasma and are collimated as beam by means of magnetic quadrupole lenses. This highly intense electron beam propagates through an undulator, an array of periodic aligned dipole magnets, which forces the electrons on a sinusoidal trajectory whereby they oscillate transversely to their direction of propagation. This process is illustrated in figure 2.2. This acceleration causes the electrons to emit spontaneous radiation with the wavelength

$$\lambda = \frac{\lambda_u}{2n\gamma^2}\left(1 + \frac{K^2}{2} + \gamma^2\theta^2\right), \tag{2.1}$$

where n is the number of the emitted harmonic, γ is the total electron energy in terms of the electron rest mass $\mathrm{E{=}m_0c^2}$, θ is the angle of the emitted radiation with respect to the direction of propagation of the electrons. The deflection parameter $K{\propto}B_0{\cdot}\lambda_u$ is proportional to the product of the on-axis undulator magnetic field B_0 and its period λ_u. If the electron beam and the generated radiation are very intense the electron motion is modified by the electric field of its own emitted light. The undulator radiation acts on the electrons in the bunch, accelerating and decelerating some of them. This results in a periodic density modulation that are separated by a distance equal to the wavelength of the emitted radiation, the so-called mi-

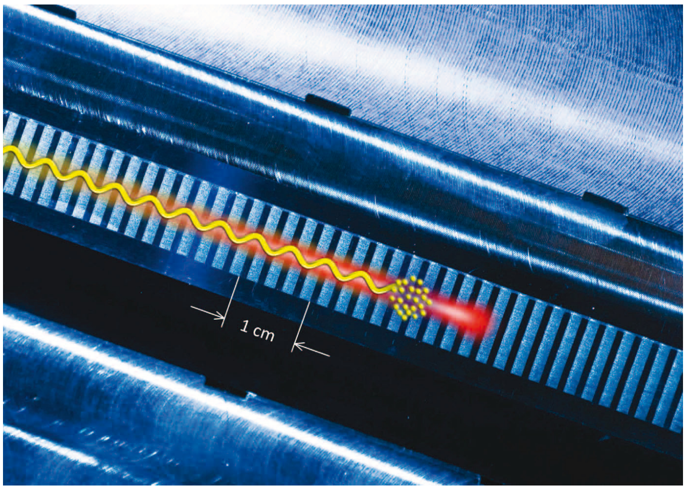

Figure 2.2: Undulator radiation. Highly-relativistic electrons (yellow) are forced on a sinusoidal trajectory by the periodic magnetic field of an undulator. As a result they emit short-wavelength radiation (red) (figure and caption taken from [34]).

crobunches. These microbunches begin to radiate as if they were single particles with enormous charge, the self amplified spontaneous emission (SASE) [35]. Consequently the overall emission is coherent because the distance between two electrons within these microbunches is smaller than the wavelength they emit. This described combination of an undulator, together with LWFA, is used as concept for a table-top FEL. The emitted radiation has to be referred to as table-top undulator radiation rather than table-top FEL radiation because the emitted radiation is incoherent and the realization of coherent emission still deserves research. The first experimental realization of monochromatized table-top undulator radiation in the water window was done in collaboration with the group of Prof. Florian Grüner (LMU, UHH) and Prof. Stefan Karsch (MPQ, LMU). The results are presented in section 4.7.

2.1.3 High Harmonic Generation

High-order harmonic generation (HHG) is a very useful source for coherent radiation in the extreme ultraviolet (XUV) and soft x-ray regime. HHG is a non-linear process which occurs when an intense ($>10^{13}$ W/cm^2) [36] laser pulse is focused into a target (gas [9], solid [37] or liquid [38]). An illustration of the process is shown in figure 2.3. The generated pulses are laserlike coherent, directional and ultrafast with photon energies in the eV–keV spectral range [40]. High harmonic generation is a prerequisite of attosecond physics due to the coherent nature of the process. Attosecond physics will be described in the next section.

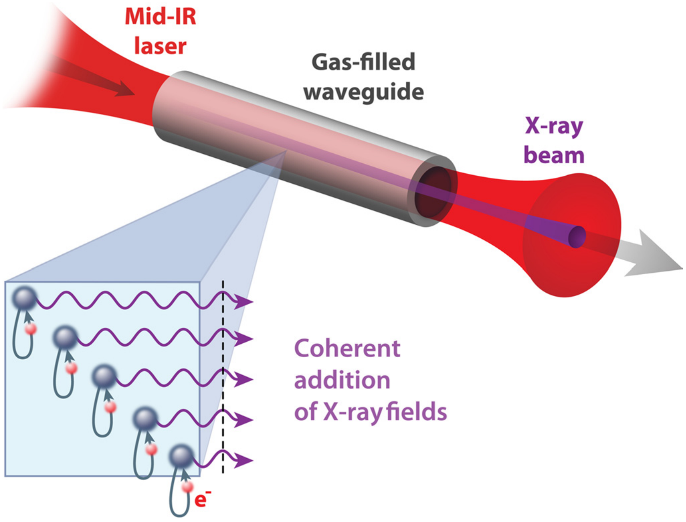

Figure 2.3: Illustration of high harmonic generation. Extreme nonlinear upconversion of a femtosecond laser light to shorter wavelengths. Phase-matched (coherent) addition of the high harmonic x-ray fields emitted by many atoms in the medium is shown (figure and caption taken from [39]).

2.2 The background of attosecond physics

2.2.1 Time scales of physical processes

Structure and dynamics in the microcosm are inherently connected by the laws of quantum mechanics. If a particle is put in a superposition of its ground state $\phi_0(x)$ of energy W_0 and the first excited state $\phi_1(x)$ of energy W_1, the superposition state is referred to as *wave packet* [41]. Solution of the Schrödinger equation for the particle's wave function $\psi(x)$ yields an oscillatory motion with the oscillation period $T_{osc}=2\pi(\hbar/\Delta W)$, where $\Delta W=W_1$-W_0. The larger the energy separation ΔW between the two eigenstates, the faster the motion of the particle in the superposition state. An energy spacing of meV implies that the fundamental time scale for the motion of molecules is on the order of tens to hundreds of femtoseconds [42]. This timescale is the motion of the chemical bond [43] and of the vibrational states of atoms in a crystal lattice [44]. The motion of individual electrons in semiconductor nanostructures, molecular orbitals or the inner shells of atoms occurs on progressively shorter intervals of time ranging from tens of femtoseconds down to attoseconds. Motion within nuclei is predicted to unfold even faster, typically on a zeptosecond time scale. An overview of observable physical processes is depicted in figure 2.4. A bound electron has a time scale in the attosecond range. A time scale often given is the time it takes an electron to complete one rad of its orbit in the ground state of hydrogen [45]: $\tau_{atomic}=\hbar/2U_H\approx 24$ as (often called the atomic unit of time), where U_H is the binding energy of the hydrogen atom (13.6 eV). The oscillation period of valence electron wave packets in bound atomic or molecular systems is on the order

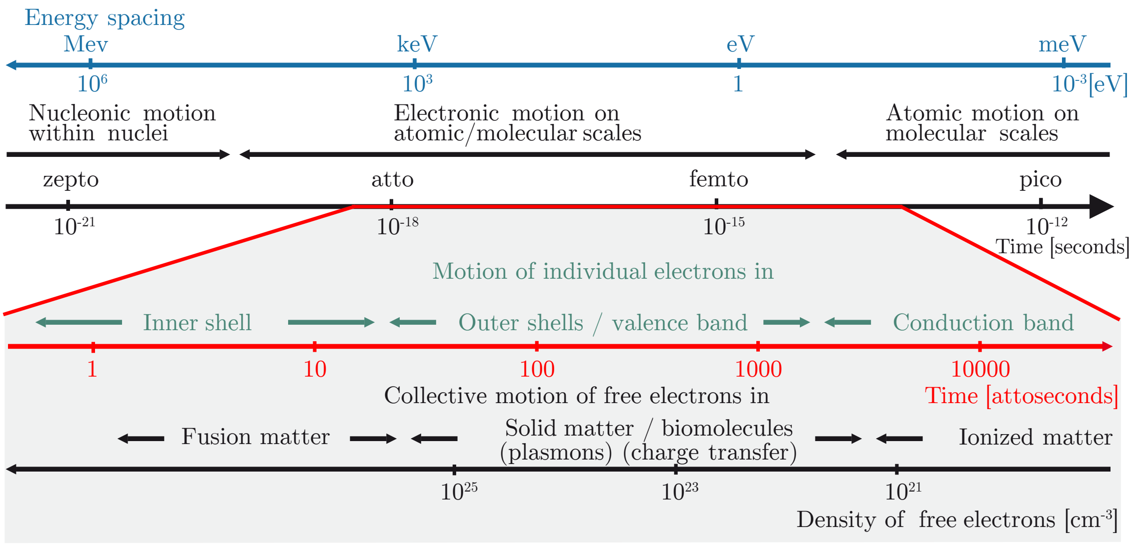

Figure 2.4: Attosecond physics is the science of electrons in motion. Characteristic time scales for microscopic motion and its connection with energy spacing between relevant stationary states (upper panel); characteristic time scales for the motion of one or several electrons and for the collective motion of an electronic ensemble (lower panel)(figure and caption taken from [41]).

of 100 as. Thus the motion of electrons inside atoms, in molecular orbitals, or confined in nanometer-scale potentials in semiconductors, like the collective dynamics of free electrons in high-density ionized gases, solid-density plasmas, or fusion targets, is naturally measured in attoseconds [41]. The generation of attosecond pulses is accessible in the XUV/soft x-ray energy range and will be described in the following section.

2.2.2 The generation of attosecond pulses

The discovery and realization of the laser [46] in 1960 was the starting point for achieving ever shorter pulses in order to resolve the dynamics of atomic processes. Most technological developments were based on mode-locking [47] or Q-switching [48]. Kerr lens mode locking [49] nowadays enables the generation of few fs pulses utilizing diode pumped Ti:sapphire crystals. They can be tuned in a large wavelength range of 650–1100 nm but are mainly used at the most efficient wavelengths near 800 nm. Smaller wavelengths and a large spectral bandwidth are necessary in order to decrease the pulse duration significantly down to the attosecond regime. This can be obtained by HHG (section 2.2.2.1) and for isolated pulses it is very beneficial to drive the HHG process with close to single-cycle pulses. Pulse energies in the µJ–mJ range are necessary for a reasonable photon flux at kHz repetition rates, since HHG is a very nonlinear and quite inefficient process. This prerequisite for HHG is realized by chirped pulse amplification (CPA) [50], the consecutive spectral pulse broadening by propagation through a gas-filled hollow-core fiber [51] and the pulse compression afterwards by aperiodic chirped multilayer mirrors [52], nowadays enabling the generation of nearly single-cycle IR laser pulses with pulse durations below 4 fs [53] and mJ pulse energies. This high intense pulses are phase stabilized and are nowadays mainly used for HHG [15], a process which is described in the following section.

2.2.2.1 High harmonic generation in gases

Up until now a common laser based on population inversion for the XUV is not realizable. The stimulated absorption rate $B_{1,2}$ and the stimulated emission rate $B_{2,1}$ strongly decreases for short wavelengths, in comparison to the spontaneous emission rate $A_{2,1}$ [54]:

$$B_{1,2} = B_{2,1} \propto A_{2,1} \ \cdot \ \lambda^3. \tag{2.2}$$

Other sources have to be found for the generation of coherent radiation in the XUV/soft x-ray range with isolated pulse durations in the fs or sub-fs range. The most prominent are FEL (section 2.1.2) and HHG. The following sections will focus on HHG as it is to date the only technique for the stable generation of attosecond pulses in the XUV with $\approx 10^9$ photons. HHG is the frequency up-conversion in non-linear multi-photon processes where N photons of the fundamental frequency ω_0 are converted to one XUV photon with the frequency $N{\cdot}\omega_0$. It was first demonstrated in solids [55] and a few years later in gases [56]. The generation of attosecond pulses in the XUV/soft x-ray range using HHG in gases was first observed in 1988 [57] and is nowadays the most spread technique. It requires laser intensities on the gas target of $>10^{13}$ W/cm^2 [36] and allowed up to now the generation of the shortest pulses of 67 as [58] and 80 as [8]. HHG in gases can be explained with the semi-classical three step model [59, 60] and its principle, as shown in figure 2.5(a). The model describes light-matter interaction, where the electric field strength of the laser is comparable in its magnitude to the electronic binding field in the atom. The strong electric field (Keldysh parameter $\gamma \leq 1$ [62]) from the laser bends the atomic binding potential. The lowered binding potential can now be tunneled by the electron because the probability for this purpose was strongly increased (1^{st} step). The freed electron senses immediately the electric field of the laser and gets accelerated. With the oscillating electric field changing its sign the electron gets accelerated in the opposing direction and is thus redirected in space back to its parent ion (2^{nd} step). There is a probability of about 10^{-5} [63] that the electron recombines with its parent ion and emits a single XUV photon with an energy, equal to the kinetic energy the electron has picked up from N laser photons during the acceleration process (3^{rd} step):

$$\hbar\omega_{\mathrm{XUV}} = N\hbar\omega_{laser}. \tag{2.3}$$

The electron follows different trajectories depending on the time (phase of the laser field) when the ionization occurs (figure 2.5(b)). When the electron ionizes at a phase

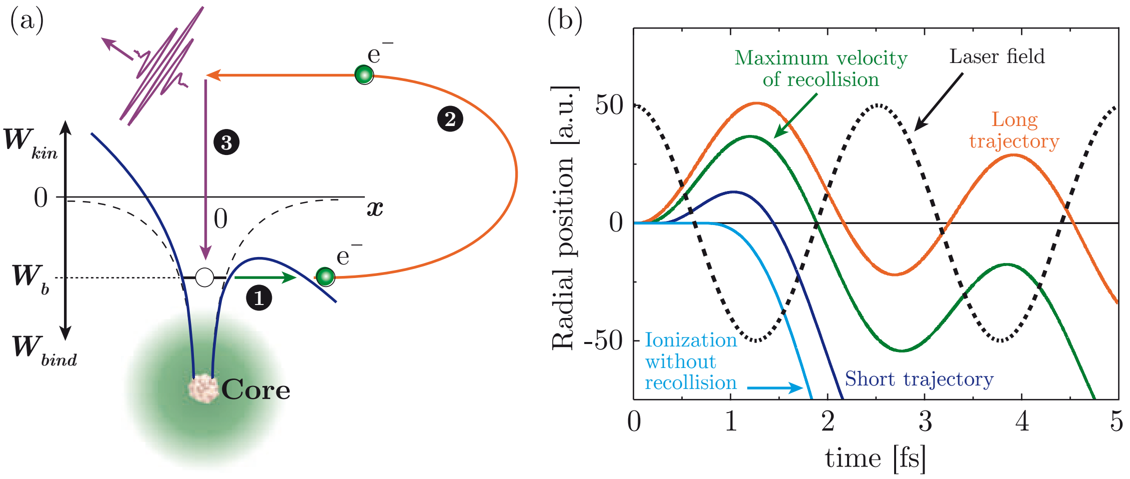

Figure 2.5: The semi-classical three step model. (a) Illustration of the three-step mechanism of HHG that leads to the creation of attosecond pulses. (b) Trajectories of the electrons involved in HHG as a function of the time (phase of the driving field) when the ionization occurs. When the electron ionizes at a phase of +0.3 radians with respect to the laser field maximum, the highest XUV photon energy is produced. Electrons emitted after and before this time follow so-called short and long trajectories, respectively. The dependence of the XUV photon energy on the instance of recombination implies that the attosecond pulses are chirped (figure and caption taken/adapted from [61]).

of +0.3 radians, with respect to the laser field maximum, the highest XUV photon energy is produced. This is referred to as the cutoff energy and is defined as:

$$E_{cutoff} = I_P + 3.17 \cdot U_P, \tag{2.4}$$

with the target atom ionization potential I_P and the ponderomotive potential of the laser $U_p = \frac{Ie^2}{2m_0\epsilon_0 c\omega_L^2}$. Electrons emitted after and before this time follow short and long trajectories, respectively. The short ones result in positively chirped low energy pulses, whereas the long ones result in negatively chirped pulses but with a lower recombination probability compared to the short ones. One can experimentally choose the preferred sort of trajectories by the position of the gas target in respect to the laser focus [41]. However, phase matching over the complete generation volume is required in order to avoid destructive interference of generated harmonics. High harmonic radiation is usually positively chirped because short trajectory high harmonics have a higher efficiency compared to the long ones. The GD scales linearly with energy and steepen when the cutoff is reached [64]. The resulting spectrum of gas harmonics show individual harmonics being spaced by $2{\cdot}\omega_0$ with a steep drop in photon number within the first few harmonics (the perturbative regime). It is followed by a plateau region which ranges up to the cutoff region. Typical measured high harmonic spectra dependent on the CEP of the laser are shown in figure 2.6. The perturbative regime and part of the plateau region is suppressed in the measurement

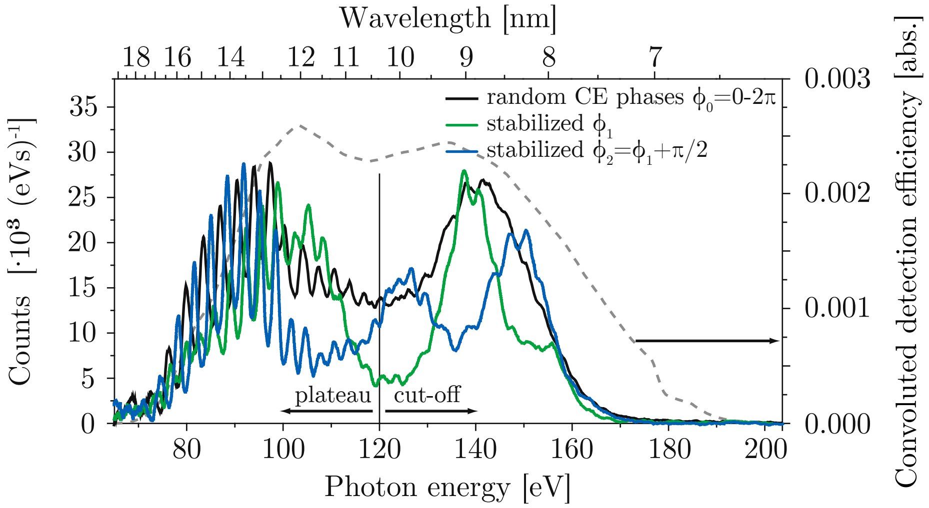

Figure 2.6: High harmonic generation in helium. Measured XUV photon spectra generated in helium shown in blue and green for different CE-phases and in black unstabilized. The theoretical detection efficiency is given by the dotted gray line (figure and caption taken/adapted from [65]).

due to the usage of a 150 nm thick Mo filter.

If the laser intensities are too large (γ« 1), the electric laser field bends the binding potential such that the electrons can leave the core freely without tunneling. A plasma is generated and the probability for recombination, thus the probability for HHG gets highly suppressed as most electrons miss their parent ion spatially due to non-vanishing kinetic energies at their release [66]. This limits a possible higher cutoff energy (equation 2.4) in terms of higher laser intensities. One must either use a gas target where the atoms have a higher binding energy (a higher ionization potential I_P) or reduce the fundamental frequency ω_0. A smaller frequency ω_0 comes along with a longer laser wavelength λ_L. Recently a 3.9 µm laser at high intensities was used to generate a high harmonic spectrum up to ≈1.6 keV which corresponds to approximately the 5000th harmonic [40]. The individually measured high harmonic spectra dependent on the driving wavelength are shown in figure 2.7.

2.2.2.2 Pulse trains and isolated attosecond pulses

High harmonics are generated every half cycle of the laser field (peaks in the electric field) generating a train of attosecond pulses [67] (figure 2.8). These pulses are spaced by $\tau=\frac{2\pi}{2\omega}$ which corresponds from Fourier analysis to a peaked spectrum with spaced harmonics by $\Delta\omega=2\omega$. Due to the spatial symmetry of gases only odd harmonics occur. Solids or liquids also show the even harmonics in the generated spectrum [37], since their spatial symmetry is broken. Absolute delay measurements of photoemission originating from different states [9] or the direct observation of electron propagation [17] require single attosecond pulses, since the observation should be

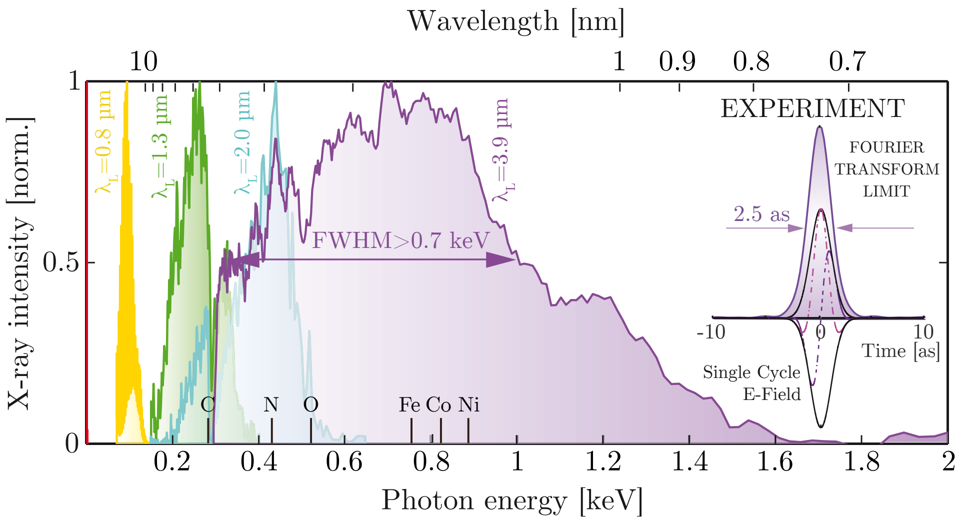

Figure 2.7: Bright coherent ultrahigh harmonics in the keV x-ray regime. Experimental HHG spectra emitted under full phase matching conditions as a function of driving-laser wavelength (yellow: 0.8 µm, green: 1.3 µm, blue: 2 µm, purple: 3.9 µm (FWHM>0.7 keV)). (Inset) Fourier transform-limited pulse duration of 2.5 as (figure taken/adapted from [40]).

related to one unique event. In principle there are two different techniques to isolate single attosecond pulses from the HHG process. One can either use temporal gating [68] by limiting the HHG process to a small time window that only one pulse is

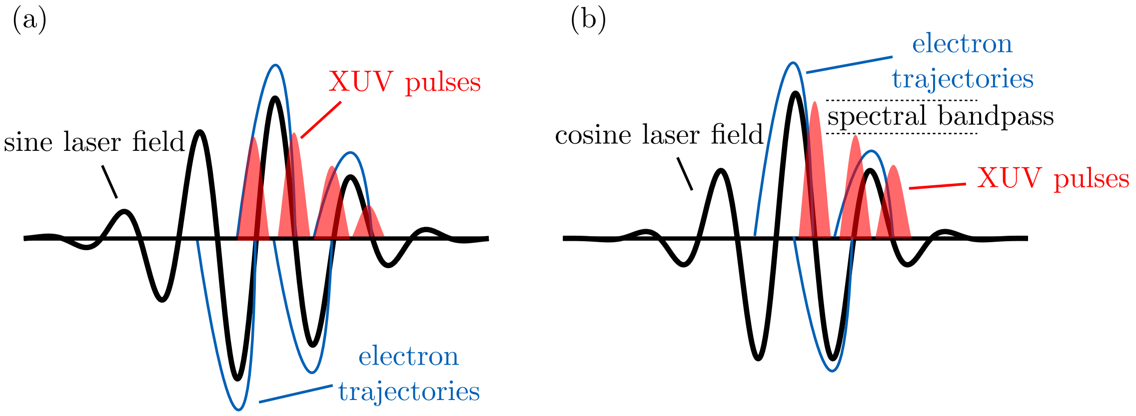

Figure 2.8: Attosecond pulse train generation and trajectories. Attosecond pulse generation in dependence of the CEP. The maximum pulse energy is indicated by its height and depends on the laser field amplitude of the half cycle before recombination. In case of a sine CEP pulse (a) this leads to two maximum energy pulses whereas for a cosine CEP pulse (b) only one single pulse with maximum energy is generated. An isolated single attosecond pulse can now be achieved by filtering the spectral cutoff region which originates from the left pulse in the right panel (dashed black).

generated or isolate one single pulse from the train (figure 2.8(b)) by spectral gating [69]. Focused few cycle laser pulses with a distinct CEP into a HHG gas target is the prerequisite for the stable generation of isolated attosecond pulses. The CEP is usually stabilized and strongly determines the electric field shape of the laser for short pulses. Furthermore the electric field strongly influences the temporal and spectral structure of the nonlinear HHG process, as can be seen in figure 2.8, where a comparison of a sine field (a) to a cosine field (b) is shown. In case of an unstabilized CEP one usually measures the CEP of each pulse with a phasemeter and assigns it to the pulses afterwards. It is known as single-shot carrier-envelope phase tagging [70]. In the case of a cosine electric field the maximum field of the central half cycle exceeds that of the neighboring oscillations which means that the cutoff region is from one single attosecond pulse. The usage of a spectral bandpass (black dashed lines in figure 2.8(b)) allows to isolate a single attosecond pulse from the HHG process.

Setup of an typical attosecond beamline

A typical normal incidence beamline setup for the generation and characterization of attosecond pulses is shown in figure 2.9. A high intensity few cycle phase-stabilized laser pulse is focused into a gas target for HHG. The generated high harmonic radiation propagates together with the laser which has, due to its lower frequency, a larger divergence than the harmonic beam. A thin metal mounted at the center of an IR transmissive pellicle is used to block the laser from the inner XUV traveling path but does a part of the harmonic spectrum transmit. One has to introduce an adjustable time delay between the now separated XUV pump and IR probe beam in

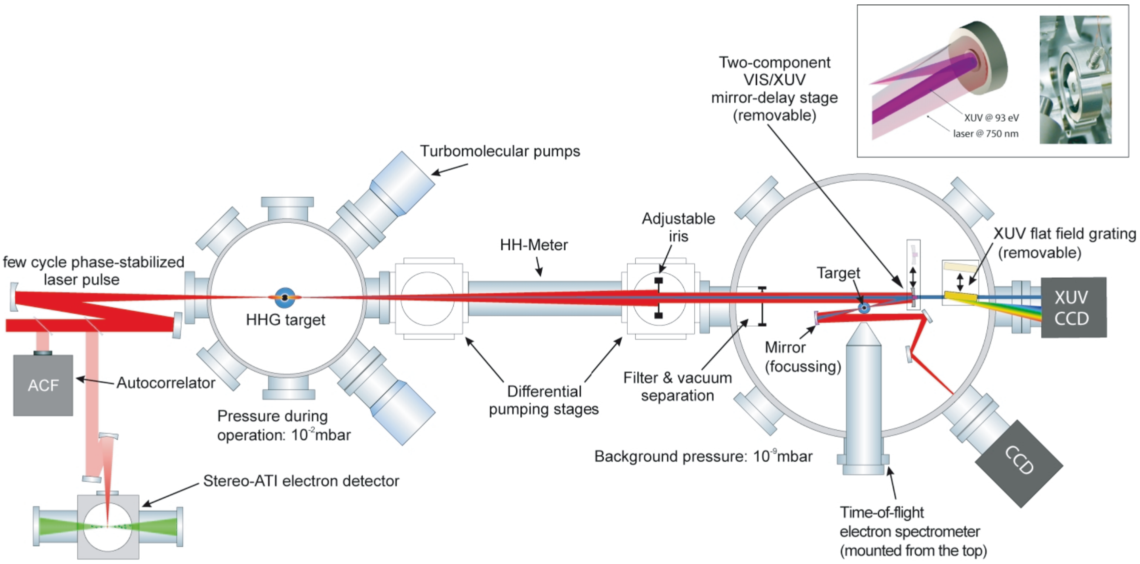

Figure 2.9: Setup of a normal incidence attosecond beamline. Typical collinear single attosecond generation setup (figure taken from [71]).

order to measure attosecond pulses by the attosecond streak camera (section 2.2.4.1). This is realized by a double mirror which reflects and focuses both the XUV and the laser beam under an angle of about 5 degree normal incidence into a target. An alternative 45 degree setup, which is used at the *AS2* beamline at MPQ, can be found in [72]. The harmonic beam is there separated in space from the laser beam by means of a perforated mirror. This allows two independent shaping paths before both pulses are combined again afterwards by a second perforated mirror. A consecutive toroidal mirror focuses both pulses into a target. This beamline setup has not been used for the results in this thesis but should be mentioned as a powerful alternative option.

The double mirror

The double mirror is shown in the box in the upper right of figure 2.9 and is a key component in this type of setup. Its inner part is coated with an XUV multilayer and is movable with respect to the outer part (which reflects the laser) by means of a precision piezo stage allowing the insertion of a time delay between both pulses. A schematic sketch and the time delay purpose is shown in figure 2.10(a) and (b), respectively. There are three tasks for the mirror which have to be fulfilled:

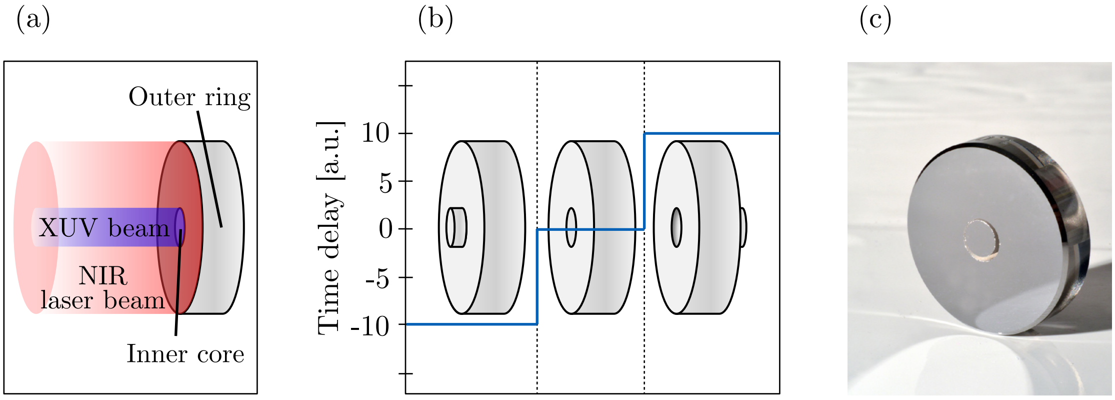

Figure 2.10: Double mirror for attosecond experiments. (a) Sketch of the double mirror. The XUV is reflected from the core (a metal filter was previously used to block the laser from the inner part) while the IR is reflected from the outer ring due to the different divergence of both beams. (b) Introduced time delay between both pulses dependent on the core position in respect to the outer ring. (c) Photograph of a coated double mirror (courtesy of Thorsten Naeser).

1. Focusing both the attosecond and laser pulse into the target. Usually a spherical substrate with a radius of curvature of ROC=25 cm, resulting in a focal length of f=12.5 cm, is used for this purpose.

2. Introducing a delay between the attosecond and laser pulse by moving the inner core (diameter in the 3–5 mm range) with respect to the outer ring. This delay

is used for the measurement of attosecond pulses by attosecond streaking [73] (section 2.2.4.1).

3. Shaping of attosecond pulses, mainly in terms of the central energy and the pulse length.

The third point will be described in the following section.

2.2.3 Shaping attosecond pulses

Shaping the attosecond pulse(s) is one of the main tasks of an optic in attosecond experiments. Attosecond optics should be in principle designed such that in the best case an absolute control of all relevant attosecond pulse parameters is achieved. These parameters are mainly the central energy, the spectral shape, the spectral phase and the pulse duration. Thus one has to know how the temporal and the spectral pulse properties are connected to each other. This connection is mathematically given by the Fourier transform, which allows a transformation of the electric field from the spectral into the temporal domain and vice versa. The one dimensional electric field of a light wave in the spectral and temporal domain is

$$E(\omega) = E_\omega e^{-i\phi_\omega} \quad \textit{respectively} \quad E(t) = E_t e^{-i\phi_t} \tag{2.5}$$

with an amplitude E_ω and E_t and the phase terms ϕ_ω, ϕ_t. One representation can be converted into the other by the Fourier transform $\mathscr{F}^+$ and its inverse $\mathscr{F}^-$:

$$E(\omega) = \mathscr{F}^+(E(t)) = \int\limits_{-\infty}^{\infty} E(t) e^{i\omega t} dt \tag{2.6}$$

and

$$E(t) = \mathscr{F}^-(E(\omega)) = \frac{1}{2\pi} \int\limits_{-\infty}^{\infty} E(\omega) e^{-i\omega t} d\omega. \tag{2.7}$$

The most important influence on the pulse duration possesses the spectral bandwidth and the spectral phase which will be addressed in the following sections.

2.2.3.1 Time-bandwidth product

For almost all calculations, a good first approximation for any ultrashort pulse is the Gaussian pulse (with zero phase). The electric field of a Gaussian pulse in its temporal representation reads like

$$E(t) = E_t e^{-\frac{t^2}{2\sigma^2}} e^{-i\omega_0 t} e^{-i\phi_t}, \tag{2.8}$$

where E_t is the field amplitude, σ defines the width, ω_0 is the central frequency and ϕ_t is the phase term. Instead of using σ to express the electric field, one usually chooses the FWHM pulse length which is defined in terms of the pulse intensity:

$$\tau_0 = \mathrm{FWHM}\left(|E(t)|^2\right) = 2\sigma\sqrt{\ln 2}. \tag{2.9}$$

Inserting this relation in equation (2.8) yields the Gaussian FWHM form:

$$E(t) = E_t e^{-2\ln 2\frac{t^2}{\tau_0^2}} e^{-i\omega_0 t} e^{-i\phi_t}. \tag{2.10}$$

In case of a vanishing phase term (ϕ_t=0), the Fourier transform of equation (2.6) can be used to retrieve the spectral shape:

$$\begin{aligned} E(\omega) = &\int_{-\infty}^{\infty} E(t)e^{i\omega t}dt = \int_{-\infty}^{\infty} E_t e^{-2\ln 2\frac{t^2}{\tau_0^2}} e^{-i\omega_0 t} e^{i\omega t} dt = \\ =&E_t \int_{-\infty}^{\infty} e^{-\frac{2\ln 2}{\tau_0^2}\cdot t^2 - i(\omega_0-\omega)t} dt = E_t\sqrt{\frac{\pi\tau_0^2}{2\ln 2}} \cdot e^{-\frac{(\omega_0-\omega)^2}{8\ln 2}\tau_0^2}. \end{aligned} \tag{2.11}$$

In the last step, the integral was evaluated using the relation $\int e^{-Ax^2-Bx}dx = \sqrt{\frac{\pi}{A}}e^{\frac{B^2}{4A}}$. For the evaluation of the bandwidth, it is valid to center the electric field and set $\omega_0 = 0$. One chooses the FWHM in terms of the intensity equal to equation (2.9) and search for the ω values where:

$$|E(\omega)|^2 = \frac{1}{2}|E(0)|^2 \tag{2.12}$$

$$|e^{-\frac{\omega^2}{8\ln 2}\tau_0^2}|^2 = \frac{1}{2}|e^0|^2 \tag{2.13}$$

$$\frac{\omega^2}{8\ln 2}\tau_0^2 = \frac{\ln 2}{2} \tag{2.14}$$

$$\omega = \pm\frac{2\ln 2}{\tau_0} \tag{2.15}$$

Since the bandwidth ranges from $-\omega$ to $+\omega$ one gets the bandwidth by $2{\cdot}\omega$ (equation 2.15) and ends up with the time-bandwidth product of:

$$\Delta\omega = \frac{4\ln 2}{\tau_0} \Leftrightarrow \Delta\omega\tau_0 = 4\ln 2 \approx 2.77. \tag{2.16}$$

Another handy formulation using common attosecond physics units is:

$$\Delta E\ [\mathrm{eV}] \cdot \tau_o\ [\mathrm{as}] \approx 1824\ [\mathrm{eV}\cdot\mathrm{as}]. \tag{2.17}$$

This time-bandwidth relation shows an inversely proportional relation and is depicted in figure 2.11. As a vanishing phase term ϕ_t has been assumed the plotted pulse length is the lower limit for a given Gaussian spectrum. Pulses which fulfill this relation are referred to as 'Fourier-limited' and cannot be any shorter. Two selections are highlighted in figure 2.11.

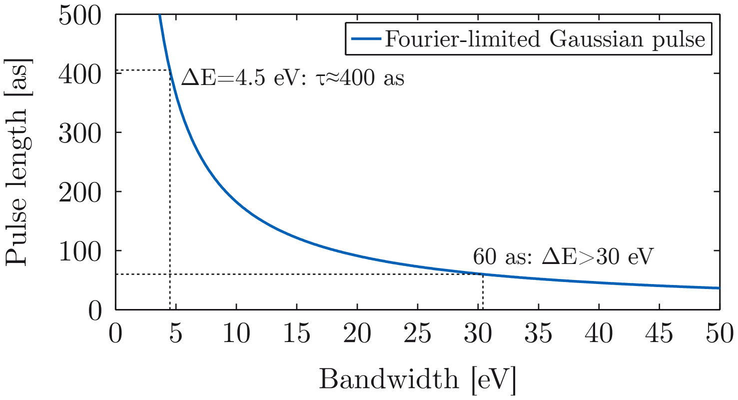

Figure 2.11: Fourier limited pulse length dependent on the spectral bandwidth. Pulse length of a Gaussian pulse dependent on its spectral bandwidth. Two examples are highlighted. A bandwidth of ≈4.5 eV is typically used in attosecond experiments, as a trade-off between spectral and temporal resolution, leading to a pulse duration of τ≈400 as. Future experiments aim for pulses around 60 as where a spectral bandwidth of more than 30 eV has to be addressed.

2.2.3.2 The spectral phase dependence

Neglecting the temporal phase term ϕ_t in the last subsection yielded a Gaussian pulse in the spectral domain (equation (2.11)) with vanishing additional spectral phase terms ϕ_ω. The spectral to temporal transform is now performed to investigate the effect of the spectral phase ϕ_ω on the pulse length of a Fourier-limited (ϕ_ω=0) test pulse. A Gaussian test pulse with a bandwidth of 30 eV and a center energy of 300 eV is assumed for the simulations (figure 2.12(a)). One combines equation (2.11) and equation (2.16) to:

$$E(\omega) = \underbrace{e^{-2\ln(2)\frac{(\omega_0-\omega)^2}{\Delta\omega^2}}}_{G_\omega} e^{-i\phi_\omega} = G_\omega e^{-i\phi_\omega}, \tag{2.18}$$

with an ω dependent spectral amplitude G_ω and the additional spectral phase term ϕ_ω. One can develop the spectral phase ϕ_ω in terms of a Taylor series around the central energy ω_0 [74]:

$$\begin{aligned} \phi_\omega = \phi(\omega) = \sum_{n=0}^{\infty} \frac{1}{n!} c_n (\omega-\omega_0)^n = \\ = c_0 + c_1(\omega-\omega_0) + \frac{1}{2} c_2 (\omega-\omega_0)^2 + ..., \end{aligned} \tag{2.19}$$

with the expansion coefficients $c_n = \frac{d^n}{d\omega^n}\phi(\omega)|_{\omega=\omega_0}$. The first term

$$c_0 = \phi_0 \tag{2.20}$$

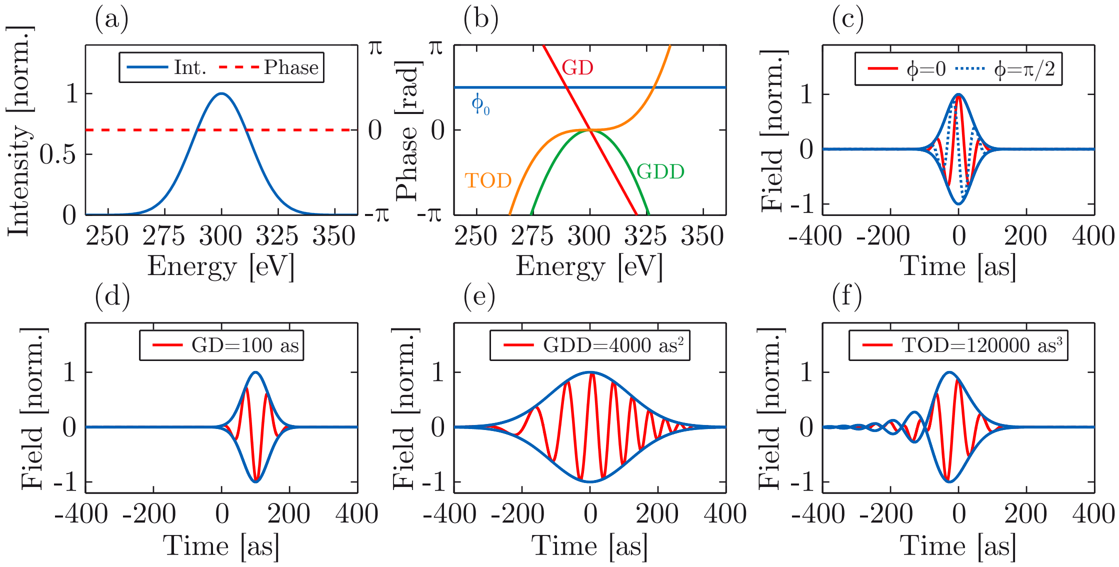

Figure 2.12: Phase influence on an attosecond test pulse. (a) A Gaussian test pulse with a bandwidth of 30 eV and a center energy of 300 eV was assumed for the simulations. (b) Spectral phase trajectories for an offset of $\phi_0{=}\pi/2$ (blue), a GD=100 as (red), a GDD=4000 as^2 (green) and a third order dispersion of TOD=120000 as^2 (orange). (c), (d), (e) and (f) show the individual effect on the pulse in the temporal domain. The blue line indicates the envelop whereas the red line depicts the shape of the electric field.

of equation (2.19) adds a constant offset to the spectral phase. An additional spectral phase term of $\pi/2$ was exemplarily assumed for the effect of the phase offset ϕ_0. While this results only in an offset in the frequency domain (blue line figure 2.12(b)) this yields a shift of the carrier-envelope phase (CEP) in the temporal domain (figure 2.12(c)). The CEP is defined as cosine when the electric field maximum coincides with the maximum of the pulse envelope, while it is sine if the electric field vanishes at the envelope maximum. The effect of the phase offset can be neglected when shaping attosecond pulses, since it does not affect the intensity shape and thus the pulse length.

The second term of equation (2.19) is related to the group delay (GD) as:

$$c_1 = \phi' = \frac{d\phi_\omega}{d\omega} := -\mathrm{GD} \tag{2.21}$$

and, throughout this thesis, is defined as the negative derivative of the phase in order to match the sign with the second derivative, the GDD. The GD is inversely proportional to the group velocity v_g: GD$\propto\frac{1}{v_g}$. The GD arises if the spectral phase slope is unequal zero (red line figure 2.12(b)) and its temporal effect is shown for a GD of 100 as in figure 2.12(d). It corresponds to a temporal shift of the pulse envelope and does not influence the pulse duration but the CEP.

The third term of equation (2.19) is related to the group delay dispersion (GDD):

$$c_2 = \phi'' = \frac{d^2\phi_\omega}{d\omega^2} := -\mathrm{GDD} \Leftrightarrow \mathrm{GDD} = \frac{d}{d\omega}\frac{1}{v_g} \tag{2.22}$$

and is the lowest order phase term which temporally broadens a pulse. Different frequencies are shifted differently far in time, thereby all frequencies are temporally lined up and the pulse gets 'chirped'. In case of a positive GDD the frequency increases ('up-chirp') in time and vice versa for a negative one ('down-chirp') [75]. An GDD of 4000 as^2 is assumed for the simulation resulting in a parabola phase profile in the spectral domain (green line figure 2.12(b)) and a broadened pulse in the time domain (figure 2.12(e)).
The last coefficient of equation (2.19) which is considered in the simulation is the third order dispersion (TOD):

$$c_3 = \phi''' = \frac{d^3\phi_\omega}{d\omega^3} := \mathrm{TOD}. \tag{2.23}$$

Third and higher order phase terms also broaden the pulse like the GDD but with a smaller effect. Figure 2.12(b) (orange line) shows the cubic parabola phase profile in the frequency domain for a TOD=120000 as^2. The effect of the TOD in the temporal domain manifests itself in an asymmetric pulse broadening (figure 2.12(f)) which is also the case for even higher order phase terms. Summarized, equation (2.19) can be rewritten with all the definitions to:

$$\begin{aligned}\phi_\omega =& \phi_0 - \mathrm{GD}(\omega_0)\cdot(\omega-\omega_0) - \frac{1}{2}\mathrm{GDD}(\omega_0)\cdot(\omega-\omega_0)^2 + \\ &+\frac{1}{6}\mathrm{TOD}(\omega_0)\cdot(\omega-\omega_0)^3 + \ldots,\end{aligned} \tag{2.24}$$

where the spectral phase is now defined by all discussed phase effects.
The previous results show that the GDD has the highest influence on the pulse length. Thus it is the most important parameter for optics, which has to be addressed, when attosecond experiments should be realized with attosecond pulses close to their Fourier limit. The pulse length is dependent on the GDD value and can be calculated by

$$\tau = \tau_0\sqrt{1+\frac{16\cdot(\ln 2)^2\cdot \mathrm{GDD}^2}{\tau_0^4}}. \tag{2.25}$$

Figure 2.13(a) shows the final pulse length when certain GDD values are added to a Fourier-limited Gaussian pulse. The black dashed line indicates the Fourier limit. Equation (2.25) shows that a pulse broadening of ≈5% appears when $\tau_0 \approx 3\sqrt{\mathrm{GDD}}$. Figure 2.13(b) depicts the final pulse length of a 60 as Fourier-limited Gaussian pulse dependent on the GDD. One example is highlighted namely the pulse is broadened to three times its duration by adding a GDD of only 4000 as^2. These results show that controlling the GDD is essential for tailored attosecond pulses.

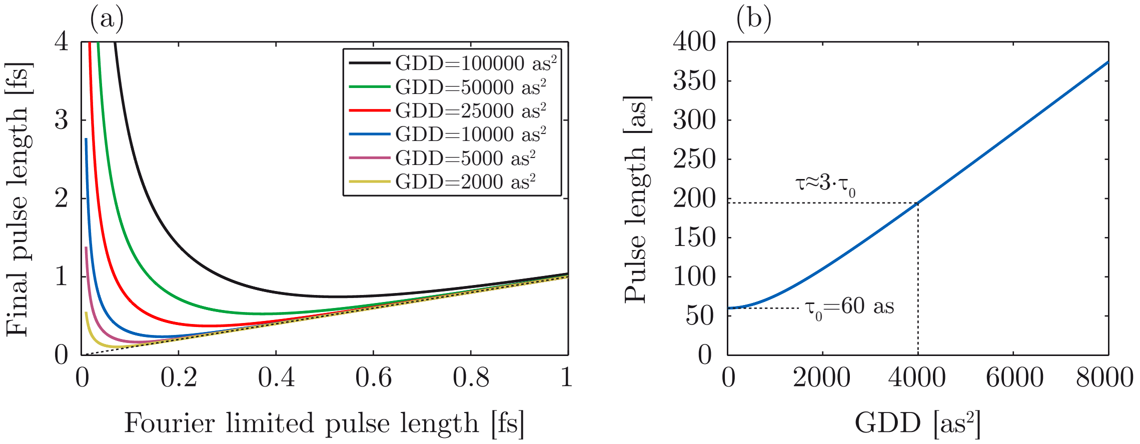

Figure 2.13: Pulse length dependence on the group delay dispersion. (a) Effective final pulse length as a result of adding certain group delay dispersion (GDD) values on a Fourier limited pulse length. (b) Pulse length broadening of a Fourier limited 60 as pulse dependent on the GDD. Adding a GDD of 4000 as^2 leads to an approximately three times longer pulse duration.

2.2.3.3 Requirements on attosecond pulse shaping optics

Each attosecond experiment requires its individual perfectly synchronized pulse. As coherent XUV/soft x-ray sources are limited in their tunability this has to be addressed by pulse shaping attosecond optics. The most important pulse requirements can be summarized based on the results from the previous sections:

- The need for **spectral selective optics**, since the **center energy** E_0 of a pulse has to be synchronized with experimental spectral requirements which is especially important in resonance measurements. This makes a high demand on multilayer accuracy. Almost all attosecond pump-probe experiments use the kinetic energy of photoelectrons as signal (section 2.2.4.1), where various electron sources may superimpose the signal of interest. The electrons may originate from e.g. Auger lines or from the co-propagating IR/VIS laser pulse on the target. The laser pulse frees electrons by multi photon above threshold ionization (ATI) at low energies up to 30–40 eV. Working at higher center energies and far off Auger lines reduces the influence of the superimposed spectra and results in a cleaner photoelectron signal. It may also facilitate shorter pulses as the required relative bandwidth $\Delta E/E$ decreases with increasing center energy. Additionally one may choose the center energy according to the transmission properties of possibly used metal filters (section 2.3.3.1) which may result in spectral cleaner pulses.

- Section 2.2.3.1 has shown the importance of the **spectral phase** ϕ_ω. Most experiments desire a Fourier-limited pulse length which presumes a flat pulse phase. Controlling high order phase terms becomes important when two-photon experiments are realized, where the photo excitation may be coherently controlled with chirped pulses [76]. Thus optics should be able to compensate or introduce a certain amount of GDD for adjustment of the pulse length and the chirp.

- The **bandwidth** and the **spectral shape** define the spectral resolution and the shortest possible pulse length τ_0. A trade-off between a high temporal resolution and a high spectral resolution has to be found, since the time-bandwidth relation (section 2.2.3.1) allows only one of them.
- **Non angular or non chromatic disperse** optics are desired, since e.g. gratings or zone plates [77] broaden the pulse in the time domain.
- A **large photon number** (in attosecond experiments typically $>10^7$ photons per second) is required for many experiments. Thus **low-loss optics** facilitating a high photon throughput are of uttermost importance as the photon flux often limits the realization of certain experiments.

2.2.4 Metrology for attosecond pulses

2.2.4.1 The attosecond streak camera

The final step after the generation and shaping of attosecond pulses is their measurement and characterization. Indirect measurement techniques have to be used as no electronics are fast enough to map their temporal structure. One way for the pulse characterization is to cross-correlate the photoemission of the XUV/soft x-ray pulse (pump) with the electric field of the driving laser (probe). The driving laser pulse is used as a probe, since it is intrinsically synchronized with the XUV pulse by the HHG process. This cross-correlation results in a time delay dependent spectral photoelectron trace which can be used to reconstruct both pulses. This method is called attosecond streak camera or atomic transient recorder [73]. Both the XUV and laser beam are focused into an interaction medium (gas, solid, liquid) where the XUV ionizes the atoms. It will be focused on neon (Ne) as an interaction medium as it has been used for the results in this thesis. The ionized electrons are freed and inherit all the characteristics of the attosecond pulse regarding energy, pulse duration and phase nevertheless with a shifted kinetic energy, i.e. reduced by the binding energy W_b of the original electron level (e.g. 21.6 eV for the Ne 2p electrons):

$$W_{kin}(t_0) = \hbar\omega - W_b. \tag{2.26}$$

After the ionization the electrons are accelerated by the electric field $E(t)$ of the laser resulting in a time dependent momentum:

$$p(t) = p(t_0) - e\int_{t_0}^{t} E(\tau)d\tau = p(t_0) - eA(t_0) + eA(t), \tag{2.27}$$

where t_0 is the time of ionization, A the vector potential and $p(t_0)=\sqrt{2mW_{kin}(t_0)}$ the instant momentum. After the laser has passed, the electron's final momentum is only dependent on the vector potential at the time of its ionization, since $A(t=\infty)=0$ when the laser is no longer present at $t=\infty$:

$$p(\infty) = p(t_0) - eA(t_0). \tag{2.28}$$

This concept is illustrated in figure 2.14. The different vector potentials at times

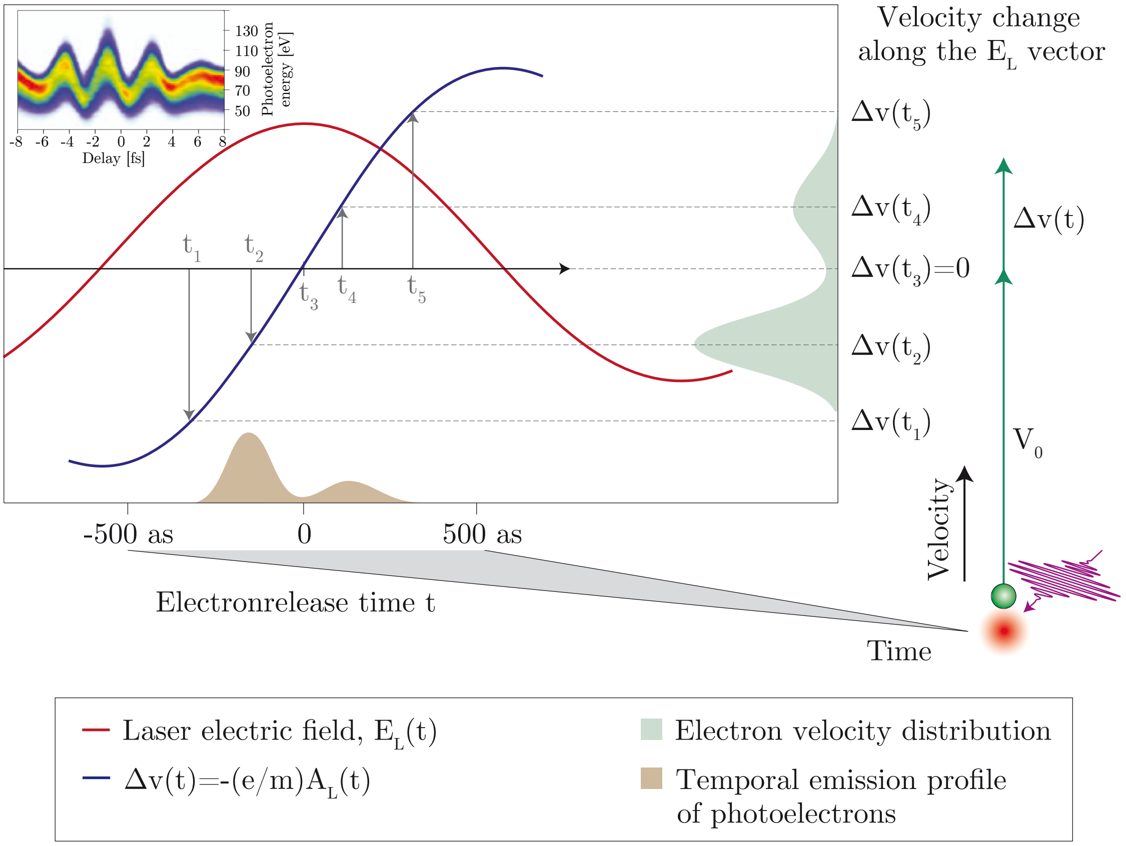

Figure 2.14: Concept of light-field driven attosecond streaking. Photoelectrons released by an attosecond XUV pulse in the presence of a strong linearly polarized laser field (red line) parallel to the electric field vector suffer a change in their velocity that is proportional to the vector potential of the field (blue line) at the moment of release. Here, $\Delta v(t)$ is proportional to the vector potential $A_L(t)$ of the electric field. This change in the final velocity is monotonic within a half wave cycle of the field, and maps the intensity profile of the attosecond XUV pulse to a corresponding final velocity distribution of photoelectrons. Recording these 'streaked' photoelectron spectra as a function of time delay with respect to the streaking field yields a streaking spectrogram (inset), from which the attosecond XUV pulse profile and chirp as well as the laser waveform can be retrieved (figure and caption taken/adapted from [78]).

t_1–t_5 map the intensity profile of the attosecond XUV pulse to a corresponding final velocity distribution of photoelectrons. Measuring the electron spectrum for different time delays between the laser and the attosecond pulse results in a streaking trace like shown in the upper left of figure 2.14. This spectrogram allows for a complete retrieval of both the vector potential of the laser and the characteristic of the attosecond pulse by FROG/CRAB [79, 80, 81, 82]. The analysis reveals the intensity as well as nonlinear phase terms (e.g. a possible chirp) of the attosecond pulse thus a complete reconstruction of the temporal structure. Summarized, attosecond streaking is sensitive not only to the XUV spectrum, but also to its phase which allows to fully characterize the XUV pulse. As the vector potential of the laser pulse is measured as well, it can also be completely characterized.

2.2.4.2 The RABBITT technique

A second technique for the characterization of attosecond pulses is usually referred to as RABBITT (Reconstruction of Attosecond harmonic Beating By Interference of Two-photon Transitions) [83, 84]. It is known that HHG occurs when an intense laser pulse is focused into a gas target. If the focused IR laser pulse consists now of several cycles, in contrast to close to single cycle in the previous sections (e.g. $\Delta\tau$=30 fs versus $\Delta\tau$=4 fs), the emitted harmonics will also be confined in short attosecond pulses, which are continuously generated every half cycle of the IR pulse, but now resulting in an attosecond pulse train (APT) with a strongly modulated XUV spectrum. The number of electric field cycles increases with longer pulses, i.e. more attosecond pulses are generated. The interference of a higher number of pulses is responsible for the strongly modulated spectrum in contrast to the superimposed plateau spectrum in figure 2.6 for the case of few cycle driver pulses. These APT can be characterized by RABBITT. Spectrally and temporally filtered XUV-APT are focused into a noble gas which gets ionized. The freed electrons exhibit kinetic energies which reflect the corresponding high harmonic photon energies (separated by $2\omega_0$). Sidebands peaks will appear in the electron energy spectrum if a moderately intense IR field is also focused into the noble gas. These sidebands are based on two-photon two-color ionization by one XUV photon and one infrared laser photon. Varying the time delay between the XUV and the IR modulates the sideband signal which originates from the interference between two processes: absorption of an XUV photon and an IR photon ($q\omega_{IR}+\omega_{IR}$), and absorption of an XUV photon and emission of an IR photon ($(q+2)\omega_{IR}$-ω_{IR}) [84]. As the width and especially the relative temporal position of a sideband maximum is determined by the phase difference between two neighboring fundamental harmonic peaks, only the oscillation of the high harmonic ionization signal in the delay dependent electron energy spectrum contains the exact spectral phase information of the XUV pulses. This allows a precise characterization of the attosecond pulse trains by RABBITT. However, the RABBITT technique will probably be limited to the lower attosecond energy regime as few cycle laser pulses, exhibiting a high electric field amplitude, are needed to push attosecond science to higher photon energies (e.g. the water window) in the near future.

2.3 Interaction of XUV and x-ray radiation with matter

The content of this section is based on the textbook 'Soft x-rays and extreme ultraviolet radiation: Principles and Applications' from David Attwood [5].

2.3.1 Optical constants in the XUV and x-ray regime

The interaction of electromagnetic waves with matter can be described by the index of refraction $n = \frac{c}{v_p}$, where c is the speed of light and v_p is the phase velocity in the medium. The phase velocity is usually decelerated in a medium, since the electric field disturbs the charges of each atom proportional to the electric susceptibility of the medium. This disturbance decreases with increasing frequency. Figure 2.15 illustrates the progression of the index of refraction dependent on the electromagnetic wave's frequency ω. It shows strong variations near IR, UV and x-ray resonances (ω_r) and the tendency toward unity for very short wavelengths. Please note that only the real part of the index of refraction is shown in figure 2.15. Its adaption to a complex refractive index is necessary in case of attenuation in the medium and will be described in the following section.

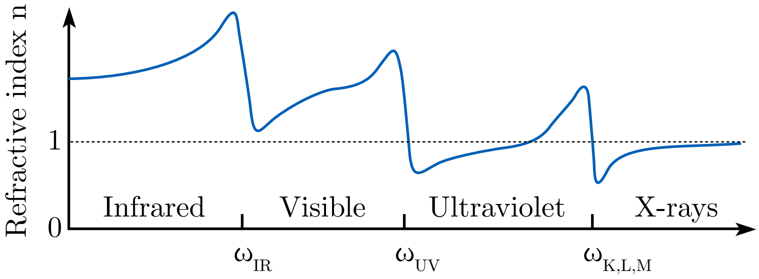

Figure 2.15: Index of refraction from the IR to the x-ray range. Index of refraction dependent on the frequency with strong variations near the resonance frequencies (figure taken/adapted from [5]).

2.3.1.1 Complex index of refraction

When electromagnetic waves get attenuated in a medium one considers this absorptive effect and defines the complex index of refraction as

$$\widetilde{n} = n + i\kappa, \tag{2.29}$$

where κ is the extinction coefficient. The real part of equation (2.29) approaches unity for electromagnetic waves with wavelengths in the XUV/soft x-ray range, since the dispersion of the medium strongly decreases. One considers the low dispersion in that energy range by rewriting equation (2.29) to the XUV/soft x-ray form:

$$\widetilde{n}(\omega) = 1 - \delta + i\beta, \tag{2.30}$$

with the dispersion δ and the extinction coefficient β. The influence of δ and β on the light-matter interaction becomes clear, when one considers the propagation of a plane wave in z-direction through a material with a refractive index n. The electric field can be written as:

$$E(z,t) = E_0 e^{-i(\omega t - zr)}. \tag{2.31}$$

The complex index of refraction is considered by:

$$\frac{\omega}{k} = \frac{c}{n} = \frac{c}{1-\delta+i\beta} \Leftrightarrow k = \frac{\omega}{c}(1-\delta+i\beta). \tag{2.32}$$

Using equation (2.32) in equation (2.31) leads to:

$$E(z,t) = \underbrace{E_0 e^{-i\omega(t-\frac{z}{c})}}_{vacuum\ propagation} \underbrace{e^{-i(\frac{2\pi\delta}{\lambda})z}}_{\phi-shift} \underbrace{e^{-(\frac{2\pi\beta}{\lambda})z}}_{decay}. \tag{2.33}$$

The first term in equation (2.33) describes the propagation of a plane wave through vacuum, the second term contributes a phase shift dependent on the dispersion δ and the last term is a damping term, accounting for absorption within the medium. The extinction coefficient β is related to the absorption coefficient α by squaring equation (2.33):

$$I = I_0 e^{-\alpha z} \Leftrightarrow \alpha = \frac{4\pi\beta}{\lambda}, \tag{2.34}$$

where I represents the Intensity and α is the inverse of the absorption length $l_{\text{abs}} = \frac{1}{\alpha}$.

2.3.1.2 Atomic scattering factor

A more fundamental description of the refractive index uses an oscillator model to describe the interaction of a photon of frequency ω with the Z electrons of an atom: The atomic scattering factor (also referred to as atomic form factor). The complex atomic scattering factor is defined as:

$$f^0(\omega) = \sum_s \frac{g_s\omega^2}{\omega^2 - \omega_s^2 + i\gamma\omega} = f_1^0(\omega) - if_2^0(\omega), \tag{2.35}$$

where $\sum\limits_s g_s{=}Z$ is the total number of electrons, ω_s is the resonance frequency of the s-th electron and γ describes the damping of the oscillation. The index of refraction can be written in dependence of the atomic scattering factor as:

$$n(\omega) = 1 - \frac{r_e n_a \lambda^2}{2\pi}\left[f_1^0(\omega) - if_2^0(\omega)\right], \tag{2.36}$$

with the classical electron radius $r_e = \frac{e^2}{4\pi\epsilon_0 mc^2}$ and the electron density per unit volume n_a. Comparing equation (2.36) and equation (2.30) yields the relation between the atomic scattering factor and the dispersion and extinction, respectively:

$$\delta = \frac{n_a r_e \lambda^2}{2\pi} f_1^0(\omega) \tag{2.37}$$

and

$$\beta = \frac{n_a r_e \lambda^2}{2\pi} f_2^0(\omega). \tag{2.38}$$

One can thus calculate the dispersion and the extinction by making use of the measured tabulated values of the atomic scattering factors by Henke et al. [85]. Figure 2.16 shows these calculated values exemplarily for carbon, scandium and oxygen. One can clearly see the characteristics of absorption edges as well as the decrease of δ and β toward higher photon energies. The index of refraction approaches unity due to these low values (10^{-2}–10^{-7}) where the values of δ and β are typically on the same order. This approach and the high absorption for XUV/soft x-ray wavelengths (equation (2.34)) results in low refraction at an interface between two materials (due to the similarity of the optical constants) and a limited penetration depth (on the order of a few hundred nm). This limits the degree of freedom of XUV/soft x-ray optics, since they have to be either very thin, be used under small grazing angles in reflection geometries or use multiple reflections from different interfaces as utilized in multilayer mirrors.

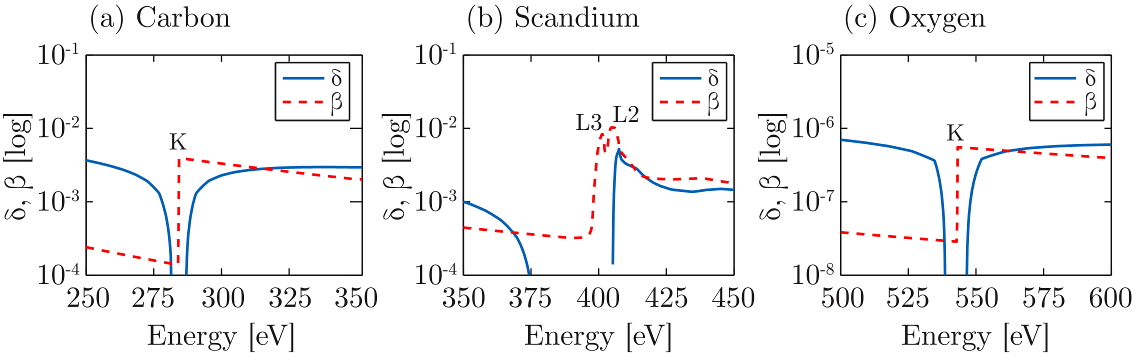

Figure 2.16: Optical constants of carbon, scandium and oxygen. The lower spectral range of the water window starts with the K-edge of carbon (a) and ends in the higher range with the K-edge of oxygen (c). Scandium (b) is a well suited material for multilayer mirrors, since the $L_{2,3}$-edge is within the water window exhibiting a strong variation of the optical constants in the vicinity of these edges. The optical constants δ (solid blue)and β (dashed red) were calculated from the tabulated atomic scattering factors f_1 and f_2 from [85].

2.3.1.3 Kramer-Kronig relation

The imaginary part $f_2^0(\omega)$, which accounts for absorption, can be measured in an intensity measurement whereas an interferometry experiment is needed for measuring the phase shift which is addressed by the dispersive real part $f_1^0(\omega)$. As interferometry is not sufficiently advanced in the case of XUV/soft x-rays, one uses the fact that both the real and imaginary part of the atomic scattering factor are related to each other by a meromorphic function. This relationship can be utilized when only one quantity is known to calculate the missing one. One uses the Kramer-Kronig relations [86] that connect the real and the imaginary part of meromorphic functions:

$$\mathrm{Im}\ F(x) = -\frac{2}{\pi} \cdot \mathscr{P}_C \int\limits_0^\infty \frac{x \cdot \mathrm{Re}\ F(t)}{t^2 - x^2} dt \tag{2.39}$$

and

$$\mathrm{Re}\ F(x) = \frac{2}{\pi} \cdot \mathscr{P}_C \int\limits_0^\infty \frac{t \cdot \mathrm{Im}\ F(t)}{t^2 - x^2} dt, \tag{2.40}$$

where $\mathscr{P}_C$ indicates taking only the non-divergent Cauchy principal part of the integral. Integrals which contain singularities can still be evaluated with the $\mathscr{P}_C$. Adapting equation (2.39) and equation (2.40) to the real and imaginary part of the atomic scattering factor yields:

$$f_1^0(\omega) = Z - \frac{2}{\pi} \cdot \mathscr{P}_C \int\limits_0^\infty \frac{u \cdot f_2^0(u)}{u^2 - w^2} du \tag{2.41}$$

and

$$f_2^0(\omega) = \frac{2\omega}{\pi} \cdot \mathscr{P}_C \int\limits_0^\infty \frac{f_1^0(u) - Z}{u^2 - \omega^2} du, \tag{2.42}$$

with the frequency ω and the number of electrons per atom Z.

2.3.1.4 Determination of the refractive index at 10–30 eV

One can determine $f_1^0(\omega)$ by equation (2.41) if $f_2^0(\omega)$ is determined through absorption measurements, across a sufficiently broad frequency range that the integral converges. This is exactly the procedure which Henke et al. [85] have used to deduce the values of f_1^0 and f_2^0 for all elements from hydrogen (Z=1) to uranium (Z=92). However, f_2^0 values are tabulated between 10 eV and 30000 eV whereas f_1^0 starts first at 30 eV. The knowledge of f_2^0 is sufficient to simulate/calculate the transmission properties of filters whereas for reflective optics like multilayer mirrors also f_1^0 has to be known. We have calculated the values of f_1^0, for the missing 10–30 eV range, by Kramer-Kronig (equation(2.41)) to extend the spectral range for simulations. Figure 2.17 shows the comparison of our calculated (solid blue) and the tabulated (dashed red) values from the CXRO database (`http://henke.lbl.gov/optical_constants/`). One finds a well agreement except at the

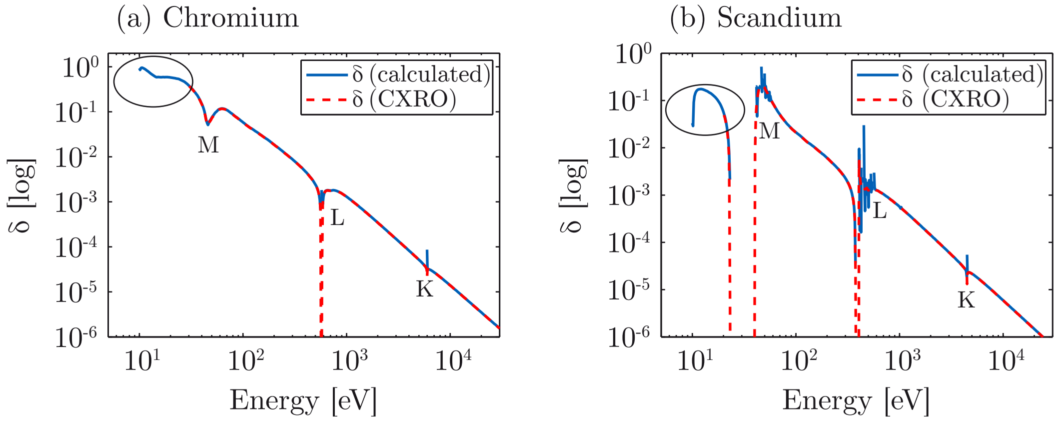

Figure 2.17: Optical constants calculated by Kramer-Kronig relations. Comparison of the calculated (solid blue) and tabulated (dashed red) values of the dispersion δ for chromium (a) and scandium (b). A well agreement is found for the whole range except at absorption edges. This mismatch, arising from simulation artifacts, was not further investigated, since only the values of the highlighted 10–30 eV range is used for the dataset.

absorption edges due to simulation artifacts arising from wrong spline reasons. A better agreement at the absorption edges was not further investigated, since only the new calculated values in the 10–30 eV range are used to extend the f_1^0/f_2^0 dataset down to 10 eV. Figure 2.17 shows the calculation exemplarily for chromium (a) and scandium (b) but they were performed for all tabulated 92 materials. The calculation of the optical constants for compounds (e.g. SiO_2 or B_4C) was also realized by using stoichiometric averaging of the atomic scattering factor and the corresponding compound density.

2.3.2 Reflective optics

Section 2.3.1.2 figured out the challenges for reflective and transmissive optics being utilized in the XUV/soft x-ray range. This section will focus on the reflective optics whereas the transmissive optics are described later in section 2.3.3.

2.3.2.1 Single interface reflectance (and transmission)

One can use e.g. metal bulk mirrors for a broadband and high reflective guidance of visible light under nearly arbitrary angles of incidence. Unlike the visible range, no comparable optics are able to be used in the XUV/soft x-ray range, as will be described in the following section and is based on [87]. If an electromagnetic wave incident under an angle α_i on an interface which is formed by two layers with the refractive indexes n_1 and n_2, it is usually reflected and transmitted (figure 2.18). The degree of reflection and transmission depends on the incident angle α, on the index of refraction of both media and on the polarization s or p. The characteristics are

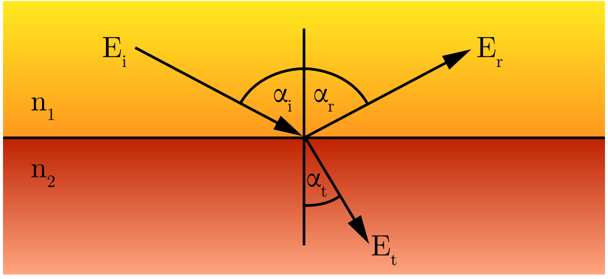

Figure 2.18: Single interface reflectivity and transmission. Reflected and transmitted electric field at an interface, formed by two materials with the index of refraction n_1 and n_2.

described by the Fresnel equations:

$$r_s = \frac{E_{rs}}{E_{is}} = \frac{\tilde{n}_1 \cos(\alpha_i) - \tilde{n}_2 \cos(\alpha_t)}{\tilde{n}_1 \cos(\alpha_i) + \tilde{n}_2 \cos(\alpha_t)} \tag{2.43}$$

$$t_s = \frac{E_{ts}}{E_{is}} = \frac{2\tilde{n}_1 \cos(\alpha_i)}{\tilde{n}_1 \cos(\alpha_i) + \tilde{n}_2 \cos(\alpha_t)} \tag{2.44}$$

$$r_p = \frac{E_{rp}}{E_{ip}} = \frac{\tilde{n}_2 \cos(\alpha_i) - \tilde{n}_1 \cos(\alpha_t)}{\tilde{n}_1 \cos(\alpha_t) + \tilde{n}_2 \cos(\alpha_i)} \tag{2.45}$$

$$t_p = \frac{E_{tp}}{E_{ip}} = \frac{2\tilde{n}_1 \cos(\alpha_i)}{\tilde{n}_1 \cos(\alpha_t) + \tilde{n}_2 \cos(\alpha_i)} \tag{2.46}$$

Here, r and t are the reflection and transmission coefficients, respectively and E represents the complex electric field amplitude, while the indices determine the polarization (s or p) and whether the incident (i), the reflected (r) or the transmitted (t) fraction is considered. The different index of refraction is considered by n_1 and n_2. Throughout this thesis, normal incidence angles are referred to as α and grazing angles as θ. When a particle hits a surface the surface reverses the component of the particle momentum, which is perpendicular to the surface. Particles above a critical momentum enter the bulk of the material. The momentum transfer from the boundary to the photon is

$$2p_z \propto q = \frac{4\pi}{\lambda} n_1 \cos\alpha. \tag{2.47}$$

Since there is no momentum change in the x- or y-direction this yields Snell's law:

$$\frac{2\pi}{\lambda} n_1 \sin\alpha_i = \frac{2\pi}{\lambda} n_2 \sin\alpha_t. \tag{2.48}$$

This equation can be used to obtain the propagation angles α inside a medium from the propagation angle α_0 in the incident medium with refractive index n_0:

$$\cos\alpha_n = \sqrt{1 - \left(\frac{n_0}{n}\right)^2 \sin^2\alpha_0}. \tag{2.49}$$

One can write the Fresnel equation in a more simple form by using equation (2.47) in equation (2.43):

$$r_s = \frac{q_1 - q_2}{q_1 + q2}. \tag{2.50}$$

The total reflection will occur for small grazing angles below a critical angle θ_c which can be obtained from equation (2.49) to:

$$\sin \theta_c \approx \sqrt{2\delta}, \text{ for } \delta << 1, \beta << \delta. \tag{2.51}$$

Using the optical constants from equation (2.30) and squaring equation (2.50) yields the single interface reflection for angles much larger than the critical angle:

$$R_{1,2} = \frac{\Delta\delta^2 + \Delta\beta^2}{4\cos^4(\alpha_1)}, \text{ for } \delta, \beta << 1, \theta >> \theta_c. \tag{2.52}$$

Summarized, the single interface reflectivity is given by the difference of the optical constants of both media and the normal incidence angle α_1. The momentum transfer can be given for both polarization:

$$s: \; q_s = 2k_\perp = \frac{4\pi}{\lambda}\widetilde{n}\cos\alpha, \text{ and for } p: \; q_p = \cos\alpha/\widetilde{n}. \tag{2.53}$$

One can separate a beam of arbitrary polarization into two components where the electric field is on the one hand parallel to the plane of incidence (p-polarization) and on the other hand perpendicular to the plane of incidence (s-polarization). Both components can have a phase delay ϕ_{sp}:

$$\vec{E} = E_s\vec{s} + E_p\vec{p}e^{-i\phi_{sp}}. \tag{2.54}$$

Both relations of the equation (2.53) can now be used to calculate the single interface reflectivity at each incidence angle depending on the polarization. Figure 2.19 shows an illustration of the single interface reflectivity in the XUV/soft x-ray range for s- and p-polarization at a vacuum-silicon interface. The following overview summarizes the most important features of these derivations (detailed analysis can be found in [87]):

1. The single interface reflectivity for s- and p-polarization drops with increasing energy as the difference in optical constants approaches 0 (equation (2.52)).

2. An increased single interface reflectivity can be found in the vicinity of an absorption edge where the optical constants exhibit discontinuities.

3. A high reflectivity of nearly 100% is found at very small grazing incidence angles below the critical angle $\sin\theta_c \approx \sqrt{2\delta}$.

4. The single interface reflectivity increases with decreasing grazing angle in case of s-polarization.

5. In the case of p-polarization, the reflectivity drops around $\theta \approx 45^o$ due to the Brewster angle. The normal incidence angle is given by $\alpha_B \approx \frac{\pi}{4} - \frac{\delta}{2}$.

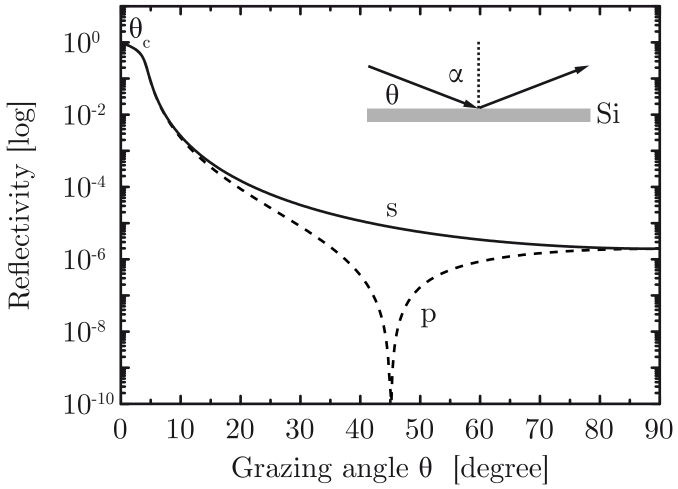

Figure 2.19: Single interface reflectivity at a vacuum-silicon interface. Single interface reflectivity dependent on the grazing angle θ and the polarization (figure taken/adapted from [88]).

2.3.2.2 Grazing incidence optics - Design concept for a three mirror grazing incidence attosecond optic

The last section has shown that the single interface reflectivity increases toward the critical angle θ_c where even total reflection occurs below this value. As a result one can use bulk reflectors at small grazing angles for a broadband and high reflectivity guidance of attosecond pulses. The single interface reflectivity at these angles additionally ensures a flat phase. However, in addition to these advantages these optics exhibit no possibility for attosecond pulse shaping. Figure 2.20 shows the simulation of a rhodium (a) and a nickel (b) bulk which have been used at the *AS2* beamline at the MPQ [72] for a broadband high reflectivity profile.

2.3.3 Transmissive optics

Besides reflective optics, transmissive optics are widely used in attosecond experiments. Whereas diffractive optics like zone plates or diffraction gratings are usually not used due to their spatial chirp properties (in the case of a zone plate a multilayer mirror could probably introduce an opposite prechirp for the support of attosecond pulses), thin (metal) filters or polarizers can be used in attosecond experiments to shape the attosecond pulses spectrally or even their polarization characteristic. Both are described in the next sections.

2.3.3.1 Thin filters for shaping HHG radiation

Attosecond experiments require the separation of the attosecond pulse and the driving pulse as has been described in section 2.2. One uses a thin (≈150–300 nm) (metal)

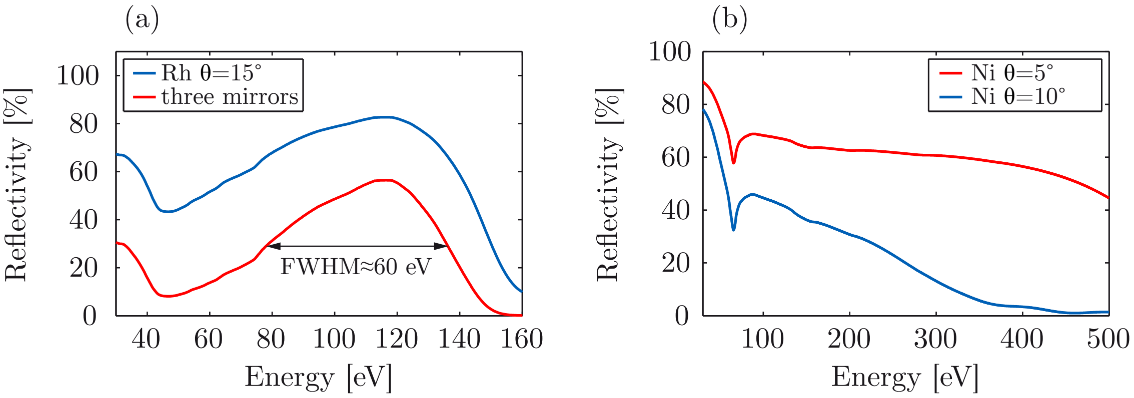

Figure 2.20: Grazing incidence bulk reflector. (a) Three rhodium (Rh) mirrors are used at a grazing angle of θ=15^o (one mirror blue line) for a total 90^o deflection and a total FWHM support of ≈60 eV (red) at a central energy around 120 eV [89]. (b) A nickel (Ni) bulk is used at 10^o (blue) grazing angle to reflect the XUV/soft x-ray spectrum into a spectrometer. This incidence angle supports energies up to the lower spectral range of the water window. Decreasing the grazing angle to θ=5^o (red) would support the whole water window spectral range.

filter which transmits part of the XUV/soft x-ray range but blocks the laser light. This spectral separation is accompanied by the opportunity of shaping attosecond pulses by the spectral characteristics of (metal) filters. Figure 2.21(a) shows the transmission of various 150 nm thick metal filters, where each element supports a characteristic spectral window. These filters are used to suppress certain energy

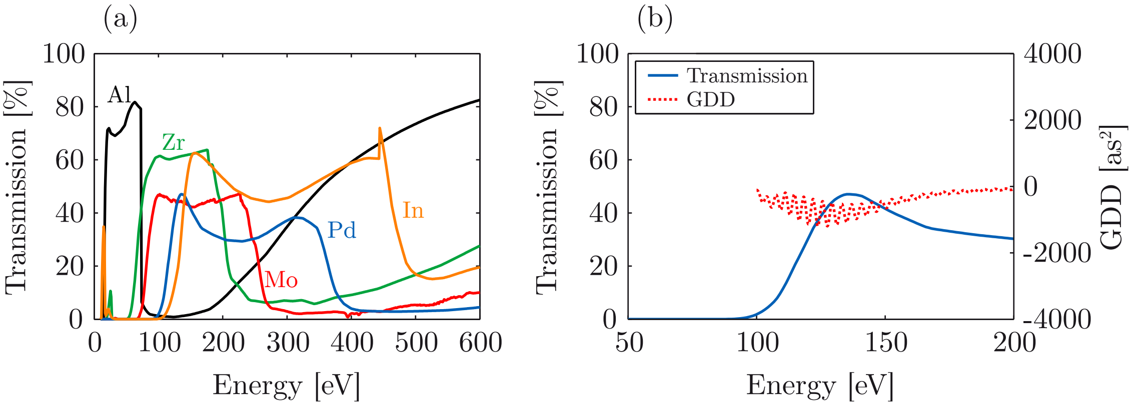

Figure 2.21: Filter transmission in the XUV/soft x-ray range. (a) Transmission characteristic of various 150 nm thick metal filters. (b) Transmission (solid blue) of a 150 nm thick palladium (Pd) filter and the corresponding GDD (dashed red). The filter introduces a slightly negative GDD above the opening edge.

ranges and allow e.g. the isolation of single attosecond pulses by acting as a spectral bandpass (section 2.2.2.2). Together with the spectral transmission characteristic one can slightly tune their spectral phase properties by varying the thickness of the material as the transmission introduces a low GDD. Figure 2.21(b) shows the introduced GDD of a 150 nm thick Pd filter upon transmission. The filter adds only a GDD below 1000 as^2 per 150 nm thickness. However, their availability is limited (figure 2.21) and one is restricted to a discrete amount of negative chirp and suppression of lower energy harmonics with a filter specific signal to noise ratio. That is the reason why filters are usually accompanied by multilayer mirrors, as they exhibit a higher degree of freedom regarding spectral filtering or phase shaping. Figure 2.22 shows the transmission characteristic of a 150 nm thick Al and Si filter, which are combined with a multilayer mirror reflecting primarily at the absorption edges of the filters. This combination increases significantly the signal to noise ratio and has been used at the *AS2* beamline at the MPQ for calibration purposes of the spectrometer.

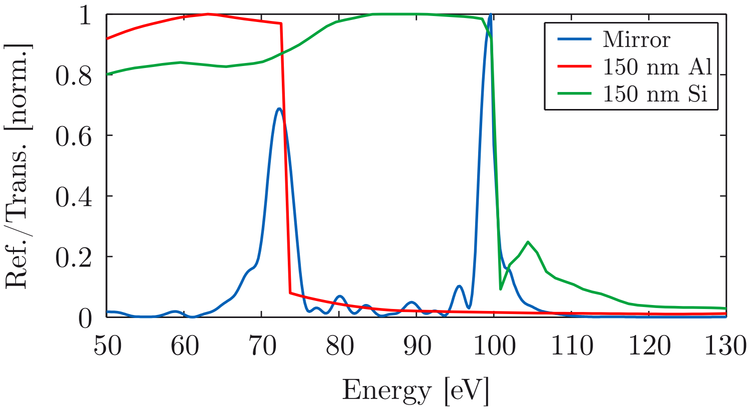

Figure 2.22: Tailored multilayer mirror at the Al and Si absorption edge. A tailored multilayer mirror for reflecting primarily at the absorption edges of Al (red) and Si (green) for an increased signal to noise ratio. The mirror consists of Si/B$_4$C layers and was designed for the *AS2* beamline at 45^o normal incidence.

2.3.3.2 Multilayer transmission polarizer

Another powerful transmissive optic for attosecond experiments is a polarizer, which shapes the polarization degree of attosecond pulses, and will be described in the following. Although transmission waveplates are conventional in the visible and NIR spectral range, they are quite extraordinary in the XUV/soft x-ray range due to the lack of strongly birefringent materials and the generally high absorption in the materials. Section 2.2 described the generation of attosecond pulses by HHG with an intense laser pulse. The attosecond pulses are linearly polarized if a linearly laser pulse is used for the generation process but one needs close to circularly polarized pulses for a time resolved XMCD measurement [90]. The polarizer has thus to fulfill the following prerequisites:

- Introducing a phase shift of 90^o between s- and p-components.
- Equal transmission amplitude of the s- and p-components.
- A bandwidth in the range of 3–4 eV for supporting attosecond pulses.
- A precise design for a certain energy (e.g. 66.2 eV at the Ni M_3-edge).

The first two points ensure a polarization transform of attosecond pulses from linear to circular. This can be realized in the XUV/soft x-ray range when the polarizer is designed and used close to the Brewster angle:

$$\alpha_B \approx \frac{\pi}{4} - \frac{\delta}{2} = 45^o - \frac{\delta}{2}. \tag{2.55}$$

The p-components are transmitted without any shaping whereas the s components are reflected, partly transmitted, reflected and so on. The principal is sketched in figure 2.23. The interference of the s-components ends up (in an ideal design) with

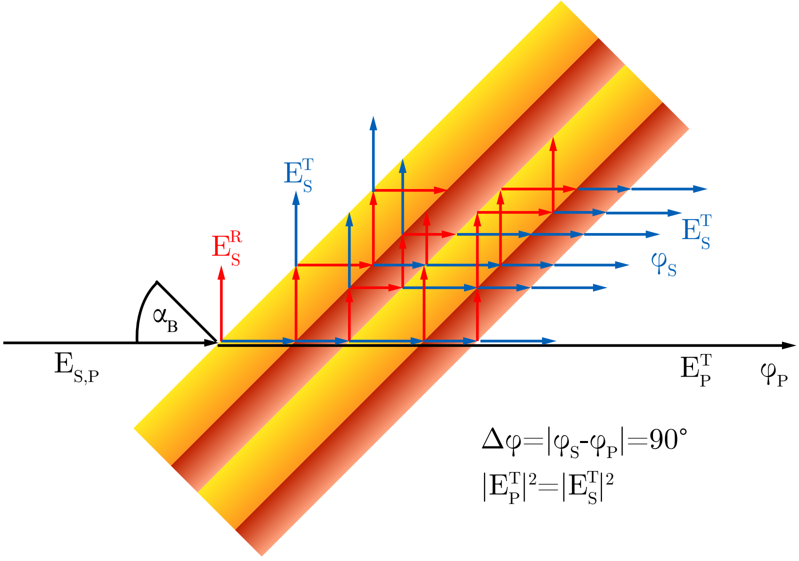

Figure 2.23: Phase retarder for the XUV. XUV/soft x-ray waveplate at the Brewster angle α_B. The p-components are transmitted, whereas the interference of the partly transmitted and partly reflected radiation of the s-components allows for an introduced phase shift of $\Delta\phi$=90^o, which transforms linearly polarized attosecond pulses to circular polarization.

a phase shift of 90^o, in respect to the p-components ($\Delta\phi$=$|\phi_s - \phi_p|$=90^o), with a simultaneous equal transmission amplitude at a certain energy ($|E_p^T|^2$=$|E_s^T|^2$). This concept ensures a polarization switch from linearly polarized attosecond pulses to almost circularly polarized ones and was used for the results in section 4.1.3. A detailed simulation of the previously described reflective or transmissive elements allows a precise prediction of attosecond pulse shaping, as their influence is given by their convolution with the incoming light $E_i(\omega)$:

$$E(\omega) = E_i(\omega)e^{-i\phi_i}r(\omega)e^{-i\phi_r}t(\omega)e^{-i\phi_t} = E_i(\omega)r(\omega)t(\omega)e^{-i(\phi_i+\phi_r+\phi_t)}, \tag{2.56}$$

where E_i represents the spectral field amplitude of the incoming light, r and t the amplitude of the reflective and transmissive element and ϕ the corresponding phase. Squaring equation (2.56) yields the intensity values ($R{=}|r|^2$, $T{=}|t|^2$, $I{=}|E|^2$).

2.4 Multilayer Mirrors

Multilayer mirrors address the issue of low single interface reflectivity as was described in section 2.3.2.1. Creating a stack of alternating layers of different materials makes use of constructive interference of partially reflected electromagnetic waves at each interface. Dependent on the working energy range and bandwidth 10–1000 interfaces are utilized. Each single interface reflectivity is still small but adding up each interface reflectivity can result in a normal incidence XUV reflectivity above 70% [91] in the vicinity of the Si L_3-edge. Constructive interference of the waves reflected at each interface can be achieved by a proper material choice and thickness design yielding a tailored reflectivity characteristic. This allows for a very precise spectrally filtering and shaping of attosecond pulses. Multilayer can be coated on arbitrary surfaces which allows for various shapes like parabolas, ellipsoids or the most commonly used spheres. A prerequisite in the XUV/soft x-ray range are super polished substrates with roughness values below one angstrom rms, which becomes clear in the roughness section 2.4.4. Summarized, multilayer mirrors can tailor attosecond pulses and can be used for beam guidance, imaging or focusing and stand out as key components in attosecond science. The development of multilayer mirrors for the XUV started in the 1970s [92], it also pushed the development in the VIS/IR as the XUV range is more challenging and achieved results in that energy range can be easily adapted to the VIS/IR range. Nowadays it's state-of-the-art in the VIS/IR range to calculate [93] or even realize [52] very complex designs by the usage of various techniques [75, 94] and fulfill different requirements such as enough photon throughput or dispersion control at the same time [1]. This development and its results were extended to the XUV/soft x-ray range in the last years for various applications such as soft x-ray microscopy [77], XUV lithography [95], astronomy [96] or time resolved attosecond spectroscopy [9]. The last-mentioned attosecond science will be extended from the XUV range to the soft x-ray water window range in the near future. Realizing high precision multilayer mirrors in the water window and their application to attosecond pulses was the main challenge of this thesis. Their theoretical background will be given in this section.

2.4.1 Multiple interface reflections and transmissions

In section 2.3.2.1 the reflectance and transmission of a single interface was described. This is now extended to a multilayer system, where multiple interface reflections and transmissions occur. One starts with the j-th layer within a stack consisting of one interface at the top and one at the bottom. The corresponding reflection coefficient reads as:

$$r_j = r_{(j-1)j} + t_{(j-1)j}t_{j(j-1)}r_{j(j+1)}e^{-2i\varphi_j} + t_{(j-1)j}t_{j(j-1)}r_{j(j-1)}r^2_{j(j+1)}e^{-4i\varphi_j} + ..., \tag{2.57}$$

where r and t are the reflection and transmission coefficients, respectively. Their indices determine at which interface the reflection and transmission occurs. The phase difference between the waves reflected at the bottom and the top interface is referred to as φ_j and can be written as:

$$\varphi_j = \frac{2\pi d_j}{\lambda} n_j \sin\theta_j, \tag{2.58}$$

where n_j is the index of refraction and θ_j the angle of incidence of the j-th layer. Figure 2.24 illustrates all these parameters. The sum in equation (2.57) converges to [98]:

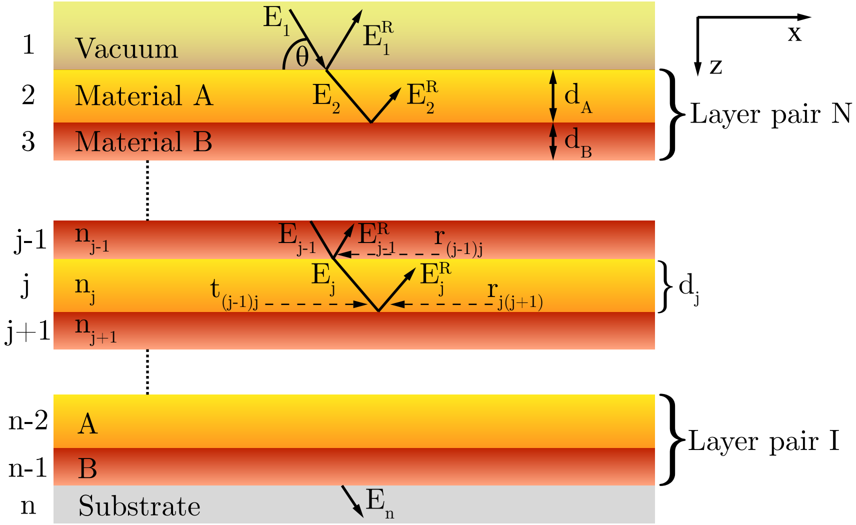

Figure 2.24: Principle of multiple reflections and transmissions within a multilayer stack. The incident electromagnetic wave is partly reflected and transmitted at each interface (figure is related to [97]).

$$r_j = \frac{r_{(j-1)j} + r_{j(j+1)}e^{-2i\varphi_j}}{1 + r_{(j-1)j}r_{j(j+1)}e^{-2i\varphi_j}}. \tag{2.59}$$

With this recursive formula one can calculate the reflectivity of the complete multilayer stack. One starts from the lowermost layer of the stack, where the reflectivity is given by the single interface reflectivity of the substrate, and the first layer, and walks through the stack. The angles θ_j can be calculated according to equation (2.49). The reflectivity is calculated layer by layer and one ends up with the overall reflectivity $r_{\mathrm{ML}} = r_1$. Its intensity is given by $R = |r_1|^2$.

2.4.2 Periodic multilayer mirrors

Depending on the experimental requisite multilayer mirrors exhibit periodic or aperiodic stack designs. A multilayer is referred to as periodic when the particular material layer thicknesses are constant throughout the stack. A periodic stack can utilize two or more different materials where the thickness of one material can be different in comparison to another one. The principle of a periodic multilayer stack, with constructive interference of all partially reflected waves at each interface, is illustrated in figure 2.25. The stack consists of two different materials in alternating order where one usually refers to the low absorbing material as *spacer* whereas the high absorbing material as *absorber*. Periodic stacks are characterized by the following parameters:

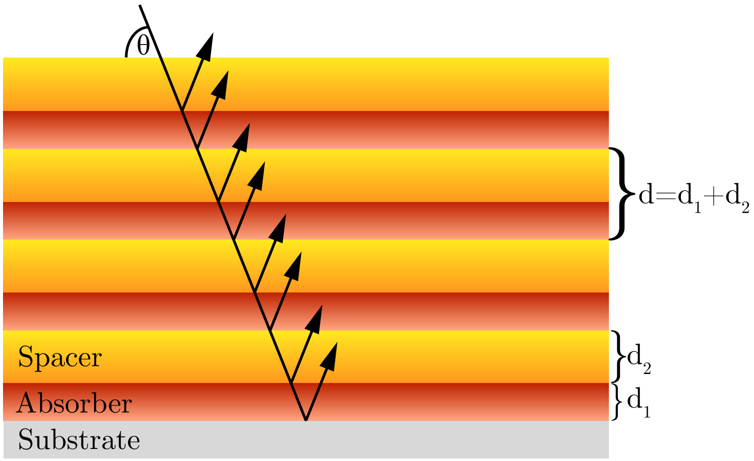

Figure 2.25: Illustration of a periodic multilayer stack. An electromagnetic wave incidents under the grazing angle θ and is partially reflected at each interface. In this case the periodic multilayer stack consists of two different materials with layer thicknesses d_1 and d_2. Their sum defines the period thickness $d{=}d_1{+}d_2$.

- The period thickness d which is constant throughout the stack.
- The period number N is the number of bilayers in a two material stack. In a more general way: How often is the period used within a stack?
- The fraction of the different layer thicknesses within one period, denoted as γ ratio. In a two material stack: $\gamma{=}\frac{d_{bottom}}{d} \Leftrightarrow d_{top}{=}d(1-\gamma)$. In the case of more than two materials per period one defines one γ_A per material A.

- The interface roughness value σ accounts for interface imperfections which decreases the single interface reflectivity.

Figure 2.26 illustrates a typical Gaussian like reflectivity and flat phase (within the bandwidth) shape of a periodic multilayer mirror. The characteristic values such as maximum reflectivity, center energy or bandwidth are influenced by the previously listed multilayer parameters. Their exact influence on the multilayer performance is analyzed in the following subsections.

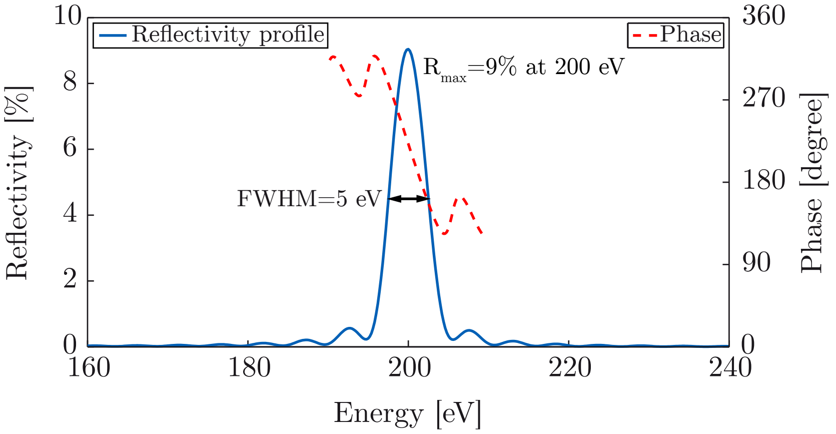

Figure 2.26: Reflectivity and phase shape of a periodic multilayer mirror. Simulated reflectivity (solid blue) and phase (dashed red) of a periodic Cr/Sc multilayer mirror. Following parameters have been used for the simulation: spacer Sc, absorber Cr, d=3.144 nm, γ=0.6, d_{Sc}=1.886 nm, d_{Cr}=1.258 nm, N=37, α=5^o.

2.4.2.1 The period thickness d

In a periodic multilayer mirror, with period thickness d, maximum mirror reflectivity is achieved when all partially reflected wave packets interfere constructively. This is the case when the stack fulfills the Bragg condition, since a multilayer stack can be seen as a one-dimensional crystal:

$$m\lambda = 2d \cdot \sin\theta \sqrt{1 + \frac{\overline{n}^2 - 1}{\sin^2\theta}}, \tag{2.60}$$

where m is the diffraction order, λ is the wavelength of the incident light, θ is the grazing angle and $\overline{n}$=1-$\overline{\delta}$ is the mean real part of the complex refractive index. Here $\overline{\delta}$ is the averaged dispersion within one period d consisting of k materials:

$$\overline{\delta} = \sum_k \frac{d_k \delta_k}{d}, \tag{2.61}$$

where d_k is the individual layer thickness and δ_k the corresponding dispersion within the period thickness d. The square root in equation (2.60) takes refraction effects into account and is sometimes neglected at normal incidence as the denominator approaches unity and $\overline{n}\approx 1$. Neglecting the square root in equation(2.60) yields the condition for maximum normal incidence reflectivity: the optical period thickness $\overline{n}d$ is equal to $\lambda/2$, i.e. $d\approx 2$ nm at 300 eV.

2.4.2.2 The gamma ratio

In case of a periodic multilayer consisting of two materials, one usually refers the ratio of the bottom layer thickness d_{bottom} to the period thickness d as $\gamma=\frac{d_{bottom}}{d}$, i.e. the fraction of *absorber* and *spacer* material within the period. One distinguishes two cases:

- $\gamma=0.5 \Rightarrow$ Referred to as *quarter-wave* stack: The (optical) thicknesses $\overline{n}d$ of *absorber* and *spacer* are exactly equal to a quarter of the wavelength. This configuration shows the maximum reflectivity per period, since the reflected intensity of a single film is defined as $R_f=4R_{12}\sin^2(m\pi\gamma)$ [87], which is maximum for $\gamma=0.5$.

- $\gamma\neq 0.5 \Rightarrow$ Referred to as *Bragg* stack: The fraction of the absorbing material is reduced which results in an increased number of contributing interfaces due to the enlarged penetration depth. The minimum of the electric field standing wave within the multilayer is in the center of the absorber layer, in case of a *Bragg* stack resulting in a higher overall reflectivity.

The best γ value for maximum reflectivity depends on the optical constants of the used materials, the angle of incidence, the energy range, since optical constants are wavelength dependent and finally on the period number N. Figure 2.27 shows the reflectivity of a high periodic (N=400) Cr/Sc multilayer mirror dependent on the energy and the γ ratio. For this specific material system maximum reflectivity is achieved for $\gamma\approx 0.6$ (d_{Sc}/d) which means that the fraction of the absorbing chromium layer is reduced to 40%. The highest reflectivity is reached close to the Sc L_3-edge at 398.7 eV. The next section will show the bandwidth dependence on the period number, yielding the best designs close to a *quarter-wave* stack, when the support of attosecond pulses should be fulfilled, i.e. a broadband mirror reflectivity with few periods which reduces the dependence on the penetration depth.

2.4.2.3 The influence of the period number N

It is clear that the more layers contribute to the overall reflectivity the higher this reflectivity value is. But the limiting factor in the XUV/soft x-ray range is the absorption. At some point the penetrating electric field is attenuated that much, that more consecutive layers do not affect the overall reflectivity any more. An approximation of the number of contributing layers will be given in the following

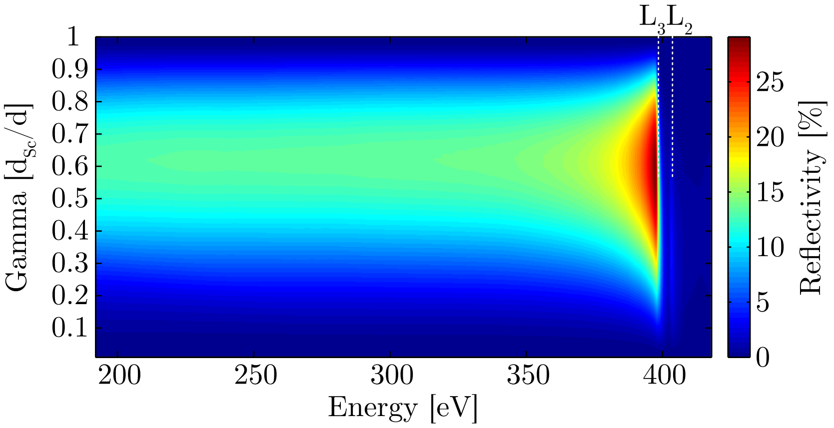

Figure 2.27: Reflectivity dependence on the γ-ratio. Simulated reflectivity of a high periodic (N=400) Cr/Sc multilayer mirror at an incidence angle of α=45^o. An interface roughness of σ=0.5 nm was assumed for the simulation.

section. The intensity of a plane wave is given by squaring equation (2.33):

$$I(z,t) = \left|\vec{E}(z,t)\right|^2 = |E_0|^2 e^{-(\frac{4\pi\beta}{\lambda})z} = I(z). \tag{2.62}$$

The intensity can be calculated after the incident light has passed $2 \cdot N$ periods (back and forth) and a mean extinction similar to equation (2.61) is assumed:

$$I(z = 2 \cdot N \cdot d) = I_0 e^{-\frac{8\pi N d}{\lambda}\overline{\beta}}, \tag{2.63}$$

where I_0 is the incident intensity and $\overline{\beta} = \sum\limits_k \frac{d_k \beta_k}{d}$. Applying the logarithm and solving for N yields:

$$N = -\frac{\lambda}{8\pi d\overline{\beta}} \ln\left(\frac{I}{I_0}\right). \tag{2.64}$$

With this equation it is possible to approximate the layer number dependent on the saturation ratio. The period number has a crucial influence on the reflectivity, but another important point for attosecond physics is the bandwidth support. The energy/wavelength resolution is linked to the period number N as follows [97]:

$$\frac{\Delta\lambda}{\lambda} = \frac{\Delta E}{E} \approx \frac{1}{mN}, \tag{2.65}$$

where m is the diffraction order. Figure 2.28 illustrates the bandwidth and reflectivity dependent on the period number. The simulations were performed for a Cr/Sc multilayer mirror centered at 300 eV at 45^o incidence angle. The reflectivity profile was calculated for each period number (resolution N=5) and the FWHM, as well as the maximum reflectivity value, was extracted. Results are shown for the sputter design (SD) and the real design, including the top chromium oxide layer. For attosecond experiments one has to find a trade-off regarding equation (2.65) as a broader

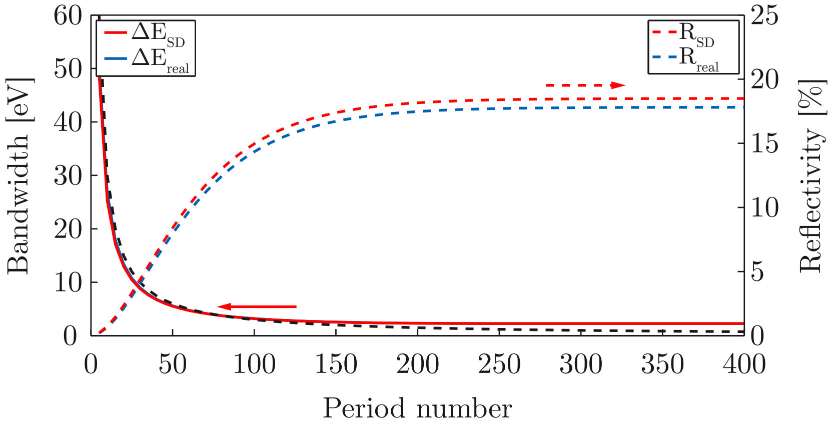

Figure 2.28: Bandwidth and reflectivity dependence on the period number N. Simulated bandwidth (solid) and reflectivity (dashed) of a Cr/Sc multilayer mirror centered at 300 eV dependent on the period number N. The design (d=2.95 nm, γ=0.6 (d_{Sc}/d), σ=0.3 nm) was chosen for an incidence angle of α=45^o. The values were extracted for the sputter design (red) and the real design (blue) which includes the top oxide layer and decreases slightly the reflectivity while having only a minor effect on the bandwidth. The dashed black line depicts the theoretical relation of equation (2.65) at 300 eV.

bandwidth support for shorter attosecond pulses comes along with a lower reflectivity (at a fixed incidence angle). But equation (2.65) allows for a higher energy resolution by using higher diffraction orders of a multilayer mirror. One possibility to overcome this bandwidth-reflectivity limitation is to increase the normal incidence angle. Figure 2.29 shows the reflectivity of a Cr/Sc mirror centered at 300 eV. Dependent on

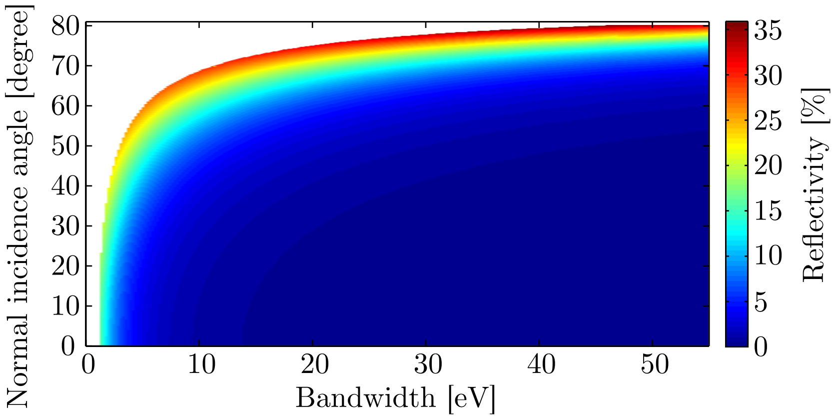

Figure 2.29: Reflectivity dependence on the bandwidth and the incidence angle. Reflectivity of a Cr/Sc multilayer mirror centered at 300 eV dependent on the bandwidth and the normal incidence angle (γ=d_{Sc}/d=0.6, σ=0.3 nm). The simulation illustrates the color boundaries where the bandwidth can be increased at constant reflectivity when it is accompanied by an increased normal incidence angle.

the bandwidth and the incidence angle, i.e. the period thickness is adjusted to the incidence angle for 300 eV. Varying the period number N allows for a bandwidth dependent calculation. Following a specific color boundary allows for an increased bandwidth at constant reflectivity when it is accompanied with the corresponding higher normal incidence angle. The last tuning parameter for a higher multilayer mirror reflectivity is just an adjustment of the incidence angle in order to achieve the required minimum reflectivity. As stated in section 2.3.2.1, the single interface reflectivity increases toward grazing angles, exhibiting almost 100% close to the critical angle θ_c, or in the vicinity of an absorption edge, where the optical constants exhibit discontinuities. Figure 2.30 shows the reflectivity of a high periodic (N=400) Cr/Sc multilayer mirror dependent on the normal incidence angle and the center energy.

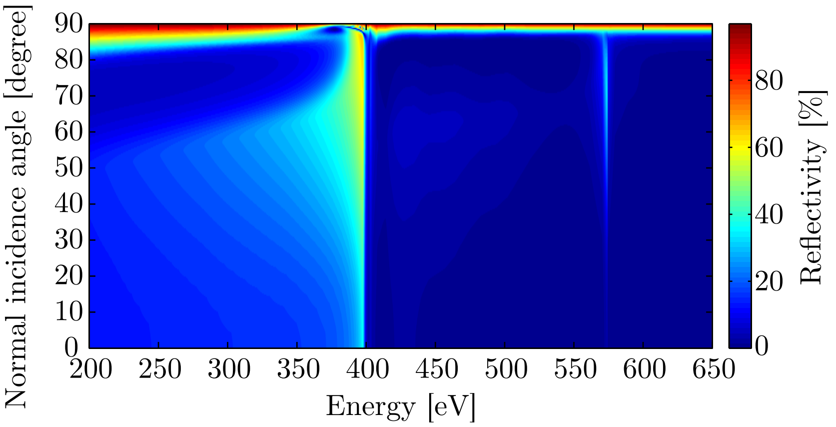

Figure 2.30: Reflectivity dependence on the incidence angle and the energy. Reflectivity of a high periodic (N=400) Cr/Sc multilayer mirror (γ=d_{Sc}/d=0.6, σ=0.3 nm) dependent on the normal incidence angle and the energy (d was adjusted for each center energy). The region of almost total reflection is clearly visible as well as the reflectivity jump close to the Sc L_3-edge (398.7 eV) and the Cr L_3-edge (574.1 eV).

2.4.3 Aperiodic multilayer mirrors

A higher degree of freedom for pulse shaping is achieved by utilizing aperiodic multilayer mirrors in contrast to periodic stacks. While each period is equal in a periodic stack, i.e. the thickness for a certain material is constant, the thicknesses are arbitrary [97] in an aperiodic stack. This facilitates addressing different frequency components by individual layer thicknesses. This allows for spectral and dispersion shaping as different frequency components are reflected at different penetration depths within the stack. Figure 2.31 illustrates the principle of aperiodic multilayer stacks. In figure 2.31(a) longer wavelengths are reflected on the top whereas short wavelengths are reflected at the bottom. Therefore, the short wavelengths are temporally delayed in respect to the longer wavelengths due to the longer penetration distance. This is defined as positive chirp, the mirror introduces a positive GDD. Vice versa in case of a

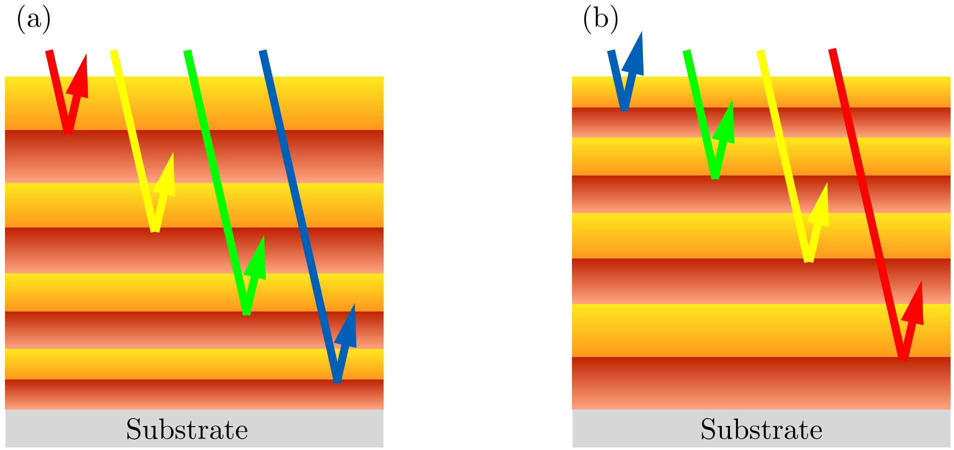

Figure 2.31: Aperiodic multilayer stack. Sketch of aperiodic multilayer stacks, where different wavelengths are reflected at different penetration depths. The almost linear decreasing/increasing of the layer thickness is used for the VIS/IR range whereas it is rather a random stack arrangement in the XUV/soft x-ray range. (a) A positively chirped multilayer stack where short wavelengths are temporally delayed in respect to the longer wavelengths due to the longer penetration distance. (b) Vice versa in case of a negatively chirped mirror.

negative chirp (figure 2.31(b)). This facilitates shaping the dispersion of an incoming attosecond pulse and tailoring the reflected pulse. Aperiodic multilayer systems in the VIS/IR spectral range (e.g. (dielectric) multilayer mirrors in CPA systems) show an almost linear decreasing or increasing (dependent on the introduced GDD) of the layer thicknesses [52] whereas aperiodic XUV/soft x-ray multilayer mirrors exhibit usually a random stack arrangement. Figure 2.32(a) depicts the design of a complex

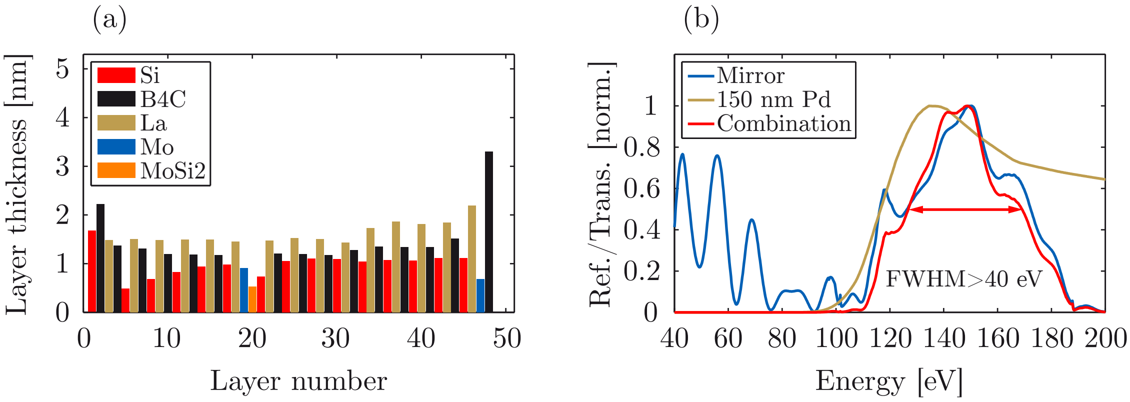

Figure 2.32: A complex aperiodic La/Mo/Si/B_4C mirror design. (a) Design of a complex aperiodic multilayer consisting of 48 different layers and five different materials. (b) Reflectivity (blue), transmission of a 150 nm thick Pd filter (brown) and their convolution (red) resulting in a bandwidth of more than 40 eV. A normal incidence angle of 5^o and a constant interface roughness of σ=0.5 nm was assumed for the simulation.

aperiodic multilayer stack consisting of 48 different layers and five different materials ($MoSi_2$ is formed after deposition [99]). This complex design has been developed for the reflection of a FWHM>40 eV and a close to Gaussian spectral profile, when it is convoluted with the transmission of a 150 nm thick Pd filter (figure 2.32(b)). A periodic stack supporting a bandwidth of 40 eV at 145 eV would, according to equation (2.65), have only four periods. That are eight layers in contrast to the 48 layers of the aperiodic system. This demonstrates why aperiodic multilayer mirrors exhibit a much higher degree of freedom in contrast to periodic stacks. Besides, one would expect that eight layers of the periodic case have a lower overall reflectivity as only a sixth of the aperiodic interface number is used. This is another advantage of aperiodic multilayer mirrors in addition to dispersion control. One can e.g. increase the reflectivity of a periodic system by switching to an aperiodic design while keeping a bandwidth of 25 eV constant. Figure 2.33 shows the comparison of a simulated periodic and an aperiodic Cr/Sc multilayer mirror. The spectral comparison of both systems is shown in (c) where the reflectivity of the aperiodic design (b) exceeds the periodic design (a), while keeping the bandwidth constant. Another requisite during the development of the aperiodic design was an unchirped mirror reflection. The calculated GDD of the aperiodic and periodic design (figure 2.33) shows almost vanishing values. The higher reflectivity would be reached at the expense of a longer pulse if a flat phase would not have been considered during design optimization, as introduced GDD broadens an incoming unchirped pulse.

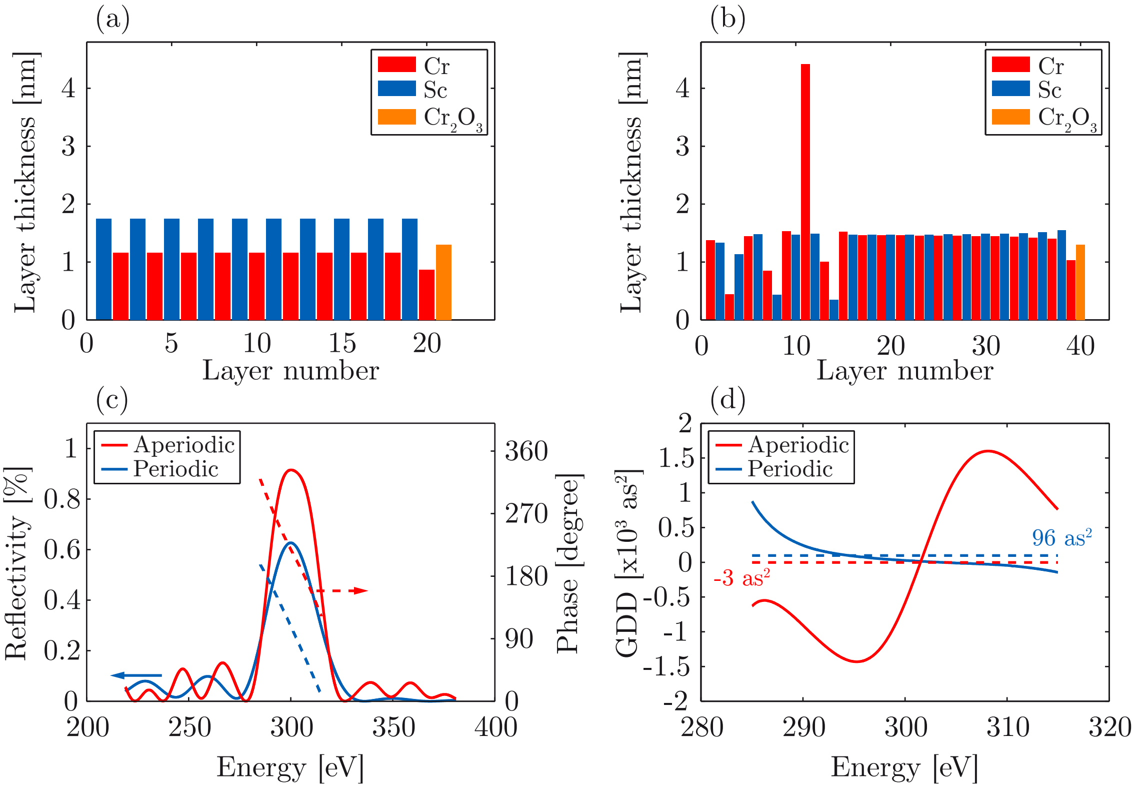

Figure 2.33: Comparison of a periodic and aperiodic design. The designs of a periodic (a) and aperiodic (b) Cr (red) and Sc (blue) multilayer mirror, including their top oxide layer, aiming for a FWHM≈25 eV reflection centered at 300 eV. (c) Simulated reflectivity (solid lines) and phase (dashed lines) of the periodic (blue) and aperiodic (red) multilayer mirror. The aperiodic design exhibits the reflectivity of the periodic design while keeping the bandwidth and phase shape almost constant, resulting in a higher integral which is proportional to the photon flux. (d) The simulated GDD (solid lines) of each design and their mean values (dashed lines), which are almost vanishing, resulting in a low temporal broadening of an unchirped pulse (Simulation parameter: σ=0.39 nm, α=45^o, d=2.95 nm, γ=d_{Sc}/d=0.6, N=10).

2.4.4 Imperfect interfaces

It is impossible to realize multilayer mirrors with perfectly abrupt and flat interfaces as finite boundaries occur during the fabrication. Interface imperfections are mainly caused by interface roughness [87] from fringed interfaces (figure 2.34(a)) or atomic displacement as intermixing or interdiffusion (figure 2.34(b)). Also chemical reactions are possible forming an interlayer, as can be observed in Mo/Si multilayer where thin $MoSi_2$ layers are formed [99, 100]. This interlayer can be considered by including an additional layer with the corresponding refractive index of the compound. One has to find a way to model these described imperfections and include it in simulations of multilayer, since it will be shown that they have a crucial effect on the reflectivity

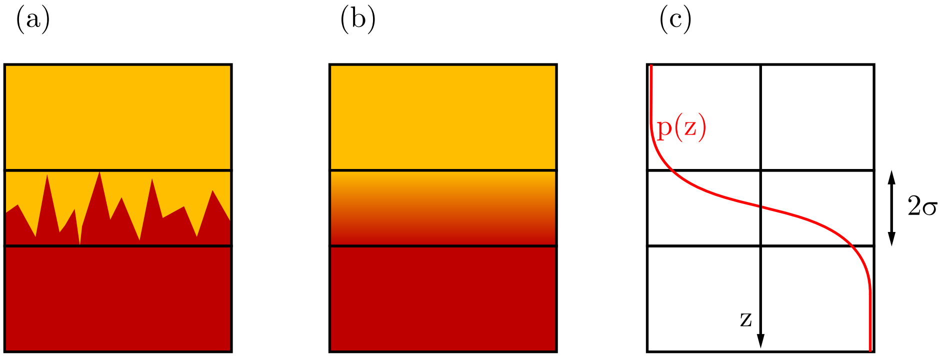

Figure 2.34: The interface roughness σ. (a) Corrugated interface. (b) Intermixing and interdiffusion of both materials. (c) Interface profile function p(z) for modeling both boundary imperfections.

performance. This is mathematically done by the interface roughness value σ. One could now include the transition zone in simulations by representing the interface by a stack of very thin layers of continuously varying refractive index [87], but this would be a very time consuming calculation especially when more than two materials are used or aperiodic stacks with a large layer number are simulated. Debye [101] and Waller [102] developed a rather elegant model to implement the roughness via Fourier transformation. An interface profile function p(z), like the one dimensional error function, is used to characterize the interface width for both roughness and diffusion (figure 2.34(c)):

$$\mathrm{p(z)} = \mathrm{erf}\left(\frac{z}{\sqrt{2}\sigma}\right), \tag{2.66}$$

with the one-dimensional Gauss error function $\mathrm{erf(x)}=\frac{2}{\sqrt{\pi}}\int_0^x e^{-\tau^2}d\tau$ and its FWHM σ. Using this profile function the reflection coefficient of the interface can be written as a Gaussian distribution:

$$r(z) = \frac{r_0}{\sigma\sqrt{2\pi}}e^{-z^2/(2\sigma^2)}. \tag{2.67}$$

A Fourier transformation of equation (2.67) yields the reflection coefficient in the momentum space:

$$r(q) = r_0 e^{-\frac{q^2\sigma^2}{2}} = r_0(\lambda)\exp\left(-\frac{8\pi^2 n^2 \sin^2(\theta)\sigma^2}{\lambda^2}\right), \tag{2.68}$$

with the wavelength dependent Fresnel coefficient $r_0(\lambda)$, the amplitude reflectivity of a perfectly abrupt boundary, and the momentum transfer $q=\frac{4\pi}{\lambda}n\sin\theta$ between the boundary and the photon. Névot and Croce extended this method of Debye and Waller to an even more realistic description [103], taking into account the different refractive indices n and the resulting different propagation grazing angles θ of material

1 and material 2:

$$r(\lambda) = r_0(\lambda) \exp\left(-\frac{8\pi^2 n_1 n_2 \sin\theta_1 \sin\theta_2 \sigma^2}{\lambda^2}\right). \tag{2.69}$$

The Névot-Croce model is used for all simulations within this thesis to account for interface imperfections. Squaring equation (2.69) yields the intensity dependence:

$$R = R_0 \exp\left[-n_1 n_2 \sin\theta_1 \sin\theta_2 \left(\frac{4\pi\sigma}{\lambda}\right)^2\right]. \tag{2.70}$$

Equation (2.70) indicates several points:

- The wider the transition zone is, the higher the roughness σ and the lower the reflectivity.
- The influence of the interface roughness σ is larger the smaller the wavelength is.
- Going from normal incidence toward grazing angles reduces the influence of σ.

Figure 2.35 indicates these influences at four different center energies. Four designs were used for 5^o normal incidence (a) and four adjusted designs for 45^o (b). The reflectivity profile was calculated for each σ (resolution=0.05 nm) and the maximum reflectivity value was extracted. The results were calculated for a bandwidth of 7 eV

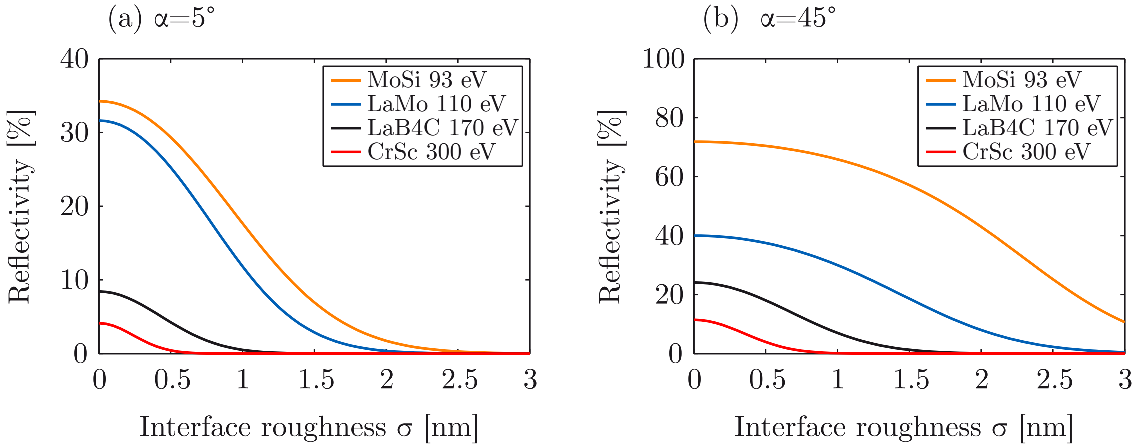

Figure 2.35: Reflectivity dependence on the interface roughness σ. Simulated maximum reflectivity at various center energies (orange: 93 eV, blue: 110 eV, black: 170 eV and red: 300 eV) dependent on the interface roughness σ and the normal incidence angle 5^o (a) and 45^o (b). A bandwidth of 7 eV, thus supporting the reflection of <300 as pulses, was assumed for the simulations. The La/Mo mirror includes a 3 nm thick B_4C capping layer.

thus supporting the reflection of <300 as pulses. Figure 2.35(a) shows that the interface roughness σ has to be smaller than 0.5 nm in order to facilitate such pulses in the water window at normal incidence. A lot of effort has been put in the development of interface optimized multilayer mirrors, due to the enormous influence of σ on the reflectivity performance. One can either reduce the intermixing/interdiffusion by the usage of barrier layers [91], smooth the layer surface with these barrier layers or polish the layer surface during fabrication. The last possibility will be described in section 3.2.3. Figure 2.36 shows the up to now highest measured normal incidence reflectivities in the XUV/soft x-ray range in comparison to the theoretical possible values. The listed realized interface roughness values were derived either from simulations or the specified reference. Summarized, one key to high reflective multilayer mirrors in the water window are interface optimized multilayer systems.

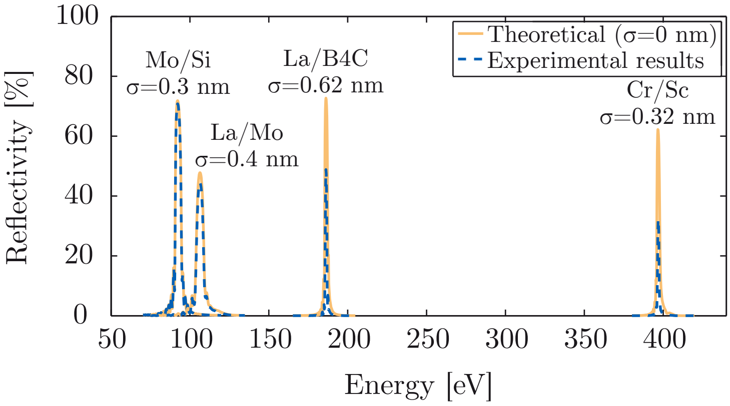

Figure 2.36: Theoretical and realized reflectivities for certain material systems. Measured maximum reflectivities in comparison to the theory. The listed realized interface roughness values were either derived from simulations or the specified reference for the material systems Mo/Si [91], La/Mo [16], La/B_4C [104] and Cr/Sc [105]. All reflectivities are realized at normal incidence (α<10^o).

2.4.5 XUV/soft x-ray multilayer material selection up to 600 eV

In principal, multilayer mirrors could be composed of almost any elements of the periodic table, but the physical (state of aggregation), chemical (material reaction) or biological (toxic) properties limit the number of elements. Besides, section 2.3.2.1 made it clear that the performance of a multilayer mainly depends on the optical constants of the used materials. The tunability of spectral characteristics or simply the achievable reflectivity in a certain energy range depends on its material system. Equation (2.52) shows that the single interface reflectivity depends on the difference of the optical constants but section 2.4.2.3 has shown that the penetration depth has to be considered in multilayer systems. It could sometimes be better to exclude a material with a high absorption, although this would lead to a high single interface reflectivity when it is combined with a low absorbing material. Reflectivity simulations were performed for the 200–600 eV energy range using the following materials: Al_2O_3, B_4C, Ba, Be, Ca, C, Co, Cr, Ge, Fe, La, Mg, Mo, Ni, Ru, Sc, Si, Ti, V, W. Each material combination was considered and the best systems were selected. As this large number of material combinations would exceed any meaningful presentation only the selected systems are shown in the following figures. Figure 2.37 depicts the real (a) and the imaginary (b) parts of the complex refractive index of suitable materials in the 200–600 eV energy range. The figure shows the characteristic mate-

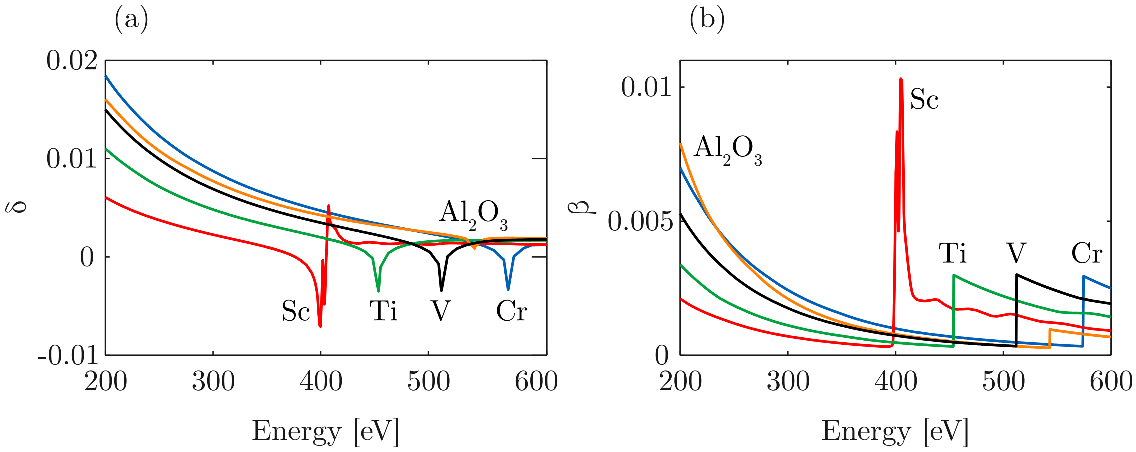

Figure 2.37: Dispersion and absorption in the 200–600 eV energy range. Optical constants of Sc (red), Ti (green), V (black), Al_2O_3 (orange) and Cr (blue) in the spectral range between 200 and 600 eV. (a) Dispersion δ, i.e. the deviation of the real part of the refractive index from unity whereas the imaginary part (extinction β) is shown in (b).

rial absorption edges at distinct energies, which are necessary for a high multilayer mirror reflectivity as has been stated in section 2.3.2.1. As can be seen in figure 2.37, δ and β are on the same order of magnitude and are decreasing with increasing energy. Deviations from this trend occur only in the vicinity of absorption edges. This was already mentioned in section 2.3.1.2. When the materials are selected one can go further and determine the single interface reflectivity of certain material combinations. According to equation (2.52) one can calculate the single interface reflectivity by using the optical constants of the used materials. A normal incidence angle of 5^o was considered for the simulation. Figure 2.38 displays the single interface reflectivity of the material combinations Cr/Sc, Ti/Ni, V/Ni, Al_2O_3/Ni and Cr/Ni. The single interface reflectivity drops from ≈0.01% at 200 eV to the 0.0001% range at 600 eV showing only strong rising in the vicinity of absorption edges. It should be mentioned that the system Ti/Ni exceeds Cr/Sc below 380 eV but only in case of single interface reflectivity. This is attributed to the high absorption of Ni in this energy range. As was mentioned in the beginning of this section, a high absorption may boost the single interface reflectivity but limits the adoption for multilayer as the number of contributing layers is restricted. All these mentioned characteristics

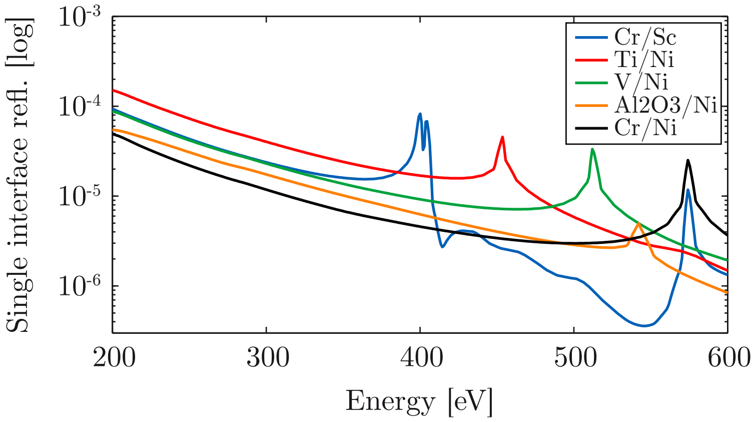

Figure 2.38: Single interface reflectivity between 200 and 600 eV. Single interface reflectivity of the material combinations Cr/Sc (blue), Ti/Ni (red), V/Ni (green), Al_2O_3/Ni (orange) and Cr/Ni (black) at 5^o normal incidence.

are attributed to the optical constants and show strong variation in the vicinity of absorption edges. Therefore, table 2.1 lists the exact absorption edges of the selected materials within the 200–600 eV energy range. All characteristic absorption

Element	Edge 1	Type 1	Edge 2	Type 2	Edge 3	Type 3
Sc [106]	398.7	L_3	403.6	L_2	498.0	L_1
Ti [107]	453.8	L_3	460.2	L_2	560.9	L_1
V [107]	512.1	L_3	519.8	L_2		
O [106]	534.1	K				
Cr [107]	574.1	L_3	583.8	L_2		
Al [106]	—	—				

Table 2.1: Absorption edges of Sc, Ti, V, Al_2O_3 and Cr between 200 and 600 eV. For each element the reference is specified from which the data was taken. All energies are given in [eV].

edges (electron binding energies) can be found in [108]. The optical constants and single interface reflectivities of certain materials for multilayer mirrors between 30 and 200 eV can be found in [109]. The previous sections have stated the influence of various parameters on the multilayer mirror performance. Figure 2.39 summarizes these variations and illustrates the maximum achievable reflectivity in the 30–600 eV energy range at 5^o normal incidence. Best suited material combinations were selected for distinct energy ranges and their ideal γ value was previously derived from simulations. Realistic interface roughness values have been used for the material systems below 200 eV whereas a value of σ=0.3 nm has been assumed for the simulations, in case of the higher energies, since this value has to be at least achieved for sufficient reflectivity values at normal incidence.

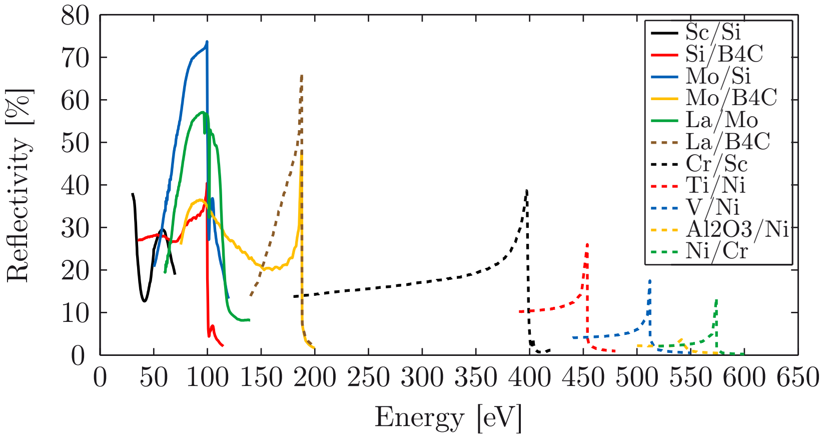

Figure 2.39: Material selection between 30 and 600 eV. The first six material systems are simulated with a period number of N=300, since more periods do not contribute to the reflectivity in this energy range. The five material systems working at higher energies are calculated with N=600, since the absorption is reduced and more layers contribute. The interface roughness values σ and the optimized γ-ratios, which were used for the simulations, are the following: $\sigma_{\mathrm{Sc/Si}}$=1.3, $\gamma_{\mathrm{Sc/Si}}$=0.4, $\sigma_{\mathrm{Si/B_4C}}$=1.3, $\gamma_{\mathrm{Si/B_4C}}$=0.6, $\sigma_{\mathrm{Mo/Si}}$=0.5, $\gamma_{\mathrm{Mo/Si}}$=0.4, $\sigma_{\mathrm{La/Mo}}$=0.4, $\gamma_{\mathrm{La/Mo}}$=0.45, $\sigma_{\mathrm{Mo/B_4C}}$=0.5, $\gamma_{\mathrm{Mo/B_4C}}$=0.5, $\sigma_{\mathrm{La/B_4C}}$=0.62, $\gamma_{\mathrm{La/B_4C}}$=0.45, $\sigma_{\mathrm{Cr/Sc}}$=0.3, $\gamma_{\mathrm{Cr/Sc}}$=0.4, $\sigma_{\mathrm{Ti/Ni}}$=0.3, $\gamma_{\mathrm{Ti/Ni}}$=0.65, $\sigma_{\mathrm{V/Ni}}$=0.3, $\gamma_{\mathrm{V/Ni}}$=0.45, $\sigma_{\mathrm{Al_2O_3/Ni}}$=0.3, $\gamma_{\mathrm{Al_2O_3/Ni}}$=0.5, $\sigma_{\mathrm{Ni/Cr}}$=0.3, $\gamma_{\mathrm{Ni/Cr}}$=0.45.

2.4.6 The Cr/Sc multilayer material system – history and status quo

This section will describe the history of results for the material system Cr/Sc being utilized for soft x-ray multilayer mirrors. The material system was first described by Salashchenko and Shamov in 1997 [110] where a reflectivity of 10.1% was realized in the vicinity of the Sc L_3-edge at 18^o normal incidence. In the year 2000 Franz Schäfers published a detailed study of certain material systems aiming for a high water window reflectivity [111]. This paper shows that Cr/Sc is a well suited material system for the lower spectral range up to the Sc L_3-edge at 398.7 eV (=3.1096 nm). In the following years much development was put into the optimization of this system for ever higher maximum reflectivity values. In 2002 Kuhlmann et al. realized a mirror for the nitrogen K_α line (392.4 eV) in the water window [112], while Fredrik Eriksson et al. aimed for the Sc edge. They exceeded Salashchenko's result and realized a normal incidence (α=2.5^o) reflectivity of 14.5% [113] at 3.11 nm. In 2006 Gullikson et al. realized the up to now highest normal incidence (9.2^o) reflectivity of 32% by using B_4C barrier layers [105]. A pure Cr/Sc system without any barrier layers was optimized by Eriksson et al. utilizing a modulated low-energy and high-flux ion assistance as a means of engineering the interface between the sub-nanometer layers on an atomic scale during magnetron sputter deposition [114]. Using this method a normal incidence (9.5^o) reflectivity of 20.7% could be realized close to the Sc edge. In section 4.8 it will be shown that we are able to exceed this value by optimizing the layergrowth itself. Using ion polishing should exceed our result further. In addition to high reflectivity values, the precision of the design realization is crucial for multilayer mirrors aiming for shaping attosecond water window pulses. The precision can be tested with aperiodic mirrors, since their spectral reflectivity behavior is quite sensitive to thickness fluctuations. At the beginning of this thesis no aperiodic Cr/Sc multilayer mirrors could be found in the literature. The first aperiodic systems were demonstrated by Bridou et al. [115] but aiming for grazing incidence (θ=1.5^o) in the keV range. Due to the low grazing angle, the designs exhibit rather thick layers in the 1–12 nm range and a layer thickness deviation from the target value around ±0.2 nm. Section 4.3 will show that much lower thickness values (0.6–2.4 nm) and a higher precision (±0.01 nm) is necessary for aperiodic Cr/Sc multilayer mirrors, for normal incidence angles in the water window. Finally, no Cr/Sc multilayer mirror was ever used for the generation of isolated attosecond pulses. This is demonstrated for the first time in section 4.9.

Chapter 4 will show the research results and the applications, which will demonstrate that Cr/Sc multilayer mirrors have reached the next level of performance on the basis of this thesis. The material system is ready for attosecond pulses in the water window spectral range.

Chapter 3

Methodology - Realization and characterization

This chapter provides all necessary information on software tools, the fabrication and the metrology of the multilayer mirrors presented in this thesis. The software tools, which are mainly used for the multilayer realization, are introduced in section 3.1. Section 3.2 describes in detail the ion beam deposition technique together with the parameters which have to be accurately analyzed and controlled for a high precision and reproducibility. The correct fabrication of multilayer mirrors requires the conversion from multilayer designs to deposition times and thus a detailed knowledge about interlayer formation, thickness compression by diffusion or even thickness increase. The subsequent sections provide information on different multilayer characterization techniques for in-situ and ex-situ analysis. Spectral ellipsometry, XUV/soft x-ray and x-ray reflectometry, transmission electron microscopy (TEM) imaging and surface profilometry have been used to characterize both the deposition rates and the characteristics of multilayer coatings. They are presented in detail in section 3.3.

3.1 Software tools

3.1.1 MATLAB

In this thesis all reflectivity and transmission calculations are based on a self-written multilayer Fresnel code algorithm written with the software `MATLAB` (version R2009a). The overall reflectivity (mirror) or transmission (polarizer, filter) is calculated together with the relevant phase based on the multiple interface reflections and transmissions (section 2.4.1). The code uses the tabulated values of the atomic scattering factors from Henke and Gullikson [85] above 30 eV or the calculated optical constants by Kramer-Kronig below 30 eV (section 2.3.1.3) in case of the XUV/x-ray spectral range. The IR/VIS/UV spectral range is covered later by describing optical constants measured with spectral ellipsometry (section 3.3.1.1). Realistic imperfect interfaces (section 2.4.4), top layer oxidation or interlayer formation like molybdenum silicide [116] are taken into account as the stack design demands.

3.1.2 Optilayer

Throughout this thesis the design program `Optilayer` (version 8.85), a Fresnel code coupled to a 'needle optimization' algorithm [94, 75] was used for the optimization (mainly chirped mirrors) of multilayer systems in combination with the self-written Fresnel code described in section 3.1.1. The most important prerequisite for a reasonable optimization is the properly chosen start design. One usually starts with a periodic multilayer system which consists of the material combination best suitable for the aimed spectral range and adjusts the layer thicknesses (optimized γ-ratio) to the central energy E of interest. The period number N of the start design is chosen according to the required spectral bandwidth ΔE and is estimated by:

$$\mathrm{N} = \frac{\mathrm{E}}{\Delta\mathrm{E}}. \tag{3.1}$$

Finally, one defines one or more target functions for the algorithm for which the start design should be optimized. The optimization can, for example, include a higher peak reflectivity, a spectral broader mirror reflectivity or in case of chirped mirrors an optimized spectral phase being realized by aperiodic layers, thus introducing a group delay dispersion in contrast to a flat phase in case of a periodic system. The needle optimization algorithm [75] starts with the periodic design and inserts small needle-like additional layers at certain positions in the stack, defined by the best benefit for the merit function. The thickness of these layers are consecutively increased or decreased until their best thickness value is achieved. Each optimization procedure consists of a certain number of iterations in which the current design is changed by random walk within user defined limits. The quality of a design $D_i(\omega)$ is quantized by the merit function MF including weights w_i (which have to be predefined) that define the importance of the individual target function $T_i(\omega)$.

$$\mathrm{MF} = \sum_i w_i (D_i(\omega) - T_i(\omega))^2. \tag{3.2}$$

The figure-of-merit function further rules whether the new design is taken as start design for the next iteration step or not. Thus every calculated design is a trade-off between different target functions and is a consequence of the start design. A user based optimization afterwards, like thin layer removal, leads to the final design. This procedure was mainly used for the results in section 4.3.

3.1.3 SRIM

The software SRIM (the stopping and range of ions in matter [117]) was used for simulations of deposition parameters. SRIM uses a Monte Carlo algorithm for the calculation of particle collisions based on published nuclear data tables of each element of the periodic table or even compounds. The simulated results such as the penetration depth of atoms into subjacent layers, the sputter yield (calculated as ejected atoms per incident ion) or the kinetic energy transfer upon collision can be exported. The software was mainly used for the results in the following deposition section 3.2.2 and the experimental results in section 4.4.

3.2 Dual ion beam deposition

Multilayer coatings are realized by various deposition techniques. On the one side the rather less used techniques chemical vapor deposition [118] or pulsed laser deposition [119, 120]. On the other side the most prominent deposition techniques magnetron sputtering [121, 122, 99, 123] or electron beam evaporation [124, 125]. The up to date highest XUV normal incidence reflectivity of 70.9% has been realized by magnetron sputtering and was measured in the vicinity of the silicon L_3-edge [91]. The highest precision control and reproducibility is realized by ion beam deposition [126, 127, 128]. This deposition technique was used for all multilayer systems in this thesis and is presented in detail in the following section.

3.2.1 Fabrication of multilayer mirrors

The ion beam deposition system (*NEXUS IBD-0* from *Veeco Instruments*) is located in a class 1000 cleanroom at the Max Planck Institute of Quantum Optics (MPQ) in Garching near Munich. Ion beam deposition and magnetron sputtering are known to be very stable. A big advantage compared to e.g. evaporation techniques is the possibility of sputtering materials independently of their characteristics (for example the melting point). This makes ion beam deposition a powerful tool allowing for a precise thickness control by sputter times without the need for in-situ thickness monitoring [129]. The system uses two external ion sources were the ion energy and the ion current can be controlled independently, which increases the degree of freedom for influencing the layer growth. A schematic sketch of the system is depicted in figure 3.1(a).

The required ions are provided by a noble gas plasma, which is generated by an inductively coupled radio frequency (RF) generator. Our system allows two noble gases, namely Krypton (Kr) and Argon (Ar). The choice of the best sputter gas depends on the target material and the aimed ion energy, which is discussed in section 3.2.2. The system consists of two independent sources, the deposition source pointing at the selected target under an angle of 35 degrees normal incidence and the assist source, which points directly to the substrate under an angle of 31 degrees

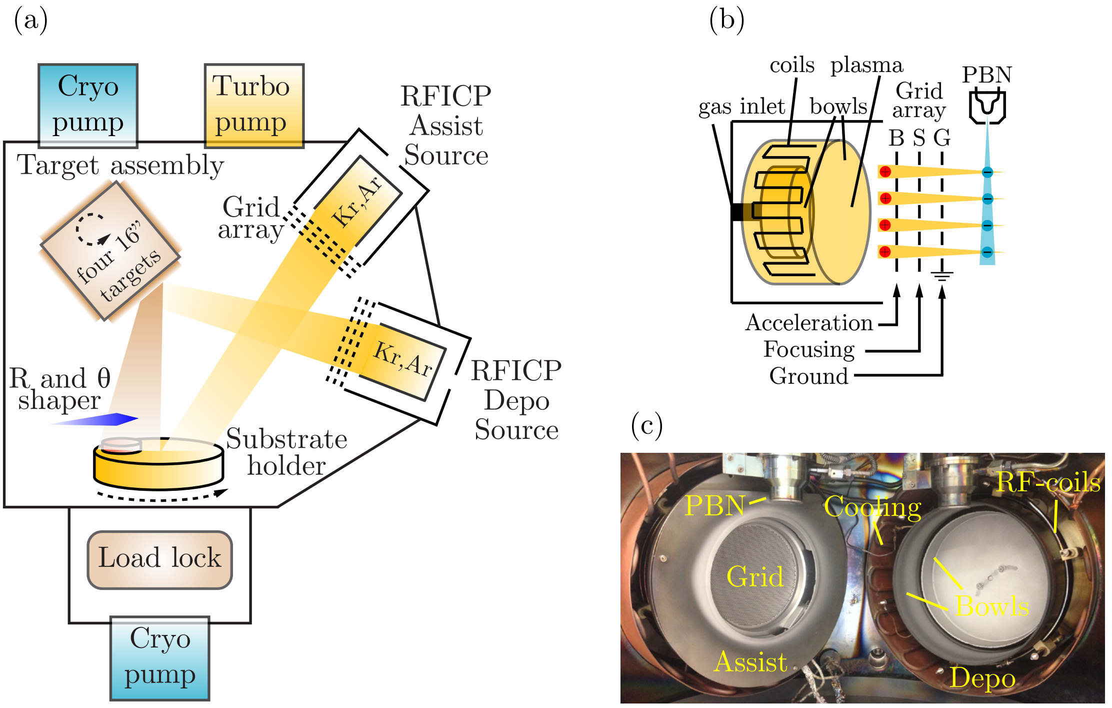

Figure 3.1: Dual ion beam deposition system. (a) Schematic setup of the dual ion beam deposition system at MPQ with load locked sample transfer, four target wheel assembly, beam shaper and rotating substrate holder. (b) Detailed side view of the plasma source. (c) Source photograph.

normal incidence. Both sources are equal in terms of their technical setup. The ions are extracted from the plasma, accelerated and focused onto the target material (in case of the deposition source) via a curved three grid ion optic [130]. The ion beam is neutralized after the grid by electrons from a plasma bridge neutralizer (PBN) tungsten (W) filament to prevent charging effects. A sketch of the source setup together with a photograph is depicted in figure 3.1(b)+(c), respectively. The neutralized ions ablate atoms of the target material disk (diameter=16 inch) on impact, which are afterwards deposited on the sample (near normal incidence) 50 cm away. This rather large distance between the target material and the substrate reduces the amount of implemented sputter gas impurities in the deposited films. Additionally, a shaper (R and θ) and a rotating sample holder (40 rpm) ensure a homogeneous deposition. Up to four different target materials can be loaded at the same time, which are attached to a rotary tower for choosing the material of interest. A cryogenic and a turbo pump are connected to the process chamber to ensure a background pressure of 10^{-8}–10^{-9} mbar, which minimizes layer contaminations during deposition. Another cryogenic pump is connected to the load unit to allow for a load locked system.

3.2.2 Deposition parameters

The layer growth can be influenced by several parameters. The most important parameter is the beam voltage which is applied to the grid for ion acceleration. The lower the kinetic energy of the sputter ions, the lower is the kinetic energy of the target atoms and vice versa. The optimum ion energy depends on the target material of interest. Besides, the suppressor voltage is responsible for focusing and determines the beam spot on the target. Another adjustable parameter is the beam current, which has a direct impact on the deposition rate. All of these parameters have a direct impact on the deposition, since they influence either the kinetic properties, the number of ablated target atoms or the divergence of the target beam. It turned out that it is not necessary to use the same parameters, for all materials, during one process. The system is stable enough to use the parameters which fit best for each material . On the other hand it is not possible to choose the parameters at random. For a beam of low divergence and a suitable focus on the target without destroying the grid optics certain parameter constellations are required [109][1].

Usually an ion current of 200 mA is achieved by a coupled RF power of 210 W. The suppressor grid has an electric potential of -200 V to the first grid and a beam voltage in the range of 400–600 V is applied. This leads to deposition rates in the range of 0.01–0.1 nm/s which ensures a very controllable deposition but rather long fabrication time of several hours (3-30 h). An overview of the deposition rates dependent on the material or acceleration voltage is listed in table 3.1.

Material	Ti	Ni	V	Al_2O_3
Sputter rate [nm/s]	0.029	0.052	0.035	0.020
Error [nm/s]	0.002	0.002	0.001	0.001

Voltage variation	Cr (600 V)	Cr (400 V)	Sc (600 V)	Sc (400 V)
Sputter rate [nm/s]	0.052	0.037	0.043	0.037
Error [nm/s]	0.002	0.001	0.001	0.001

Table 3.1: Material dependent sputter rates. Overview of the deposition rates for certain materials dependent on the target material or the applied beam voltage.

The kinetic energy of the target atoms and their sputter yield (ejected atoms per incident ion) can directly be manipulated by the sputter voltage and the sputter gas

---

[1]

$$0.6 < V_b/(V_b + V_s) < 0.8 \tag{3.3}$$

$$I \sim 2{\cdot}3216\sqrt{40/Z_a}10^{-9}(2{\cdot}2/(1+1))(V_b + V_s)^{3/2} \tag{3.4}$$

All values are dimensionless. Here V_b and V_s is the beam and the suppressor grid voltage, respectively. I is the beam current, Z_a is the atomic number of the sputter gas.

as described previously. These kinetic energies show further different penetration depths into an already deposited material layer. This penetration depth directly influences the interface roughness (section 2.4.4) and therefore the performance of a multilayer system. Thereby one has to find the best trade-off between the optimum kinetic energy of the sputtered atoms for an optimized layer growth of defect-free, dense, smooth layers [131] and a low penetration depth into the subjacent layer to prevent layer intermixing [132]. Throughout this thesis kinetic target energies, sputter yields and penetration depths have been calculated using the Monte-Carlo simulation software SRIM (section 3.1.3). Figure 3.2(a) displays as example the kinetic energy (solid lines) of Ni atoms dependent on the sputter gas Kr (red) or Ar (blue) and the corresponding sputter yield (dashed lines).

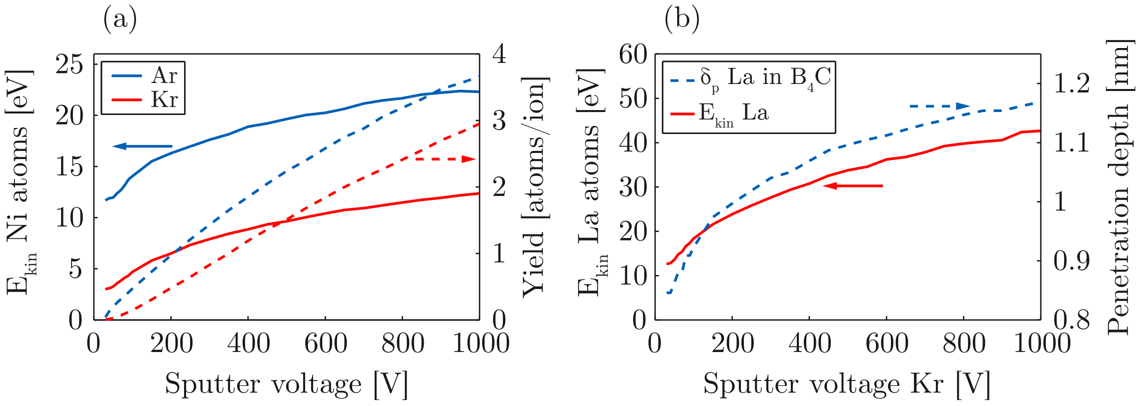

Figure 3.2: Kinetic energy, sputter yield and penetration depth dependent on the sputter voltage. (a) Kinetic energy (solid lines) and sputter yield (dashed lines) of Ni atoms dependent on the sputter voltage and the used sputter gas Kr (red) or Ar (blue). (b) Kinetic energy (solid red line) of La atoms and the resultant penetration depth (dashed blue line) into a B_4C layer.

As a result, the kinetic energy is approximately doubled by using Ar instead of Kr as sputter gas. Additionally one can calculate the kinetic energy of a certain target atom, dependent on the sputter voltage, and out of this kinetic energy the penetration depth into a subjacent layer. Figure 3.2(b) depicts the kinetic energy of La atoms dependent on the sputter voltage of Kr ions and the resultant penetration depth into a B_4C layer. A rather large penetration depth in the 1 nm range is found for this system. For both gases sputter yields and target energies have been calculated for the default sputter voltage of 600 V. The results for the materials Cr, Sc, Ti, Ni and V are summarized in table 3.2. One finds Kr to be best suited for the multilayer realization as a kinetic energy of ≈10 eV is well suited for an optimized layer growth [131].

Material	Yield (Kr)	Yield (Ar)	E_{kin} (Kr)	E_{kin} (Ar)
Cr	1.3	2.0	9.7	19.6
Sc	0.6	0.9	10.9	24.4
Ti	0.6	1.0	12.0	26.9
Ni	1.8	2.6	10.4	20.2
V	0.7	1.1	11.7	27.6

Table 3.2: Simulated sputter yield and kinetic energy of certain target materials. Sputter yield [target atoms/sputter gas atom] and the kinetic energy [eV] for Cr, Sc, Ti, Ni and V. The default sputter voltage of 600 V was used for the simulation, accelerating 50000 ions toward the target material under an angle of 35 degrees normal incidence.

3.2.3 Interface polishing with ions

In reality, multilayer interfaces are not perfectly abrupt (figure 3.3(a)) but washed out, which can result from the formation of alloys, non-negligible diffusion or due to the dimensions of the target atoms arising roughness. The diffusion can be reduced by reducing the kinetic energy and therefore the penetration depth whereas the formation of alloys can only be stopped by the use of barrier layers (e.g. B_4C layers are used as barrier in Mo/Si systems to avoid the formation of $MoSi_2$ [91]). Moreover the interface roughness is unlikely to be constant from the bottom to the top of the stack due to subsequent deposition of layers onto already roughened layers. This will accumulate roughness and is illustrated in figure 3.3(b).

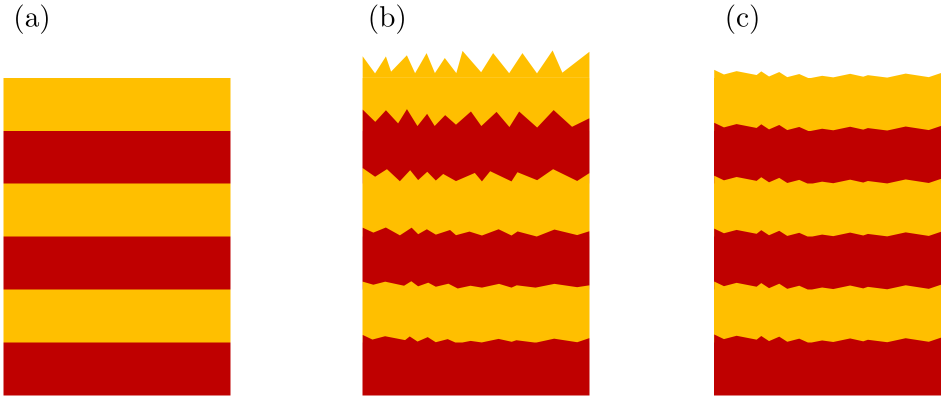

Figure 3.3: Roughness accumulation and interface polishing. (a) Theoretical model of a perfect multilayer stack. (b) The effect of roughness accumulation, where the roughness increases from bottom to top. (c) The small starting roughness stays constant throughout the whole stack due to interface polishing.

This roughness accumulation can be stopped by frequent interface polishing with ions (figure 3.3(c)). The second plasma source (assist) was used within this thesis to polish interfaces from multilayer systems and therefore improve their performance.

As mentioned the ions are directly accelerated toward the substrate and transfer their energy to already deposited layers. Much lower kinetic ion energies are necessary, compared to the deposition source, to maintain the layer structure on the substrate. A sputter yield slightly larger than zero is needed to ensure that interface polishing occurs. Indeed surface polishing should not lead to a contamination of the stack which requires a small penetration depth into the polished layer. Table 3.3 summarizes the sputter yields of a La layer which should be polished with Kr ions.

Voltage [V]	Sputter yield [atoms/ion]	Penetration depth [nm]
10	0.0000	0.44
20	0.0000	0.54
30	0.0226	0.62
40	0.0824	0.68
50	0.1246	0.74

Table 3.3: Lanthanum interface polishing with krypton. Acceleration voltage for krypton ions, the corresponding sputter yield of lanthanum atoms and the penetration depth of krypton atoms into the lanthanum layer.

As a result the polishing voltage of ≈30 eV is found with a not vanishing sputter yield and a rather low penetration depth of ≈0.6 nm for Kr ions into the La layer.

3.2.4 Deposition deviations

A high thickness precision is needed as XUV/soft x-ray multilayer mirrors consist of very thin layers (e.g. d_{Cr}≈0.6 nm for a Cr/Sc multilayer mirror working at the Sc L_3-edge at normal incidence). Additionally it is the prerequisite for the design realization of aperiodic multilayer systems. Therefore deposition deviations have to be analyzed and taken into account when sputter times are calculated for a certain mirror design. One point is a change of the deposition rate which can originate from hutches in the target material. Due to the ablation of the material, hutches can be generated by the focused ion beam after several months. A new flat area can be used for deposition by rotating the target material. Figure 3.4(a) depicts the deposition rate for three different silicon areas. This material was selected because it is the most used target material and has therefore the highest degree of ablation. It shows a possible high deviation of the deposition rate on the order of up to 10% dependent on the flatness of the surface. The deposition rate is additionally directly influenced by the sputter voltage (table 3.1) or by any change of the deposition/system parameters. For example, it turned out that a simple target exchange is responsible for a change of the deposition rate because the mounting process slightly changes the angle of the material disk. Therefore the deposition rates have to be calibrated if anything is changed. These deviations are on the order of up to 5% and are shown in Figure 3.4(b). Figure 3.4(c) shows the six different possible target areas together with the

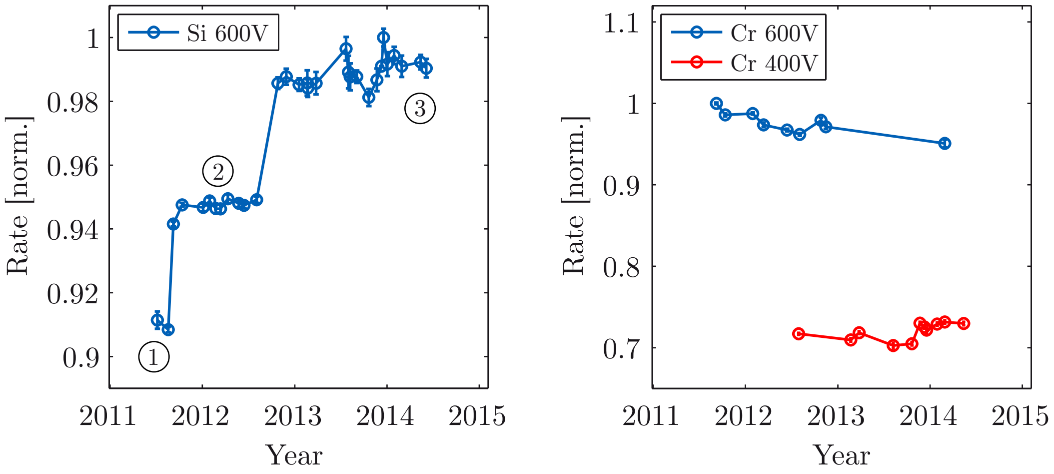

(a) Target rotation

(b) Sputter voltage

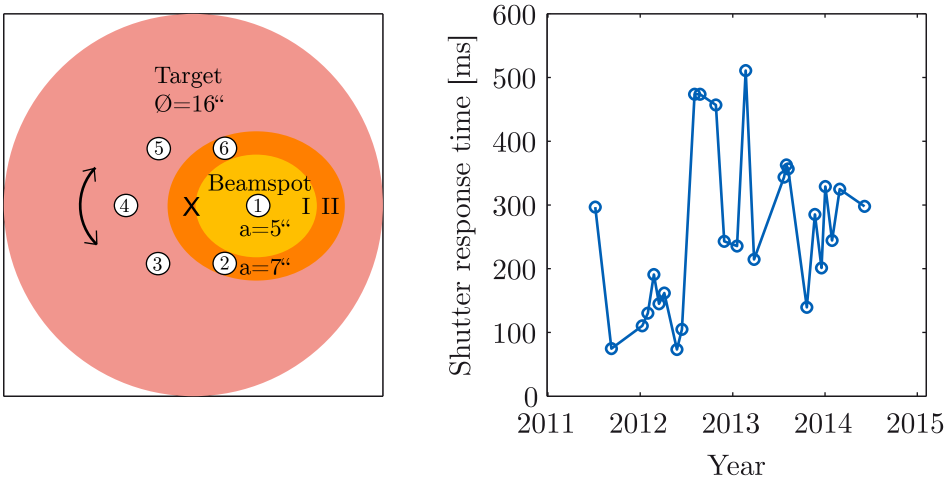

(c) Beamsize

(d) Shutter response

Figure 3.4: Deposition rate deviation and ion beam size. (a) Deposition rate and error range of silicon dependent on three different areas on the target material disk (deposited with a sputter voltage of 600 V). (b) Rate fluctuations together with the error of chromium deposited with a sputter voltage of 600 V (blue) or 400 V (red). (c) Six different target areas can be selected by rotating the target material disk (diameter=16 inch) where material is ablated by the focused ion beam (I: core focus, II: whole illuminated area). (d) Calculated response times of the shutter.

core focus of the ion beam (I) and the whole influenced area (II). Another factor for deviations arises from the shutter. The shutter blocks the substrate when rotating to another target, to prevent deposition during a target change after one layer has been finished. Since it has a non-negligible impact on the deposition, the response has to be taken into account for multilayer fabrication. The shutter is pneumatically controlled and has a response time which enables additional deposition as the sputter time is elapsed. This response time is in the range of 100–500 ms (figure 3.4(d))and changes when the pneumatic pressure is changed or the shutter gets bent after several depositions. The shutter is calibrated by comparing a ≈400 nm thick bulk, deposited in one run, with a multilayered bulk which was realized by the deposition of 800 layers with a thickness of 0.5 nm. The shutter closes 800 times and is responsible for a higher bulk thickness compared to the bulk deposited in one run without the shutter. The additional layer thickness per step is in the order of 0.005–0.025 nm which results in a total thickness increase of 4–20 nm. This deviation is resolvable by surface profilometry and taken into account when the sputter times are calculated.

The last point of possible deviations is thickness loss due to diffusion of the target materials. A high periodic (N=400) multilayer is realized with well-known deposition rates and shutter response time and one compares the theoretical stack height with the measured one. The measured difference related to the number of interfaces (=799) makes even losses per interfaces on the order of 0.01 nm resolvable. A selection of certain material systems, together with their diffusion loss per interface, is depicted in figure 3.5.

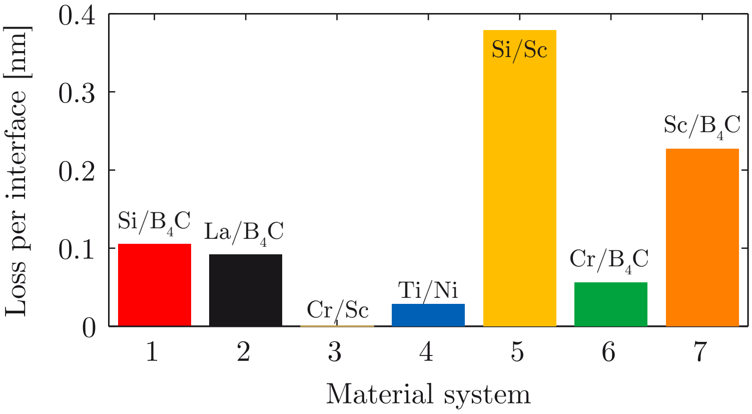

Figure 3.5: Diffusion of certain material combinations. Selection of certain material systems and their loss per interface due to diffusion. Si/Sc shows the highest loss per interface of almost 0.4 nm whereas no loss is found for Cr/Sc.

3.2.5 Conversion of a mirror design to deposition times

The high stability of ion beam deposition allows for a temporal control of the layer thicknesses by sputter times. Each target layer thickness of the design is therefore converted into an individual sputter time. The thickness loss is compensated by an increase of the sputter time, whereas the influence of the shutter and small uncertainties due to the switching process of the ion beam are taken into account by decreasing the sputter time by the determined values. A `MATLAB` algorithm is used to include all previously described deviations and calculate all sputter times. It further generates converted process files for the ion beam system. The calculated sputter times are used afterwards to determine the real design where top layer oxidation or interlayer formation is included. The characteristics of the real design differs slightly from the sputter design and must be known for a realistic simulation. The correct consideration of all parameters and the validity of the interface models is confirmed by the agreement between simulated and measured XUV and XRR measurements in periodic and aperiodic multilayer mirrors and will be presented in chapter 4.

3.3 Analysis techniques

3.3.1 In-situ techniques

3.3.1.1 Spectral ellipsometry

White light spectral ellipsometry is a comprehensive measurement technique, which makes use of phase and amplitude modulation of radiation upon reflection off a sample at a fixed angle of incidence [133]. Ellipsometry can therefore be used for in-situ measurements for analyzing or even control multilayer structured samples during deposition. An in-situ white light spectral ellipsometer (*M-2000VI* and *EC-400* from *Woollam*) was used for the following measurements and is directly mounted to the process chamber under an angle of incidence of α=75^o. The corresponding setup sketch is shown in figure 3.6. Furthermore one can reveal physical characteristics like

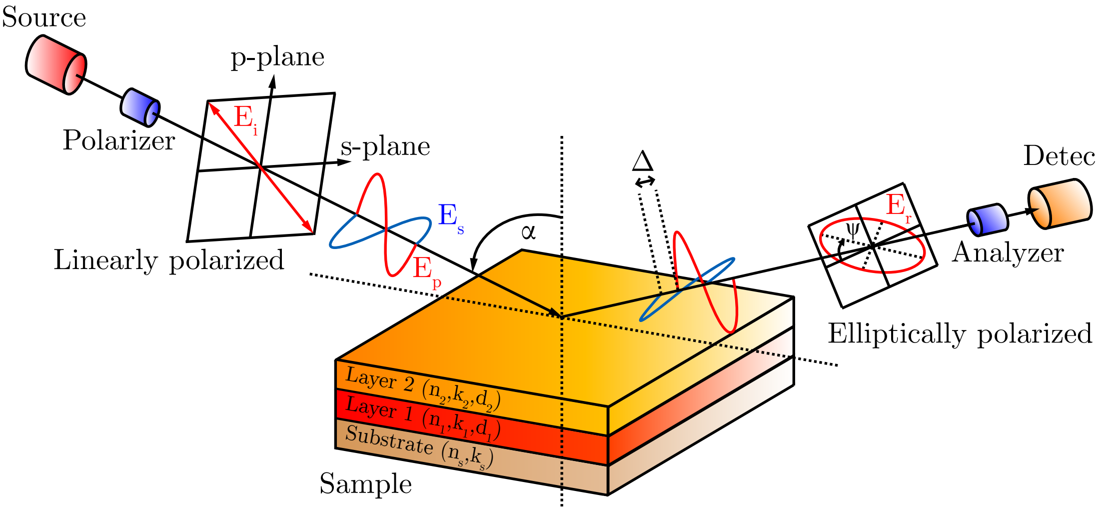

Figure 3.6: Spectral ellipsometry setup. Sketch of the ellipsometer setup. The linearly polarized light is elliptically polarized upon sample reflection. The reflection coefficients as well as the phases of s and p are measured and determine the ellipsometric parameters Δ and Ψ. The angle of incidence is α=75^o.

the optical constants in the IR/VIS/UV spectral range or the structure of a sample as well as chemical properties like layer oxidation of certain materials [134]. Spectral ellipsometry was used within this thesis to study layer growth, rate calibration, oxidation processes, surface polishing or for measuring the IR/VIS/UV optical constants of the deposited materials, since the density differs slightly from literature values, which results in slightly different optical constants. A double mirror for example, which is commonly used in attosecond streaking experiments (figure 2.10), often has the same coating for the core (reflecting the XUV) and the ring (reflecting the IR with $R_{IR} \approx 50\%$). The knowledge of the real optical constants of the used materials in the IR range allows for the determination of the IR pulse shaping upon reflection. The previously mentioned changes of the phase and amplitude are material as well as wavelength dependent and are mainly influenced by the sample structure. Linearly polarized light is elliptically polarized after adjusted reflection and is described by the ellipsometric parameters $\Psi(\lambda)$ and $\Delta(\lambda)$, which are defined by the ratio of the reflection coefficients of the s- and p-polarized light:

$$\rho = \frac{r_p}{r_s} = \frac{|r_p|}{|r_s|} e^{i(\varphi_p - \varphi_s)} = \tan(\Psi) e^{i\Delta}. \tag{3.5}$$

Here, r_p and r_s are the reflection coefficients of the p and s components and determine Ψ by $\tan\Psi = \frac{|r_p|}{|r_s|}$ and the phase difference of the p and s components is related to $\Delta = \varphi_p - \varphi_s$. A reference measurement is not necessary, since one uses ratios, which additionally makes spectral ellipsometry less prone to intensity fluctuations. Δ and Ψ pairs are measured for each wavelength λ, which allows for the calculation of the optical constants $\widetilde{n}$ and the thickness of the material, using the appropriate Fresnel coefficients (equations (2.43)–(2.46)).

The used *M-2000VI* ellipsometer supports, together with an Xe lamp, a spectral working range from 370–1695 nm. A typically used raw spectrum, including the unavoidable atmospheric absorption lines, is shown in figure 3.7. Using this broad

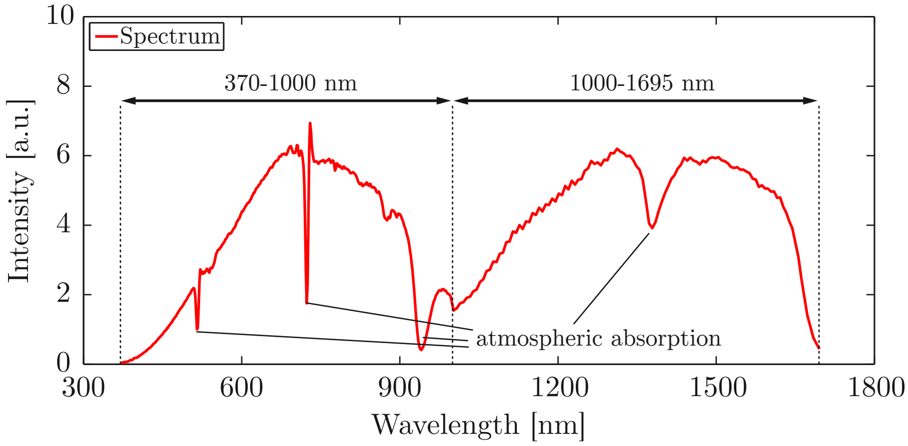

Figure 3.7: Spectral ellipsometry spectrum. Raw spectrum of the ellipsometer ranging from 370–1695 nm. The spectrum includes unavoidable atmospheric absorption lines [135, 136].

spectrum allows for the measurement of the optical constants of a sample in a large spectral range. Individual layer thicknesses can be fitted when the optical constants of the materials are known. The measurement technique is very accurate for measuring single layers or few layer stacks with an accuracy of <0.1 nm, when correctness of the underlying layer model can be assumed. As multilayered stacks reach higher complexity, the models also become more and more complex and the appropriate fit becomes less unique, which limits ellipsometry to low layer systems when high accuracy is required. The analysis of the ellipsometric data within this thesis was performed with the software EASE (version 1.60). Appropriate fit models are already implemented and will be presented in detail in the following.
In-situ ellipsometry requires models on both the optical constants and the structure of the stack for a reasonable fit of the layer thicknesses. One starts with a two layer system Si_{cryst}/SiO_2, since materials are usually deposited on crystalline silicon wafers, where a thin native SiO_2 layer is formed on top. Both the average offset angle (can originate from an imperfect alignment or from a bent sample) and the native SiO_2 layer thickness is fitted ellipsometrically. This individual sample information is included in the consecutive model. Typical SiO_2 thicknesses range between 1.5 and 2.5 nm and offset angles of about 0 ± 0.05^o are found. A third layer is now added to the model and in-situ data acquisition, as well as the deposition, is started. Optical constants of the deposited materials have to be measured previously to ensure a material specific model and achieve a reasonable fit of the layer thickness during deposition. The measurement of these optical constants differs for metals and dielectrics.

Optical constants and deposition rates of Ti, Ni and V

Optical constants of metals can be determined from ellipsometrically recorded data of thick (typically >100 nm) bulk samples, due to the limited penetration depth of IR/VIS/UV radiation in metals. When the layer is optical thick, the ellipsometric parameters Ψ and Δ do not change with increasing layer thickness and the optical constants can be extracted by making use of only one metal-vacuum interface. Averaging a time interval of $t\approx30$ min, after this thickness is reached, includes statistical factors. One can fit the individual layer thickness for each time step once the optical constants are known. The extracted optical constants of Ti, Ni, and V together with the fitted thicknesses are plotted in figure 3.8(a)+(b), figure 3.8(c)+(d) and figure 3.8(e)+(f), respectively. The results show the necessity of these measurements, since the deposited layer constants differ slightly from values found in the literature. The thickness fit becomes less unique when the limit of transparency is reached. The extracted Ti deposition rate is 0.033 ± 0.002 nm/s fitted from thicknesses smaller than 70 nm (figure 3.8(b)). In case of Ni a deposition rate of 0.069 ± 0.003 nm/s is found for thicknesses smaller than 65 nm in contrast to V, which shows a deposition rate of only 0.046 ± 0.002 nm/s where thicknesses smaller than 95 nm were used for the fit. When the ellipsometrically measured deposition rates are divided by the correction factor of 1.27, one finds a good agreement to the values listed in table 3.1. The

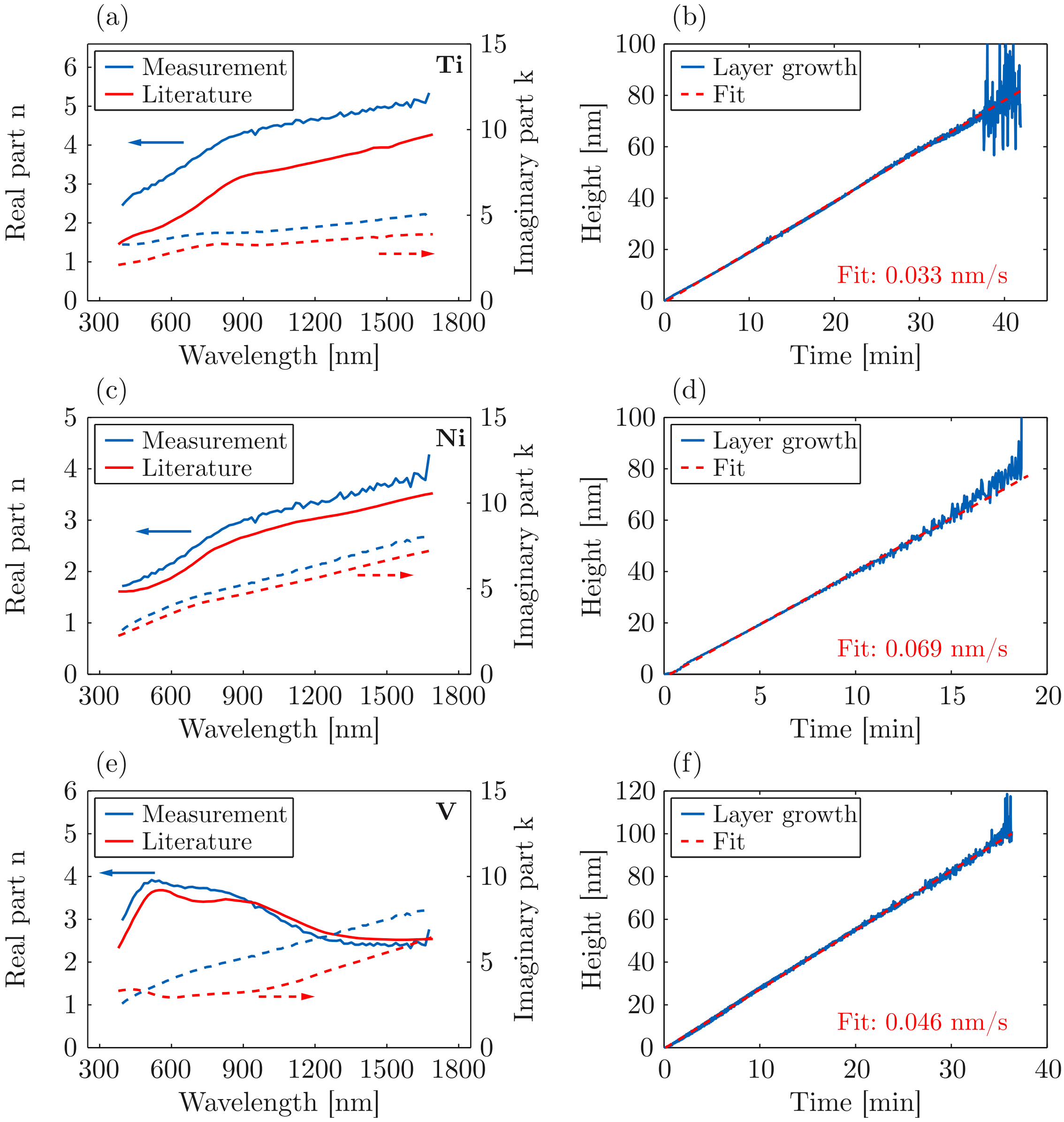

Figure 3.8: Measured optical constants of metals using spectral ellipsometry. Measured optical constants (blue) together with the values found in the literature (red) for (a) Ti [137], (c) Ni [138] and (e) V [139], respectively. (b), (d) and (f) show the corresponding layer growth (blue), the individual fit (dashed red) and the deposition rate value.

necessity of the correction factor will be shown later in section 4.3.

Optical constants and deposition rate of Al_2O_3

In contrast to the previously analyzed metals, the dielectric material Al_2O_3 remains transparent in the IR/VIS/UV range for even thick layers of a few hundred nm.

Therefore the thickness and the optical constants have to be fitted simultaneously during the layer growth. The Cauchy dispersion formula can be used to describe the wavelength dependent optical properties of Al_2O_3 [140]:

$$n(\lambda) = B_0 + \sum_{j=1}^{i} \frac{B_j}{\lambda^{2j}} \overset{i=2}{=} A + \frac{B}{\lambda^2} + \frac{C}{\lambda^4}. \tag{3.6}$$

The first two factors of the series are sufficient to describe the measured dispersion of Al_2O_3, thus only the parameters A, B and C are used. This description is only valid for ideal transparent materials, where the extinction coefficient k in the complex index of refraction $n + ik$ is almost zero. Absorption would be included by

$$k(\lambda) = \alpha e^{12400\beta(\frac{1}{\lambda} - \frac{1}{\gamma})}, \tag{3.7}$$

where α, β and γ are fit parameters. A possible absorption region of the deposited Al_2O_3 layer was included in the fit to prove the correct assumption of equation (3.6). This previously described approach was used and the ellipsometrically recorded data was dynamically fitted. Figure 3.9 displays a typical dynamic data acquisition together with the corresponding fit (dashed black) for certain selected wavelengths.

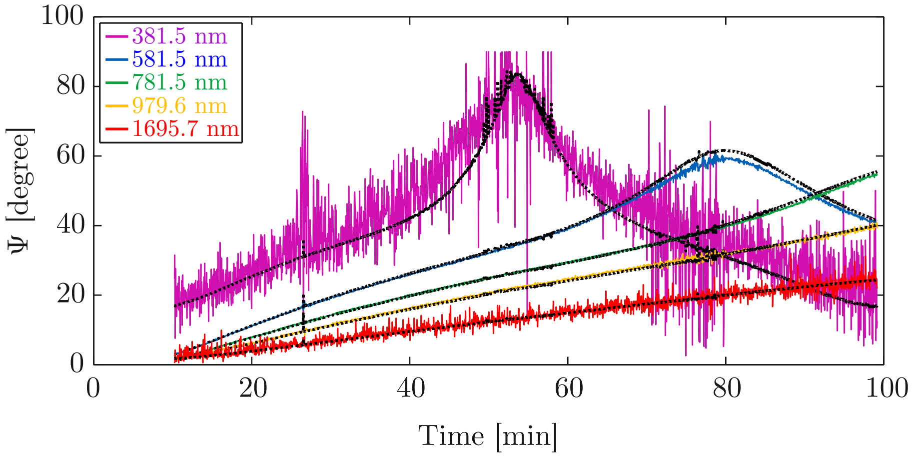

Figure 3.9: Dynamic data acquisition of the ellipsometric parameter Ψ. Measured ellipsometric data plotted for certain wavelengths during Al_2O_3 deposition. The dashed black lines display the appropriate fits using the Cauchy parameters of table 3.4. The shutter was closed below 10 min and no reasonably data was acquired for t<10 min.

The appropriate extracted parameters of the Cauchy formula are listed in table 3.4. No absorption is found in case of the fit and in the literature, which proves the assumption of equation (3.6) to describe the dispersion of the Al_2O_3 layer. Figure 3.10(a) shows a comparison of the extracted optical constants (blue) and the values from literature (red) whereas figure 3.10(b) depicts the layer growth (blue) and the fitted (red) deposition rate of 0.024±0.002 nm/s, again in agreement with the value of table 3.1, if the correction factor of 1.27 is taken into account.

	A	B	C	α
Measurement	1.672	0.00799	0.00004	0
Literature	1.751	0.00632	-1.0152	0

Table 3.4: Comparison of Cauchy parameters for Al_2O_3. Fitted Cauchy parameters of an Al_2O_3 layer out of an ellipsometric measurement in comparison to the values found in the literature [141].

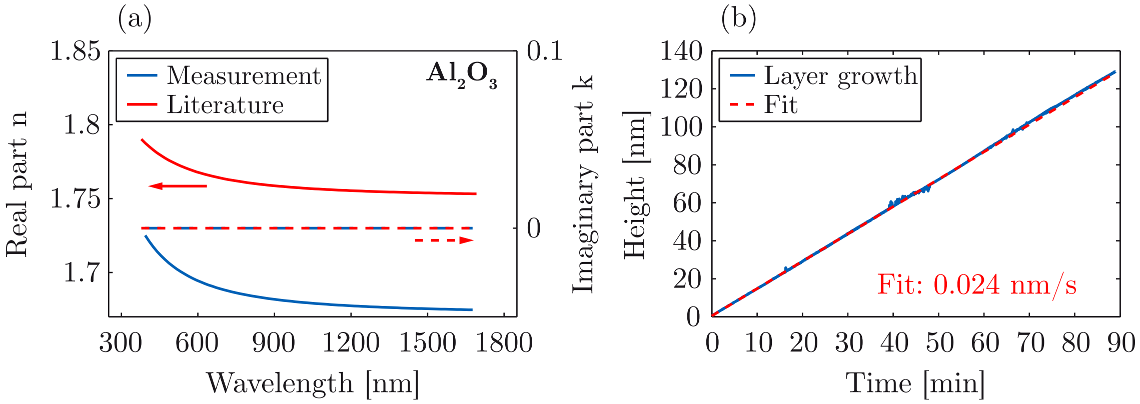

Figure 3.10: Measured optical constants of a dielectric using spectral ellipsometry. (a) Measured optical constants (blue) of Al_2O_3 together with the values found in the literature (red) [141]. (b) Measured layer growth (blue) and the corresponding fit (dashed red) indicating a deposition rate of 0.024 nm/s.

The constant thickness increase and its agreement with profilometry values for all materials, independent of the substrate, confirms the correctness of the used models.

3.3.2 Ex-situ techniques

In addition to the in-situ technique described in the previous section there are several ex-situ measurement techniques commonly used to analyze multilayer structures after the deposition process. These are described in the following sections.

3.3.2.1 XUV/soft x-ray reflectometry

An absolute reflectivity measurement of a multilayer mirror requires a stable and well calibrated XUV/soft x-ray source, which is fulfilled at a synchrotron. Most of the measurements in this thesis have been done at the beamline 6.3.2 of the *Center for X-Ray Optics* (CXRO) at the *Advanced Light Source* (ALS) [142]. Different XUV/soft x-ray optical components as gratings, multilayer mirrors and apertures allow for the adjustment of the XUV/soft x-ray energy from 30 eV to 1300 eV. The measured reflectivity accuracy depends mainly on the spectral purity of the incoming light, since undesired wavelengths are also reflected by the multilayer mirror, which leads to a measured reflectance deviating from the supposed one. Therefore, an order suppressor has been installed lately at the beamline in order to suppress high order light, leading nowadays to a reflectivity accuracy of 0.14%. For a Cr/Sc multilayer with 30% peak reflectivity, this would result in an absolute accuracy of about 0.04%. The setup together with the critical specifications are shown in figure 3.11. The raw

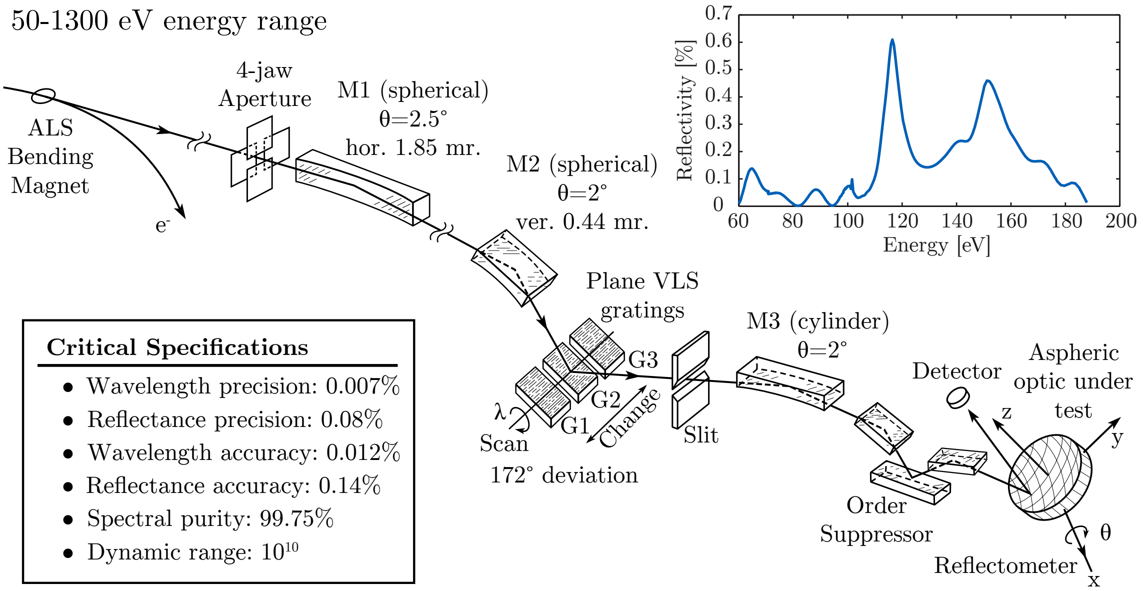

Critical Specifications

- Wavelength precision: 0.007%
- Reflectance precision: 0.08%
- Wavelength accuracy: 0.012%
- Reflectance accuracy: 0.14%
- Spectral purity: 99.75%
- Dynamic range: 10^{10}

Figure 3.11: ALS reflectometry beamline. Sketch of the ALS beamline 6.3.2 (Figure taken/adapted from [142]); critical specifications are shown, please see text for more details. The small inset shows as example the XUV/soft x-ray measurement of the aperiodic design of figure 2.32.

value of the reflectance R_{exp} is defined as [143]:

$$R_{exp} = \frac{(I_R - D)k_R/I_R^R}{(I_0 - D)k_0/I_0^R}. \tag{3.8}$$

With I_0^R the readings of the electrometer for incident and reflected signals, respectively, $k_{0,R}$ the corresponding calibration factors of the electrometer, D the dark signal of the detector and the stored electron currents $I_{0,R}^R$ corresponding to direct and reflected signals. Other XUV/soft x-ray reflectivity measurements in this thesis were carried out at the PTB beamline at BESSY II in Berlin with a similar setup and accuracy [143].

The measured XUV/soft x-ray reflectivity is analyzed by comparing the measured data with the target reflectivity. The best case the measured reflectivity matches the simulated target reflectivity. Otherwise one fits the target design to match the measured data. The realized reflectivity shows either a shift in the central energy, due to a wrong realization of the period thickness (can be adjusted by a constant thickness correction factor), or a broadening of the bandwidth which results from thickness fluctuations (linear increasing or decreasing correction factor). The peak reflectivity can finally be fitted by the interface roughness value σ. Figure 3.12(a) shows an image of a realized two inch ‘quadrant mirror’, where each quadrant reflects a certain central energy and by simply rotating the mirror one can choose the spectral range of interest. Figure 3.12(b) shows as example the results of the two measured and fitted witness samples corresponding to the 95 eV or 170 eV quadrant. One finds only a slight shift of the aimed central energy. This mirror found its application in the coarse spectral characterization and calibration of a laser-plasma driven undulator XUV/soft x-ray source.

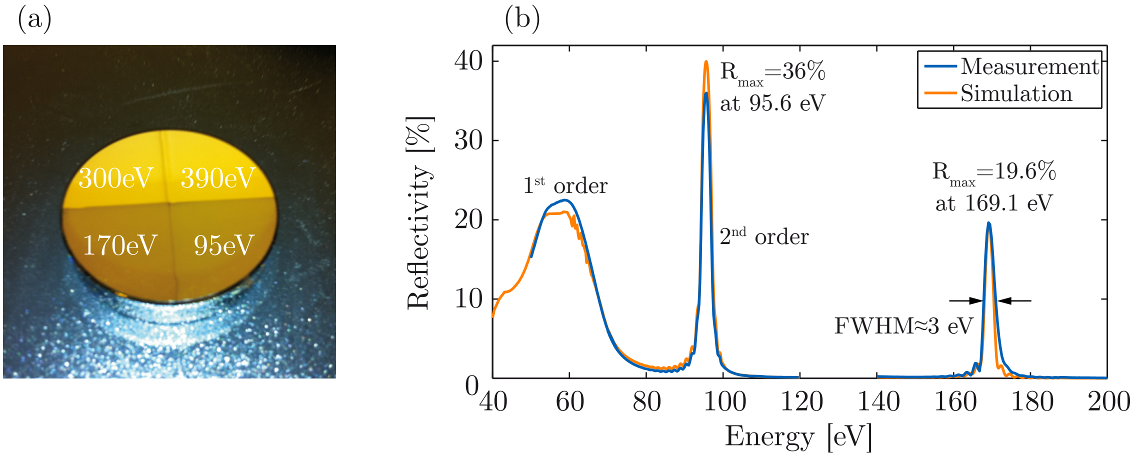

Figure 3.12: Quadrant mirror and the corresponding XUV measurements. (a) Picture of the realized ‘quadrant mirror’ where each quadrant aims for a certain spectral range. (b) XUV/soft x-ray measurement (blue line) and the corresponding simulation (orange) for a Mo/Si multilayer (left measurement: $N=25$, $\gamma=0.4$, $d=19.3$ nm, $\sigma=0.6$ nm, $\alpha=45^o$) and a La/B_4C multilayer (right measurement: $N=70$, $\gamma=0.5$, $d=5.34$ nm, $\sigma=0.8$ nm, $\alpha=45^o$). The measured Mo/Si reflectivity includes the first and second order mirror reflection, aiming for a small bandwidth reflectance under $\alpha=45^o$ as related to equation (2.65).

3.3.2.2 Grazing incidence hard x-ray reflectometry (XRR)

Grazing incidence x-ray reflectometry (XRR, also GIXR) is a powerful analyzing method to gain information on the multilayer structure [87, 144] and it reveals information on the Névot-Croce roughness factor [103]. Throughout this thesis measurements were performed using a Mo K_α source at a wavelength of $\lambda=0.071$ nm$\widehat{=}$17.4 keV. The corresponding experimental setup is plotted in figure 3.13(a).

A *Göbel* mirror converts the x-ray beam coming from an x-ray tube into a parallel beam. The mirror consists of multilayer with laterally graded thickness, deposited onto a paraboloid surface, which additionally monochromatizes the beam by separating the Mo K_α- from the Mo K_β-line. Three apertures, one before the sample (typical width: 20 µm) and two behind the sample (typical slit widths are 100/150 µm) define

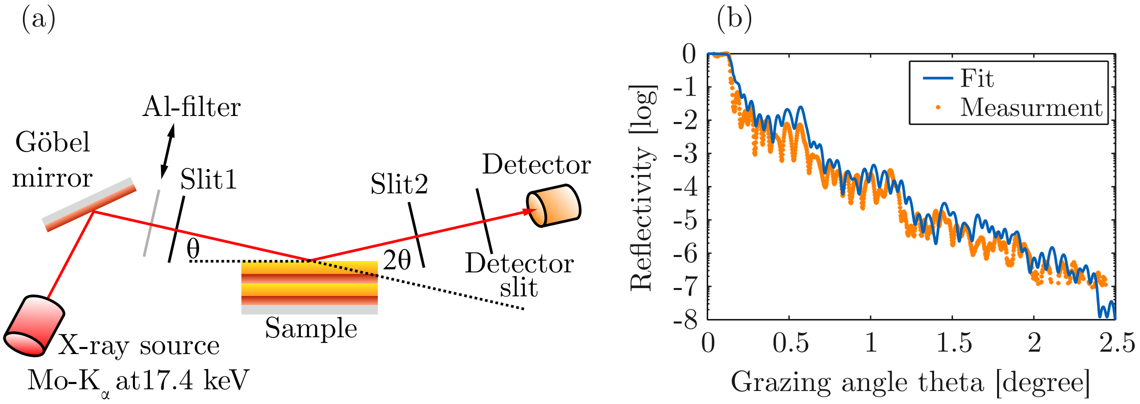

Figure 3.13: Grazing incidence hard x-ray reflectometry (XRR). (a) XRR setup: A *Göbel* mirror monochromatizes and parallelizes the hard x-ray beam. Slit 1 (width: 20 µm) limits the divergence, slit 2 is used for the background suppression and the detector slit width of 150 µm determines the angle resolution. (b) XRR measurement (orange) of an aperiodic multilayer mirror (design of figure 2.32) and the corresponding fit (blue).

the illumination function and the acceptance angle. The sample and the photo diode detector are mounted on rotating stages for an angle-resolved intensity measurement. Each sample is rotated under a grazing angle $\theta \approx 0^o$–5^o, with respect to the incident radiation, and the detector is moved under 2θ to measure the reflected intensity from the sample. In case of a periodic multilayer mirror one measures the Bragg peaks where the period thickness and the peak angle corresponds to Bragg's law (equation (2.60)) with increasing order. Indeed the big advantage of XRR becomes obvious when aperiodic multilayer mirrors are measured, since this measurement technique is very sensitive to thickness fluctuations and one can therefore prove the deposition accuracy of multilayer mirrors. Figure 3.13(b) displays the measurement and the fit of the aperiodic design of figure 2.32. This sensitivity is used for the analysis of aperiodic Cr/Sc water window mirrors in section 4.3.
The procedure of data acquisition and analysis:

- The average dark signal of ≈1 ct/s is subtracted.
- The range 0^o–0.5^o is measured with a 3 mm thick aluminum filter to ensure a constant source power for all angles and eliminating voltage dependent source emission. The filter attenuates the intensity and ensures a signal, which is below the saturation threshold of the detector. Measuring an overlapped angle range with and without the filter leads to the correction factor of the filter.
- At grazing angles only part of the beam illuminates the sample and can be reflected toward the detector. This effect is compensated analytically by incorporating the measured illumination function.
- The absolute reflectivity is given by $\frac{signal}{\mathrm{s}}$ normalized to the intensity at total

reflection.

The self-written multilayer Fresnel code described in section 3.1.1 was used for a final retrieval of the multilayer structure from the measurements. Signal averaging due to the finite source and the beam divergence is included in the simulation to ensure a correct comparison of the measurement and the simulation. It should be mentioned that the extracted Névot-Croce roughness from XRR measurements can be lower than the corresponding value from XUV measurements, which were described in the previous section. One reason could be an increasing roughness throughout the stack. Due to the deeper penetration of hard x-rays compared to XUV/soft x-ray radiation, the average Névot-Croce roughness is measured farther within the stack by XRR. Surface roughness for example has a minor effect on hard x-rays while it has a major impact on soft x-rays. Additionally material impurities may affect the XUV and XRR measurements differently or differences originate from a bent sample or alignment errors.

3.3.2.3 Transmission Electron Microscopy (TEM)

Transmission electron microscopy (TEM) is a high resolution technique (spatial point resolution <0.1 nm [145]), which allows for the analysis of the cross section of a specimen [146]. For this thesis multilayer cross section pictures have been taken with an electron microscope *TITAN* of *FEI* [147] using 300 keV electrons. A condenser system below the electron source focuses the electron beam onto the sample and, due to scattering and absorption, the transmitted electrons contain information about the sample structure. The beam is further focused by objective lenses and projector lenses expand the beam onto the imaging surface, e.g. a phosphor screen. Figure 3.14 (a) illustrates the setup whereas (b) displays a cross section example (the first seven periods of a Mo/Si multilayer deposited on a silicon wafer). TEM imaging requires the preparation of ultra-thin cross section samples which is achieved by mechanically grinding and polishing followed by ion milling with argon ions. TEM cross section images were taken of multilayer coated silicon wafer witness samples and the results are shown and analyzed in section 4.4.

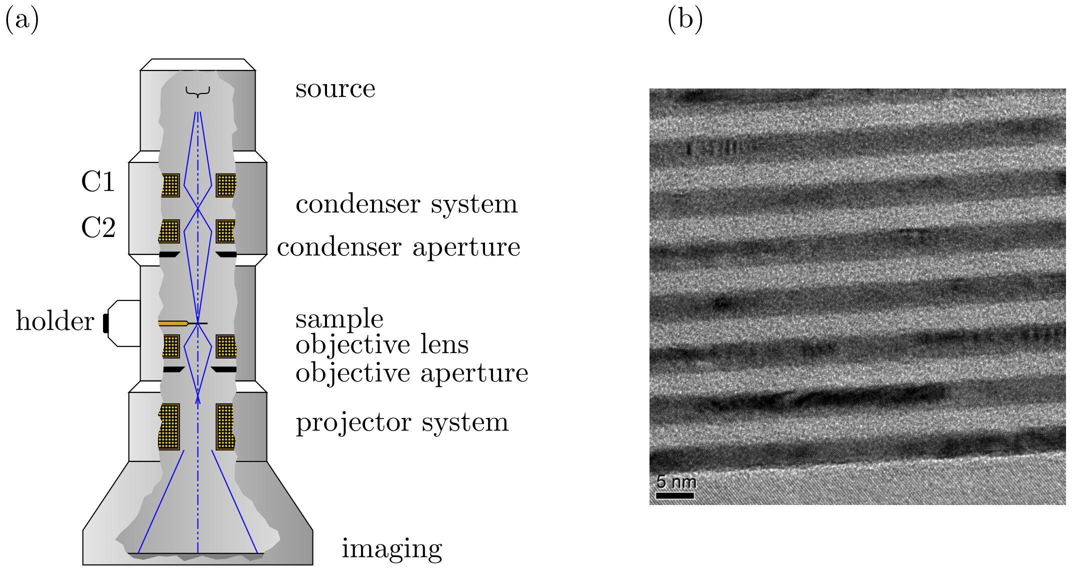

Figure 3.14: TEM setup and multilayer cross section. (a) TEM setup sketch (taken from [148]). (b) Cross section image of a Mo/Si multilayer (d=6.95 nm, γ=0.4) where molybdenum is the absorber (dark) and silicon the spacer (bright).

3.3.2.4 Surface profilometry

Surface profilometry is an analysis method being used for accessing the surface profile of a sample. Here a *Dektak 150 Stylus Profiler* (*Veeco*) has been used for the measurements (figure 3.15(a)). A stylus scans the surface along one line on typical

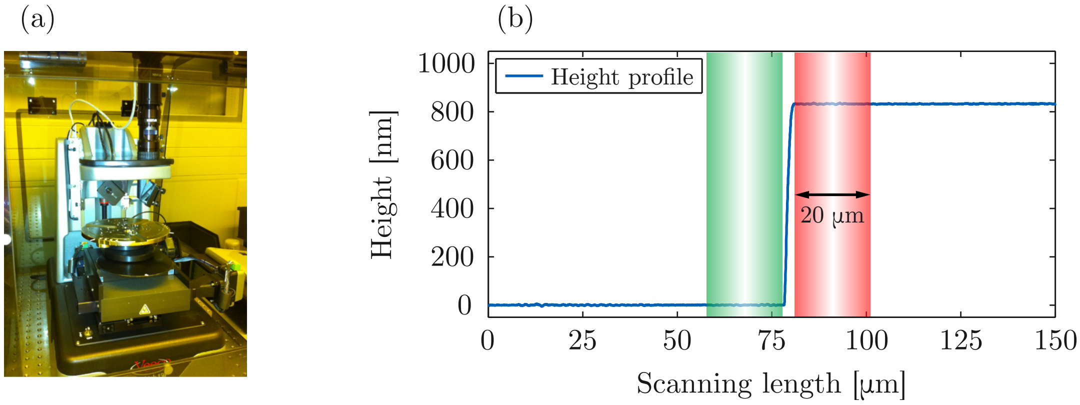

Figure 3.15: Surface profilometry. (a) Picture of the surface profiler located in the MPQ cleanroom. (b) Measured height profile along 150 µm. The lower and upper height is averaged along 20 µm located next to a ≈3 µm broad step.

length scales between a few µm to several mm and a connected LVDT is used for measuring the linear displacement. Only a relative height difference can be measured and therefore a leveling process, after the measurement, is necessary to determine the absolute height difference of interest. The typical error of one measurement, originating from mechanical noise, is on the order of 3–5 nm. As a large number of measurements reduces this error to a statistical error, a number of twelve points were measured with each point being measured twice, from low to high and vice versa. The mean value of the 24 acquired heights gives the total stack height of the coating and the standard deviation determines the statistical error to less than 0.4%. The best suited are thick samples between 250 and 900 nm, which have been used in this thesis for rate calibration, the impact of the shutter on the deposition or comparison measurements for the deduction of thickness loss in multilayer samples and therefore to access the value of diffusion losses. A typical measurement scan with a scanning length of 150 µm is shown in figure 3.15. The leveling length is 20 µm which is used to determine the absolute height difference.

Chapter 4

Research results and applications of multilayer optics

This chapter will present the research results on the realization and optimization of periodic and aperiodic multilayer systems being used in either reflection geometry or in transmission. Their application to water window pulses as well as attosecond pulses is shown. Section 4.1 shows the realization of transmissive (multi)layers for tailored filter systems which are commercially not available. Also a transmissive waveplate is presented to switch attosecond pulses from linear polarization to circular, a prerequisite for time resolved XMCD measurements. The subsequent section 4.2 addresses the potential of barrier layers and aperiodic designs for an improved mirror performance whereas section 4.3 demonstrates their application in attosecond science. High periodic systems have been realized and, by analyzing deposition effects such as height factors or top layer oxidation, the material system and the deposition could be well controlled resulting in a layer thickness error beyond 0.1 angstrom. This allows the realization of positively and negatively chirped Cr/Sc attosecond water window multilayer mirrors for attosecond pulse compression or controlling the photo excitation in two-photon experiments [76] in the future. Section 4.4 will present detailed results on the optimization of Cr/Sc multilayer systems by means of tailoring the kinetic parameters during the deposition and utilizing ion beam polishing for improved multilayer interfaces. The influence of material contamination on the mirror performance is analyzed in section 4.5. The subsequent section 4.6 will demonstrate how high precision multilayer mirrors enable coherent diffractive imaging in the XUV by filtering one harmonic peak out of a HHG spectrum. The first measurement of water window x-ray pulses from a laser-plasma driven undulator at 300 eV is presented in section 4.7 while section 4.8 aims for even higher photon energies, high periodic Cr/Sc and Ti/Ni mirrors for the Sc L_3-edge (398.7 eV) and the Ti L_3-edge at 453.8 eV. Section 4.9 finalizes this chapter by the characterization of attosecond soft x-ray pulses at 145 eV utilizing optimized Cr/Sc attosecond multilayer mirrors. The up till now highest photon energy where attosecond pulses from a table-top HHG source have been characterized by attosecond electron streaking.

4.1 Transmissive multilayer optics

Multilayer systems are mainly used as reflective element in the XUV/soft x-ray range. This is attributed to the high absorption of a transmissive element in this spectral range and the limited degree of shaping pulses in comparison to the high degree of freedom of reflective mirrors. However, as described in section 2.3.3 multilayer can be used as transmissive element, such as filters or polarizer, to shape attosecond pulses. These thin filters and a polarizer multilayer will be presented in the following sections.

4.1.1 Protecting multilayer systems against oxidation

Multilayer mirrors are capped with passivation layers such as Si, which forms a stable SiO_2 passivation layer, or B_4C to protect the subjacent layers against oxidation and thus a damage of the multilayer system. Lanthanum is a well suited element to demonstrate this oxidation effect, since it is well-known to strongly oxidize. The oxidation of La was studied and quantified using surface profilometry and light microscopy. A 150 nm thick La layer deposited onto two equal Si wafers. One sample was studied after the lift-off procedure with a light microscope and the second one was used for height measurements utilizing surface profilometry. Figure 4.1 depicts a selection of three light microscope images and the corresponding height measurement dependent on time. The light microscope images allow the tracking of the oxidation process as the La layer color changed constantly. However, surface profilometry revealed an even deeper insight into the time evolution of the oxidation process. During the first 75 min the height of the bulk increases at a rate of ≈2 nm/min until a first saturation around 300 nm is achieved. Nevertheless, oxidation continued for the first 24 h until the bulk height was maintained constant at ≈350 nm for at least 30 following days. This strong oxidation process definitely requires a capping with a passivation layer. This has to be taken into account in case of reflective optics and

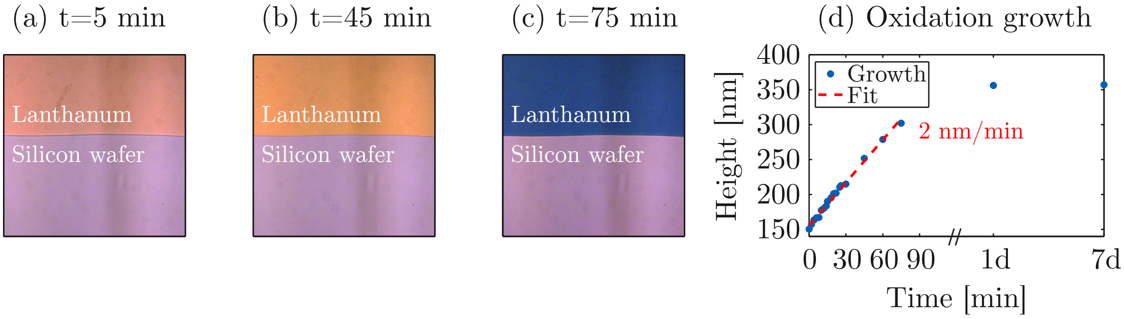

(a) t=5 min (b) t=45 min (c) t=75 min (d) Oxidation growth

Figure 4.1: Oxidation of a 150 nm thick lanthanum bulk. Light microscope images after (a) t=5 min, (b) t=45 min and (c) t=75 min allow the visual tracking of the oxidation process. (b) The corresponding height measurement (blue) is plotted against time and was linearly fitted for t<70 min to extract the thickness increase per time of 2 nm/min.

in case of transmissive optics at the bottom of the stack. This becomes clear when the fabrication process of transmissive elements is described in the next section.

4.1.2 Fabrication of freestanding transmissive multilayer systems

All the following fabrication steps are conducted in a class 1000 clean room environment in order to keep the contamination level as low as possible during sample handling. A silicon wafer is used as temporary substrate and is spin-coated with a PMMA photoresist. The arbitrary multilayer structure is applied on top of this resist by ion beam deposition. A thin adhesive Kapton foil is now placed on top of the multilayer system to improve the stability by reducing the stress on the multilayer structure introduced by the glue during its curing time. The glue is used to mount a curved metal washer on top of the Kapton foil. Finally, the photoresist is dissolved by an appropriate solvent and the Si wafer substrate is carefully removed. As the substrate and the photoresist is removed, one has to use a capping layer not only at the top but also at the bottom of the multilayer system to protect the system against oxidation. An illustration of the fabrication process is shown in figure 4.2(a)+(b). Applying this process allows the realization of freestanding multilayer systems with an aperture up to 8 mm (figure 4.2(c)) and a minimum thickness of ≈50 nm. Freestanding scandium filters, $B_4C/La/B_4C$ or various polarizers have been realized with this technique, since these systems are commercially not available.

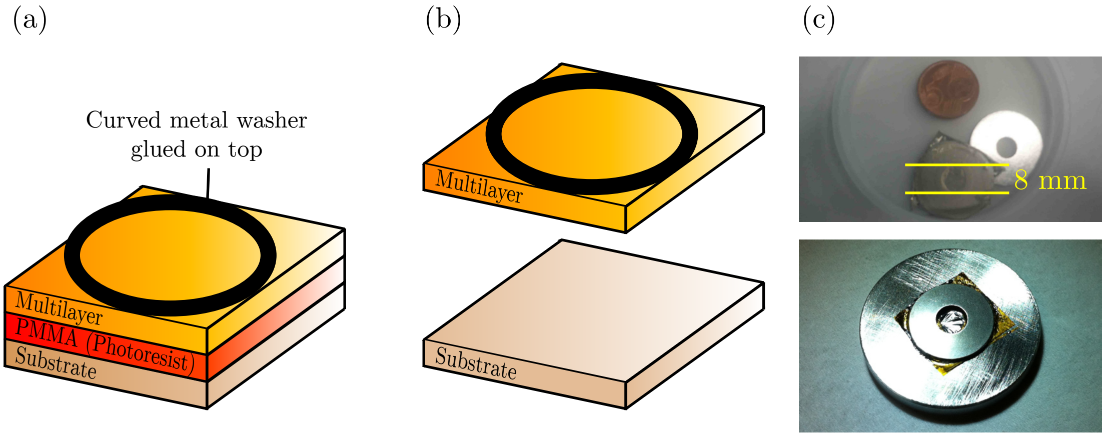

Figure 4.2: Fabrication of freestanding multilayer systems. (a) A curved metal washer is glued on top of the multilayer. (b) Dissolving the photoresist facilitates the realization of freestanding multilayer systems. (c) Photograph of a scandium filter with an aperture of 8 mm (top) and a mounted polarizer on top of an aluminum disc with a diameter of 1 inch (bottom).

4.1.3 Transmissive filters and a multilayer polarizer

Section 2.3.3.2 has described the possibility of using multilayer systems as a polarizer. When they are used under an angle of incidence close to the Brewster angle ($\approx 45^o$ in the XUV: see equation (2.55)) the p-polarized components are transmitted and the s-polarized components are partly transmitted and reflected at each interface (see figure 2.23). The multilayer system can be designed such that a phase shift of 90^o is introduced for the s-components in respect to the p-components and additionally with a transmission of both components that T_s equals T_p. This switches linearly polarized attosecond pulses to circularly polarized pulses for all ultrashort time resolved experiments, which benefit from circularly polarized HHG radiation such as ultrafast measurements on chiral systems, magnetic systems and other spin-polarized systems. Figure 4.3(a) depicts the transmission properties of both polarization components and the phase difference between ϕ_s and ϕ_p dependent on the photon energy. The corresponding multilayer design is illustrated in figure 4.3(b). The design was chosen for future time resolved XMCD measurements [90] at 66 eV close to the nickel M_3-edge. The simulation shows an equal transmission of $\approx 5\%$ for both polarization components and an introduced phase shift close to $\Delta\phi = 90^o$ at 66 eV. The illustrated multilayer system of figure 4.3(b) was realized as transmissive freestanding element utilizing the fabrication process of section 4.1.2. In order to measure the polarization and transmission characteristics of the waveplate a multilayer mirror as reflective element was additionally designed and realized. This analyzer mirror (Si/B_4C, N=20, d=14.38 nm, γ=0.5) is also used close to the Brewster angle at 45^o

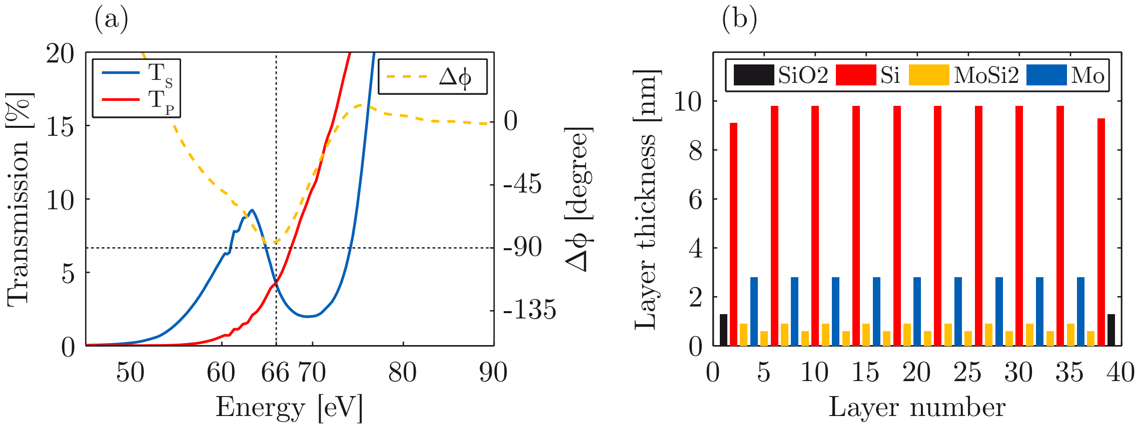

Figure 4.3: Transmission behavior and design of a polarizer multilayer. (a) Simulated spectral transmission behavior and phase difference of the multilayer waveplate for an angle of incidence of 45^o. The waveplate is designed for a nominal photon energy of 66 eV where T_s (solid blue) equals T_p (solid red) and a phase shift (dashed orange) of nearly 90^o is introduced. (b) Realistic design of the waveplate composed of Si (red) and Mo (blue) where the SiO_2 (black) is built due to oxidation and the asymmetric Mo/Si_2 layers are formed when a Mo/Si material system is utilized [99].

allowing for a high extinction ratio R_s/R_p, since most fraction of the p-components is transmitted. Figure 4.4(a) shows the simulated reflectivity of the s-components (solid blue) and the extinction ratio R_s/R_p (dashed red), i.e. the suppression factor of reflected p-components compared to s-components. This ratio is larger than 50 over

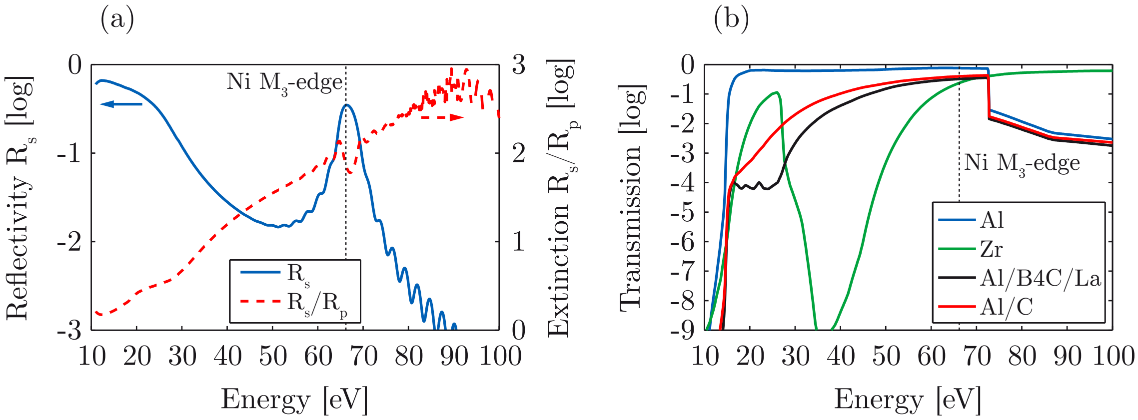

Figure 4.4: Multilayer mirror for polarization analysis and tailored filter systems. (a) Reflectivity of the s-polarization (solid blue) and the extinction ratio R_s/R_p (dashed red). (b) Transmission of certain filter materials: 200 nm Al (blue), 150 nm Zr (green), 200 nm Al/70 nm B_4C/40 nm La (black) and 200 nm Al/50 nm C (red).

the entire reflection bandwidth. The reflectivity for s-polarization has a peak value of 34% at 66 eV and a reflection bandwidth of 4.6 eV (FWHM). Together with the polarizer, which supports as pulses still with good ellipticity as can be seen later in the measured results, both elements can be used for sub-fs time resolution. As seen in figure 4.4(a) the analyzer mirror loses its polarizing capability, i.e. the extinction approaches 1, for low photon energies below 40 eV, while at the same time its reflectivity increases again for that energy range. Therefore, one has to suppress the low energy components as these low polarization separations superimpose in a non-energy resolving measurement as this one with the energy range of interest around 66 eV. As standard Al or Zr filters are not appropriate for this task, tailored filter systems have to be realized. Freestanding B_4C/La/B_4C filters and La/B_4C deposited on an Al filter have been realized in order to suppress the low energy components. Figure 4.4 depicts the transmission properties of certain filter systems showing that La/B_4C is well suited for a high suppression of the low energy components and fulfilling an almost high transmission of >30% when it is combined with aluminum. After the theoretical analysis of the waveplate and the analyzer mirror, together with their realization by ion beam deposition, the characteristics have been analyzed utilizing high harmonic radiation. The high harmonic radiation hits the waveplate under an angle of incidence of α_1 close to the Brewster angle and the transmitted polarization manipulated radiation is analyzed afterwards with the analyzer mirror also with an angle of incidence α_2 close to the Brewster angle. An illustration of the setup is shown in figure 4.5(a). The incidence angle of the analyzer mirror is set to α_2=45^o

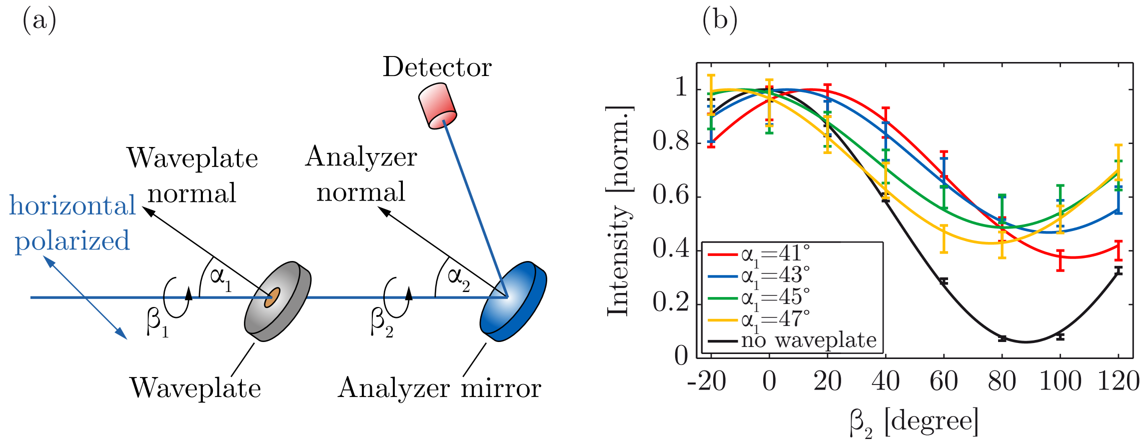

Figure 4.5: Setup for the waveplate analysis and ellipticity measurements. (a) Setup for the polarization measurement. Waveplate and analyzer mirror can be rotated around the beam axis by β_1 and β_2 as well as tilted by α_1 and α_2, respectively. The HHG radiation before the waveplate is linearly horizontal polarized. (b) Measurement results of the β_2 scans without and with waveplate for different angles α_1. The larger the deviation from the Brewster angle, the stronger is the modulation depth (the smaller the ellipticity) and the stronger the shift in β_2. In case of this measurement an Al/C filter was used to prefilter the high harmonic radiation (data courtesy of Jürgen Schmidt).

whereas the orientation angle of the waveplate is set to β_1=-45^o. This ensures equal components of s and p in the coordinate system of the waveplate although the high harmonic radiation is linearly horizontal polarized. Rotating the analyzer mirror by an angle β_2 around the optical beam axis allows for an intensity dependent measurement and analyzing the polarization characteristic of the transmitted radiation after the waveplate. An intensity measurement for certain waveplate orientation angles α_1 is depicted in figure 4.5(b). In addition, the measurement without the waveplate determines the effective extinction of the analyzer mirror. The extinction of the analyzer mirror is evaluated to be 60 which is in agreement to the simulation, hence the fraction of unpolarized radiation of the low energy radiation that leaks through the filter can be assumed to be small. As a result of the α_1 dependent measurement the highest ellipticity value of ϵ=0.75 is found in case of α_1=45^o, which is a good agreement to the simulated value of ϵ=0.79. The successful implementation of a multilayer transmission quarter waveplate was demonstrated, for the first time, utilizing high harmonic radiation. The waveplate was realized as freestanding foil without any support for a higher transmission efficiency. The used bandwidth of 4–5 eV FWHM supports attosecond pulses and allows for a polarization switch from linearly polarized attosecond pulses to highly elliptically polarized attosecond pulses close to circular. This ensures a high time resolution in future XMCD measurements. A closer look on the theoretical aspects as well as additional measurements and evaluation results can be found in the publication: J. Schmidt, A. Guggenmos, M. Hofstetter, S. H. Chew, and U. Kleineberg, "Generation of circularly polarized high harmonic radiation using a transmission multilayer quarter waveplate," *Optics Express* (in press).

4.2 Barrier layers and advantage of aperiodic mirrors

The crucial parameter for the performance of multilayer mirrors in the water window range is the interface roughness σ, particularly when the σ value, according to equation (2.70), approaches the order of the layer thickness. Section 2.4.4 has described the opportunity of optimizing interfaces by using barrier layers, such as carbon based materials, because carbon is well known to act as a barrier/smoothening layer. One carbon based material which is usually used due to its easy handling as sputter material is B_4C [105, 91]. We have investigated the potential of B_4C as a barrier layer for the optimization of our ion beam deposited Cr/Sc system. Two high periodic (N=300) Cr/Sc multilayer mirrors have been realized, one with thin B_4C barrier layers (0.1 nm pure B_4C should remain after compensating the diffusion loss) and the other mirror without any barrier usage. No effort was put into the precision of the center energy because the analysis of the barrier influence was the topic of interest. Both mirrors have been analyzed after the realization by GIXR and soft x-ray reflectometry. Figure 4.6 shows the measurement results in case of XRR (a) and soft x-ray reflectometry (b). Both the hard x-ray and the soft x-ray measurements indicate a better performance in the case of a pure system without any barrier layers. The data was fitted to extract the period thickness d, γ and σ and to compare both material systems. Table 4.1 summarizes the evaluated parameters. The analysis of the multilayer system with barrier layers yields an XRR roughness value of σ=0.27 nm whereas

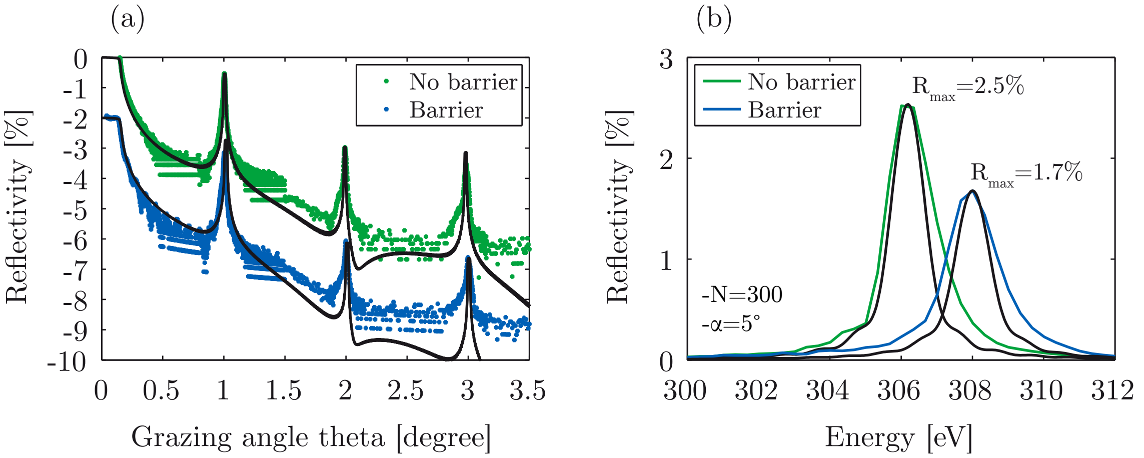

Figure 4.6: Analysis of barrier layers for an improved mirror performance. (a) XRR measurement of the pure Cr/Sc (green) system and with B_4C barrier layers (blue) where the barrier data is shifted by *0.01 for clarity reasons. (b) Soft x-ray reflectometry measurement indicating a better performance in case of the pure system which exhibits the maximum reflectivity of the barrier mirror. Both mirrors have been realized for a planned normal incidence (α=5^o) reflectance at 300 eV. The black solid lines show the corresponding fits.

System	Method	d [nm]	σ [nm]	γ
No barrier	Target	2.086		0.5
	XRR	2.0475	0.18	0.54
	Soft x-ray	2.0425	0.55	0.54
Barrier	Target	2.086		0.5
	XRR	2.038	0.27	0.48
	Soft x-ray	2.031	0.57	0.48

Table 4.1: Comparison of the multilayer mirror performance with B_4C barrier layers. Evaluated values of the period thickness d, σ and γ dependent on the measurement technique and in comparison to the target for both the pure Cr/Sc system and with barrier layers. The thickness of the B_4C layer was chosen such that ≈0.1 nm remains after the compensation of diffusion loss.

the pure system shows a rather low hard x-ray roughness value of only σ=0.18 nm. This tendency is also visible in the soft x-ray data where the pure system shows a maximum reflectivity value of 2.5% (corresponds to σ=0.55 nm) in contrast of only 1.7% (corresponds to σ=0.57 nm) for the barrier system. This difference to the literature [105] may arise from the sputter technique. Whereas these optimizations have been realized with magnetron sputtering our dense ion beam deposited layers show a reduced performance when B_4C is used as barrier layer.

Section 2.4.3 has shown that aperiodic multilayer mirrors have a higher degree of freedom regarding spectral shaping in comparison to periodic multilayer mirrors. It was previously stated that the reflectivity can either be increased by lowering the interface roughness value σ or by using an aperiodic design. The aperiodic multilayer can show a higher reflectivity compared to a periodic design while keeping the bandwidth and the phase shape almost constant (figure 2.33). This theoretical analysis is now experimentally verified. A periodic multilayer mirror (N=7, d=5.5 nm) for a bandwidth reflection of FWHM≈35 eV around 300 eV is compared to an optimized aperiodic stack design for an incidence angle of $\alpha=67.5^o$ (a deflection of $90^o+45^o=135^o$). Figure 4.7 illustrates the comparison of the measurements. The fit of the XRR data indicates a roughness value of σ=0.27 nm for the periodic mirror (figure 4.7(a)) whereas the fit of the aperiodic design (figure 4.7(b)) shows a reduced value of σ=0.22 nm. This result is also proven by soft x-ray reflectometry where the maximum reflectivity could be increased to 3.5% in case of the aperiodic design in comparison to only 1.9% for the periodic multilayer mirror (figure 4.7(d)). The aperiodic design offers thus a higher photon flux due to the increased integral while keeping the bandwidth of ≈35 eV almost constant. These results show that aperiodic multilayer mirrors are powerful systems for exceeding the performance of periodic designs. The opportunity of increasing the photon flux, shaping the spectral reflectivity and dispersion set aperiodic mirrors as key components for attosecond physics. Their potential for shaping attosecond water window pulses will be analyzed in the next

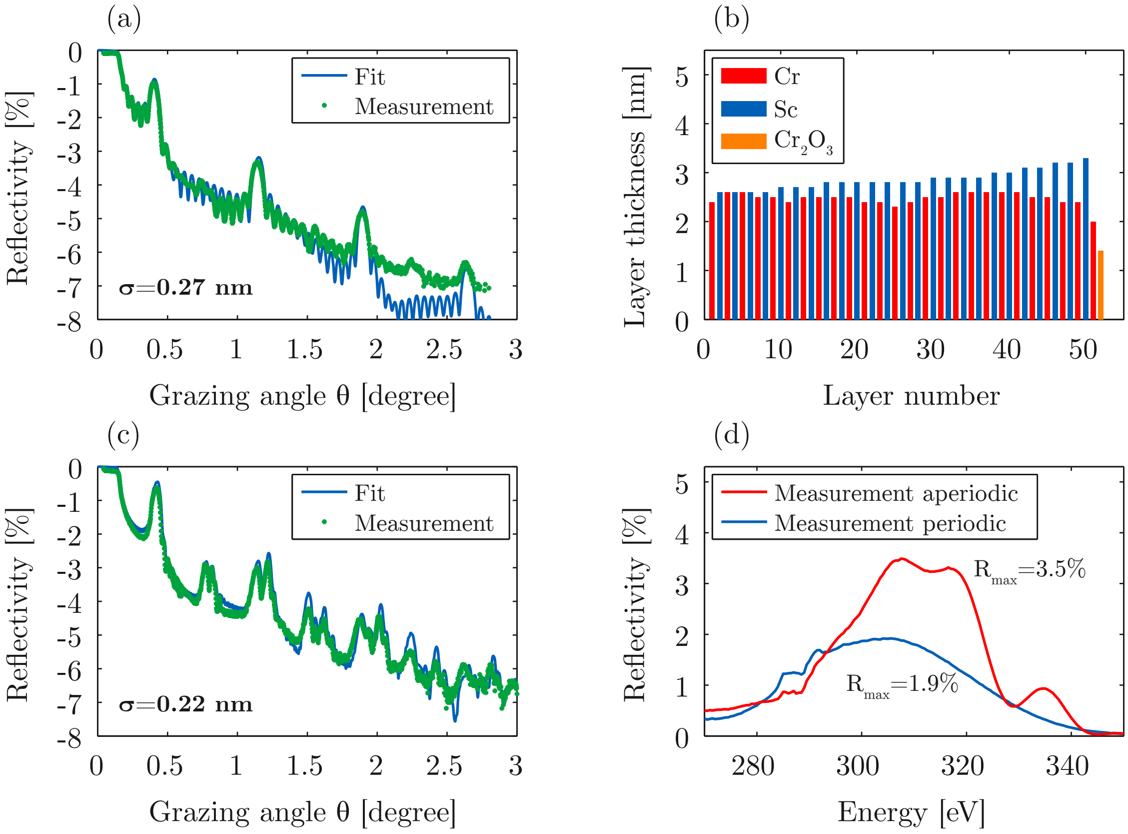

Figure 4.7: Reflectivity comparison of periodic and aperiodic multilayer mirrors. (a) XRR measurement (green) of a periodic Cr/Sc system (N=7, d=5.5 nm) where the fit (blue) yields an interface roughness of σ=0.27 nm. (b) Design of the aperiodic multilayer mirror with arbitrary thicknesses of Cr (red) and Sc (blue) layers and the native chromium oxide at the top (orange). (c) XRR measurement (green) of the aperiodic stack where the fit (blue) reveals a reduced interface roughness of only σ=0.22 nm. (d) Soft x-ray reflectometry measurement of both mirrors demonstrating a higher integral for the aperiodic (red) design (R_{max}=3.5%) in comparison to the periodic (blue) multilayer mirror (R_{max}=1.9%). Both mirrors were designed for a bandwidth reflection of ΔE≈35 eV at a normal incidence angle of α=67.5^o.

section.

4.3 Aperiodic Cr/Sc multilayer mirrors for water window pulses

Extending single attosecond pulse technology from currently sub-200 eV to the water window spectral range may enable, for the first time, the unique investigation of ultrafast electronic processes within the core states of biomolecules as proteins or other organic materials. Aperiodic multilayer mirrors serve as key components to shape these attosecond pulses with a high degree of freedom and enable tailored short pulse pump-probe experiments. The following section will present the results on the development of chirped Cr/Sc multilayer mirrors for the water window, their precise realization utilizing ion beam deposition with sub-angstrom layer thickness control and their future application for attosecond pulse shaping in the water window spectral range. Most results within this section have been published in [149, 150, 151].

4.3.1 Background

Previous sections have already shown that multilayer XUV/soft x-ray multilayer mirrors serve as key components for steering attosecond pulses from high harmonic radiation [20]. As these pulses pave the way toward the observation of electron dynamics in atoms, molecules or solid surfaces/nanostructures with an unprecedented temporal precision [152, 9, 153] their control is of uttermost importance. It has been shown that aperiodic multilayer mirrors exhibit the required degree of freedom for the tailored shaping of attosecond XUV pulses [2, 154]. Extending this technology [155] to the soft x-ray water window spectral range may enable not only the generation of ever shorter (isolated) pulses [8, 156], but allow for the access to deeper electron core levels which facilitates the investigation of electron dynamics in biomolecules [19, 157]. The Cr/Sc material system is the most appropriate choice for multilayer mirrors in the 250–400 eV photon energy range [110, 111], where the maximum normal incidence reflectivity is reached in the vicinity of the Sc L_3-edge at 398.7 eV. Up to now broadband aperiodic Cr/Sc multilayer mirrors have been investigated only theoretically for the water window [158, 159] or have been realized at grazing angles for the keV range [115]. Previous experiments have shown that aperiodic multilayer mirrors can control the attosecond pulse dispersion around 100 eV [2, 154, 160] being used, for example, for resonant excitation of distinct atomic core states [161]. Extending this control, into the soft x-ray water window spectral range, requires multilayer optics with sub-angstrom layer precision as their spectral amplitude and phase are extremely sensitive to even the smallest thickness errors of only a fraction of the nominal layer thickness [162], typically around 1 nm [113]. The following section will present one periodic Cr/Sc multilayer mirror demonstrating a precise layer thickness control. This precise thickness control is the prerequisite for realizing aperiodic designs in this spectral range. Two aperiodic chirped Cr/Sc multilayer mirrors are designed via numerical algorithms [75] and fabricated by the ion beam deposition system (section 3.2), utilizing the high degree of layer thickness control. The periodic mirror and the chirped mirrors are characterized by GIXR and soft x-ray reflectometry. An excellent agreement between the simulated reflectivity (based on the ideal multilayer design) and the measured reflectivity is shown, which allows for a retrieval of the experimentally realized multilayer stack structure. Using the measured reflectivity and simulated spectral phase data (derived from the experimental multilayer structure) the temporal response to a chirped single attosecond pulse at ≈320 eV has been calculated. This had to be analyzed theoretically as a complete pulse characterization by attosecond electron streaking up to now is not possible due to the lack of attosecond sources with sufficient photon flux.

4.3.2 Ion beam deposition methodology

4.3.2.1 Deposition procedure of the multilayer mirrors

The periodic small bandwidth Cr/Sc multilayer mirror, as well as the broadband aperiodic multilayer mirrors, have been fabricated using the load-locked dual ion beam deposition system which is described in section 3.2.

4.3.3 Lateral homogeneity and vertical precision

A shaper has been designed to improve the lateral homogeneity as displayed in figure 4.8(a). Deposition rates with and without the shaper have been determined by surface profilometry (details in section 3.3.2.4) and XUV reflectivity (details in section

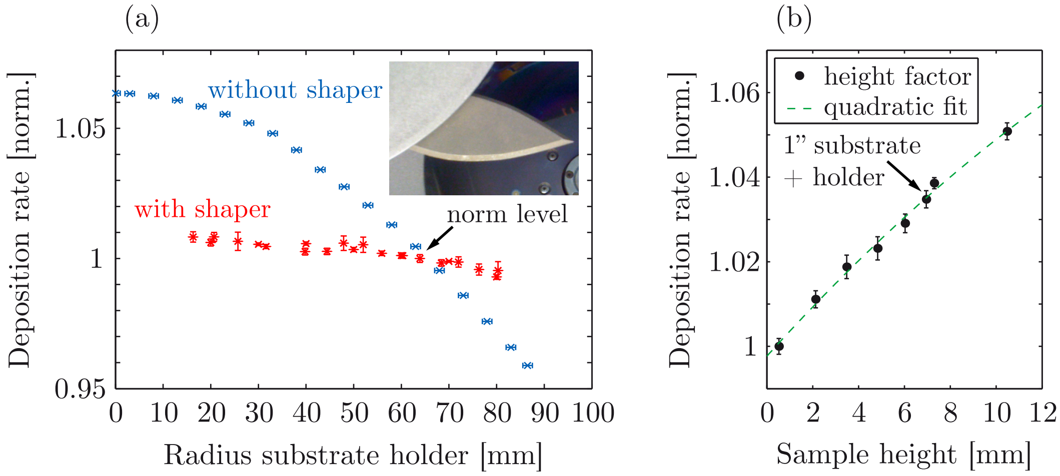

Figure 4.8: Lateral homogeneity and the deposition rate height factor. (a) Lateral (radial) homogeneity of the deposition rates with (red) and without shaper (blue). The picture shows a detail of the shaper. (b) Rate dependence on the sample height. A quadratic fit coincides quite well with the measured data, since the tapered surface is quadratically dependent on the distance.

3.3.2.1) measurements (comparing the central energy) on a set of Mo/Si multilayer mirrors at various radial positions on the substrate holder. The lateral homogeneity could be improved from about ±5% to less than ±0.5% across the full diameter of the substrate holder. For typical 1 inch substrates the maximum homogeneity deviation is less than 0.2%. The shaper was routinely used for multilayer depositions within this thesis. Besides lateral homogeneity, the deposition rate also depends on the sample height and has to be understood and taken into account for a correct implementation of mirror designs. This pure geometrical dependence can be retrieved analytically from the distance D between the imaginary target point of divergence and the substrate holder as the tapered surface of the ablated material beam scales quadratically with the distance. The relation of the sputter rate dependent on the sample height reads like:

$$\Gamma = \frac{N}{A \cdot 1\mathrm{s}} \Leftrightarrow \frac{\Gamma_2}{\Gamma_1} = \frac{A_1}{A_2} = \left(\frac{d_1}{d_2}\right)^2 = \left(\frac{D - h_1}{D - h_2}\right)^2, \tag{4.1}$$

where Γ indicates the rate, N the number of atoms, A the surface, h the sample height and d is the distance from the sample surface to the extended target focus as imaginary point source (1: reference norm level, 2: various sample heights). The target rates have been calibrated by a lift-off procedure and consecutive surface profilometry. Figure 4.8(b) shows the measured deposition rate normalized to a 525 µm thick standard silicon wafer. The deposition rate of a standard one inch substrate deviates from this silicon wafer by ≈3.5% and would manifest itself in an equal shift in the central energy.

4.3.4 Multilayer deposition precision

4.3.4.1 Study of the top layer oxidation

Detailed analysis of the top layer of a multilayer mirror is essential to correctly model its reflectivity as it influences the superposition of the incident and reflected radiation. Many materials oxidize when being brought to atmosphere, where sputtered material is lost to build the 'natural' oxide layer. Spectral ellipsometry was used in-situ and ex-situ within a wavelength range of 370-1695 nm (see section 3.3.1.1) to study such oxidation processes [133]. Spectral ellipsometry allows for the retrieval of both the optical constants and the layer thicknesses of simple structures from the measured ellipsometry parameters

$$\tan\Psi = |r_\mathrm{p}/r_\mathrm{s}| \quad \text{and} \quad \Delta = \varphi_\mathrm{p} - \varphi_\mathrm{s}, \tag{4.2}$$

where $r_\mathrm{p,s}$ are the reflection coefficients and $\varphi_\mathrm{p,s}$ indicates the phase of the p and s polarization as a function of the spectral wavelength. A prerequisite of the oxide analysis is the knowledge of the optical constants of the deposited Cr and Sc layers in the UV/VIS/IR range. Spectral ellipsometry measurements have been utilized to extract the optical constants from 'optical thick' bulk layers and additional the layer growth evolution as well as the deposition rate. A detailed description of the method can be found in section 3.3.1.1. The results of the measurements together with a comparison of the literature are depicted in figure 4.9. For the analysis of

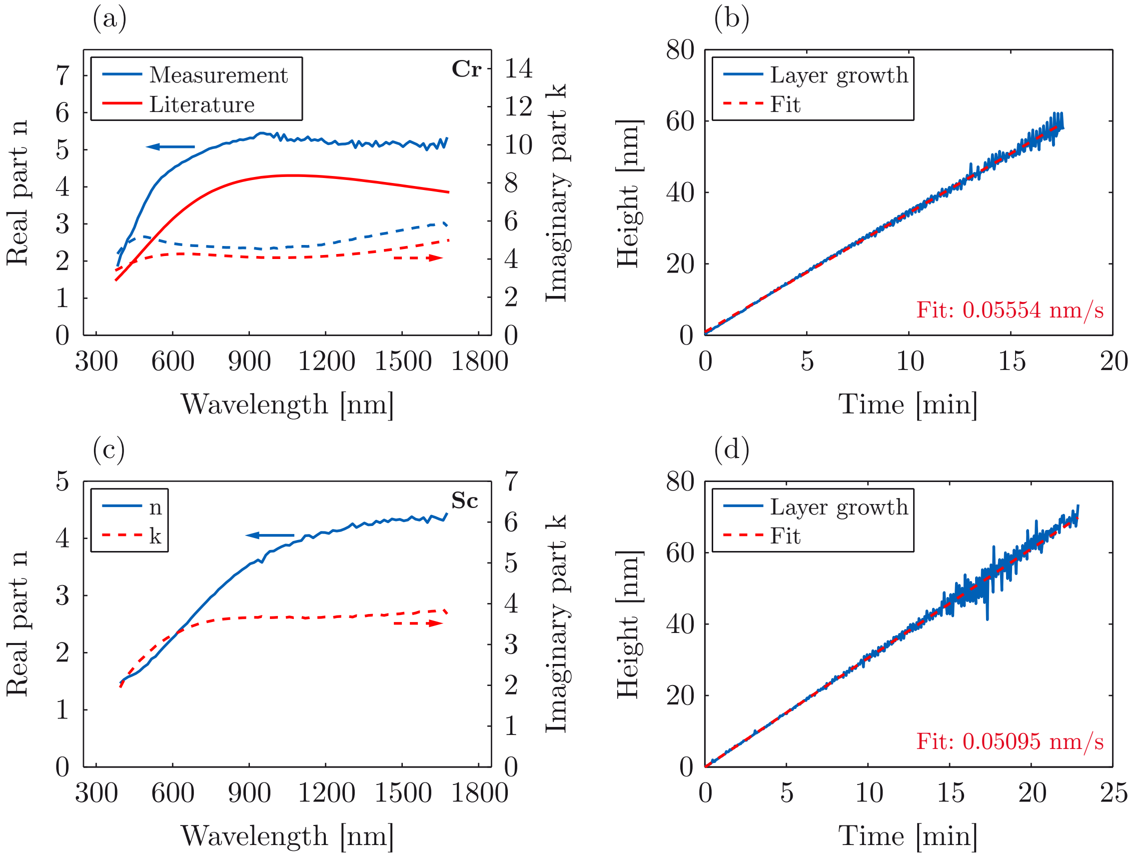

Figure 4.9: Measured optical constants of Cr and Sc using spectral ellipsometry. Measured optical constants (blue) together with the values found in the literature (red) for (a) Cr [163] and (c) Sc (literature values are only available in the XUV/x-ray range [85] or below 190 nm [164]). (b) and (d) show the corresponding layer growth (blue), the individual fit (dashed red) and the deposition rate value.

the oxide layers an approximately 8 nm thick single Cr or Sc layer was deposited on a silicon wafer. The natural SiO_2 layer thickness of the wafer was retrieved by ellipsometry before the coating and the grown material thickness was analyzed directly after the coating process under vacuum conditions, thus without bringing the samples to air. The measured data was fitted with a three layer (Si, SiO_2, Cr or Sc) model as displayed in figure 4.10. After the layer thickness analysis the samples are then brought to air for 24 hours, before been again analyzed to study the built up oxide layers and the thickness loss of the material layer from which the oxide is built. The optical constants of Cr and Sc have been measured previously as depicted in figure 4.9. The optical constants for chromium oxide were taken from the Woollam

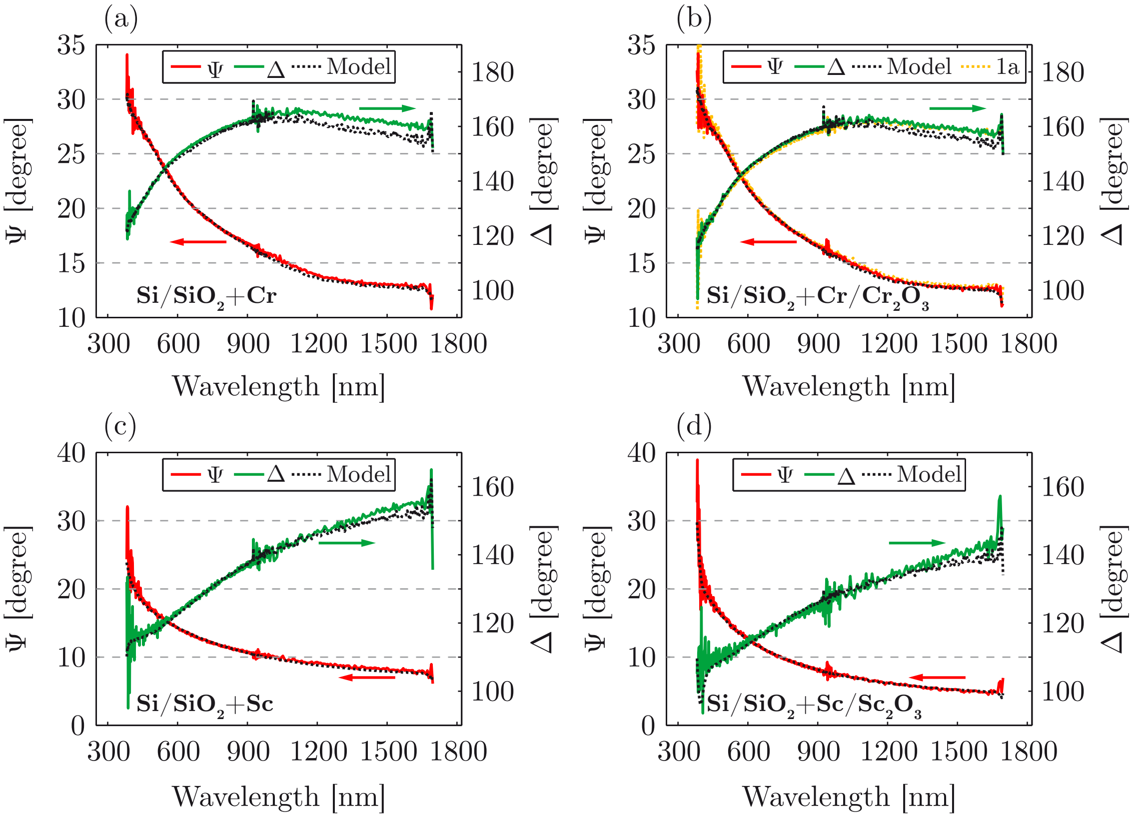

Figure 4.10: Chromium oxide and scandium oxide analysis using spectral ellipsometry. Ellipsometric parameters Ψ (red) and Δ (green) and the corresponding fitted model (dashed black). The data is taken from samples with pure 8 nm thick layers of (a) chromium and (c) scandium and is compared to data measured after 24 h of oxidation (b) Cr/Cr_2O_3, and of (d) Sc/Sc_2O_3, respectively. In (b) additional data after one year of oxidation is included, showing no measurable change in the data and indicating that Cr is well suited as passivation layer.

database whereas scandium oxide was approximated with a Cauchy layer [165] (with the Cauchy parameters A=1.163, B=0.01493, C=0.0065) because it is impossible to measure the optical constants of such thin dielectric layers directly. As a result, it is found that a loss of 0.31±0.04 nm of Cr forms a 1.40±0.46 nm thick Cr_2O_3 layer and 2.92±0.29 nm pure Sc forms a 6.72±0.24 nm thick Sc_2O_3 layer. This is in full agreement with surface profilometry which showed a gain of 1.3±0.7 nm for Cr/Cr_2O_3 and 3.9±0.8 nm for Sc/Sc_2O_3 compared to a pure 200 nm bulk. The knowledge of the material loss and the oxide thickness is crucial for a correct simulation of a multilayer mirror reflectivity. Figure 4.11 shows a comparison of three different fits for a soft x-ray reflectometry measurement using the old oxide model (a guess: 1 nm Cr forms 1.4 nm Cr_2O_3), the new oxide model and assuming no oxide formation. Using the new oxide data leads to a better agreement with the measurement, especially in terms of the spectral positions of the side oscillations. It is also clear that each oxide model

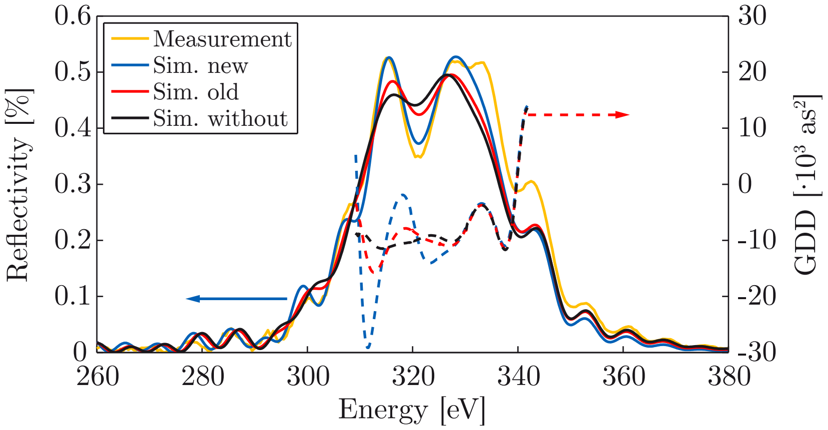

Figure 4.11: Comparison of different oxide models. Comparison of a soft x-ray measurement (orange) of an aperiodic Cr/Sc multilayer mirror and three different types of simulation. One with an old oxidation model (red), the new model (blue) which was extracted from the ellipsometric measurements, and assuming no oxide formation (black). Shown is the comparison of the reflectivity profile (solid lines) and the corresponding GDD (dashed lines).

has an enormous influence on the shape of the GDD. Throughout the following sections reflectivity simulations and designs take into account the new oxide model.

4.3.4.2 Mirror design implementation

Besides systematic deviations of the sputter system and analyses of the top layer oxidation, a detailed knowledge about the interface losses of each distinct material combination is important to ensure a correct simulation and implementation of a multilayer. The interface loss of our ion beam sputtered Cr/Sc multilayer system has been analyzed in comparative studies of single layer and multilayer stacks using surface profilometry indicating no interface loss.

4.3.4.3 Characterization by soft/hard x-ray reflectometry

The vertical periodicity accuracy was evaluated with respect to systematic and random layer thickness deviations inside the Cr/Sc multilayer system, by fabricating a high periodic Cr/Sc multilayer mirror with an intended period thickness of d=1.953 nm and a period number of N=400 on an Si (100) wafer. The mirror design was chosen according to a near normal incidence (5 degree off normal) peak reflectivity at a photon energy of 320 eV. The total deposition time of this multilayer system was about 5 h. The high periodic Cr/Sc multilayer mirror has been analyzed by soft x-ray reflectometry at the reflectometry beamline 6.3.2 at the ALS [142]. The results are depicted in figure 4.12(a). Figure 4.12(b) shows additionally the witness sample, measured by Mo-K$_\alpha$ XRR. Both measurements have been evaluated with respect

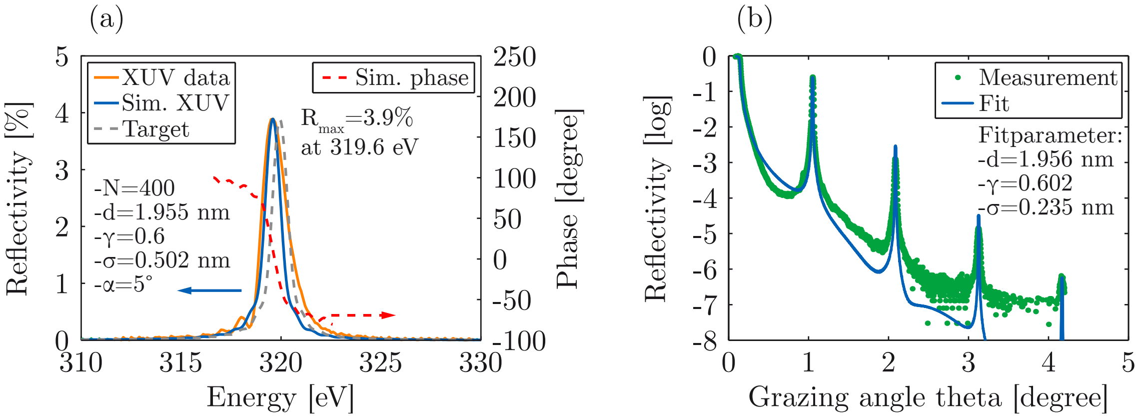

Figure 4.12: High periodic Cr/Sc multilayer mirror for 320 eV. (a) Soft x-ray reflectometry measurement (orange) of a high periodic (N=400) Cr/Sc multilayer stack together with the fit (blue) and the target at 320 eV (dashed gray). The dashed red curve illustrates the simulated phase shape. (b) XRR measurement (green) and the fit (blue) for the same mirror as in (a).

to the period thickness d, the γ-ratio, representing the ratio of the scandium layer thickness to the multilayer period, and the Névot-Croce [103] interface roughness factor σ. The soft x-ray reflectometry measurement at 5^o normal incidence reveals a peak reflectivity of 3.9% at a photon energy of E_{center}=319.6 eV. The average period thickness is extracted from the fit to be d=1.955 nm and the interface roughness is estimated to be σ=0.502 nm. The measured reflectivity bandwidth is only slightly larger than expected from the simulation. This indicates a very high vertical periodicity of the deposited multilayer stack with almost negligible random thickness errors. This is confirmed by hard x-ray grazing incidence reflectometry (GIXR). It reveals a period thickness of d=1.956 nm with a multilayer interface roughness of only σ=0.235 nm, again with very sharp and high contrast Bragg peaks due to the high periodicity of the multilayer stack. While the period thickness and the γ-ratio of both measurements almost perfectly agree, the deviation in the evaluated interface roughness parameter ($\sigma_{\text{Soft x-ray}}$=0.502 nm to σ_{XRR}=0.235 nm) can be attributed to contamination of the Sc layers. An energy dispersive x-ray spectroscopy measurement (see section 4.5) indicates ≈13% Cu contamination stemming from the target backing plate, which severely affects the soft x-ray peak reflectivity, while it has only minor influence to the hard x-ray reflectometry measurement. For the aperiodic multilayer results, described in section 4.3.5, the contamination of the Sc layers was suppressed by mounting a larger Sc sputtering target, which diminishes the spill-out of the ion beam on the backing plate. Furthermore, the different penetration depth of the soft and hard x-ray radiation may reveal different roughness values, because accumulating roughness as well as the interface PSD [87] is weighted differently.

4.3.4.4 Characterization by surface profilometry

As third measurement, the total multilayer stack thickness has been measured by surface profilometry. A set of 24 line scans across different positions of a shadowed deposition edge has been performed. The measured overall thickness together with the mean value and the aimed total stack thickness, based on the calibrated single layer deposition rates of Cr and Sc, is plotted in figure 4.13. The average total stack thickness of 782.96 nm, with a standard deviation of SD=0.70 nm, differs from the target value (782.3 nm) only by about 0.6 nm although 400 periods, i.e. 800 layers, were deposited.

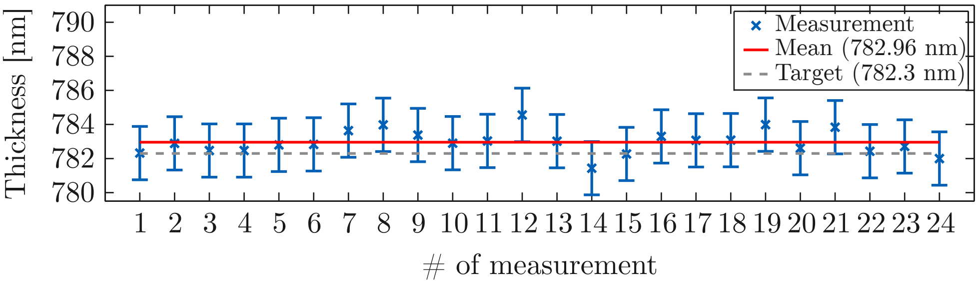

Figure 4.13: Surface profilometry of a high periodic Cr/Sc mirror. Surface profilometry measurement of the same multilayer as in figure 4.12. The mean value (red) is evaluated from 24 thickness measurements (blue). Also shown is the target stack thickness (dashed gray).

4.3.4.5 Comparison of the methods

In summary the retrieved data from different measurement techniques shows a remarkable agreement with the design based on the model in section 4.3.4.2 and is summarized in table 4.2. The absolute period (layer) deviation can be estimated to be 0.15%. This is the necessary prerequisite for the realization of aperiodic chirped multilayer systems as will be proven in the following. Both the spectral reflectivity

Method	Total [nm]	d [nm]	σ [nm]	γ	Deviation [%]
Target	782.3	1.953		0.6	
Profilometry	782.96	1.9546			0.08
XRR	783.5	1.956	0.235	0.602	0.15
Soft x-ray	783.1	1.955	0.502	0.6	0.10

Table 4.2: Comparison of different analysis techniques of the 320 eV mirror. Comparison of the evaluated total stack thickness, the period thickness d, the interface roughness σ, the γ-ratio and the period deviation from the target design.

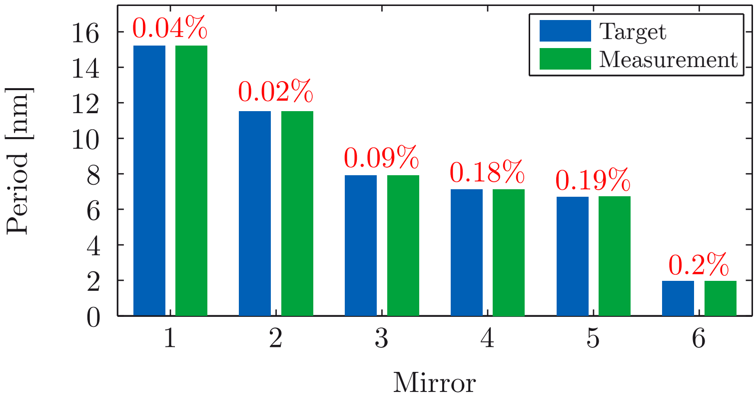

Figure 4.14: Mirror precision for different center energies. Target period (blue) and the measurement (green) of various multilayer mirrors. The mirrors were designed and realized for different center energies and normal incidence angles. The deviation from the target value is listed. The corresponding mirror parameters are summarized in table 4.3.

amplitude and the phase respond very sensitively to even the smallest layer thickness deviations on an atomic 0.1 nm scale. This almost perfect control allows for the realization of very precise multilayer mirrors in terms of center energy. Figure 4.14 illustrates the measured period thickness values of various mirrors aiming for different center energies and incidence angles. The corresponding center energies as well as the normal incidence angle are listed in table 4.14.

Mirror	1	2	3	4	5	6
Center energy [eV]	40	83	115	90	95	320
α	5^o	45^o	45^o	5^o	5^o	5^o
Target period [nm]	15.2	11.52	7.9	7.12	6.7	1.953
Measured period [nm]	15.206	11.518	7.908	7.134	6.713	1.957
Deviation [%]	0.04	0.02	0.09	0.18	0.19	0.2

Table 4.3: High precision multilayer mirrors - Target and measurement. Center energy, normal incidence angle α and the target and measured values of the period thickness for the sketch in figure 4.14.

4.3.5 Chirped multilayer mirrors

Based on the layer accuracy achieved with the high periodic Cr/Sc multilayer results, as presented in section 4.3.4, a set of two different broadband aperiodic Cr/Sc multilayer mirrors was simulated and optimized aiming for the reflection of single attosecond pulses from the high harmonic plateau in the water window spectral range around a photon energy of 326 eV. Time resolved attosecond experiments are nowadays well established in the sub 120 eV XUV photon energy range [9, 166, 153]. With ever improving few cycle laser development toward higher pulse energies, this regime will be extended into the soft x-ray water window spectral range. Using thin filters for attosecond pulse shaping in this energy regime is limited to fixed opening and absorption edges of the materials used and thus restricts the degree of freedom. This leaves multilayer mirrors as the only key components for tailored spectral filtering and shaping of an attosecond water window pulse. For that reason a negatively chirped aperiodic Cr/Sc multilayer mirror, optimized for reflecting sub-70 as pulses from HHG at a central photon energy of 326.3 eV (Ar L_1-edge) with a bandwidth of about 30 eV, was developed for future resonant attosecond photo ionization experiments. A positively chirped mirror was realized for comparison reasons.

4.3.5.1 Characteristics of the chirped Cr/Sc multilayer mirrors

The two different aperiodic Cr/Sc multilayer mirrors have been optimized by the thin film program `Optilayer`, a Fresnel code coupled to a needle optimization algorithm [75, 94] which is described in section 3.1.2. While the first multilayer mirror has been designed for the introduction of an averaged negative chirp (within this thesis, the group delay dispersion is the negative second derivative of the spectral phase, GDD=$-d\phi^2/d\omega^2$) of approximately -8000 as^2 to compensate a possible positive chirp of the high harmonic plateau, a second mirror with similar parameters has been designed to introduce an averaged positive chirp of approximately $+8000$ as^2. Both mirrors have been designed such that their central energy coincides with the L_1-edge of Ar (326.3 eV) at an incidence angle of 45 degree. The optimized stack designs are shown in figure 4.15, where the negative (a) and the positive (b) design consists of around 95 individual layers. The design has been chosen according to their robustness of GDD against small layer thickness errors, which will be proven in section 4.3.5.2. Typical layer thicknesses are between 1 and 2 nm, with the thinnest layers

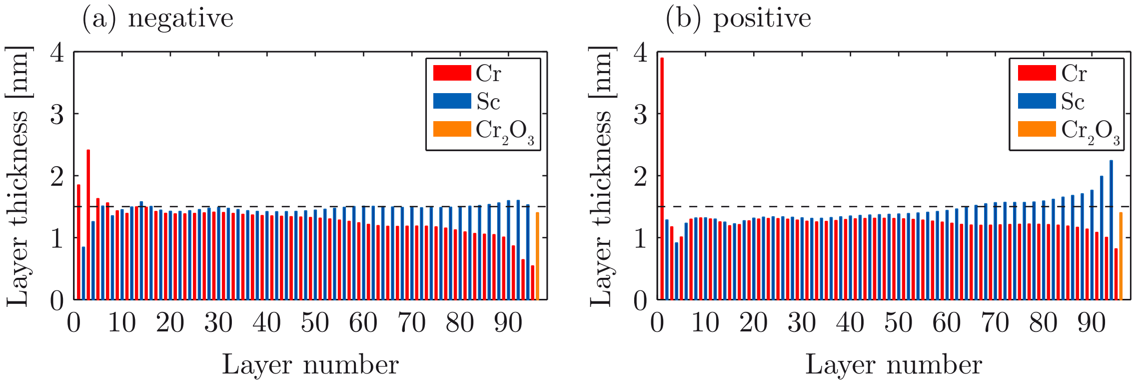

Figure 4.15: Design of negatively and positively chirped Cr/Sc mirrors. Multilayer stack designs of the aperiodic Cr (red) and Sc (blue) layers for the introduced (a) negative and (b) positive GDD. An arbitrary line with a layer thickness of d=1.5 nm (dashed black) is depicted for comparison reasons.

going down to 0.5 nm. For both designs a top layer of 1.4 nm Cr_2O_3 out of 0.3 nm Cr has been included in the model. These designs principally prove the large degree of freedom in customizing water window attosecond pulses both in space (substrate shape and incidence angle) and time, utilizing aperiodic Cr/Sc multilayer mirrors. After the experimental realization of both designs, the accuracy was first checked by surface profilometry. The total stack height, including the oxide layer, for the negative mirror was calculated to be 131.2 nm and for the positive mirror 130.9 nm. Out of the profilometry data a measured total stack height of 131.4±0.6 nm is retrieved for the negative and 131.1±0.7 nm for the positive mirror which is in well agreement with the target stack height. The second accuracy check was conducted by Mo-K_α grazing incidence reflectometry, since this method is well known to be sensitive especially for aperiodic multilayer systems. The measured and fitted data is plotted in figure 4.16. For the fitting procedure a perfect implementation of the start design of figure 4.15 was assumed, thus no thickness errors were included in the fit. The only fitting parameters that were optimized for the agreement with the measurement data were the roughness parameter and the chromium oxide layer thickness (together with the necessary chromium loss) within the error range, which has been determined ellipsometrically in section 4.3.4.1. Although only these fitting parameters are allowed, a nearly perfect agreement between the simulated aperiodic systems and the XRR measurement is found. Together with the profilometry data, this is a strong indication of an accurate implementation of the chirped multilayer systems. Soft x-ray reflectometry measurements of both chirped multilayer systems are presented and discussed later in section 4.3.5.2.

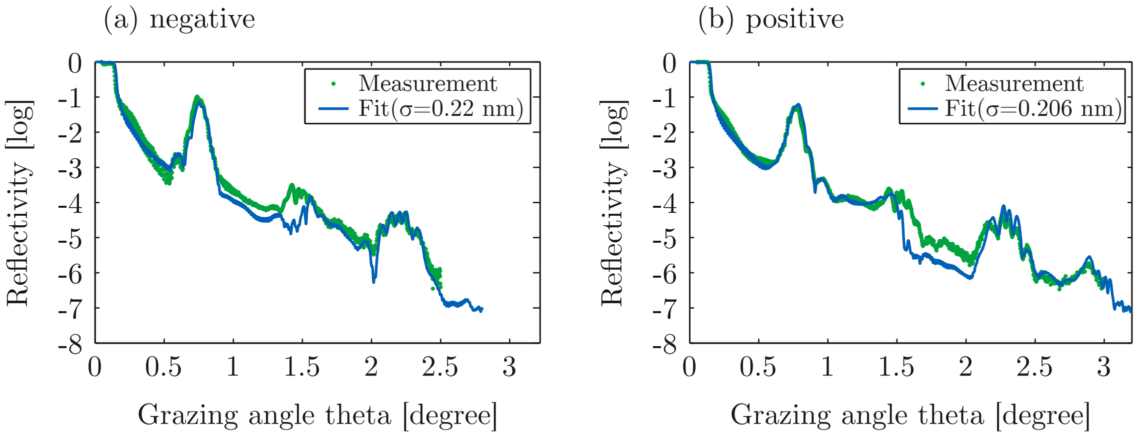

Figure 4.16: XRR measurement of negatively and positively chirped Cr/Sc multilayer mirrors. XRR measurement (green) and the fit (blue) for the negatively chirped mirror in (a) and for the positively one in (b), respectively. The data of the negative mirror has been fitted with a roughness parameter of σ=0.22 nm whereas the positive shows a slightly lower value of σ=0.206 nm. The noise level of the XRR measurement is on the order of approximately $3.5 \cdot 10^{-7}$. Therefore the measurement data for the negative mirror is clipped at around $\theta \approx 2.5^o$ whereas the positive mirror extends up to $\theta \approx 3^o$.

The introduction of chirp upon reflection can be visualized by standing wave simulations. The electrical field intensity (electrical field squared), normalized to the incoming intensity, has been calculated from the design at the surface and inside both multilayer systems and is displayed in figure 4.17. It is clearly shown that the standing wave peak position decreases in photon energy in case of the negatively chirped mirror shown in figure 4.17(a), while it increases with increasing depth for the positively chirped mirror in figure 4.17(b). The negatively chirped mirror thus delays the lower energy pulse spectrum, with respect to the higher frequencies, and vice versa for the positively chirped mirror. This is similar to the illustration of aperiodic mirrors in figure 2.31.

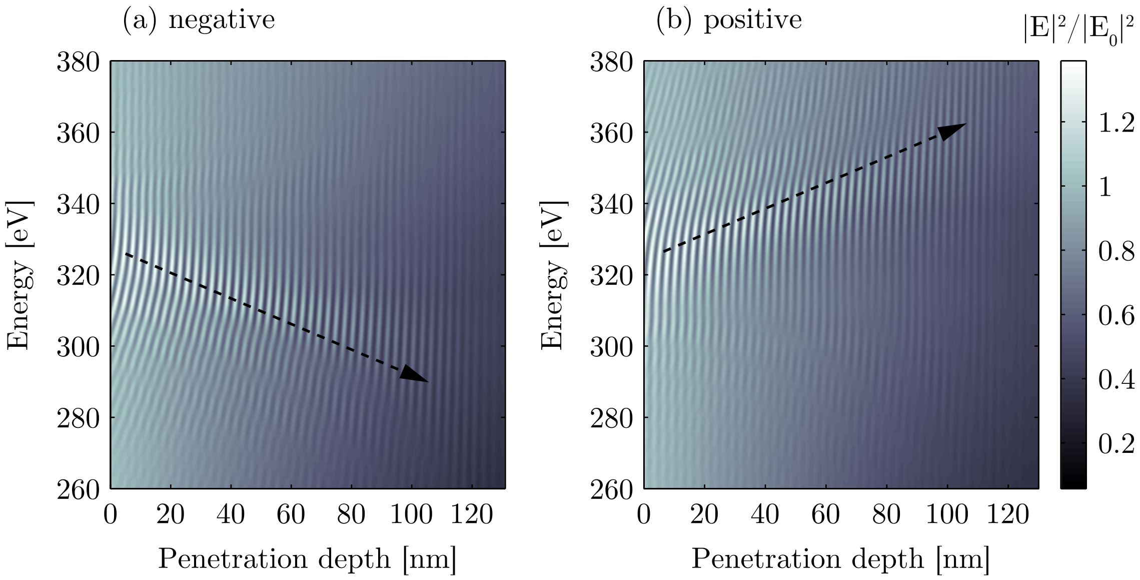

Figure 4.17: Electric field intensity distribution inside chirped mirrors. Calculated field intensity distribution (normalized to the incoming intensity) of the standing wave field inside the (a) negatively and (b) positively chirped aperiodic Cr/Sc multilayer. Both multilayer systems have been optimized for an averaged GDD of approximately ±8000 as^2.

4.3.5.2 Soft x-ray reflectometry and layer thickness errors

Finally, soft x-ray reflectometry measurements were carried out at the beamline 6.3.2 of the ALS [142] to retrieve the reflectivity profile in the energy range for which the mirror designs aim at an incidence angle of 45 degree. A comparison of the simulated and measured soft x-ray reflectivity for both chirped mirrors is shown in figure 4.18. The reflectivity simulations were performed using a self-written Fresnel code (section 3.1.1) and the start designs retrieved from the `Optilayer` optimization procedure [75]. An average Névot-Croce roughness factor of σ=0.49 nm has been retrieved from simulations to account for interfacial imperfections. Both the central energy

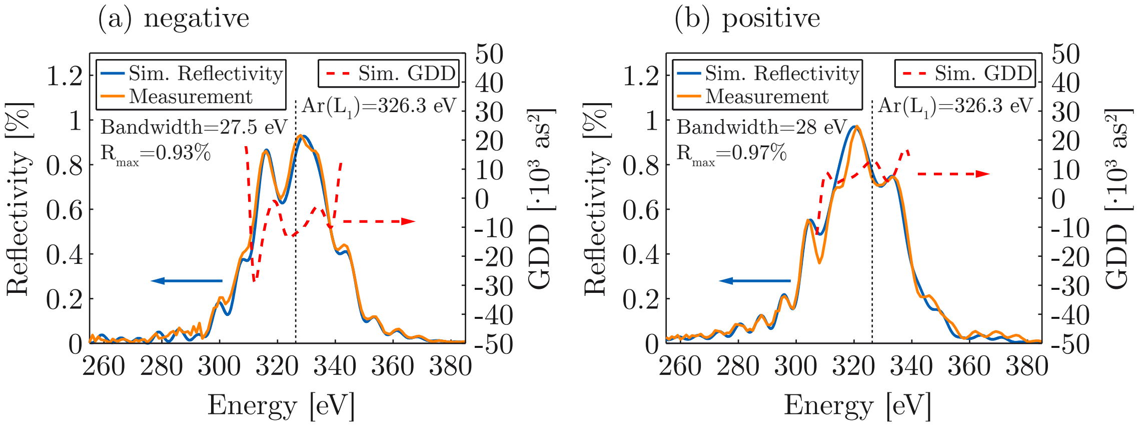
(a) negative

(b) positive

Figure 4.18: Soft x-ray measurement of aperiodic Cr/Sc mirrors. Soft x-ray reflectivity measurement (brown) and simulation (blue) for the (a) negatively and (b) positively chirped Cr/Sc multilayer together with the corresponding simulated GDD (dashed red).

and the side peaks of the measurements and the designs coincide very well and indicate a nearly perfect experimental implementation of the simulated multilayer stack designs of figure 4.15. Also shown is the calculated evolution of the GDD within the reflectivity bandwidth of both multilayer systems, indicating an averaged GDD of ±8000 as^2. Both multilayer systems are very similar in terms of peak energy, spectral bandwidth and peak reflectivity and only differ by the sign of their GDD. Note that the spectral multilayer phase (and thus the GDD) is not accessible by simple reflectivity measurements. Measurements of the spectral phase, by soft x-ray reflectometry, have been reported by detecting the standing-wave assisted total electron yield from the multilayer surface as a function of the photon energy around the Bragg peak [167, 168]. While this method is very suitable for periodic multilayer systems, its accuracy is limited when applied to aperiodic systems with a weak standing wave. On the other hand one can characterize the spectral phase with two attosecond methods, the RABBITT-technique (section 2.2.4.2) [83, 84] or by attosecond photoelectron streaking spectroscopy providing access to a full characterization of the reflected attosecond pulse both in amplitude and phase [2, 8]. However, for the water window the implementation of both attosecond techniques has not been established yet due to a lack of sufficient photon flux from HHG attosecond sources in this spectral range. Here we analyze and estimate the influence of the layer errors on the reflectivity and the GDD via simulations. The rather perfect match of the designed and the measured reflectivity in figure 4.18 proofs the correct elimination of systematic deposition errors and leaves only random errors to be analyzed. Both the simulated reflectivity and the GDD of the original design of the negatively chirped multilayer is compared to slightly modified designs. The designs have been chosen randomly by joggling each layer thickness within predefined limits and the merit function (MF) of the reflectivity, as well as the corresponding averaged GDD value, was calculated to analyze the quality of reflectivity and GDD simulations:

$$\mathrm{MF} = \sqrt{\frac{1}{N}\sum_{i=1}^{N}\left(R_{(sim),i} - R_{(soft\ x-ray),i}\right)^2}, \tag{4.3}$$

where N is the total number of wavelength sampling with an integer i representing the position of the sampling equally spaced. 100 designs have been averaged per allowed error and both the reflectivity and the GDD deviations have been calculated. Designs with an overall stack height deviation of more than 0.8% have been left out due to discrepancy with profilometry investigations. From figure 4.19(a) it can be deduced, that the average random thickness error is less than 0.5%, corresponding to an average layer thickness error of approximately 0.05 angstrom. Figure 4.19(b) shows, that the GDD mean value stays nearly constant independent of the layer errors. The upper limit of the layer errors of 0.5% corresponds to a maximum mean GDD error of approximately ±150 as^2. To summarize the results, we have a standard deviation of ≈0.024% in the soft x-ray reflectivity and a mean GDD of -8090±150 as^2 for the aperiodic negatively chirped Cr/Sc multilayer mirror.

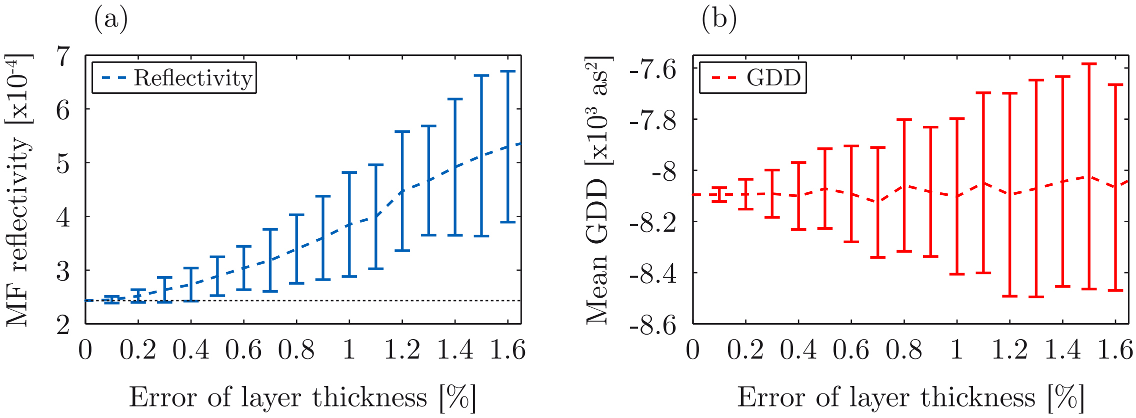

Figure 4.19: Merit function and GDD dependence on layer thickness errors. (a) Merit function for the simulated reflectivity and the soft x-ray measurement for different layer thickness errors. (b) Mean GDD for different layer errors.

4.3.5.3 Time domain simulation

An attosecond pulse from the high harmonic plateau regime, with a positive GDD of +8000 as^2 in the energy range of the mirror has been assumed, which is reflected off the negatively chirped mirror. The resulting pulse after reflection is displayed both in the spectral and in the temporal domain in figure 4.20. As a result, the pulse is compressed to a single 69 as pulse with an almost symmetric temporal pulse form and very minor pre and post pulse contributions. The pulse is almost compressed to a Gaussian Fourier limit of 66 as given by the spectral bandwidth of the multilayer

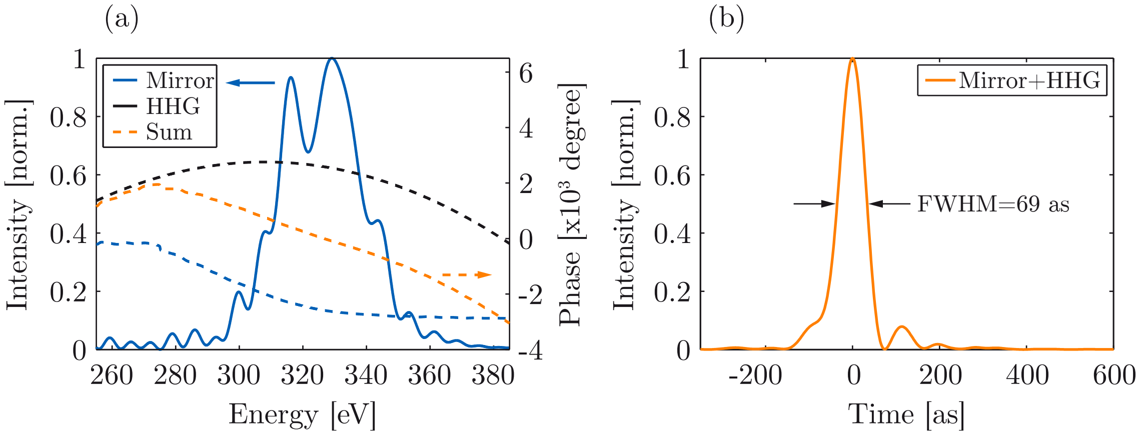

Figure 4.20: Chirp compensation and pulse compression by an aperiodic mirror. (a) Intensity profile (solid blue) together with the phase (dashed blue) of the mirror, HHG (dashed black) and the sum (dashed orange). (b) Simulated temporal pulse response of a positively chirped attosecond pulse from the high harmonic plateau after compression by the negatively chirped Cr/Sc multilayer mirror.

of 27.5 eV. Please note, that the assumed positive GDD of 8000 as^2 of the HHG plateau at 326 eV probably exaggerates the real GDD in the harmonic spectrum in this photon energy range by a factor of four [64]. However, the development, optimization and fabrication of negatively chirped multilayer mirrors with less GDD in the -1000 as^2 to -2000 as^2 range is even easier to achieve. In this respect, the current results display the high dispersion scenario possible to achieve with a single multilayer reflection.

4.3.6 Conclusions

This section has shown the ability to realize multilayer structures by ion beam deposition with sub-angstrom layer thickness errors, by compensating all systematic errors which arise from the deposition procedure. Based on that, two chirped Cr/Sc multilayer mirrors for the water window photon energy range have been realized, introducing an averaged GDD of approximately ±8000 as^2. Such chirped mirrors can be used in the near future to e.g. compress attosecond pulses down to a pulse duration of 70 as. A good agreement between the targeted and measured reflectivity was found and the desired spectral phase was derived from simulations. Direct temporal attosecond pulse measurements by attosecond electron streaking will be a task for the near future, when HHG sources with sufficient photon flux in the cut-off region, applicable to generate single attosecond pulses, reach up to approximately 350 eV.

4.4 Ion polished Cr/Sc multilayer mirrors for high reflectivity

The development of attosecond soft x-ray sources ranging into the water window spectral range is also driving the development of suited broadband multilayer optics for steering and shaping attosecond pulses. The relatively low intensity of current HHG soft x-ray sources calls for an efficient use of photons, thus the development of low-loss multilayer optics is of utmost importance. This section presents the results on the realization of broadband Cr/Sc attosecond multilayer mirrors with nearly atomically smooth interfaces by an optimized ion beam deposition and assisted interface polishing process. The realization and improvements are verified by spectral ellipsometry, TEM and soft/hard x-ray reflectometry. Most of these results have been published in [169, 170, 171].

4.4.1 Background

Highly reflective multilayer mirrors for the water window spectral range [157] have become of great interest over the last decades [113, 112, 172, 173]. It was already described in the introduction (chapter 1) that the water window serves as almost perfect spectral range for the investigation of biological processes as the carbon atoms of tissue are highly absorbing, while their natural aqueous environment is transparent in comparison. That is the reason why various applications are aiming for this spectral range to get physical access to biologically relevant processes by utilizing, for example, high-resolution microscopy [19, 77, 174], time-resolved attosecond (soft) x-ray spectroscopy [9, 161] or (x-ray) astronomy [175, 96]. All these applications have one point in common, they demand multilayer mirrors for beam steering, spectral shaping or as focusing elements with a high photon throughput, thus low-loss multilayer optics. Low photon loss can be accomplished by accurate deposition processes and lowest interface imperfections of such mirrors (see section 2.4.4). This section will focus on the extension of mirror technology for attosecond pulses from currently sub-200 eV [16, 154] to the water window spectral range. This will provide not only new insight into the dynamics of ultrafast core-shell electron wave packets [176], measured by time resolved spectroscopy, but will also push forward the investigation of biomolecules and cells in attosecond time resolved soft x-ray microscopy experiments [152, 177]. Figure 2.7 has shown that attosecond pulses can be generated by HHG in gases ranging up to the keV region [40]. However, the available photon numbers are, especially for low cross section experiments [178, 179], not sufficiently high and thus demand optics with a high reflectivity. Section 2.4.6 and figure 2.39 have shown that Cr/Sc is the most appropriate multilayer material combination in the lower spectral half of the water window up to about 400 eV [180, 111], where the highest reflectivity can be achieved in the vicinity of the Sc L_3-edge at 398.7 eV. One big advantage of this material combination is that no alloys are formed, since they have no overlap in the phase diagram [181]. This theoretically facilitates an almost perfectly abrupt interface, the requisite for a high reflectivity (see section 2.4.4). Periodic multilayer mirrors in the water window have layer thicknesses of only 1–2 nm and their reflectivity is strongly influenced by the interface roughness σ. The influence of the interface roughness on the reflectivity is described by the model of Névot-Croce [103] and is explicitly shown again, since it is the main topic of this section. According to equation (2.69) the influence can be described as:

$$R = R_0 \exp\left[-n_1 n_2 \sin\theta_1 \sin\theta_2 \left(\frac{4\pi\sigma}{\lambda}\right)^2\right]. \tag{4.4}$$

Here R_0 is the reflectance of an ideal structure with interface roughness σ=0 nm. Besides the possibility of using barrier layers like B_4C [105, 182], one can minimize the interface roughness by manipulating the interface roughness evolution [183, 114] during the layer by layer growth by optimizing the deposition process as being proven in the following sections.

4.4.2 Methodology and mirror parameters

4.4.2.1 Using krypton or argon as sputter gas

Section 3.2.2 described the possibility of using krypton or argon as sputter gas for the ion beam deposition process. The sputter atom transfers its kinetic energy to the target atom and influences through the kinetics the layer growth. Table 3.2 summarizes the simulation values for the sputter yield and the kinetic energy of certain target materials dependent on the sputter gas. Krypton should be better for the deposition of Cr/Sc as a kinetic energy of 10 eV is well suited for an optimized layer by layer growth [131], using argon shows two times as much. Certain multilayer mirrors have been realized to verify the simulated influence of the sputter gas and a reduced kinetic energy of the target atoms on the multilayer mirror performance. The design of all four mirrors was equal (N=80, d=2.95 nm, γ=0.6) but the parameters for the deposition were different. One mirror was realized with the *default* sputter voltage of 600 V, one with a reduced value of 500 V and one with a further reduced sputter voltage of 400 V. All these three mirrors have been realized with krypton as sputter gas whereas the last one was fabricated using the *default* sputter voltage of 600 V but argon as sputter gas. Their performance was analyzed by XRR and is depicted in figure 4.21. The XRR data confirms the simulation results that, in case of Cr/Sc multilayer mirrors, Kr should be used as sputter gas. The data also indicates that the *default* sputter voltage of 600 V is probably too high and should be reduced down to at least 400 V. This reduces the kinetic energies of the scandium and chromium atoms which facilitates a better layer by layer growth resulting in a lower interface roughness and therefore in a higher reflectivity as shown in figure 4.21. Summarized, a further investigation of the influences of deposition parameters will result in optimized Cr/Sc attosecond water window multilayer mirrors. A detailed

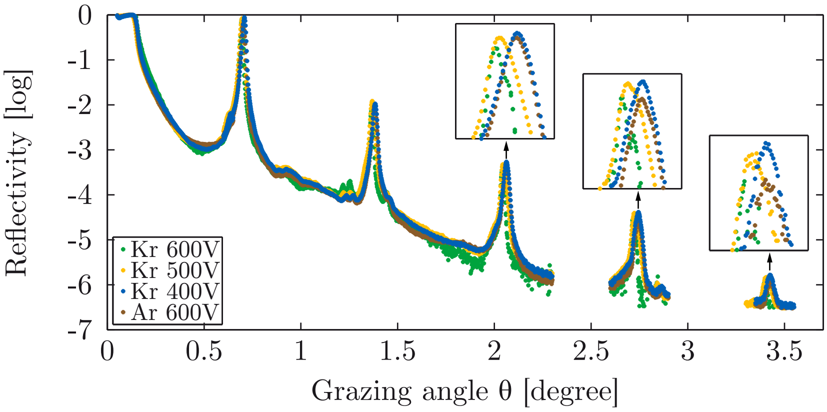

Figure 4.21: Comparison of krypton and argon as sputter gas. XRR measurements of multilayer mirrors which were realized with different deposition parameters. Kr as sputter gas and a sputter voltage of 600 V (green), Kr as sputter gas and a sputter voltage of 500 V (orange), Kr as sputter gas and a sputter voltage of 400 V (green) and Ar as sputter gas and a sputter voltage of 600 V (brown). The small insets show a magnification of the Bragg peak reflectivity indicating the highest reflectivity, thus the lowest interface roughness, in case of Kr and 400 V. The design was for all four mirrors equal (N=80, d=2.95 nm, γ=0.6).

explanation of the deposition setup can be found in section 3.2. For the purpose of the examinations carried out, all the multilayer stacks were deposited on crystalline Si (100) wafers with a native SiO_2 layer of approximately two nanometers, as previous ellipsometry measurements revealed (section 4.3).

4.4.2.2 Defining optimized deposition parameters

Three different sets of deposition parameters were composed in order to verify and further improve previously achieved results: *default*, *optimized* and *optimized+assist*. The *default* parameter set includes deposition parameters which have been optimized for materials suitable for attosecond multilayer mirrors beyond 200 eV, like Si, Mo, La or B_4C [16, 2, 160, 168]. For the *optimized* sets the deposition of Cr and Sc is refined in terms of kinetic energy. One huge impact on the interface quality is attributed to the penetration depth of target atoms into an already deposited layer. Figure 4.22 shows simulation results, where scandium atoms penetrate with different kinetic energies into a chromium layer. The penetration depth of scandium increases with increasing kinetic energy thus optimizing this kinetic prospect results in an optimized interface quality. The complete refinement of the deposition parameters is based on Monte-Carlo simulations using the software SRIM [117]. Thereby the best trade-off between the optimum kinetic energy of the sputtered atoms for an optimized layer growth of defect-free, dense, smooth layers [131] and a low penetration depth into the subjacent layer to prevent layer intermixing [132] is investigated and identified. The kinetic energies of the target atoms Cr and Sc are simulated dependent on the

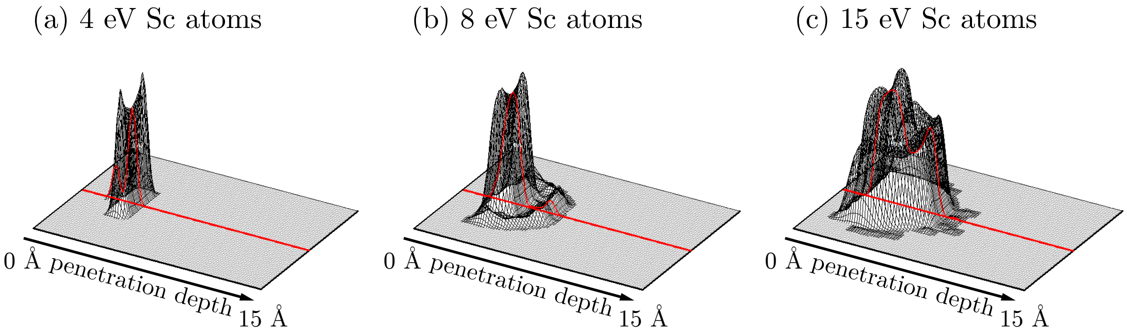

Figure 4.22: Penetration depth of scandium into a chromium layer. The penetration distribution of Sc atoms in a Cr layer is shown. The initial kinetic energy of the scandium atoms is (a) 4 eV, (b) 8 eV and (c) 15 eV where the penetration depth increases with increasing kinetic energy. The kinetic energies of Sc atoms correspond to beam voltages of 100 V, 400 V and 1000 V with Kr as sputter gas.

kinetic energy of the krypton ions. From those results the penetration depth into the subjacent layer can be deduced. The results are depicted in figure 4.23. A value

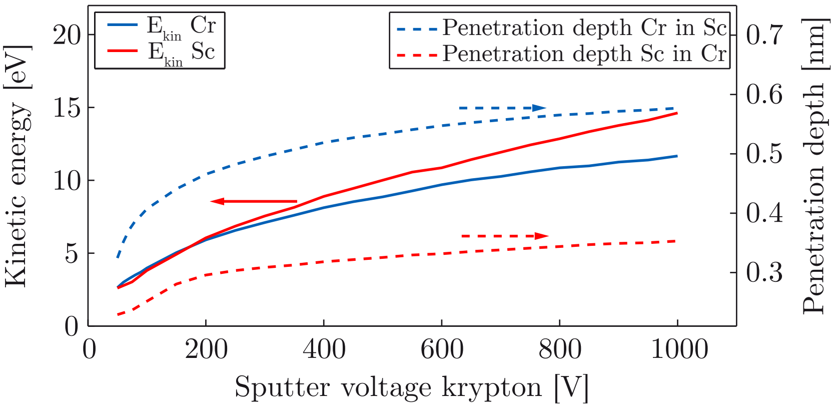

Figure 4.23: Kinetic energy and penetration depth of Cr and Sc. Monte-Carlo simulated kinetic energies (solid lines) and averaged penetration depths (dashed lines) at the interface for chromium (blue) and scandium (red) atoms dependent on the kinetic energy of the Kr ions.

of 10 eV is set as optimal kinetic energy to ensure an optimized layer growth. The *default* process parameter set uses 600 eV Kr ions, which results in kinetic energies of the sputtered Cr atoms slightly below 10 eV, but with a rather large penetration depth (≈0.55 nm) into the subjacent Sc layer. The kinetic energy for krypton in the *optimized* parameter set is set to 400 eV, according to the result in section 4.4.2.1. This is to ensure a kinetic energy slightly below 10 eV for Sc as well as to reduce additionally for both materials the average penetration depth in each other at the interfaces. The last parameter set *optimized+assist* is identical to the parameter set *optimized*, with one important difference: the assist plasma source (figure 3.1) was used for ion polishing every 10^{th} Cr layer, thus after every 10^{th} period. Previous profilometry measurements showed that no loss in height is caused by the polishing process with the chosen parameters and only surface smoothing occurs. The sputter yields and penetration depths of the Kr ions during the ion beam polishing was calculated similar to section 3.2.3. The results in dependence on the kinetic energy of the Kr ions is depicted in table 4.4. The evaluation of the simulated data indicates two results: A kinetic energy of 50 eV shows a non-vanishing sputter yield, but is not too high for sputtering already deposited material, and Cr is preferred as a polishing layer. Although scandium shows an even smaller sputter yield (≈0.003 atoms/ion), the larger penetration depth (≈0.95 nm) of 50 eV krypton ions leads to more krypton implantation. Therefore, chromium was considered as the suitable polishing layer. The polishing step was realized with Kr ions accelerated toward the substrate under 31^o normal incidence with a kinetic energy of 50 eV for 60 s. This kinetic energy ensures an almost vanishing sputter yield (≈0.01 atoms/ion) and a rather low penetration depth of ≈0.5 nm. Please note that both the repetition (every 10^{th} period) and the duration (for 60 s) of the polishing step have been chosen as a trade-off between the overall deposition time and the smoothing effect, as working with two plasma sources introduces additional ramping and parameter stabilization steps and a high degree of interface roughness accumulation during a 10 period growth was not expected in contrast to an 80 period growth. This assumption is confirmed in section 4.4.3.

$E_{kin,Kr}$ [eV]	$Yield_{Cr}$ [atoms/ion]	$Yield_{Sc}$ [atoms/ion]	$\delta_{p,Cr}$ [nm]	$\delta_{p,Sc}$ [nm]
10	0.0000	0.0000	0.00	0.00
20	0.0000	0.0000	0.00	0.00
30	0.0003	0.0001	0.48	0.80
40	0.0040	0.0013	0.51	0.88
50	0.0116	0.0032	0.55	0.95
60	0.2180	0.0066	0.57	1.01

Table 4.4: SRIM results for polishing Sc and Cr interfaces with Kr ions. Sputter yield and penetration depth dependent on the kinetic energy of Kr ions and the layer material.

4.4.2.3 Analysis by spectral ellipsometry

The first analysis of interface polishing with the assist source was realized by spectral ellipsometry. The technique itself is described in section 3.3.1.1. Spectral ellipsometry gives access to the optical constants of thin films and is therefore a very powerful tool to analyze optical properties of thin films. The effect of ion polishing should be measurable with spectral ellipsometry because optimized interfaces reduce the fraction of scattered light which should reduce the measured mean dispersion <n> of a multilayer stack.

The ion beam deposition system is equipped with an in-situ spectral ellipsometer, thus allowing for ellipsometric measurements under vacuum conditions as well as analyzing produced multilayer mirrors during deposition and directly afterwards. Two Cr/Sc multilayer mirrors were fabricated, equal in terms of design (N=100, d=2.95 nm, γ=0.6: 300 eV at α=45^o) and sputter voltage (*optimized*: 400 V), but different in the layer growth. One mirror was realized without ion polishing whereas for the other one ion polishing was performed on every Cr layer (thus a hundred times) for 60 s with Kr atoms of a kinetic energy of 50 eV. Both mirrors were analyzed afterwards with spectral ellipsometry and the corresponding result is plotted in figure 4.24. It can be seen that the ion polishing procedure led to hardly any change in the optical properties of the polished mirror, with regard to the unpolished one. The effect of interface polishing should be clearly visible for samples with a higher number of periods, as roughness evolves through the stack. The period number was increased to N=500, i.e. 999 interfaces, and the period thickness was reduced to d=1.565 nm, aiming for a realistic mirror reflection in the vicinity of the Sc L_3-edge at 10^o normal incidence. We compare two multilayer stacks, where both are identical in terms of mirror parameters N, d and γ, but only one was realized with ion polishing where every 10th Cr layer was polished for 60 s with Kr atoms of a kinetic energy of 50 eV. Since metals get 'optically thick' in the VIS/IR spectral range at a thickness of ≈80 nm, only the last ≈50 periods contribute to the ellipsometric analysis. Roughness has an impact on the measurement, thus it is resolvable by spectral ellipsometry [184]. The influence of the assisted polishing effect on the multilayer stack evolution was now investigated again by measuring the ellipsometric

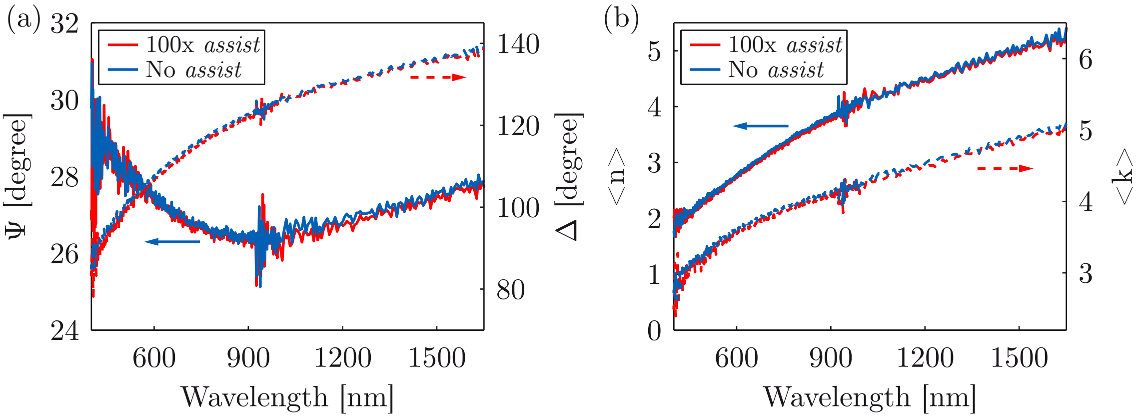

Figure 4.24: Ellipsometric analysis of a polished Cr/Sc mirror with N=100. (a) Raw and unprocessed ellipsometric data where the ellipsometric parameters Ψ and Δ are plotted against the wavelength. (b) Mean dispersion <n> and mean extinction <k>, calculated from the raw data using EASE, and plotted against the wavelength. The polished mirror is shown in red whereas the unpolished one in blue.

parameters Ψ and Δ, and calculating the stack's mean dispersion and extinction <n> and <k>. Since the total stack height, proven by surface profilometry, is identical for both multilayer mirrors, the ellipsometrically determined overall absorption is also expected to be the same (material amount is equal). The only measurable effect remaining is decreased dispersion due to decreased interface roughness and thus reduced scattering. These effects, nearly constant absorption and decreasing dispersion, are visible in the comparison of the polished and non-polished multilayer mirrors, measured via spectral ellipsometry, and are displayed in figure 4.25. The comparison of the ellipsometric analysis of the two different mirror designs proves the accumulation of roughness in a high periodic stack (figure 3.3(b)). Even though the number of polishing steps is half compared to the low periodic (N=100) design, the change in the raw data and in the calculated mean optical constants of the high periodic (N=500) mirror is more significant. For the low periodic mirror, roughness accumulation plays a minor role in why the optical constants of the unpolished mirror do not differ remarkably from those of the polished mirror. In contrast for the high periodic mirror, accumulation of roughness during the layer growth plays a major role.

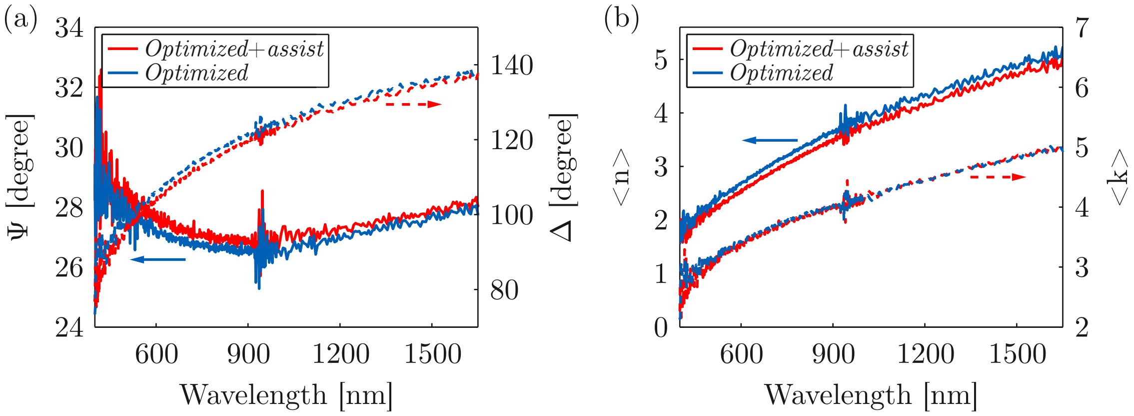

Figure 4.25: Ellipsometric analysis of a polished Cr/Sc mirror with N=500. (a) Measured ellipsometric parameters Ψ and Δ for the assisted polished (red) and non-polished (blue) multilayer mirror. (b) The calculated mean dispersion <n> and extinction <k> for both systems. The absorption stays nearly constant while the dispersion could be decreased by polishing, thus reduced scattering due to lower interface roughness.

4.4.2.4 Multilayer mirror design

The previous section has shown that spectral ellipsometry can be used to analyze the polishing effect in high periodic multilayer mirrors. A modified mirror design was chosen for further investigation, as high periodic multilayer mirrors are not favored for attosecond pulses and future attosecond sources are likely to generate a usable number of photons first of all in the lower energy range of the water window. Periodic mirrors were designed for a central energy of 300 eV and a FWHM bandwidth of 4 eV at an angle of incidence of 45 degrees (figure 4.26). The mirror parameters were chosen as a trade-off between a high number of interfaces, thus a high degree of analyzable roughness evolution and a high peak reflectivity, but also supporting the broadband reflection of sub-500 attosecond pulses. Three sets of deposition parameters (*default*, *optimized*, *optimized+assist*) were utilized for the fabrication of periodic Cr/Sc multilayer mirrors with a period number of N=80, a period thickness of d=2.95 nm and a gamma ratio of γ=d_{Sc}/d=0.6, resulting in individual layer thicknesses for Cr and Sc of d_{Cr}=1.18 nm and d_{Sc}=1.77 nm, respectively. Simulations reveal a peak reflectivity of $R_{max}\approx 16\%$ when an interface roughness of σ=0.3 nm is assumed. Current state-of-the-art Cr/Sc multilayer mirrors with interface roughness values of σ=0.31-0.35 nm have been achieved by magnetron sputtering deposition [185] with quasi single-atomic barrier layers [105, 182] to prevent interdiffusion. The goal was to decrease the interface roughness without barrier layers from $\sigma\approx$0.5 nm [149] and achieve comparable or better interface qualities than current state-of-the-art achievements. This should be realized by ion beam deposition plus recurring ion polishing, because the ion polishing process can be better controlled than the barrier layer deposition, thus resulting in a better multilayer structure accuracy.

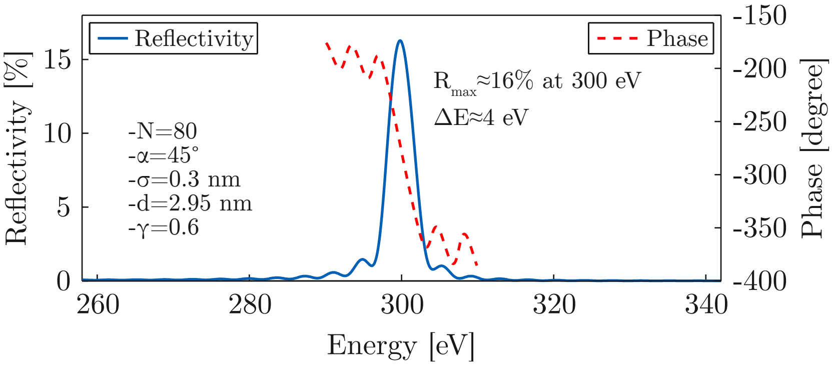

Figure 4.26: Simulation of an ion polished Cr/Sc mirror. Soft x-ray simulation of the reflectivity (blue solid) and phase (dashed red) with the defined mirror parameters indicated at the left.

4.4.3 Analysis methods and results

4.4.3.1 Stability of the deposition process analyzed by surface profilometry

To prove the accuracy and the stability of the deposition process, the total stack height was measured, after the deposition by surface profilometry, and was compared to the theoretical value. Simulations reveal a theoretical total stack height of 237.1 nm (including the top chromium oxide layer) and could experimentally be confirmed by surface profilometry with a measured total stack thickness of 237.4±0.9 nm for all three samples.

4.4.3.2 Characterization by hard x-ray reflectometry

Hard x-ray reflectometry (XRR) measurements, using a molybdenum K_α source with a wavelength of $\lambda \approx 0.071$ nm, were performed to analyze the mirror performance. A comparison of the measured XRR data of the three different mirrors is shown in figure 4.27. When comparing the intensities of the higher order Bragg peaks, where the impact of interface roughness is larger, one can clearly see the improvement caused by the tailoring of the deposition parameters. While the *default* and the *optimized* stack reveal a similar reflectivity e.g. in the 4^{th} order Bragg peak (inset in figure 4.27), a more than five times higher reflectivity could be revealed in the *optimized+assist* stack. Out of the fitting procedure for each measurement, a mean interface roughness value of σ=0.26 nm for the *default*, σ=0.24 nm for the *optimized* and σ=0.21 nm for the *optimized+assist* parameter set can be obtained with a 0.01 nm error range.

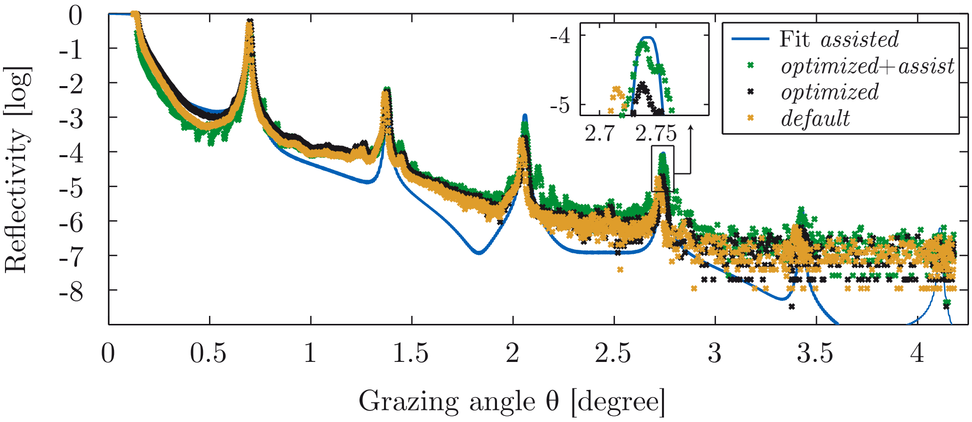

Figure 4.27: XRR measurement of optimized and polished multilayer systems. Hard x-ray reflectometry data for the three different mirrors (brown: *default*, black: *optimized*, green: *optimized+assist*). The lowest interface roughness, thus the highest peak intensities, shows the *optimized+assist* mirror. Only the fit of the interface polished mirror is shown (blue).

4.4.3.3 Characterization by transmission electron microscopy

For further investigation, analysis by TEM was performed to get detailed information about the growth evolution within the stack. TEM investigations were carried out using an *FEI Titan 80-300* TEM/STEM field emission TEM operated at 300 kV, equipped with an *EDAX* detector for energy dispersive x-ray spectroscopy and a *Gatan Tridiem* image filter for electron energy loss spectroscopy measurements. For high angle annular dark field (HAADF) imaging in scanning TEM (STEM) mode a detector from *Fischione Instruments* (Model 3000) is attached. Conventional TEM cross section specimens were prepared by cutting, gluing into a brass holder, slicing, grinding, dimpling and double-sided Ar ion beam milling at 5 degree grazing and 4 keV. The latter was performed until a physical hole was achieved using a liquid nitrogen cooled, precision ion polishing system (*Gatan Model 491*). TEM cross section measurements were carried out on witness samples grown on Si (100). Their period number of N=80 and their small period thickness of d=2.95 nm made these coatings perfectly suited for TEM analysis. TEM images of the coatings are shown in figure 4.28. The upper row displays the top six periods of each coating (topmost layer is assumed to be Cr_2O_3 [149]) and the lower row shows the seven bottom periods of each stack close to the substrate interface, starting with the Sc layer. The top and bottom layers were chosen for investigation because if changes occur they will be more pronounced at these regions. Alternating bright and dark layers, observed in the TEM images, corresponds to scandium and chromium respectively which has also been verified using HAADF imaging in scanning TEM mode. Necessary care has been taken, during TEM specimen preparation and image acquisition, that change in thickness or focus is not responsible for the observed effects. Please note that the

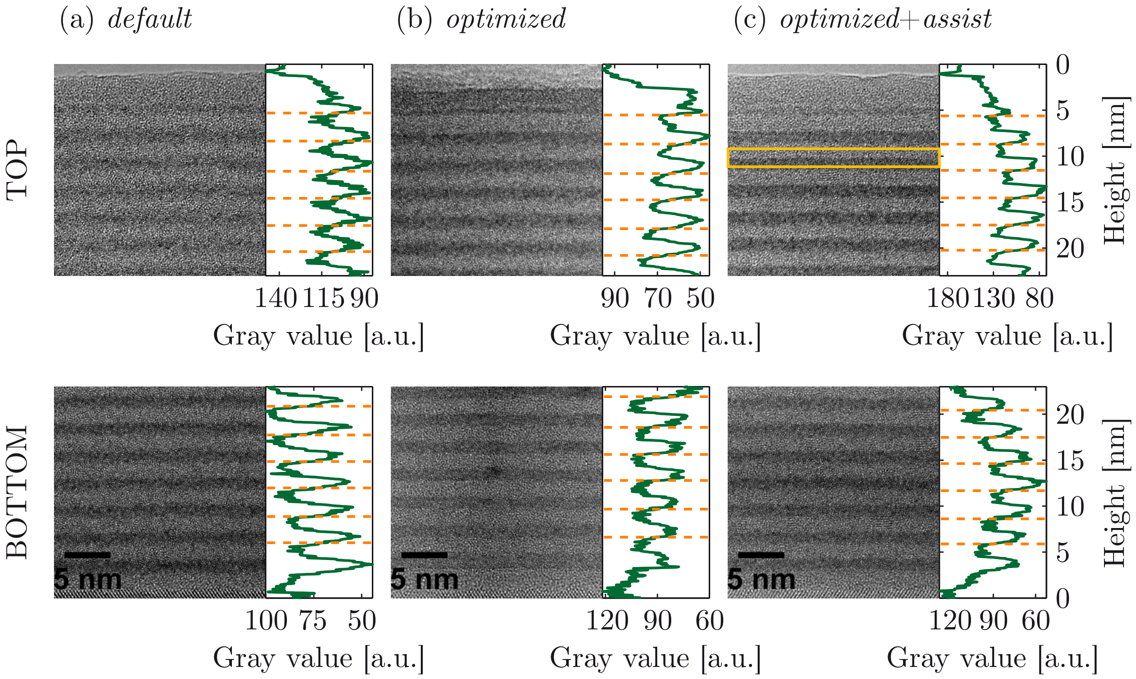

Figure 4.28: TEM analysis of the (non-) polished Cr/Sc mirrors. TEM cross section images of the multilayer evolution from bottom (lower panel) to top (upper panel) with the (a) *default*, (b) *optimized* and (c) *optimized+assist* parameters including the assisted interface polishing. The images show a multilayer detail of 23 nm x 23 nm with a 5 nm scale bar in the bottom images. Next to each image the line-outs of the gray value analysis is shown. More information can be found in the text.

images of figure 4.28 show TEM raw data, thus unprocessed contrast data. Films that are almost complete amorphous nanolayers with an occasional nanocrystalline phase can be observed from the TEM data. Therefore electron diffraction on polycrystalline layers is not observed, but charge density dependent data is measured instead. For the *default* parameter set (figure 4.28(a)), layers are clearly distinguishable at the bottom of the stack whereas they show a significant degree of intermixing at the top which is determined on the basis of the diminishing layer contrast. With the *optimized* parameter set (figure 4.28(b)) the layers at the bottom and the top are comparable with regard to image contrast, while for the additionally polished multilayer (figure 4.28(c)) the layers at the top seem to show a decreased intermixing and an increased layer-to-layer interface abruptness. In addition the averaged gray values (parallel to the interface), along the 23 nm x 23 nm unprocessed TEM images, were evaluated to visualize the interface between the layers. The corresponding line-outs are depicted next to each image. The bottom periods are almost comparable as a high difference in roughness evolution is not expected for the first starting periods. This is different at the top periods. For the *default* parameter set a strong zig-zag pattern occurs, indicating a worsened interface roughness whereas for the *optimized* set a transition to a more sinusoidal line-out occurs. In case of the polished mirror an almost rectangular profile with flat plateaus can be observed, at the bottom and the top, indicating very well separated layers with the lowest interface roughness. Summarized, the best layer characteristic and stack evolution has been achieved by an *optimized* kinetic energy deposition and by ion polishing the Cr layer of every 10^{th} period. This results in clearly distinguishable layers, both at the bottom and at the top of the stack, and significantly improved layer-to-layer interfaces without roughness accumulation over an eighty period stack. For a more quantitative insight into the stack evolution, the power spectral density (PSD) [186] was determined and the resultant interface roughness σ was calculated:

$$\sigma = \left(\int_{f_{min}}^{f_{max}} \mathrm{PSD}(f_x) df_x \right)^{1/2} . \tag{4.5}$$

The small orange rectangle of figure 4.28(c) is shown enlarged in figure 4.29(a). The pixel position where the transition from one material to the other occurs was determined by applying a self-written contrast analyzer algorithm. We have averaged 0.2 nm ($\widehat{=}$13 pixel as a trade-off between resolving the PSD and not addressing too high frequency components) neighbor pixels along the 23 nm (1410 pixel) distance (parallel to the interface) as well as 0.65 nm (40 pixel) in the Sc and Cr regime (along the layer growth) to determine the mean plateau value in the central layer region, to prevent an erroneous data analysis due to intensity fluctuations which occur in TEM measurements. This simplified approach leads to the orange height profile in figure 4.29(a), which describes the interface. For the one dimensional case, where the

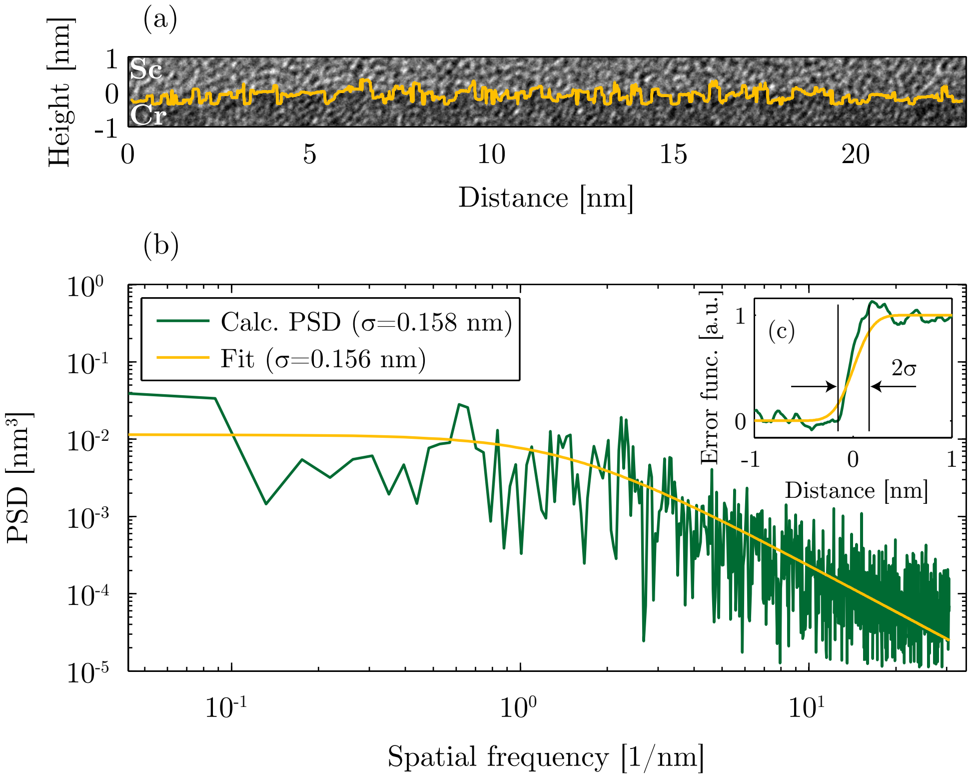

Figure 4.29: PSD analysis of the polished Cr/Sc mirror. (a) Enlarged interface of the Sc layer on top of Cr together with the interface transition (orange), which was determined by a self-written contrast analyzer algorithm. (b) Corresponding calculated PSD (green) together with the fit (orange) and the obtained interface roughness values. These results correspond to the selected interface of the *optimized+assist* multilayer mirror, which is depicted as orange rectangle in figure 4.28(c). (c) The small inset shows the averaged height profile along the 23 nm length (green) together with an error function defined by the PSD fitted roughness value (orange) (see equation (2.66)).

topography of a profile describes its height z(x), the PSD is defined by:

$$\mathrm{PSD}(f_x) \approx L\left[\frac{1}{N}\sum_{k=1}^{N} z_k \cdot \exp\left(2\pi i \cdot x_k \cdot f_x\right)\right]^2, \tag{4.6}$$

with the length position $x_k{=}k\cdot L/N$ and spatial frequencies $f_x{=}j/L$, $j{=}1,2,\ldots,N/2$. The calculated and fitted PSD, according to equation (4.6), is depicted in figure 4.29(b) for the interface section in figure 4.29(a). Using equation (4.5), an interface roughness of $\sigma{=}0.158{\pm}0.005$ nm can be calculated and a fitted value of $\sigma{=}0.156{\pm}0.005$ nm is obtained. Finally, the PSD results are compared, where each pixel contributes to the roughness value, against the averaged height profile of the line-out in figure 4.28. The comparison of the averaged height profile, with the error function being defined by the fitted PSD roughness value, is depicted in figure

4.29(c) and shows a good agreement. This result proves the robustness of our analysis method. To get a quantitative insight on the roughness evolution within the stacks with better statistics, dependent on the deposition parameters and on the order of the interfaces (i.e. from Cr to Sc and vice versa), the interface roughness value for each interface, in the six TEM cross sections shown in figure 4.28, was determined. The results are summarized in table 4.5. The values distinguish between the bottom and the top periods, the order of the interface as well as the used deposition parameter set. Please note that due to the diminishing layer contrast, the extraction of roughness values for the top interfaces of the TEM cross section in the *default* case (figure 4.28(a)) was not possible. The evaluated interface roughness values agree with the Monte-Carlo simulations in section 4.4.2.2. The roughness of Cr on top of Sc is higher than the reverse. This can be attributed to the higher penetration depth. A further step of improvement may be to decrease the kinetic energy of Cr to even lower values, since the penetration depth of Cr in Sc seems to be the crucial parameter for the interface roughness. Finally, figure 4.30 shows a complete TEM image of the polished multilayer stack *optimized+assist* and confirms the homogeneity of the multilayer stack. In addition to the previously shown TEM analysis results, an easy step of improvement toward an even lower interface roughness would be to start in future Cr/Sc multilayer mirrors with Cr as the first layer, since our choice with Sc forms scandium silicide [187, 188] as TEM analysis has shown. Therefore the good surface roughness (<0.1 nm) either of silicon wafers or fused silica substrates is lost with the first interface.

Location	interface	*default*	*optimized*	*optimized+assist*
TOP	Cr on Sc	[]	0.33 ± 0.06	0.31 ± 0.06
	Sc on Cr	[]	0.26 ± 0.06	0.17 ± 0.04
BOTTOM	Cr on Sc	0.30 ± 0.05	0.19 ± 0.03	0.22 ± 0.06
	Sc on Cr	0.20 ± 0.06	0.16 ± 0.05	0.17 ± 0.05

Table 4.5: Comparison of roughness analysis obtained from TEM. Comparison of the evaluated interface roughness values σ [nm], dependent on the interface direction and the used deposition parameter set. The displayed roughness values are averaged over seven periods at the bottom and six periods at the top and take the error into account. *Default* top ([]) could not be evaluated due to the high roughness.

4.4.3.4 Optimization proof by soft x-ray data of high periodic mirrors

To finally prove the concept of optimizing the kinetic energy and ion polishing interfaces of the Cr/Sc system, soft x-ray reflectometry is used as a final analyzing method. The measurements were done at the reflectometry beamline 6.3.2 at the ALS and the PTB at BESSY II. To increase the impact of possible roughness accumulation on the reflectivity (equation (4.4)), we have increased the period number

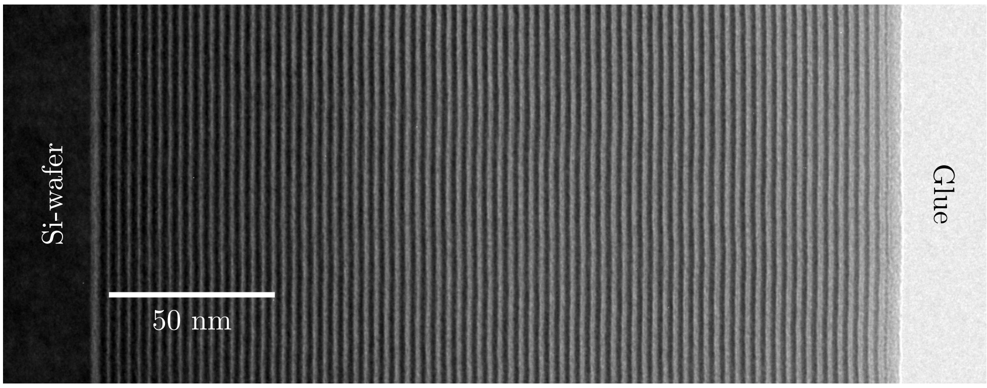

Figure 4.30: TEM image of the interface polished Cr/Sc multilayer mirror. TEM cross section image of the whole multilayer stack for the additional polished multilayer. Please note that the first bright layer after the Si wafer is accidentally formed by scandium silicide.

to N=400 and decreased the period thickness to d=2.084 nm, thus increased the crucial σ/d-ratio. These mirrors were designed for a central energy of 300 eV but now for a normal incidence angle of 5^o. The results of the soft x-ray measurements for the three different deposition parameter sets is shown in figure 4.31. The soft x-ray

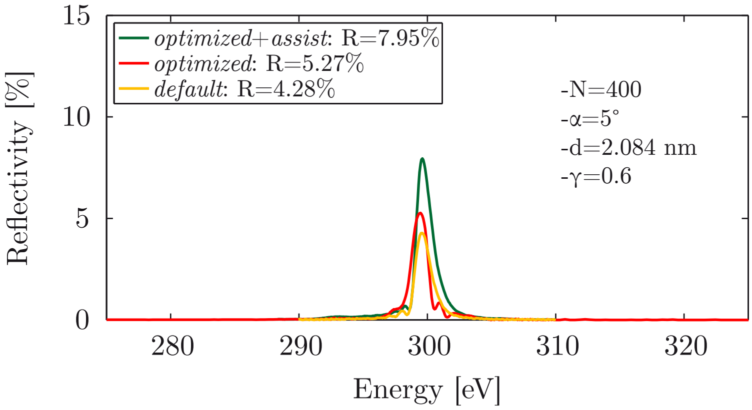

Figure 4.31: Soft x-ray measurements of the *default* and tailored Cr/Sc multilayer mirrors. Soft x-ray reflectometry measurement for the *default* (orange), *optimized* (red) and *optimized+assist* (green) set proving the right tendency of the optimization concept. As result the highest reflectivity of ≈8% can be achieved in case of the additional polished multilayer mirror. The corresponding mirror parameters are depicted on the right.

reflectometry confirms the findings from the XRR and TEM analysis. The highest reflectivity of approximately 8% is achieved for the polished mirror. The reflectivity curves have been fitted for each of the three mirrors and the obtained roughness values are listed in table 4.6. As a note to the accuracy of the fabrication process it should be mentioned that the simulated and planned center energy was 300 eV and the highest reflectivity value of the polished mirror was measured at 299.6 eV, thus only a shift of 0.13% in the center energy.

4.4.3.5 Comparison of the evaluated data

The interface roughness results of the previous analysis are summarized in table 4.6. While identical measures from the XRR and TEM analysis are found, the soft x-ray values are higher. This can be partly explained by the lower penetration depth of soft x-rays in comparison to hard x-ray radiation. One finds different roughness values due to the fact that accumulated roughness as well as the interface's power spectral density [87] is weighted differently. Surface roughness for example has a minor effect on hard x-rays, whereas it has a major impact on soft x-rays. Besides that the higher period number N as well as the lower period thickness d of the soft x-ray samples yields intrinsically higher roughness values.

Method	*default*	*optimized*	*optimized+assist*
XRR	0.26	0.24	0.21
TEM	0.26	0.24	0.21
Soft x-ray reflectometry	0.51	0.49	0.41

Table 4.6: Comparison of the roughness values for the (non-) polished Cr/Sc mirrors obtained from different analysis methods. Comparison of the evaluated interface roughness values σ [nm], dependent on the analysis method and the used deposition parameter set. More information can be found in the text.

4.4.4 Conclusions

These results prove the reduction of the interface roughness of water window Cr/Sc multilayer mirrors by ion polishing. Broadband attosecond mirrors for the reflection of sub-500 as pulses have been realized. The ion beam deposited nanolayer growth was optimized by tweaking the deposition parameters of Cr/Sc multilayer mirrors, mainly by tailoring the kinetic energy of the target atoms, where the optimization was theoretically accompanied by Monte-Carlo simulations. Besides, an important step toward an almost perfect layer growth was realized by additionally assisted ion beam interface polishing. Using a well-suited kinetic energy for the target materials (Cr and Sc) and additional interface polishing for tailored attosecond multilayer mirrors will increase the reflectivity dramatically. Almost atomically smooth interfaces with roughness values of $\sigma \approx 0.16$ nm were demonstrated. The future challenge is to realize such a value for each interface in a (almost high) periodic normal incidence multilayer mirror and push the reflectivity to an even higher value at 300 eV for the first attosecond experiments. Such low-loss mirrors will for the first time enable attosecond-resolved experiments on biological samples in the water window spectral range or pave the way toward shorter pulse durations [189] than the currently achieved 67 as [58] to 80 as [8], by filtering a multi-octave cut-off spectrum from future HHG soft x-ray sources. By the usage of various optimization steps it was possible to increase the peak reflectivity and the integral of attosecond water window multilayer mirrors. Figure 4.32 depicts the comparison between the start of the thesis and after the optimization methods. For the *AS2* setup at MPQ (α=45^o)

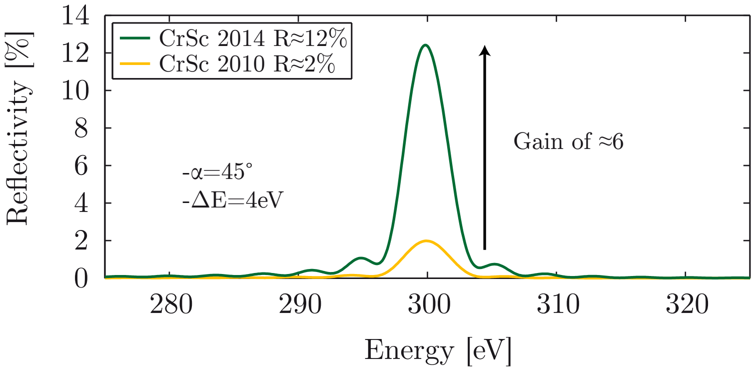

Figure 4.32: Reflectivity gain due to the optimization process. Simulation comparison of the reflectivity status in 2010 (start of the thesis: orange) and 2014 (green) for the *AS2* setup at MPQ.

a gain of ≈6 could be achieved in terms of peak reflectivity, in case of integral (which means photon flux) it is almost one order of magnitude.

4.5 EDX measurements for contamination analysis

In addition to a high layer thickness accuracy (section 4.3) and optimized interfaces (section 4.4) the material purity has an enormous impact on the multilayer performance. The soft x-ray measurement of the periodic and aperiodic mirror comparison in figure 4.7(d) shows strong absorption modulations in the vicinity of the carbon K-edge at 284.2 eV. This can be attributed to carbon contamination in the target materials. EDX [190] measurements were carried out in order to resolve the contamination within the multilayer systems. An electron acceleration voltage of either U=25 kV or U=10 kV was used to measure the individual x-ray emission spectrum of each sample. Four different samples have been utilized to measure the contamination of each deposited target material: A Cr bulk, a Sc bulk, the Cr/Sc/B_4C multilayer from figure 4.6 and a Si wafer as reference sample. Table 4.7 lists up the evaluation of the acquired EDX data. There are several elements which contaminate the target layers and originate from different deposition factors. The iron (Fe) and carbon (C) fraction can be attributed to the target shutter because it is made out of steel.

Cr bulk			Sc bulk		
Element	Mass [%]	Atom [%]	Element	Mass [%]	Atom [%]
C_K	1.13	4.69	C_K	1.07	4.23
Si_K	1.20	2.13	Si_K	1.77	3.01
Cr_L	88.82	85.26	Sc_K	64.45	68.26
Fe_L	8.85	7.91	Cu_L	32.71	24.51

Si wafer			Cr/Sc/B_4C multilayer		
Element	Mass [%]	Atom [%]	Element	Mass [%]	Atom [%]
C_K	2.50	5.66	B_K	12.54	36.73
Si_K	97.50	94.34	C_K	4.71	12.41
			Si_K	0.70	0.79
			Sc_K	16.36	11.53
			Cr_L	49.10	29.90
			Fe_L	5.57	3.16
			Cu_L	11.02	5.49

Table 4.7: Energy dispersive x-ray analysis to identify contamination. EDX measurement of a chromium bulk (top left, thickness=1200 nm on a silicon wafer), a scandium bulk (top right, thickness=700 nm on a silicon wafer), a silicon wafer as reference (bottom left, thickness=525 µm) and a Cr/Sc multilayer with B_4C barrier layers (bottom right). The measurements were done with an electron acceleration voltage of either U=25 kV or U=10 kV. The higher voltage includes usually elements with higher K-shell energies. The table lists the data for U=10 kV, since the results are comparable for our samples.

As a consequence of this, the shutter was shifted ≈5 cm away from the deposition beam to ensure that no material is ablated from the target shutter and deposited on the sample. The measured fraction of silicon is a consequence of the Si wafer on which the materials are deposited. It cannot be minimized but can be neglected as it should not be part of the layer material system. The fraction of copper (Cu) originates from the copper plate on which the targets are bonded. A small scandium plate (diameter=12 inch) was used in the beginning for reasons of economy. As the EDX data reveals the necessity of a larger target material area a scandium foil was used to cover part of the copper plate. The influence of the target shutter and the copper plate was considered, minimized and was verified by new EDX measurements where the evaluation resulted in the values of table 4.8. The fraction of silicon in the data was reduced, by using much thicker material bulks compared to the results in table 4.7, and the fraction of carbon, which is close to the detection limit and could also originate from surface contamination. As a consequence of the still pronounced copper contamination, in case of the scandium target, a further modification was conducted. The ion beam spot size was measured with an aluminum foil during deposition (according to figure 3.4) and the scandium foil was replaced by a well positioned larger scandium target (diameter=14 inch) in respect to the beam size analysis. These modifications facilitate the deposition of high purity layers.

Cr bulk			Sc bulk		
Element	Mass [%]	Atom [%]	Element	Mass [%]	Atom [%]
C_K	0.9	3.78	Si_K	0.92	1.55
Si_K	0.25	0.45	Sc_K	82.34	86.08
Cr_L	98.85	95.77	Cu_K	16.74	12.38

Table 4.8: Energy dispersive x-ray analysis after considered contamination influences. EDX measurement of a chromium bulk (left, thickness=2400 nm on a silicon wafer) and a scandium bulk (right, thickness=2400 nm on a silicon wafer) with reduced contamination. The measurements were done with an electron acceleration voltage of U=10 kV.

Another contamination issue occurred during the investigation of ion beam polishing (section 4.4). A soft x-ray measurement of an interface polished Cr/Sc multilayer mirror revealed a shift in the target center energy and two well pronounced side peaks occurred in the measured reflectivity spectrum (figure 4.33(a)). Analysis and fitting of the data combined with data from surface profilometry indicated an additional ≈0.5 nm layer for each usage of the assist source. By further investigation and exclusion of several deposition factors it was possible to identify the ramping step of the assist source to be responsible for the additional layer. Due to the normal incidence angle of 31^o and the rather high beam voltage of U=800 V material was ablated from the inner part of the substrate shutter by means of rescattering. This ramping step deposited ≈0.5 nm in 3 min (corresponds to 0.0028 nm/s) from the substrate shutter onto the sample and was clearly identified by doubling the ramping time to 6 min,

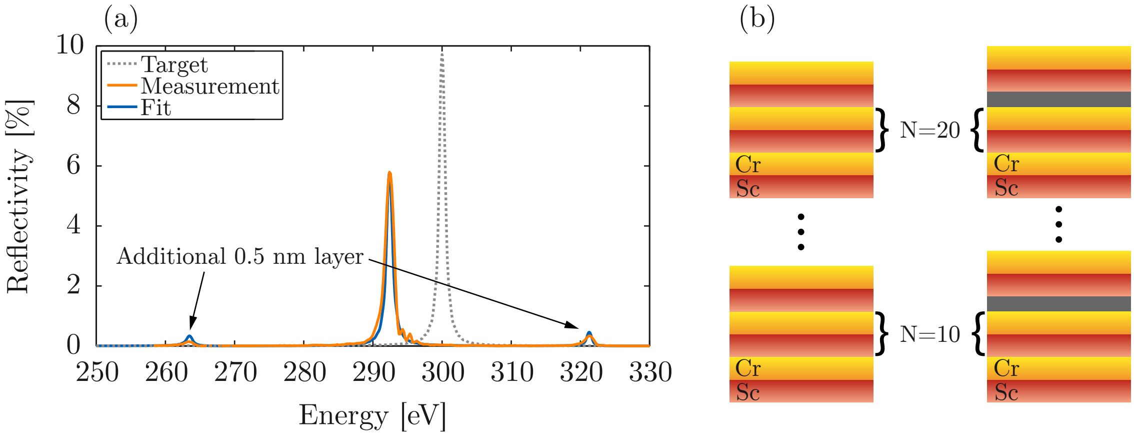

Figure 4.33: Soft x-ray measurement of contaminated multilayer systems. (a) Soft x-ray measurement (orange) and fit (blue) of a high periodic (N=400) multilayer mirror having unexpected additional layers. These additional layers yield to a shift in the central energy compared to the target (dashed gray) and are responsible for the two side peaks in the reflectivity spectrum. The assist ramp step was identified as reason for the additional layers. (b) The assist source is used every 10^{th} period for interface polishing resulting in a N=400 period stack in 40 additional layers (gray).

which led to an additional layer of ≈1 nm (two times as much). Figure 4.33(b) illustrates this additional layer deposition after every 10^{th} period when the assist source is used for ion beam polishing. The additional layer could be eliminated by reducing the beam voltage during the assist ramping step from 800 V down to 400 V.

4.6 Coherent diffraction imaging with high harmonics in the XUV

The combination of an HHG source and very precise multilayer mirrors in terms of central energy allows for the spectral filtering of a single harmonic peak from the HHG spectrum. This narrow band isolation facilitates the monochromatic illumination and coherent diffraction imaging (CDI) of samples in the XUV. The following section will present results on CDI in the XUV utilizing multilayer mirrors and HHG. These results were realized in collaboration with Dr. Michael Zürch (group of Prof. Christian Spielmann) and the group of Prof. Jens Limpert in Jena. Most results have been published in [191].

Short wavelength sources, combined with lensless imaging methods such as CDI, paved the way for microscopy with a resolution well below the wavelength of visible light. The resolution of a CDI experiment can be estimated as a function of the relative bandwidth [192]:

$$\Delta \mathrm{r} = \frac{\mathrm{Oa}\Delta\lambda}{\lambda}, \tag{4.7}$$

where O is the linear oversampling ratio, a is the object size and $\Delta\lambda/\lambda$ is the relative bandwidth of the illuminating light. Figure 2.6 has shown an HHG spectrum using a ≈4 fs IR driving pulse resulting in a rather large relative bandwidth and consequently in a low resolution according to equation (4.7). Long driving pulses would lower the relative bandwidth, but also the conversion efficiency at the same time decreasing the resolution as well, if integration time is kept constant. Utilizing an XUV source based on a high repetition rate fiber CPA system with subsequent nonlinear compression in an Xe gas filled hollow core fiber [193] allows for a higher XUV photon flux compared to typically used Ti:sapphire lasers. Two specially designed XUV multilayer mirrors allow for the spectral filtering of a single narrow-bandwidth harmonic peak and addi-

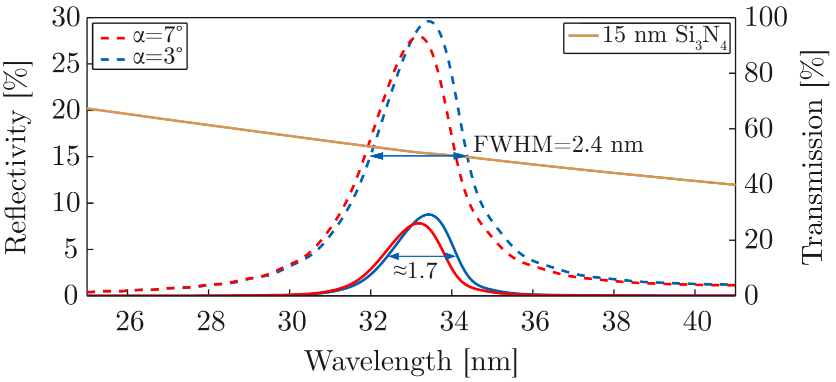

Figure 4.34: XUV multilayer mirrors for CDI experiments. Reflectivity shape of one (dashed lines) and two (solid lines) mirror reflections at α=7^o (red) and α=3^o (blue) normal incidence (design parameters for both mirrors: Si/B_4C, N=20, d=18.92 nm, γ=0.65).

tionally focus the radiation (figure 4.34). A sketch of the complete setup is illustrated in figure 4.35(a). The mirrors have been used in a z-fold geometry, where

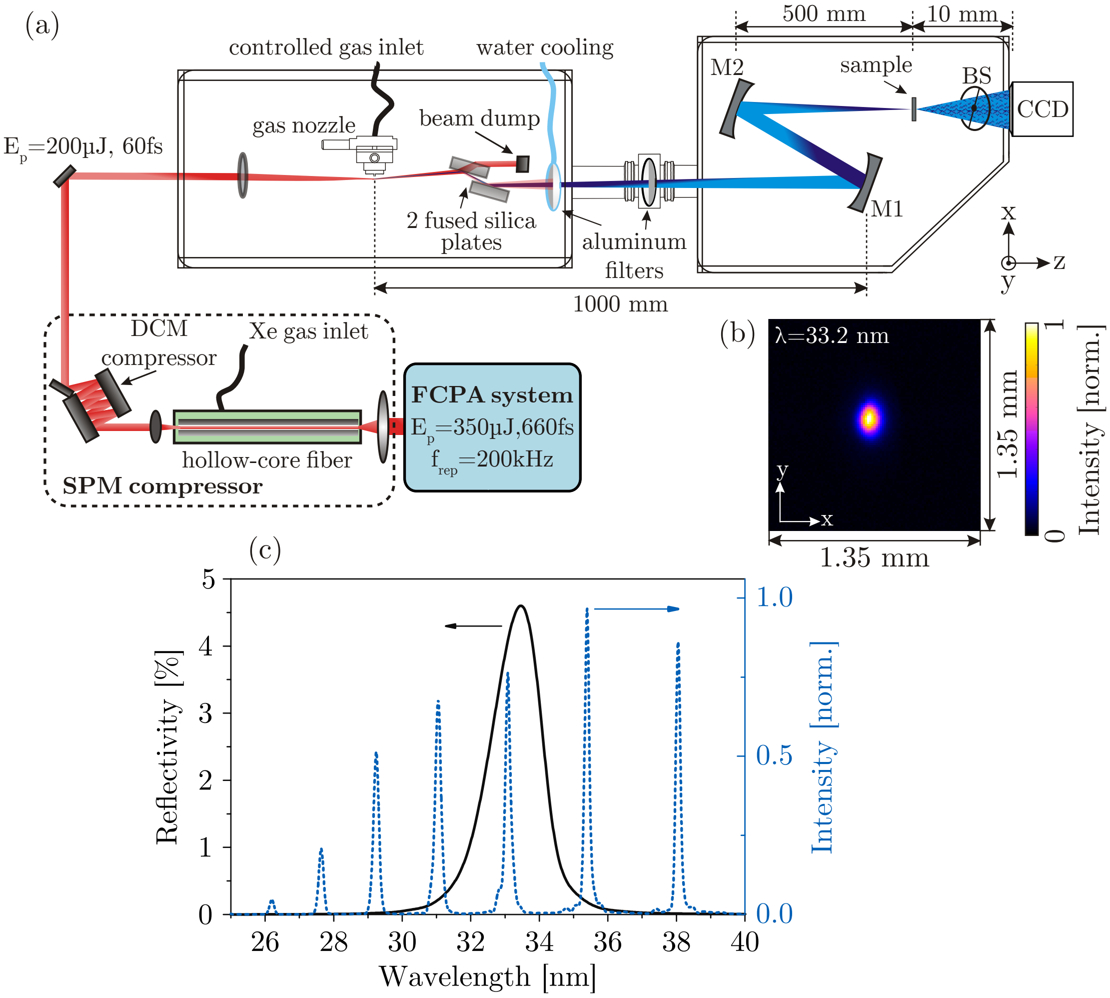

Figure 4.35: Setup for coherent diffractive imaging in the XUV range. (a) The pulses of a fiber based CPA system are spectrally broadened in a xenon filled hollow-core fiber and subsequently compressed with DCM. The HHG is driven with 40 W of average power into Kr gas. Two fused silica plates with anti-reflection coating for the IR are mainly reflecting the XUV light. The spectral selection of the 31^{st} harmonic at 33.2 nm is realized by a pair of aluminum filters followed by two concave XUV multilayer mirrors. The curved mirrors refocus the light tightly onto the sample. The diffracted light is captured by an XUV sensitive CCD. A beamstop (BS) suppresses the strong central speckle. (b) Measured XUV beam profile 20 mm behind the rear focus reveals good spatial beam properties. (c) The XUV multilayer mirrors have an overall reflectivity of 4.6% in combination with the transmission through a 15 nm thin Si_3N_4 membrane (solid black line) for the selected single harmonic line (dotted blue line) (figure and caption adapted/taken from [191]).

the first concave mirror collimates the XUV radiation and the second concave mirror focuses the prefiltered light onto the sample. The mirrors have been designed for a central wavelength of 33.2 nm at α=7^o normal incidence. To reduce the influence of aberrations the incidence angle was shifted toward α=3^o normal incidence in the experiment. This results in a shift in terms of central wavelength of the mirror's reflectivity profile. Figure 4.34 depicts the reflectivity shape of one mirror reflection (dashed lines) and both reflections (solid lines) for the design angle (red) and the angle, which has been used in the experiment (blue). The results show the big advantage of utilizing two mirror reflections whereby the bandwidth of ≈2.4 nm from one mirror is decreased to ≈1.7 nm (factor $\approx\sqrt{2}$) and moreover the suppression of neighbor harmonics is squared. The smaller normal incidence angle in the experiment in comparison to the design value shifts the central wavelength by ≈0.2 nm toward longer wavelengths. Figure 4.34 also shows the transmission characteristic of a 15 nm thin Si_3N_4 membrane (solid brown) on which a sample was planed to be fabricated. The transmission slope only has a minor effect on the central wavelength. The slight shift of ≈0.2 nm in terms of central wavelength, due to the modified incidence angle, only has a minor effect on the aimed spectral filtering of the single harmonic peak at 33.2 nm as the neighbor peaks are >2 nm away. The experimental setup, the focused beam profile and typically generated narrowband XUV harmonics are shown in figure 4.35.

The XUV multilayer mirrors select the 31st harmonic of the IR laser resulting in a monochromatic illumination with a relative bandwidth of $\Delta\lambda/\lambda$=1/220 (λ=33.2 nm). This relative bandwidth allows for a resolution of Δr<26 nm (according to equation (4.7)), which is below the wavelength of the illuminating light.

4.7 Soft x-ray water window pulses from a LWFA driven undulator

The combination of an undulator together with LWFA is used as a concept for a table-top FEL utilizing multilayer mirrors for shaping the generated radiation. More details can be found in section 2.1.2. The first experimental realization of monochromatized table-top undulator radiation in the water window is presented in the following section and was realized in collaboration with the group of Prof. Florian Grüner (LMU, UHH) and Prof. Stefan Karsch (MPQ, LMU). More details can be found in [194]. Andreas Richard Maier was responsible for the project and is preparing a manuscript.

It has already been stated that the water window spectral range is of high interest for various applications to get, for example, physical access to dynamics in biomolecules. The development of suitable sources for this spectral range is the prerequisite for the realization of experiments. A selection of sources was already described in section 2.1. Combining LWFA with an undulator allows for the development of an XUV/soft x-ray source, where the emitted undulator radiation wavelength can be tuned over a broad spectral range by controlling the electron beam energy (equation (2.1)). The experimental setup for the generation of laser-plasma driven undulator radiation is depicted in figure 4.36. A terawatt IR laser is focused into a variable length, hydrogen-filled gas cell resulting in the generation of electrons in the 250–450 MeV range. The electrons are collimated by a fully motorized doublet of permanent magnet quadrupole lenses [195] and propagate through an undulator. As the electrons travel through a miniature rotatable undulator, XUV/soft x-ray pulses are generated. A dipole magnet after the undulator separates the electrons and x-rays in space allowing for the spectral characterization of the electrons by means of a scintillating screen. A set of three different multilayer mirrors behind the dipole magnet allows for the spectral shaping of the XUV/soft x-ray pulses. The three multilayer systems have been realized on concave spherical substrates aiming for three different center energies: 95 eV utilizing a Mo/Si system and 200 eV respectively 300 eV with Cr/Sc. The corresponding design parameters are listed in table 4.9. The experiment demonstrates the study of undulator radiation across the range of 95 eV to 300 eV. The photon energy range is determined by the electron beam energies which are limited by the driver laser parameters. Figure 4.37 shows table-top undulator radiation

Energy	Material system	N	d [nm]	γ
95 eV	Mo/Si	20	9.61	0.4
200 eV	Cr/Sc	26	4.48	0.4
300 eV	Cr/Sc	38	2.98	0.4

Table 4.9: Multilayer mirror parameters for the undulator experiment. Three multilayer mirrors have been realized to spectrally shape the generated photon spectrum from a laser-plasma driven undulator.

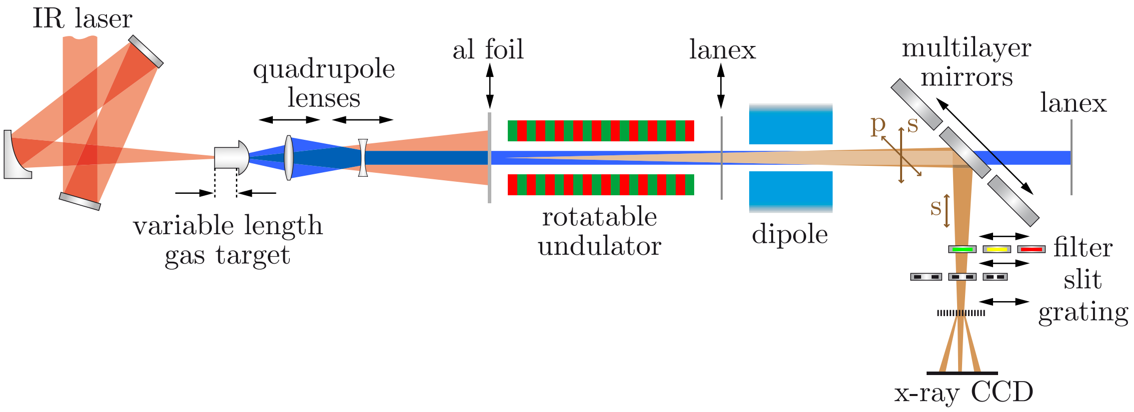

Figure 4.36: Experimental setup for generating laser-plasma driven undulator radiation. The laser (red) is focused into a gas cell, generating electrons in the range of 250–450 MeV. Residual laser light after the cell is blocked by a 20 µm tick Al filter. The electrons (blue) are focused by quadrupole lenses and propagate through an undulator, where the electrons move on a sinusoidal trajectory, emitting radiation up to the water window spectral range. A dipole magnet after the undulator bends the electron beam downwards onto a scintillating screen for spectral characterization, and thus separates the x-ray beam (brown) from the electrons in space. The XUV/soft x-ray pulses are reflected by multilayer mirrors 90^o off the beam axis into an x-ray spectrometer. The x-ray beam polarization, indicated by brown arrows, can be tuned by rotating the undulator. P-polarization is in terms of mirror reflectivity not recommended, since the angle of incidence is 45^o degree, thus close to the Brewster angle (figure and caption taken/adapted from [194]).

which has been measured with the 95 eV Mo/Si multilayer mirror in combination with a 250 nm thick Zr filter and a 500 µm entrance slit at the spectrometer. The single shot spectrum has the $\pm\ 1^{st}$ diffraction order at 13.0 nm ($\widehat{=}$95 eV), with a shot-to-shot reproducibility of 0.2 nm rms. The bandwidth of 7.0% rms is set by the mirror reflectivity profile which was calibrated indipendently at the ALS. However, in the lineout of figure 4.37 (blue) it appears broader due to the finite size of the spectrometer entrance slit. A gold coated mirror with a flat reflectivity profile was also used to reference the effect of the Mo/Si mirror. Using the gold mirror leads to a broadband measured undulator radiation, covering the range of ≈7–14 nm, whereas the multilayer mirror facilitates the control of the central photon wavelength and bandwidth independent of the stability of electron beam parameters.

The Cr/Sc multilayer mirrors have been designed to measure undulator radiation at 200 eV and 300 eV, respectively. Figure 4.38 depicts, for each of the three realized mirrors, the measured XUV/soft x-ray reflectometry data (orange) from the ALS together with the corresponding fit (blue). Each measurement profile is reproduced very well by the fit indicating well understood material systems. Figure 4.38(d) shows measured undulator radiation in the water window, which has been filtered with the 296.6 eV ($\widehat{=}$4.18 nm) mirror and a 200 nm thick Pd filter. The presented spectrum (orange) is averaged over 10 shots due to a comparably low spectrometer

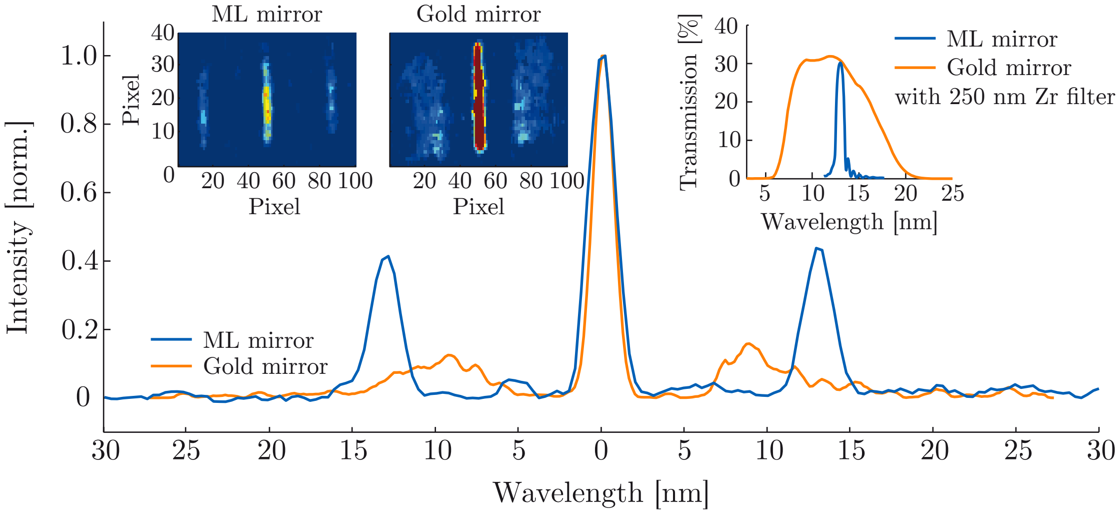

Figure 4.37: Comparison of gold and multilayer mirror filtered undulator radiation. Normalized lineouts of filtered table-top undulator radiation reflected from the multilayer mirror (blue) and gold coated mirror (orange). The relative intensities of the zeroth and ±1st diffraction order vary, as the zeroth order from the broadband gold mirror has a richer spectral content and therefore appears more intense compared to the widely dispersed first order. The -1st diffraction order after the ML mirror peaks at λ=12.94 nm and λ=12.88 nm, which is in excellent agreement with the central wavelength of the ML mirror at λ_0=12.93 nm. Please note that, due to the 500 µm slit, the measured bandwidth $\Delta\lambda/\lambda$=0.15 is dominated by the source size and larger than the actually reflected bandwidth of 6.8 eV. The spectra are lineouts from the raw CCD images (insets to the left) of the undulator spectrum recorded with a 500 µm entrance slit and a 250 nm Zr filter after the multilayer mirror (left) and gold mirror(right). The inset on the right shows the transmission from undulator to target, i.e. the measured mirror reflectivity combined with the transmission of a 250 nm Zr filter (figure and caption taken/adapted from [194] and courtesy of Andreas Richard Maier).

signal at this photon energy. The corresponding spectrum fit is indicated by three Gaussians (blue). The evaluated ± 1st diffraction order is at 3.9 nm within the shown error bars (gray area) of the measurement. It is the the highest measured photon energy from a plasma-driven undulator reported until now. The number of emitted photons is (2.7±1.1)$\cdot 10^5$ at 6 nm and (2.5±0.8)$\cdot 10^5$ at 4 nm, respectively. This result proves photon numbers on the order of 10^5 per pulse with a duration of few-fs and a bandwidth of ≈3% rms independent of the photon energy. A. R. Maier is the owner of the measured and evaluated undulator radiation data.

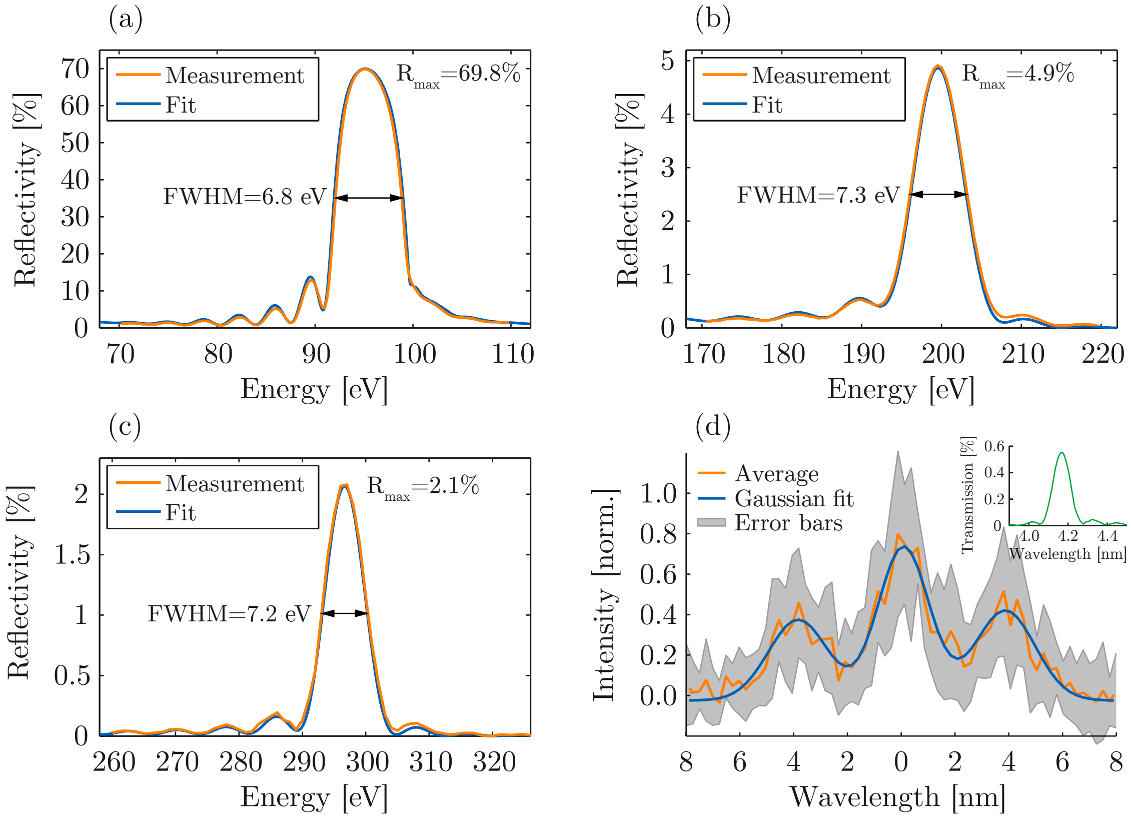

Figure 4.38: Water window pulses from a LWFA driven undulator. (a), (b) and (c) measured (orange) and fitted (blue) XUV/soft x-ray reflectivity of the three multilayer mirrors under 45 degree normal incidence. (d) Undulator radiation reflected from the water window mirror (4.18 nm) in combination with a 200 nm Pd filter in the spectrometer. The inset shows the transmission of the mirror/filter combination. Without the transmission grating 900±300 photons per pulse are recorded at the CCD camera. Due to the low grating efficiency (about 8% efficiency at 4 nm) each measured spectrum contains only a few tens of photons and the spectrum is averaged over 10 shots (orange). The gray area marks one standard deviation of the signal. The fitted spectrum (blue, three Gaussians) has a -1st diffraction order at 3.9 nm, a deviation of less than 10% compared to the mirror characterization, which can be explained by the statistics with low photon number. No entrance slit was used for this measurement. The radiation bandwidth is 2.4% rms, as verified by the independent mirror characterization, although it appears broader in the above measured spectrum due to the extended source size ((d) figure and caption taken/adapted from [194] and courtesy of Andreas Richard Maier).

4.8 Multilayer mirrors for the Sc L_3-edge and Ti L_3-edge

Section 2.3.2.1 has shown that a maximum mirror reflectivity can be achieved in the vicinity of absorption edges of the materials used. Figure 2.39 shows that in the case of a Cr/Sc multilayer mirror the highest reflectivity can be achieved in the vicinity of the Sc L_3-edge at 398.7 eV. Two mirrors have been fabricated in order to test the deposition with *optimized* kinetic energies, which is described in section 4.4. One mirror was realized with the *default* deposition parameters whereas the second one was realized with *optimized* kinetic energies of the target atoms. Both mirrors are high periodic (N=500) systems and were designed for a normal incidence reflection close to the Sc L_3-edge. A first soft x-ray reflectometry scan determined the angle where maximum reflectivity is achieved at λ=3.12 nm. This angle was then used for the spectral scan to determine the reflectivity profile dependent on the energy. Figure 4.39 depicts the results of the soft x-ray measurement for the *default* (green) and *optimized* (orange) parameter set. The maximum reflectivity could be increased from 10.4% (*default*) to 21% (*optimized*), which means that the peak reflectivity is improved by more than a factor of two in the vicinity of the Sc L_3-edge. This is, up till now, the highest reflectivity value at normal incidence for a pure Cr/Sc multilayer mirror in the vicinity of the Sc L_3-edge. A higher peak reflectivity could only be achieved by the use of B_4C barrier layers [105]. Please note that ion beam interface polishing has not been used up till now for our ion beam deposited Cr/Sc

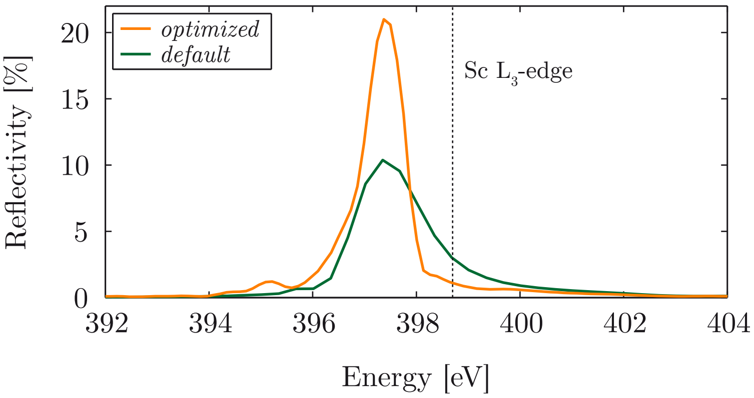

Figure 4.39: Multilayer mirrors for the Sc L_3-edge. Soft x-ray measurement of two high periodic (N=500) Cr/Sc multilayer mirrors. One was realized with the *default* deposition parameters (green) whereas the second one with *optimized* parameters (orange). The *default* mirror shows a maximum reflectivity of 10.4% at a normal incidence angle of α=4.1^o (corresponds to σ=0.46 nm). The *optimzed* deposition parameters increase this value by more than a facor of two resulting in a peak reflectivity of 21% at 8.6^o normal incidence (corresponds to σ=0.39 nm). Both mirrors have a target period thickness of d=1.567 nm.

multilayer mirrors working at this center energy. Interface polished high periodic Cr/Sc multilayer mirrors should show an even more improved peak reflectivity.

For a higher photon energy one switches from Sc based systems to Ti based systems facilitating a high mirror reflectivity at the Ti L_3-edge at 453.8 eV. A high periodic (N=700) Ti/Ni multilayer mirror with 1400 layers has been realized for the Ti L_3-edge at normal incidence. An optimum γ-ratio of $\gamma=d_{\mathrm{Ti}}/d=0.65$ was used resulting in layer thicknesses of $d_{\mathrm{Ti}}=0.912$ nm and $d_{\mathrm{Ni}}=0.491$ nm. The soft x-ray measurement reveals a peak reflectivity of 0.82% at 452.8 eV and 12.5^o normal incidence. The measurement (orange) and the corresponding fit (blue) is shown in figure 4.40. This rather low reflectivity can be attributed to the high interface roughness of $\sigma=0.533$ nm which was extracted from the fit. For the optimization of this material system one should reduce the period number because accumulation of roughness (figure 3.3(b)) is definitely very pronounced in a 1400 layer stack. Reducing the kinetic energy of both target materials and using ion beam assisted interface polishing similar to the Cr/Sc system should improve the performance of Ti/Ni multilayer mirrors.

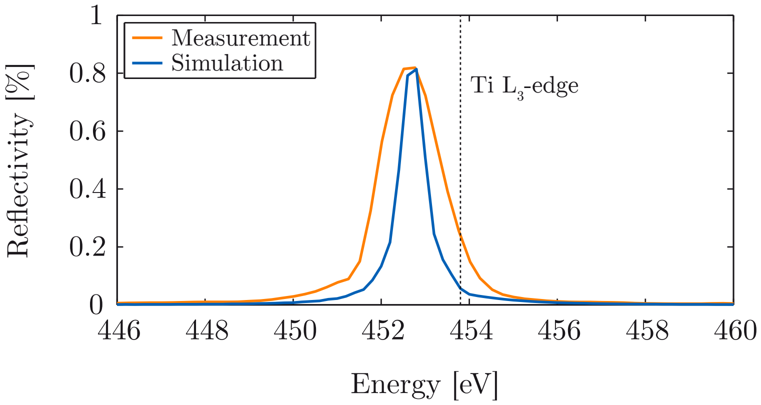

Figure 4.40: Multilayer mirror for the Ti L_3-edge. Soft x-ray measurement (orange) and the corresponding fit (blue) of a high periodic (N=700) Ti/Ni multilayer mirror. The measurement was realized at 12.5^o normal incidence and reveals an interface roughness of $\sigma=0.533$ nm. The corresponding design parameters are $\gamma=d_{\mathrm{Ti}}/d=0.65$ nm and $d=1.4028$ nm.

4.9 Cr/Sc multilayer mirrors for attosecond pulses at 145 eV

This final section will present the first application of Cr/Sc multilayer mirrors to attosecond science. The material system has been optimized for attosecond pulses and is now applied to these pulses for the first time. Most of the results have been published in [171]. The development of attosecond soft x-ray sources toward photon wavelengths below 10 nm is also driving the development of suited broadband multilayer optics for steering and shaping attosecond pulses, as presented in this thesis. As a final result this section will demonstrate that current attosecond experiments in the sub-200 eV range also benefit from the improvement of water window multilayer optics, since their design can be adjusted to the lower energy range. Cr/Sc multilayer mirrors, optimized by tailored material dependent deposition and interface polishing, are utilized for the generation of single attosecond pulses from a high harmonic cut-off spectrum at a central energy of 145 eV. Isolated attosecond pulses have been measured by soft x-ray-pump/NIR-probe electron streaking experiments and characterized using frequency-resolved optical gating for complete reconstruction of attosecond bursts (FROG/CRAB). The results demonstrate that Cr/Sc multilayer mirrors can be used as efficient attosecond optics for reflecting attosecond pulses with a pulse duration of 600 as at a photon energy of 145 eV, which is a prerequisite for present and future attosecond experiments in this energy range.

It has been shown that the development and optimization of highly reflective near-normal incidence multilayer mirror optics, for the water window spectral range [157], has been a topic of intensive research over the recent past [113, 112]. Their driving force is the prospect of high-resolution soft x-ray microscopy [19, 77], soft x-ray astronomy [175, 96], new optics for soft x-ray FELs [182] or time-resolved attosecond soft x-ray spectroscopy [20, 196]. The previous sections have demonstrated that these multilayer mirrors provide a unique approach for beam steering, spatial and spectral shaping as well as spectral phase control with reasonably low reflective losses. It will be shown that optimizing the Cr/Sc material system is not only a key to future attosecond experiments in the water window [149], but also facilitates a promising choice for realizing new attosecond experiments at around 130-160 eV, the energy range where attosecond sources with sufficient photon flux are nowadays already available [197], but multilayer optics are very limited. The dominating generation process for single isolated attosecond pulses is HHG in gases [40] driven by intense phase-stabilized few-cycle laser pulses [69]. Multilayer mirrors allow for spectral filtering of the broadband high harmonic spectrum in the XUV/soft x-ray range with a very high precision upon reflection [2, 168]. Central energy and bandwidth of the reflected spectrum can be designed in a flexible manner by the proper choice of layer materials and the multilayer stack design [16]. Figure 4.41 shows a simulation comparison of certain established multilayer material systems reflecting (attosecond) HHG pulses with a central energy of 145 eV and a FWHM bandwidth of 3 eV at an angle of normal incidence of 5 degree. The parameters were chosen as a trade-off

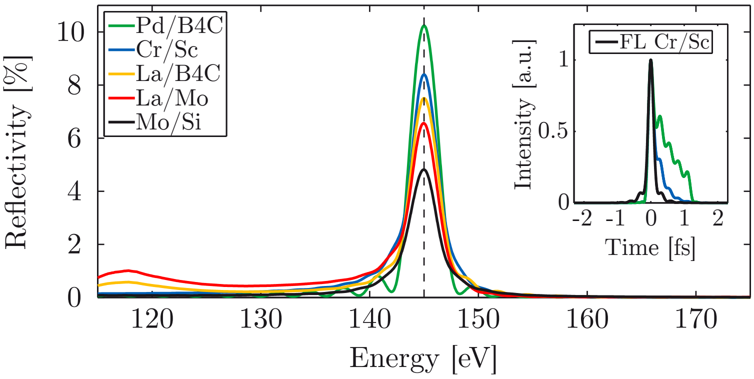

Figure 4.41: Comparison of certain material systems at 145 eV. Simulation comparison of certain multilayer material systems for the reflection of a FWHM bandwidth of 3 eV centered at 145 eV. The small inset shows a comparison of the Cr/Sc and Pd/B_4C system in the time domain including the transmission through a 200 nm thick palladium (Pd) filter. The black line shows the Fourier limit (FL) of the Cr/Sc mirror reflection.

between spectral and temporal resolution in high-resolution attosecond experiments.

The simulations show only a weak suppression of unwanted low energy out-of-band radiation in the range of ≈120 eV with lanthanum (La) based multilayer mirrors (La/Mo, La/B_4C). The inevitable and commonly used metal filter for blocking the near-infrared (NIR) laser radiation (typically a 200 nm thick palladium (Pd) filter) cannot be used to eliminate the out-of-band radiation due to its transmission properties. As a result, chirped plateau harmonics are not sufficiently suppressed by such multilayer reflectors, which is a prerequisite for filtering isolated single attosecond pulses from the cut-off area of the high harmonic spectrum. This suppression of low energy out-of-band radiation is essential for attosecond spectroscopy experiments for e.g. delay measurements [9] or direct observation of electron propagation [17]. Well established Mo/Si mirrors, which are widely used in attosecond experiments at photon energies below the silicon L_3-edge at ≈100 eV, suffer from very low reflectivity above 100 eV. Other molybdenum based multilayer systems like Mo/B_4C, Mo/Y, Mo/Be or Mo/Sr, which on the one hand can provide a higher degree of out-of- band radiation suppression (for Mo/B_4C) accompanied with a higher reflectivity (Mo/Y, Mo/Be, Mo/Sr) [198, 199, 200, 201] but on the other hand suffer from strong spectral modulations around the main reflectivity Bragg peak by Kiessig fringes and therefore introduce additional GDD, which broadens the pulse in the time domain. Furthermore, Mo/Sr is not stable and shows long-term degradation, and beryllium is strongly toxic, thus limiting experimental adoption. A reflection comparison in the time domain of multilayer mirrors composed of Cr/Sc and a highly reflective system, here as example Pd/B_4C [202], is shown in the small inset of figure 4.41, which already takes the transmission and the spectral phase of a 200 nm thick Pd filter into account. Whereas the pulse reflection of the Cr/Sc mirror is close to its Fourier limit and exhibits a Gaussian pulse shape, the Pd/B_4C system shows unwanted temporal pulse broadening due to GDD as well as temporal modulations resulting from the multilayer reflectivity fringes. However, the Cr/Sc multilayer mirror system combines all the advantages required for applications with HHG attosecond pulses: Sufficient throughput due to the optimized reflectivity [169], suppression of out-of-band radiation components (in case of the lanthanum based systems a thicker filter can increase the suppression in the 120 eV range but reduces the overall throughput as well) and a nearly (Fourier limited) Gaussian pulse profile, both in the spectral and temporal domain. The corresponding mirror parameters (period thickness d, ratio γ, interface roughness σ, period number N and capping) applied in the simulations of figure 4.41, for a FWHM bandwidth of 3 eV centered at 145 eV, are depicted in table 4.10. The

System	d [nm]	γ	σ [nm]	N	capping
Cr/Sc	4.371	0.4	0.5	65	1.4 nm nat. oxide
La/B_4C	4.402	0.5	0.8	50	—
La/Mo	4.423	0.5	0.4	56	3 nm B_4C
Pd/B_4C	4.402	0.6	0.84	44	—
Mo/Si	4.376	0.5	0.5	60	1.5 nm nat. oxide

Table 4.10: Mirror parameters for certain material systems at 145 eV. Overview of the used mirror parameters for the simulation of figure 4.41.

experimental realization of the Cr/Sc attosecond multilayer mirror was performed by dual ion-beam sputtering technique [149] together with a tailored interface polishing process [169] for a higher mirror reflectivity. For a later characterization by attosecond streaking, the mirror was also analyzed by two independent measurement techniques, hard x-ray reflectometry and XUV/soft x-ray reflectometry. The XRR measurement, utilizing a molybdenum K_α source with a wavelength of $\lambda \approx 0.071$ nm, was performed on a flat witness sample, grown on a silicon (100) wafer with a native SiO_2 layer. A comparison of the measured and simulated XRR data of the Cr/Sc attosecond mirror is shown in figure 4.42. The fitting procedure of the XRR measurement, including the native Cr_2O_3 top layer, reveals only a 0.2% shift of the aimed period thickness and a Névot-Croce [103] interface roughness of σ=0.198 nm as even the 9^{th} Bragg order is well resolved. The 5^{th} Bragg order is not completely suppressed and points to a period thickness ratio of γ=0.405. The multilayer still shows a pronounced periodicity as indicated by very sharp Bragg peaks, even though every 10^{th} period the chromium layer was polished with krypton (Kr) ions (section 4.4.2.2). The strong periodicity is the prerequisite for a flat spectral phase upon reflection without additionally introduced GDD.

We have also analyzed the Cr/Sc mirror reflectivity at near-normal incidence by XUV/soft x-ray reflectometry, which was performed on a second witness sample. The measured reflectivity profile, together with its simulation and target curve, is shown in figure 4.43. The Cr/Sc attosecond mirror design exhibits a maximum reflectivity

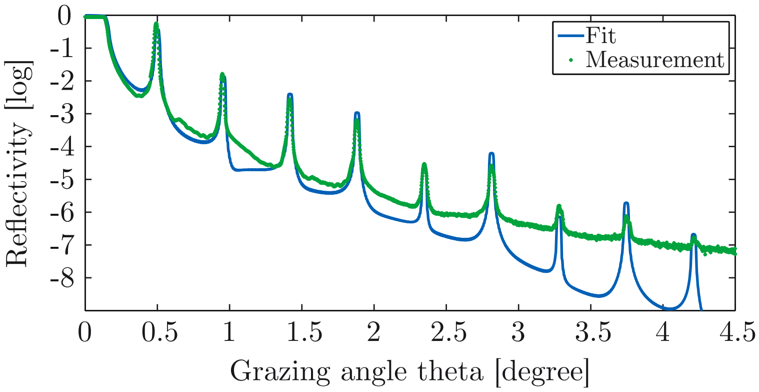

Figure 4.42: XRR measurement of the 145 eV attosecond mirror. Hard x-ray reflectometry measurement (green dots) and the fit (solid blue) of the Cr/Sc attosecond mirror.

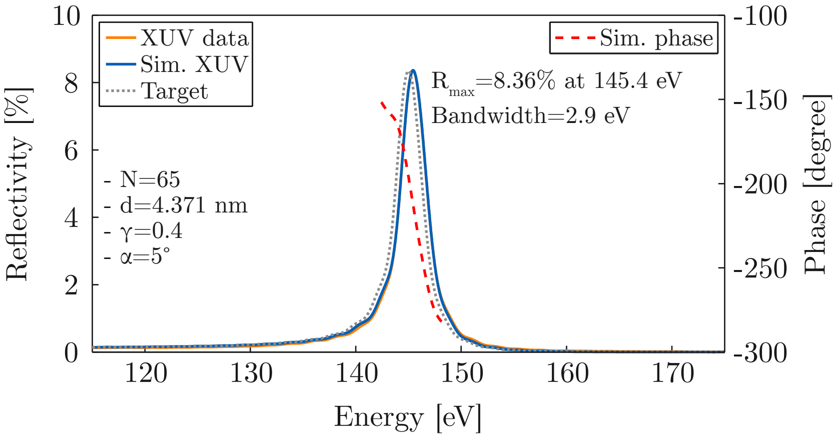

Figure 4.43: XUV/soft x-ray measurement of the 145 eV attosecond mirror. XUV/soft x-ray reflectometry measurement (solid orange), the corresponding fit (solid blue) and the target design (dotted gray) together with the simulated phase (dashed red). The mirror design parameters are listed on the left side.

of R_{max}=8.36% centered at 145.4 eV and reflects over the intended bandwidth of ≈3 eV, as depicted by the solid brown line in figure 4.43. We find a perfect match of the simulation (solid blue) and the measurement, with only a 0.27% shift of the measured peak wavelength from the target wavelength (dotted gray). The XUV/soft x-ray measurement was carried out at the PTB beamline at BESSY II in Berlin.

As a final application of this Cr/Sc multilayer mirror to attosecond pulses at 145 eV, an attosecond electron streaking experiment was performed to characterize the mirrors temporal attosecond pulse response. High harmonics have been generated in a neon (Ne) gas jet (200 mbar, <4 fs, 1.5 mJ, f=40 cm), resulting in a high harmonic spectrum with a cut-off energy ranging up to 150 eV, and are then focused by means of a Cr/Sc multilayer-coated double mirror in a second Ne gas jet for photoionization. To characterize the attosecond pulses upon reflection from the Cr/Sc multilayer mirror, the well established XUV/soft x-ray pump/NIR probe streaking technique [73] was used. Here, both the attosecond soft x-ray pulse and the NIR laser pulse are focused by a double mirror (figure 2.10) into neon gas. The soft x-ray pulse photoionizes Ne atoms, which frees photoelectrons from the 2p shell, which are then momentum-streaked by the co-propagating temporally synchronized and phase stabilized NIR laser's electric field. The inner part of the double mirror can be moved with respect to the outer part, to introduce a temporal delay between the soft x-ray pulse, which is reflected at the mirror core, and the laser pulse, which is reflected at the outer ring. Changing the delay between the laser and the soft x-ray attosecond pulse yields a typical streaking spectrogram (figure 4.44(a)). FROG/CRAB [79] analysis allows for a complete reconstruction of both the intensity and the phase of the soft x-ray attosecond pulse, as well as the vector potential of the streaking laser field from a recorded spectrogram (figure 4.44a). Figure 4.44(b) shows the result of the appropriate FROG/CRAB retrieval as described in [80, 81]. The retrieved intensity and phase of the soft x-ray pulse are depicted in figure 4.44, once in the spectral (c) and once in the temporal (d) domain. Shifted by the binding energy of the

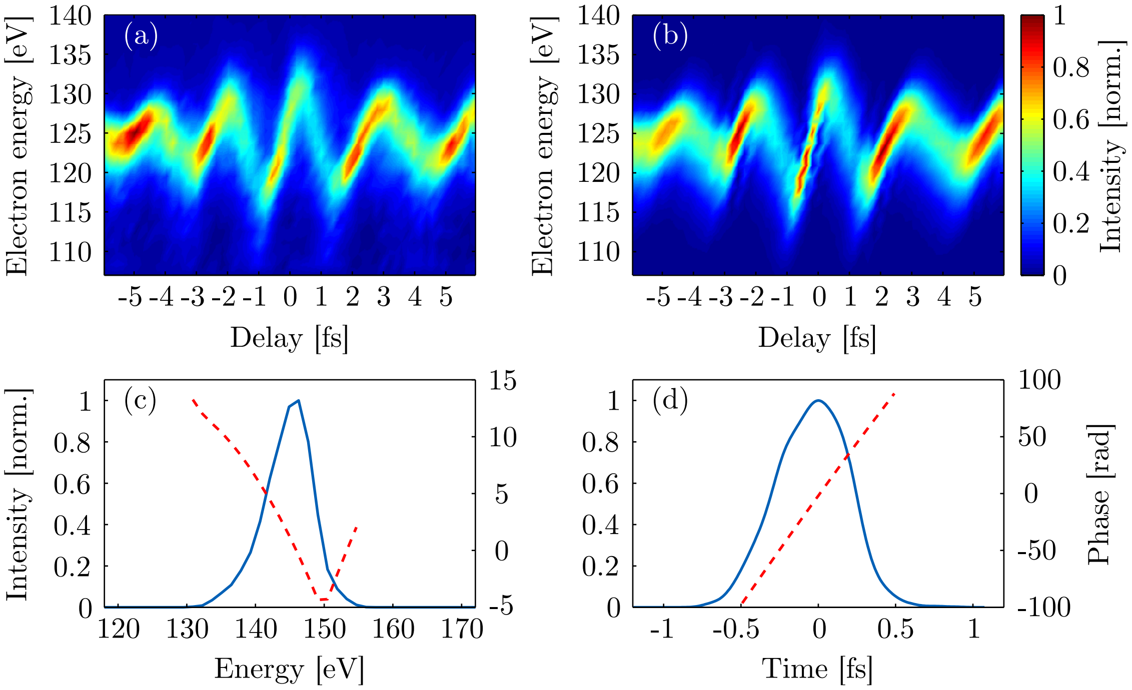

Figure 4.44: Attosecond electron streaking at a photon energy of 145 eV. Results of an attosecond electron streaking experiment for pulse characterization in neon utilizing the Cr/Sc multilayer mirror. (a) Measured electron streaking trace and (b) the retrieved trace performed by FROG/CRAB analyses. (c) The retrieved soft x-ray pulse (solid blue) and the phase (dotted red) in the spectral domain. (d) Soft x-ray pulse and phase in the temporal domain.

Ne-2p electrons (21.6 eV) the soft x-ray pulse shows a central energy of 145.6 eV which is in agreement to the target and the previously described results. With the retrieved spectral bandwidth and phase being the most prominent sources of uncertainty, the temporal error can be estimated to be about 20 as. From the retrieved amplitude and phase, an attosecond pulse duration of about 580 as is found in the temporal domain which is in excellent agreement with the previous estimations (based solely on the mirror reflectivity plus the assumption of a flat mirror phase). A perfect Gaussian Fourier limited pulse with 2.9 eV bandwidth has a duration of 629 as. In summary, an optimized Cr/Sc multilayer mirror has been developed and applied for reflecting single isolated attosecond pulses at a photon energy of 145 eV with a pulse duration of 580 as which is, to the best of our knowledge, 27 eV higher than the recent energy limit in table-top attosecond pump studies [17]. This experimental achievement now paves the way for attosecond experiments above 130 eV, the soft x-ray photon energy range which was not addressed until very recently. The true benefit of this achievement is in its scaling toward the preparation of attosecond pulses at even higher photon energies ranging into the water window spectral range, which will give access to even deeper bound electronic core states and open up new possibilities for attosecond experiments on biomolecules in the foreseen future. These results have shown the generation and characterization of isolated attosecond pulses, for the first time in the soft x-ray range at 145 eV, which is up until now the highest central energy for characterized table-top attosecond pulses.

Chapter 5

Conclusions and outlook

Conclusions: The realization, optimization, development and characterization of periodic and aperiodic multilayer optics for (attosecond) pulse shaping in the XUV/soft x-ray range has been presented.

The main improvement was realized with the material combination of Cr and Sc but other materials like Si, B_4C, Mo, La, Ti Ni benefit from the adoption of this knowledge. It has been proven that Cr/Sc can cover the spectral range between 140 eV to around 400 eV, where the optimized material system nowadays already enables attosecond experiments in the lower energy regime and will be the key system for attosecond science in the water window spectral range above 284 eV. The huge improvement in the ion beam deposition control, as well as the detailed knowledge of the material properties evaluated from various characterization methods, resulted in excellent agreement between the measurements and multilayer simulations.

A transmissive multilayer system has been designed, fabricated and characterized to transform linearly polarized attosecond pulses to almost circularly polarized. This allows for e.g. XMCD measurements combined with a high temporal resolution.

High precision and high reflective periodic multilayer mirrors have been investigated for the subsequent realization and characterization of aperiodic attosecond mirrors for attosecond pulse shaping in the water window with a high degree of freedom. An investigation of deposition effects and the study of the oxidation process in detail enabled an almost perfect implementation of negatively and positively chirped multilayer designs for future attosecond pulse compression.

The material system Cr/Sc has been optimized by tailoring the kinetic deposition parameters and additionally interface polishing utilizing krypton ions. The optimization process was accompanied by simulations and has been verified by various physical characterization techniques. Together with a detailed study of material contaminations and their subsequent removal, high reflective normal incidence mirrors could be realized at the lower spectral range of the water window as well as in the vicinity of the Sc L_3-edge. The measurements show until now the highest realized peak reflectivity values of pure (without barrier layers) Cr/Sc multilayer mirrors.

Two very precise multilayer mirrors in terms of central wavelength have been realized for an imaging experiment. These mirrors have been applied for the spectral filtering of a single narrowband HHG peak to allow for monochromatized illumination of a sample and to resolve the sample structure with a sub-wavelength resolution of 26 nm (corresponding to 0.8λ) by CDI.

Three different multilayer mirrors have been realized, characterized and applied to spectrally shape radiation from a laser-plasma driven undulator. The experiment proves the successful isolation and characterization of XUV/soft x-ray pulses at three different central energies where the highest energy could be realized in the water window close to 300 eV. It is the highest measured photon energy from a laser-plasma driven undulator reported until now.

An optimized Cr/Sc multilayer mirror has been developed and applied for the generation of isolated attosecond pulses at a photon energy of 145 eV and a pulse duration of 580 as. The benefit of this material system in comparison to others has been investigated indicating close to Fourier limited pulse reflections, a prerequisite for attosecond experiments with a high temporal resolution. For the first time in the soft x-ray range at 145 eV, the pulses have been characterized by attosecond electron streaking, which is the highest central energy for characterized table-top attosecond pulses to date.

Outlook: The presented optimization concepts for the Cr/Sc system were only the first steps. A more accurate analysis of the best kinetic energy of chromium and scandium for the ion beam deposition and the ion beam interface polishing, probably with individual sputter voltages for each material, would push the reflectivity and photon throughput to even higher values. This would relax the constraint on future attosecond sources as a higher mirror reflectivity can come along with a lower provided photon flux from the source.

The concept is in principle not limited by the material system and can improve the multilayer optics at even higher energies (e.g. V/Ni in the ≈450–500 eV range) or can be adopted to boron based systems (e.g. La/B_4C). High reflective mirrors close to the boron K-edge (188 eV$\widehat{=}$6.6 nm) may shift the EUVL wavelength from 13.5 nm down to 6.7 nm and enable further shrinking of a transistor size. Figure 2.36 has shown that La/B_4C mirrors can theoretically achieve equal or even higher reflectivity values close to the boron K-edge than current state-of-the-art Mo/Si mirrors in the vicinity of the silicon L_3-edge.

Attosecond physics will overlap with the boron edge on the way toward higher energies and would also benefit from such an optimized material system. Ever higher photon energies will enable a higher spectral, temporal and spatial resolution and allow for the probing of electron dynamics of ever more material systems as deeper electron core-shells can be addressed. Reaching the famous water window spectral range will extend the attosecond techniques to biomolecules and may facilitate attosecond *in vivo* experiments.

The concept of chirped mirrors, which are nowadays commercially available for the VIS/IR spectral range, found its way toward the XUV and even the soft x-ray range by ever improved layer accuracy and may find its application in the control of photoionized electrons by chirped few-cycle attosecond pulses [203] or in shaping possibly future attosecond FEL pulses by chirped grazing incidence mirrors.

Summarizing, the outlook of attosecond physics goes toward ever higher photon energies and ever shorter pulses allowing the investigation of electron dynamics in matter and may even lead to their control. High precise periodic and tailored aperiodic multilayer mirrors will serve as key components for those future experiments, for the generation of single attosecond pulses and their shaping, as nowadays they already are.

Data archiving

The experimental raw data, evaluation files, and original figures can be found on the Data Archive Server of the Laboratory for Attosecond Physics at the Max Planck Institute of Quantum Optics:

Every single folder name is related to the figure number in this thesis and contains exactly one `MATLAB` script and all necessary data to reproduce the figure. Most of the data is kept as raw data and all data manipulation is performed by the commented `MATLAB` script and therefore easily reproducible. Loading the script and pressing `F5` reproduces all figures. The `MATLAB` script generates the figure which is finally saved as `FigX_Y.fig` and `FigX_Y.ai`, for compatibility reasons with `Adobe Illustrator`. The `FigX_Y.ai` file was opened in `Adobe Illustrator` and the font size, font name, color coding (RGB) and the image size was adjusted to ensure the correct appearance in the thesis. This layout-converted figure was saved as `FigX_Y_converted.ai` and `FigX_Y_converted.pdf` (detailed information is provided in a `readme.txt` if another procedure was used for the figure realization). The `pdf`-file was used as input in the LaTeX (Lamport TeX by Leslie Lamport) script which generated the complete thesis. Figures which are produced without any data (e.g. drawings) were designed in `Adobe Illustrator` and saved as `FigX_Y.ai` and `FigX_Y.pdf`. The software versions which were used for this procedure are `MATLAB R2009a` and `Adobe Illustrator CS2`.

Bibliography

[1] V. Pervak, C. Teisset, A. Sugita, S. Naumov, F. Krausz, and A. Apolonski, "High-dispersive mirrors for femtosecond lasers," Optics Express **16,** 10220 (2008).

[2] M. Hofstetter, M. Schultze, M. Fieß, B. Dennhardt, A. Guggenmos, J. Gagnon, V. S. Yakovlev, E. Goulielmakis, R. Kienberger, E. M. Gullikson, F. Krausz, and U. Kleineberg, "Attosecond dispersion control by extreme ultraviolet multilayer mirrors," Optics Express **19,** 1767–1776 (2011).

[3] C. Morawe and M. Osterhoff, "Hard X-Ray Focusing with Curved Reflective Multilayers," X-Ray Optics and Instrumentation **2010,** 1–8 (2010).

[4] J.-M. André, R. Benbalagh, R. Barchewitz, M.-F. Ravet, A. Raynal, F. Delmotte, F. Bridou, G. Julié, A. Bosseboeuf, R. Laval, G. Soullié, C. Rémond, and M. Fialin, "X-ray Multilayer Monochromator with Enhanced Performance," Applied Optics **41,** 239 (2002).

[5] D. Attwood, *Soft X-Rays and Extreme Ultraviolet Radiation: Principles and Applications* (Cambridge University Press, 2007).

[6] H. Von Klüber, "Production of a High Resolving Power by means of Multilayer Coatings," Nature **169,** 790–791 (1952).

[7] A. F. Turner and P. W. Baumeister, "Multilayer Mirrors with High Reflectance Over an Extended Spectral Region," Applied Optics **5,** 69 (1966).

[8] E. Goulielmakis, M. Schultze, M. Hofstetter, V. S. Yakovlev, J. Gagnon, M. Uiberacker, A. L. Aquila, E. M. Gullikson, D. T. Attwood, R. Kienberger, F. Krausz, and U. Kleineberg, "Single-Cycle Nonlinear Optics," Science **320,** 1614–1617 (2008).

[9] M. Schultze, M. Fieß, N. Karpowicz, J. Gagnon, M. Korbman, M. Hofstetter, S. Neppl, A. L. Cavalieri, Y. Komninos, T. Mercouris, C. A. Nicolaides, R. Pazourek, S. Nagele, J. Feist, J. Burgdörfer, A. M. Azzeer, R. Ernstorfer, R. Kienberger, U. Kleineberg, E. Goulielmakis, F. Krausz, and V. S. Yakovlev, "Delay in Photoemission," Science **328,** 1658–1662 (2010).

[10] A. L. Cavalieri, N. Müller, T. Uphues, V. S. Yakovlev, A. Baltuška, B. Horvath, B. Schmidt, L. Blümel, R. Holzwarth, S. Hendel, M. Drescher, U. Kleineberg, P. M. Echenique, R. Kienberger, F. Krausz, and U. Heinzmann, "Attosecond spectroscopy in condensed matter," Nature **449,** 1029–1032 (2007).

[11] M. Uiberacker, T. Uphues, M. Schultze, A. J. Verhoef, V. Yakovlev, M. F. Kling, J. Rauschenberger, N. M. Kabachnik, H. Schröder, M. Lezius, K. L. Kompa, H.-G. Muller, M. J. J. Vrakking, S. Hendel, U. Kleineberg, U. Heinzmann, M. Drescher, and F. Krausz, "Attosecond real-time observation of electron tunnelling in atoms," Nature **446,** 627–632 (2007).

[12] M. I. Stockman, M. F. Kling, U. Kleineberg, and F. Krausz, "Attosecond nanoplasmonic-field microscope," Nature Photonics **1,** 539–544 (2007).

[13] T. Uphues, M. Schultze, M. F. Kling, M. Uiberacker, S. Hendel, U. Heinzmann, N. M. Kabachnik, and M. Drescher, "Ion-charge-state chronoscopy of cascaded atomic Auger decay," New Journal of Physics **10,** 025009 (2008).

[14] M. Krüger, M. Schenk, and P. Hommelhoff, "Attosecond control of electrons emitted from a nanoscale metal tip," Nature **475,** 78–81 (2011).

[15] A. L. Cavalieri, E. Goulielmakis, B. Horvath, W. Helml, M. Schultze, M. Fieß, V. Pervak, L. Veisz, V. S. Yakovlev, M. Uiberacker, A. Apolonski, F. Krausz, and R. Kienberger, "Intense 1.5-cycle near infrared laser waveforms and their use for the generation of ultra-broadband soft-x-ray harmonic continua," New Journal of Physics **9,** 242 (2007).

[16] M. Hofstetter, A. Aquila, M. Schultze, A. Guggenmos, S. Yang, E. Gullikson, M. Huth, B. Nickel, J. Gagnon, V. S. Yakovlev, E. Goulielmakis, F. Krausz, and U. Kleineberg, "Lanthanum–molybdenum multilayer mirrors for attosecond pulses between 80 and 130 eV," New Journal of Physics **13,** 063038 (2011).

[17] S. Neppl, R. Ernstorfer, A. L. Cavalieri, C. Lemell, G. Wachter, E. Magerl, E. M. Bothschafter, M. Jobst, M. Hofstetter, U. Kleineberg, J. V. Barth, D. Menzel, J. Burgdörfer, P. Feulner, F. Krausz, and R. Kienberger, "Direct observation of electron propagation and dielectric screening on the atomic length scale," Nature **517,** 342–346 (2015).

[18] J. Kirz, C. Jacobsen, and M. Howells, "Soft X-ray microscopes and their biological applications," Quarterly Reviews of Biophysics **28,** 33–130 (1995).

[19] T. Gorniak, R. Heine, A. P. Mancuso, F. Staier, C. Christophis, M. E. Pettitt, A. Sakdinawat, R. Treusch, N. Guerassimova, J. Feldhaus, C. Gutt, G. Grübel, S. Eisebitt, A. Beyer, A. Gölzhäuser, E. Weckert, M. Grunze, I. A. Vartanyants, and A. Rosenhahn, "X-ray holographic microscopy with zone plates applied to

biological samples in the water window using 3rd harmonic radiation from the free-electron laser FLASH," Optics Express **19,** 11059–11070 (2011).

[20] M. Hentschel, R. Kienberger, C. Spielmann, G. A. Reider, N. Milosevic, T. Brabec, P. Corkum, U. Heinzmann, M. Drescher, and F. Krausz, "Attosecond metrology," Nature **414,** 509–513 (2001).

[21] M. Otendal, T. Tuohimaa, U. Vogt, and H. M. Hertz, "A 9keV electron-impact liquid-gallium-jet x-ray source," Review of Scientific Instruments **79,** 016102 (2008).

[22] X. Liu, J. Lægsgaard, U. Møller, H. Tu, S. A. Boppart, and D. Turchinovich, "All-fiber femtosecond Cherenkov radiation source," Optics Letters **37,** 2769–2771 (2012).

[23] T. Higashiguchi, B. Li, Y. Suzuki, M. Kawasaki, H. Ohashi, S. Torii, D. Nakamura, A. Takahashi, T. Okada, W. Jiang, T. Miura, A. Endo, P. Dunne, G. O'Sullivan, and T. Makimura, "Characteristics of extreme ultraviolet emission from mid-infrared laser-produced rare-earth Gd plasmas," Optics Express **21,** 31837 (2013).

[24] F. R. Elder, A. M. Gurewitsch, R. V. Langmuir, and H. C. Pollock, "Radiation from Electrons in a Synchrotron," Physical Review **71,** 829–830 (1947).

[25] A. Buck, M. Nicolai, K. Schmid, C. M. S. Sears, A. Sävert, J. M. Mikhailova, F. Krausz, M. C. Kaluza, and L. Veisz, "Real-time observation of laser-driven electron acceleration," Nature Physics **7,** 543–548 (2011).

[26] E. Esarey, C. B. Schroeder, and W. P. Leemans, "Physics of laser-driven plasma-based electron accelerators," Reviews of Modern Physics **81,** 1229–1285 (2009).

[27] A. Pukhov and J. Meyer-ter Vehn, "Laser wake field acceleration: the highly non-linear broken-wave regime," Applied Physics B **74,** 355–361 (2002).

[28] A. J. Gonsalves, K. Nakamura, C. Lin, D. Panasenko, S. Shiraishi, T. Sokollik, C. Benedetti, C. B. Schroeder, C. G. R. Geddes, J. van Tilborg, J. Osterhoff, E. Esarey, C. Toth, and W. P. Leemans, "Tunable laser plasma accelerator based on longitudinal density tailoring," Nature Physics **7,** 862–866 (2011).

[29] A. Buck, Ph.D. thesis, Ludwig-Maximilians-Universität München, München, 2011.

[30] X. Wang, R. Zgadzaj, N. Fazel, Z. Li, S. A. Yi, X. Zhang, W. Henderson, Y.-Y. Chang, R. Korzekwa, H.-E. Tsai, C.-H. Pai, H. Quevedo, G. Dyer, E. Gaul, M. Martinez, A. C. Bernstein, T. Borger, M. Spinks, M. Donovan, V. Khudik, G. Shvets, T. Ditmire, and M. C. Downer, "Quasi-monoenergetic laser-plasma acceleration of electrons to 2 GeV," Nature Communications **4,** 1988 (2013).

[31] C. G. R. Geddes, C. Toth, J. van Tilborg, E. Esarey, C. B. Schroeder, D. Bruhwiler, C. Nieter, J. Cary, and W. P. Leemans, "High-quality electron beams from a laser wakefield accelerator using plasma-channel guiding," Nature **431,** 538–541 (2004).

[32] F. Grüner, S. Becker, U. Schramm, T. Eichner, M. Fuchs, R. Weingartner, D. Habs, J. Meyer-ter Vehn, M. Geissler, M. Ferrario, L. Serafini, B. v. d. Geer, H. Backe, W. Lauth, and S. Reiche, "Design considerations for table-top, laser-based VUV and X-ray free electron lasers," Applied Physics B **86,** 431–435 (2007).

[33] M. Fuchs, R. Weingartner, A. Popp, Z. Major, S. Becker, J. Osterhoff, I. Cortrie, B. Zeitler, R. Hörlein, G. D. Tsakiris, U. Schramm, T. P. Rowlands-Rees, S. M. Hooker, D. Habs, F. Krausz, S. Karsch, and F. Grüner, "Laser-driven soft-X-ray undulator source," Nature Physics **5,** 826–829 (2009).

[34] M. Fuchs, Ph.D. thesis, Ludwig-Maximilians-Universität München, München, 2010.

[35] K.-J. Kim, "Three-Dimensional Analysis of Coherent Amplification and Self-Amplified Spontaneous Emission in Free-Electron Lasers," Physical Review Letters **57,** 1871–1874 (1986).

[36] B. Kim, J. An, Y. Yu, Y. Cheng, Z. Xu, and D. E. Kim, "Optimization of multi-cycle two-color laser fields for the generation of an isolated attosecond pulse," Optics Express **16,** 10331 (2008).

[37] J. A. Wheeler, A. Borot, S. Monchocé, H. Vincenti, A. Ricci, A. Malvache, R. Lopez-Martens, and F. Quéré, "Attosecond lighthouses from plasma mirrors," Nature Photonics **6,** 829–833 (2012).

[38] P. Heissler, E. Lugovoy, R. Hörlein, L. Waldecker, J. Wenz, M. Heigoldt, K. Khrennikov, S. Karsch, F. Krausz, B. Abel, and G. D. Tsakiris, "Using the third state of matter: high harmonic generation from liquid targets," New Journal of Physics **16,** 113045 (2014).

[39] T. Popmintchev, M.-C. Chen, A. Bahabad, M. Gerrity, P. Sidorenko, O. Cohen, I. P. Christov, M. M. Murnane, and H. C. Kapteyn, "Phase matching of high harmonic generation in the soft and hard X-ray regions of the spectrum," PNAS **106,** 10516–10521 (2009).

[40] T. Popmintchev, M.-C. Chen, D. Popmintchev, P. Arpin, S. Brown, S. Ališauskas, G. Andriukaitis, T. Balčiunas, O. D. Mücke, A. Pugzlys, A. Baltuška, B. Shim, S. E. Schrauth, A. Gaeta, C. Hernández-García, L. Plaja, A. Becker,

A. Jaron-Becker, M. M. Murnane, and H. C. Kapteyn, “Bright Coherent Ultrahigh Harmonics in the keV X-ray Regime from Mid-Infrared Femtosecond Lasers,” Science **336,** 1287–1291 (2012).

[41] F. Krausz and M. Ivanov, “Attosecond physics,” Reviews of Modern Physics **81,** 163–234 (2009).

[42] T. Brabec and F. Krausz, “Intense few-cycle laser fields: Frontiers of nonlinear optics,” Reviews of Modern Physics **72,** 545–591 (2000).

[43] A. H. Zewail, “Femtochemistry: Atomic-Scale Dynamics of the Chemical Bond,” The Journal of Physical Chemistry A **104,** 5660–5694 (2000).

[44] A. Rousse, C. Rischel, and J.-C. Gauthier, “Femtosecond x-ray crystallography,” Reviews of Modern Physics **73,** 17–31 (2001).

[45] P. H. Bucksbaum, “The Future of Attosecond Spectroscopy,” Science **317,** 766–769 (2007).

[46] T. H. Maiman, “Stimulated Optical Radiation in Ruby,” Nature **187,** 493–494 (1960).

[47] D. E. Spence, P. N. Kean, and W. Sibbett, “60-fsec pulse generation from a self-mode-locked Ti:sapphire laser,” Optics Letters **16,** 42 (1991).

[48] R. W. Hellwarth, “Theory of the Pulsation of Fluorescent Light From Ruby,” Physical Review Letters **6,** 9–12 (1961).

[49] K. X. Liu, C. J. Flood, D. R. Walker, and H. M. van Driel, “Kerr lens mode locking of a diode-pumped Nd:YAG laser,” Optics Letters **17,** 1361 (1992).

[50] D. Strickland and G. Mourou, “Compression of amplified chirped optical pulses,” Optics Communications **56,** 219–221 (1985).

[51] N. Karasawa, R. Morita, H. Shigekawa, and M. Yamashita, “Generation of intense ultrabroadband optical pulses by induced phase modulation in an argon-filled single-mode hollow waveguide,” Optics Letters **25,** 183 (2000).

[52] V. Pervak, A. V. Tikhonravov, M. K. Trubetskov, S. Naumov, F. Krausz, and A. Apolonski, “1.5-octave chirped mirror for pulse compression down to sub-3 fs,” Applied Physics B **87,** 5–12 (2006).

[53] B. Schenkel, J. Biegert, U. Keller, C. Vozzi, M. Nisoli, G. Sansone, S. Stagira, S. De Silvestri, and O. Svelto, “Generation of 3.8-fs pulses from adaptive compression of a cascaded hollow fiber supercontinuum,” Optics Letters **28,** 1987 (2003).

[54] A. Einstein, “On the Quantum Theory of Radiation,” Physikalische Zeitschrift **18,** 121–128 (1917).

[55] P. A. Franken, A. E. Hill, C. W. Peters, and G. Weinreich, “Generation of Optical Harmonics,” Physical Review Letters **7,** 118–119 (1961).

[56] G. H. C. New and J. F. Ward, “Optical Third-Harmonic Generation in Gases,” Physical Review Letters **19,** 556–559 (1967).

[57] M. Ferray, A. L’Huillier, X. F. Li, L. A. Lompre, G. Mainfray, and C. Manus, “Multiple-harmonic conversion of 1064 nm radiation in rare gases,” Journal of Physics B: Atomic, Molecular and Optical Physics **21,** L31 (1988).

[58] K. Zhao, Q. Zhang, M. Chini, Y. Wu, X. Wang, and Z. Chang, “Tailoring a 67 attosecond pulse through advantageous phase-mismatch,” Optics Letters **37,** 3891–3893 (2012).

[59] R. Santra and A. Gordon, “Three-Step Model for High-Harmonic Generation in Many-Electron Systems,” Physical Review Letters **96,** 073906 (2006).

[60] P. B. Corkum, “Plasma perspective on strong field multiphoton ionization,” Physical Review Letters **71,** 1994–1997 (1993).

[61] M. F. Kling and M. J. J. Vrakking, “Attosecond Electron Dynamics,” Annual Review of Physical Chemistry **59,** 463–492 (2008).

[62] L. V. Keldysh, “Ionization in the field of a strong electromagnetic wave,” Soviet Physics JETP **20,** 1307–1314 (1965).

[63] A. Scrinzi, M. Y. Ivanov, R. Kienberger, and D. M. Villeneuve, “Attosecond physics,” Journal of Physics B: Atomic, Molecular and Optical Physics **39,** R1 (2006).

[64] Y. Mairesse, A. d. Bohan, L. J. Frasinski, H. Merdji, L. C. Dinu, P. Monchicourt, P. Breger, M. Kovačev, R. Taïeb, B. Carré, H. G. Muller, P. Agostini, and P. Salières, “Attosecond Synchronization of High-Harmonic Soft X-rays,” Science **302,** 1540–1543 (2003).

[65] H. W. Schweinberger, Ph.D. thesis, Ludwig-Maximilians-Universität München, München, 2014.

[66] V. V. Strelkov, A. F. Sterjantov, N. Y. Shubin, and V. T. Platonenko, “XUV generation with several-cycle laser pulse in barrier-suppression regime,” Journal of Physics B: Atomic, Molecular and Optical Physics **39,** 577 (2006).

[67] P. M. Paul, E. S. Toma, P. Breger, G. Mullot, F. Augé, P. Balcou, H. G. Muller, and P. Agostini, “Observation of a Train of Attosecond Pulses from High Harmonic Generation,” Science **292,** 1689–1692 (2001).

[68] F. Calegari, M. Lucchini, M. Negro, C. Vozzi, L. Poletto, O. Svelto, S. D. Silvestri, G. Sansone, S. Stagira, and M. Nisoli, “Temporal gating methods for the generation of isolated attosecond pulses,” Journal of Physics B: Atomic, Molecular and Optical Physics **45,** 074002 (2012).

[69] A. Baltuška, T. Udem, M. Uiberacker, M. Hentschel, E. Goulielmakis, C. Gohle, R. Holzwarth, V. S. Yakovlev, A. Scrinzi, T. W. Hänsch, and F. Krausz, “Attosecond control of electronic processes by intense light fields,” Nature **421,** 611–615 (2003).

[70] N. G. Johnson, O. Herrwerth, A. Wirth, S. De, I. Ben-Itzhak, M. Lezius, B. Bergues, M. F. Kling, A. Senftleben, C. D. Schröter, R. Moshammer, J. Ullrich, K. J. Betsch, R. R. Jones, A. M. Sayler, T. Rathje, K. Rühle, W. Müller, and G. G. Paulus, “Single-shot carrier-envelope-phase-tagged ion-momentum imaging of nonsequential double ionization of argon in intense 4-fs laser fields,” Physical Review A **83,** 013412 (2011).

[71] M. Schultze, E. Goulielmakis, M. Uiberacker, M. Hofstetter, J. Kim, D. Kim, F. Krausz, and U. Kleineberg, “Powerful 170-attosecond XUV pulses generated with few-cycle laser pulses and broadband multilayer optics,” New Journal of Physics **9,** 243 (2007).

[72] M. Fieß, M. Schultze, E. Goulielmakis, B. Dennhardt, J. Gagnon, M. Hofstetter, R. Kienberger, and F. Krausz, “Versatile apparatus for attosecond metrology and spectroscopy,” Review of Scientific Instruments **81,** 093103 (2010).

[73] R. Kienberger, E. Goulielmakis, M. Uiberacker, A. Baltuska, V. Yakovlev, F. Bammer, A. Scrinzi, T. Westerwalbesloh, U. Kleineberg, U. Heinzmann, M. Drescher, and F. Krausz, “Atomic transient recorder,” Nature **427,** 817–821 (2004).

[74] I. Walmsley, L. Waxer, and C. Dorrer, “The role of dispersion in ultrafast optics,” Review of Scientific Instruments **72,** 1–29 (2001).

[75] A. V. Tikhonravov, M. K. Trubetskov, and G. W. DeBell, “Optical coating design approaches based on the needle optimization technique,” Applied Optics **46,** 704–710 (2007).

[76] V. S. Yakovlev, J. Gagnon, N. Karpowicz, and F. Krausz, “Attosecond Streaking Enables the Measurement of Quantum Phase,” Physical Review Letters **105,** 073001 (2010).

[77] W. Chao, J. Kim, S. Rekawa, P. Fischer, and E. H. Anderson, “Demonstration of 12 nm Resolution Fresnel Zone Plate Lens based Soft X-ray Microscopy,” Optics Express **17,** 17669–17677 (2009).

[78] F. Krausz and M. I. Stockman, “Attosecond metrology: from electron capture to future signal processing,” Nature Photonics **8,** 205–213 (2014).

[79] R. Trebino, K. W. DeLong, D. N. Fittinghoff, J. N. Sweetser, M. A. Krumbügel, B. A. Richman, and D. J. Kane, “Measuring ultrashort laser pulses in the time-frequency domain using frequency-resolved optical gating,” Review of Scientific Instruments **68,** 3277–3295 (1997).

[80] J. Gagnon and V. S. Yakovlev, “The robustness of attosecond streaking measurements,” Optics Express **17,** 17678–17693 (2009).

[81] J. Gagnon, E. Goulielmakis, and V. S. Yakovlev, “The accurate FROG characterization of attosecond pulses from streaking measurements,” Applied Physics B **92,** 25–32 (2008).

[82] Y. Mairesse and F. Quéré, “Frequency-resolved optical gating for complete reconstruction of attosecond bursts,” Physical Review A **71,** 011401 (2005).

[83] H. G. Muller, “Reconstruction of attosecond harmonic beating by interference of two-photon transitions,” Applied Physics B **74,** 17–21 (2002).

[84] R. López-Martens, K. Varjú, P. Johnsson, J. Mauritsson, Y. Mairesse, P. Salières, M. B. Gaarde, K. J. Schafer, A. Persson, S. Svanberg, C.-G. Wahlström, and A. L'Huillier, “Amplitude and Phase Control of Attosecond Light Pulses,” Physical Review Letters **94,** 033001 (2005).

[85] B. L. Henke, E. M. Gullikson, and J. C. Davis, “X-Ray interactions: photoabsorption, scattering, transmission, and reflection at E=50-30000 eV, Z=1-92,” Atomic Data and Nuclear Data Tables **54,** 181–342 (1993).

[86] R. D. L. Kronig, “On the theory of dispersion of x-rays,” Journal of the Optical Society of America **12,** 547 (1926).

[87] E. Spiller, *Soft X-ray optics* (SPIE Optical Engineering Press, Bellingham, WA, 1994).

[88] F. Eriksson, Ph.D. thesis, Linköping University, 581 83 Linköping, Sweden, 2004.

[89] M. Fieß, Ph.D. thesis, Ludwig-Maximilians-Universität München, München, 2010.

[90] C. Boeglin, E. Beaurepaire, V. Halté, V. López-Flores, C. Stamm, N. Pontius, H. A. Dürr, and J.-Y. Bigot, “Distinguishing the ultrafast dynamics of spin and orbital moments in solids,” Nature **465,** 458–461 (2010).

[91] S. Bajt, J. B. Alameda, J. Barbee, Troy W., W. M. Clift, J. A. Folta, B. Kaufmann, and E. A. Spiller, "Improved reflectance and stability of Mo-Si multilayers," Optical Engineering **41,** 1797–1804 (2002).

[92] E. Spiller, "Reflective multilayer coatings for the far uv region," Applied Optics **15,** 2333 (1976).

[93] M. Trubetskov, A. Tikhonravov, and V. Pervak, "Time-domain approach for designing dispersive mirrors based on the needle optimization technique Theory," Optics Express **16,** 20637 (2008).

[94] V. Yakovlev and G. Tempea, "Optimization of chirped mirrors," Applied Optics **41,** 6514–6520 (2002).

[95] C. Wagner and N. Harned, "EUV lithography: Lithography gets extreme," Nature Photonics **4,** 24–26 (2010).

[96] D. Martínez-Galarce, R. Soufli, D. L. Windt, M. Bruner, E. Gullikson, S. Khatri, E. Spiller, J. C. Robinson, S. Baker, and E. Prast, "Multisegmented, multilayer-coated mirrors for the Solar Ultraviolet Imager," Optical Engineering **52,** 095102–095102 (2013).

[97] J. H. Underwood and T. W. Barbee, "Layered synthetic microstructures as Bragg diffractors for X rays and extreme ultraviolet: theory and predicted performance," Applied Optics **20,** 3027 (1981).

[98] L. G. Parratt, "Surface Studies of Solids by Total Reflection of X-Rays," Physical Review **95,** 359–369 (1954).

[99] A. L. Aquila, F. Salmassi, F. Dollar, Y. Liu, and E. Gullikson, "Developments in realistic design for aperiodic Mo/Si multilayer mirrors," Optics Express **14,** 10073 (2006).

[100] U. Kleineberg, H.-J. Stock, A. Kloidt, B. Schmiedeskamp, U. Heinzmann, S. Hopfe, and R. Scholz, "Interface Stability and Silicide Formation in High Temperature Stable MoxSi1-x/Si Multilayer Soft X-Ray Mirrors Studied by Means of X-Ray Diffraction and HRTEM," physica status solidi (a) **145,** 539–550 (1994).

[101] P. Debye, "Interferenz von Röntgenstrahlen und Wärmebewegung," Annalen der Physik **348,** 49–92 (1913).

[102] I. Waller, "Zur Frage der Einwirkung der Wärmebewegung auf die Interferenz von Röntgenstrahlen," Zeitschrift für Physik **17,** 398–408 (1923).

[103] L. Névot and P. Croce, "Caractérisation des surfaces par réflexion rasante de rayons X. Application à l'étude du polissage de quelques verres silicates," Revue de Physique Appliquee **15,** 761–779 (1980).

[104] Y. Platonov, J. Rodriguez, M. Kriese, E. Gullikson, T. Harada, T. Watanabe, and H. Kinoshita, "Multilayers for next generation EUVL at 6.Xnm," In *Proc. SPIE, EUV and X-Ray Optics: Synergy between Laboratory and Space II*, **8076,** 80760N (2011).

[105] E. M. Gullikson, F. Salmassi, A. L. Aquila, and F. Dollar, "Progress in short period multilayer coatings for water window applications," http://www.osti.gov/scitech/servlets/purl/932470 (2006).

[106] M. Cardona and L. Ley, *Photoemission in Solids I : General Principles*, 1 ed. (Springer-Verlag, Berlin, Heidelberg, New York, 1978).

[107] J. C. Fuggle and N. Mårtensson, "Core-level binding energies in metals," Journal of Electron Spectroscopy and Related Phenomena **21,** 275–281 (1980).

[108] D. Attwood, E. Gullikson, M. Howells, K.-J. Kim, J. Kirz, J. Kortright, I. Lindau, Y. Liu, P. Pianetta, A. Robinson, J. Scofield, J. Underwood, G. Williams, and H. Winick, *X-ray Data Booklet*, 3 ed. (Lawrence Berkeley National Laboratory, University of California, Berkeley, CA, 2009).

[109] M. Hofstetter, Ph.D. thesis, Ludwig-Maximilians-Universität München, München, 2011.

[110] N. N. Salashchenko and E. A. Shamov, "Short-period X-ray multilayers based on Cr/Sc," Optics Communications **134,** 7–10 (1997).

[111] F. Schäfers, "Multilayers for the EUV/soft X-ray range," Physica B **283,** 119–124 (2000).

[112] T. Kuhlmann, S. Yulin, T. Feigl, N. Kaiser, T. Gorelik, U. Kaiser, and W. Richter, "Chromium-scandium multilayer mirrors for the nitrogen K-alpha line in the water window region," Applied Optics **41,** 2048–2052 (2002).

[113] F. Eriksson, G. A. Johansson, H. M. Hertz, E. M. Gullikson, U. Kreissig, and J. Birch, "14.5% near-normal incidence reflectance of Cr Sc x-ray multilayer mirrors for the water window," Optics Letters **28,** 2494–2496 (2003).

[114] F. Eriksson, N. Ghafoor, F. Schäfers, E. M. Gullikson, S. Aouadi, S. Rohde, L. Hultman, and J. Birch, "Atomic scale interface engineering by modulated ion-assisted deposition applied to soft x-ray multilayer optics," Applied Optics **47,** 4196 (2008).

[115] F. Bridou, F. Delmotte, P. Troussel, and B. Villette, “Design and fabrication of X-ray non-periodic multilayer mirrors: Apodization and shaping of their spectral response,” Nuclear Instruments and Methods in Physics Research Section A **680,** 69–74 (2012).

[116] E. Chi, J. Shim, J. Kwak, and H. Baik, “Silicide formation by solid-state diffusion in MO/Si multilayer thin films,” Journal of Materials Science **31,** 3567–3572 (1996).

[117] J. F. Ziegler, M. D. Ziegler, and J. P. Biersack, “SRIM – The stopping and range of ions in matter (2010),” Nuclear Instruments and Methods in Physics Research Section B **268,** 1818–1823 (2010).

[118] F. Hamelmann, G. Haindl, J. Schmalhorst, A. Aschentrup, E. Majkova, U. Kleineberg, U. Heinzmann, A. Klipp, P. Jutzi, A. Anopchenko, M. Jergel, and S. Luby, “Metal oxide/silicon oxide multilayer with smooth interfaces produced by in situ controlled plasma-enhanced MOCVD,” Thin Solid Films **358,** 90–93 (2000).

[119] Z. Wang, H. Zhao, Q. Yao, J. Xu, and H. Kimura, “Structure and magnetism of ZnO/Co multilayers prepared by pulsed laser deposition,” Crystal Research and Technology **47,** 799–803 (2012).

[120] K. Siraj, M. Khaleeq-ur Rahman, M. S. Rafique, M. Z. Munawar, S. Naseem, and S. Riaz, “Pulsed laser deposition and characterization of multilayer metal-carbon thin films,” Applied Surface Science **257,** 6445–6450 (2011).

[121] K. M. Skulina, C. S. Alford, R. M. Bionta, D. M. Makowiecki, E. M. Gullikson, R. Soufli, J. B. Kortright, and J. H. Underwood, “Molybdenum/beryllium multilayer mirrors for normal incidence in the extreme ultraviolet,” Applied Optics **34,** 3727 (1995).

[122] S. Bajt, D. G. Stearns, and P. A. Kearney, “Investigation of the amorphous-to-crystalline transition in Mo/Si multilayers,” Journal of Applied Physics **90,** 1017–1025 (2001).

[123] P. N. Rao, M. Nayak, G. S. Lodha, S. K. Rai, A. K. Srivastava, M. H. Modi, and A. Sagdeo, “Fabrication and Evaluation of Large Area Mo/Si Soft X-Ray Multilayer Mirrors at Indus SR Facilities,” Advances in Optical Technologies **2012,** 1–8 (2012).

[124] I. V. Kozhevnikov, L. L. Balakireva, A. I. Fedorenko, I. A. Kopealets, V. E. Levashov, A. N. Stetsenko, I. I. Struk, and A. V. Vinogradov, “Synthesis and measurement of Os-Si multilayer mirrors optimized for the wavelength 380 Å,” Optics Communications **125,** 13–17 (1996).

[125] S. Rajesh, V. Arivazhagan, and M. M. Parvathi, “Structural, optical and electrical properties of vacuum evaporated PbSe/ZnSe multilayer thin films,” In *AIP Conference Proceedings*, **1451,** 197–199 (AIP Publishing, 2012).

[126] D. L. Voronov, P. Gawlitza, R. Cambie, S. Dhuey, E. M. Gullikson, T. Warwick, S. Braun, V. V. Yashchuk, and H. A. Padmore, “Conformal growth of Mo/Si multilayers on grating substrates using collimated ion beam sputtering,” Journal of Applied Physics **111,** 093521 (2012).

[127] A. El Hajj, B. Lucas, M. Chakaroun, R. Antony, B. Ratier, and M. Aldissi, “Optimization of ZnO/Ag/ZnO multilayer electrodes obtained by Ion Beam Sputtering for optoelectronic devices,” Thin Solid Films **520,** 4666–4668 (2012).

[128] M. Grigonis and É. J. Knystautas, “C/Si multilayer mirrors for the 25–30-nm wavelength region,” Applied Optics **36,** 2839 (1997).

[129] A. Kloidt, K. Nolting, U. Kleineberg, B. Schmiedeskamp, U. Heinzmann, P. Müller, and M. Kühne, “Enhancement of the reflectivity of Mo/Si multilayer x-ray mirrors by thermal treatment,” Applied Physics Letters **58,** 2601–2603 (1991).

[130] G. Aston and H. R. Kaufman, “Ion Beam Divergence Characteristics of Three-Grid Accelerator Systems,” AIAA Journal **17,** 64–70 (1979).

[131] G. K. Hubler and J. A. Sprague, “Energetic particles in PVD technology: particle-surface interaction processes and energy-particle relationships in thin film deposition,” Surface and Coatings Technology **81,** 29–35 (1996).

[132] C. M. Gilmore and J. A. Sprague, “Interface mixing of energetic metals deposited onto metals,” Surface and Coatings Technology **83,** 146–150 (1996).

[133] E. Gerald and J. Jellison, “Data Analysis for Spectroscopic Ellipsometry,” in *Handbook of Ellipsometry*, F. A. Jenkins and H. E. White, eds., (William Andrew Publishing, Norwich, NY, 2005), pp. 237–296.

[134] O. Auciello and A. R. Krauss, “In Situ Real-Time Characterization of Thin Films,” Measurement Science and Technology **13,** 644 (2002).

[135] P. R. Spyak, J. H. LaMarr, and K. J. Thome, “Errors in laboratory measurements resulting from atmospheric absorption near 1380 nm,” In *Proc. SPIE Earth Observing Systems II*, **3117,** 208–216 (1997).

[136] H. Horvath, “Atmospheric light absorption-A review,” Atmospheric Environment **27,** 293–317 (1993).

[137] D. W. Lynch and W. R. Hunter, "Introduction to the Data for Several Metals," in *Handbook of Optical Constants of Solids*, 3 ed., E. D. Palik, ed., (Academic Press, 1998), pp. 240–241.

[138] D. W. Lynch and W. R. Hunter, "Comments on the Optical Constants of Metals and an Introduction to the Data for Several Metals," in *Handbook of Optical Constants of Solids*, 1 ed., E. D. Palik, ed., (Academic Press, 1997), pp. 322–323.

[139] G. Guizzetti and A. Piaggi, "Vanadium (V)," in *Handbook of Optical Constants of Solids*, 2 ed., E. D. Palik, ed., (Academic Press, 2012), pp. 483–485.

[140] Z.-Y. Wang, R.-J. Zhang, H.-L. Lu, X. Chen, Y. Sun, Y. Zhang, Y.-F. Wei, J.-P. Xu, S.-Y. Wang, Y.-X. Zheng, and L.-Y. Chen, "The impact of thickness and thermal annealing on refractive index for aluminum oxide thin films deposited by atomic layer deposition," Nanoscale Research Letters **10,** 1–6 (2015).

[141] T. Lichtenstein, *Handbook of Thin Film Materials* (University of Rochester, 1979).

[142] E. M. Gullikson, S. Mrowka, and B. B. Kaufmann, "Recent developments in EUV reflectometry at the Advanced Light Source," In *Proc. SPIE Emerging Lithographic Technologies V*, **4343,** 363–373 (2001).

[143] F. Scholze, J. Tümmler, and G. Ulm, "High-accuracy radiometry in the EUV range at the PTB soft x-ray beamline," Metrologia **40,** S224 (2003).

[144] S. Singh, S. Basu, P. Bhatt, and A. K. Poswal, "Kinetics of alloy formation at the interfaces in a Ni-Ti multilayer: X-ray and neutron reflectometry study," Physical Review B **79,** 195435 (2009).

[145] A. Wochnik, Ph.D. thesis, Ludwig-Maximilians-Universität München, München, 2012.

[146] S. Venkatesan, M. Döblinger, C. Daumont, B. Kooi, B. Noheda, J. T. M. D. Hosson, and C. Scheu, "Influence of strain on the electronic structure of the TbMnO3/SrTiO3 epitaxial interface," Applied Physics Letters **99,** 222902 (2011).

[147] A. Zürner, J. Kirstein, M. Döblinger, C. Bräuchle, and T. Bein, "Visualizing single-molecule diffusion in mesoporous materials," Nature **450,** 705–708 (2007).

[148] E. Jensen, "Example: Transmission Electron Microscope System," http://www.texample.net/tikz/examples/transmission-electron-microscope/ (2015).

[149] A. Guggenmos, R. Rauhut, M. Hofstetter, S. Hertrich, B. Nickel, J. Schmidt, E. M. Gullikson, M. Seibald, W. Schnick, and U. Kleineberg, “Aperiodic CrSc multilayer mirrors for attosecond water window pulses,” Optics Express **21,** 21728–21740 (2013).

[150] A. Guggenmos, M. Hofstetter, R. Rauhut, B. Nickel, E. Gullikson, and U. Kleineberg, “Aperiodic multilayer mirrors for attosecond soft x-ray pulses,” In *Proc. SPIE, Advances in X-Ray/EUV Optics and Components VII*, **8502,** 850204 (2012).

[151] A. Guggenmos, M. Hofstetter, R. Rauhut, C. Späth, S. Hertrich, B. Nickel, S. Yang, E. M. Gullikson, J. Schmidt, M. Seibald, W. Schnick, F. Krausz, and U. Kleineberg, “Broadband multilayer mirror and diffractive optics for attosecond pulse shaping in the 280-500 eV photon energy range,” EPJ Web of Conferences **41,** 01011 (2013).

[152] G. Sansone, F. Kelkensberg, J. F. Pérez-Torres, F. Morales, M. F. Kling, W. Siu, O. Ghafur, P. Johnsson, M. Swoboda, E. Benedetti, F. Ferrari, F. Lépine, J. L. Sanz-Vicario, S. Zherebtsov, I. Znakovskaya, A. L’Huillier, M. Y. Ivanov, M. Nisoli, F. Martín, and M. J. J. Vrakking, “Electron localization following attosecond molecular photoionization,” Nature **465,** 763–766 (2010).

[153] S. Neppl, R. Ernstorfer, E. M. Bothschafter, A. L. Cavalieri, D. Menzel, J. V. Barth, F. Krausz, R. Kienberger, and P. Feulner, “Attosecond Time-Resolved Photoemission from Core and Valence States of Magnesium,” Physical Review Letters **109,** 087401 (2012).

[154] M. Suman, G. Monaco, M.-G. Pelizzo, D. L. Windt, and P. Nicolosi, “Realization and characterization of an XUV multilayer coating for attosecond pulses,” Optics Express **17,** 7922–7932 (2009).

[155] G. Sansone, L. Poletto, and M. Nisoli, “High-energy attosecond light sources,” Nature Photonics **5,** 655–663 (2011).

[156] D. H. Ko, K. T. Kim, J. Park, J.-h. Lee, and C. H. Nam, “Attosecond chirp compensation over broadband high-order harmonics to generate near transform-limited 63 as pulses,” New Journal of Physics **12,** 063008 (2010).

[157] C. Spielmann, N. H. Burnett, S. Sartania, R. Koppitsch, M. Schnürer, C. Kan, M. Lenzner, P. Wobrauschek, and F. Krausz, “Generation of Coherent X-rays in the Water Window Using 5-Femtosecond Laser Pulses,” Science **278,** 661–664 (1997).

[158] Y. Uspenskii, D. Burenkov, T. Hatano, and M. Yamamoto, “Optimal Design of Multilayer Mirrors for Water-Window Microscope Optics,” Optical Review **14,** 64–73 (2007).

[159] T. Tsuru, “Reflection Passband Broadening by Aperiodic Designs of EUV/Soft X-ray Multilayers,” In *AIP Conf. Proc.*, **879,** 1524–1530 (2007).

[160] C. Bourassin-Bouchet, M. Stephens, S. de Rossi, F. Delmotte, and P. Chavel, “Duration of ultrashort pulses in the presence of spatio-temporal coupling,” Optics Express **19,** 17357–17371 (2011).

[161] A. J. Verhoef, A. V. Mitrofanov, X. T. Nguyen, M. Krikunova, S. Fritzsche, N. M. Kabachnik, M. Drescher, and A. Baltuška, “Time-and-energy-resolved measurement of Auger cascades following Kr 3d excitation by attosecond pulses,” New Journal of Physics **13,** 113003 (2011).

[162] H. Jiang, J. Zhu, J. Xu, X. Wang, Z. Wang, and M. Watanabe, “Determination of layer-thickness variation in periodic multilayer by x-ray reflectivity,” Journal of Applied Physics **107,** 103523 (2010).

[163] A. D. Rakić, A. B. Djurišić, J. M. Elazar, and M. L. Majewski, “Optical properties of metallic films for vertical-cavity optoelectronic devices,” Applied Optics **37,** 5271–5283 (1998).

[164] J. I. Larruquert, J. A. Aznárez, J. A. Méndez, A. M. Malvezzi, L. Poletto, and S. Covini, “Optical Properties of Scandium Films in the Far and the Extreme Ultraviolet,” Applied Optics **43,** 3271 (2004).

[165] F. Jenkins and H. White, *Fundamentals of Optics*, 4 ed. (McGraw-Hill, New York, 2001).

[166] G. Sansone, E. Benedetti, F. Calegari, C. Vozzi, L. Avaldi, R. Flammini, L. Poletto, P. Villoresi, C. Altucci, R. Velotta, S. Stagira, S. D. Silvestri, and M. Nisoli, “Isolated Single-Cycle Attosecond Pulses,” Science **314,** 443–446 (2006).

[167] A. Aquila, F. Salmassi, and E. Gullikson, “Metrologies for the phase characterization of attosecond extreme ultraviolet optics,” Optics Letters **33,** 455–457 (2008).

[168] C. Bourassin-Bouchet, S. de Rossi, J. Wang, E. Meltchakov, A. Giglia, N. Mahne, S. Nannarone, and F. Delmotte, “Shaping of single-cycle sub-50-attosecond pulses with multilayer mirrors,” New Journal of Physics **14,** 023040 (2012).

[169] A. Guggenmos, S. Radünz, R. Rauhut, M. Hofstetter, S. Venkatesan, A. Wochnik, E. M. Gullikson, S. Fischer, B. Nickel, C. Scheu, and U. Kleineberg, “Ion polished Cr/Sc attosecond multilayer mirrors for high water window reflectivity,” Optics Express **22,** 26526–26536 (2014).

[170] A. Guggenmos, S. Radünz, R. Rauhut, M. Hofstetter, S. Venkatesan, A. Wochnik, C. Scheu, E. Gullikson, S. Fischer, B. Nickel, and U. Kleineberg, "Attosecond broadband multilayer mirrors for the water window spectral range," In *Proc. SPIE, Advances in X-Ray/EUV Optics and Components IX*, **9207,** 92070L (2014).

[171] A. Guggenmos, S. Radünz, R. Rauhut, S. Venkatesan, A. Wochnik, C. Scheu, E. Gullikson, S. Fischer, B. Nickel, F. Krausz, and U. Kleineberg, "Optimizing broadband attosecond Cr/Sc water window multilayer mirrors," In *Frontiers in Optics*, p. FTh1G.6 (OSA, 2014).

[172] F. Eriksson, N. Ghafoor, L. Hultman, and J. Birch, "Reflectivity and structural evolution of Cr/Sc and nitrogen containing Cr/Sc multilayers during thermal annealing," Journal of Applied Physics **104,** 063516 (2008).

[173] A. I. Fedorenko, V. V. Kondratenko, Y. P. Pershin, O. V. Poltseva, E. N. Zubarev, L. L. Balakireva, V. V. Didyk, and V. V. Burtsev, "Structure and optical properties of multilayer X-ray mirrors for long wave part (3.1–4.4 nm) of "water window"," Crystal Research and Technology **29,** 1139–1147 (1994).

[174] T. Salditt and T. Dučić, "X-Ray Microscopy for Neuroscience: Novel Opportunities by Coherent Optics," in *Super-Resolution Microscopy Techniques in the Neurosciences*, No. 86 in *Neuromethods*, E. F. Fornasiero and S. O. Rizzoli, eds., (Humana Press, 2014), pp. 257–290.

[175] M. Santos-Lleo, N. Schartel, H. Tananbaum, W. Tucker, and M. C. Weisskopf, "The first decade of science with Chandra and XMM-Newton," Nature **462,** 997–1004 (2009).

[176] C. Liu, Z. Zeng, R. Li, Z. Xu, and M. Nisoli, "Attosecond photoionization for reconstruction of bound-electron wave packets," Physical Review A **90,** 013403 (2014).

[177] L. Belshaw, F. Calegari, M. Duffy, A. Trabattoni, L. Poletto, M. Nisoli, and J. Greenwood, "Ultrafast Electron Dynamics in an Amino Acid Measured by Attosecond Pulses," In *The European Conference on Lasers and Electro-Optics*, p. CFIE_1_4 (Optical Society of America, 2013).

[178] M. Schultze, A. Wirth, I. Grguras, M. Uiberacker, T. Uphues, A. J. Verhoef, J. Gagnon, M. Hofstetter, U. Kleineberg, E. Goulielmakis, and F. Krausz, "State-of-the-art attosecond metrology," Journal of Electron Spectroscopy and Related Phenomena **184,** 68–77 (2011).

[179] K. Varjú, P. Johnsson, R. López, T. Remetter, E. Gustafsson, J. Mauritsson, M. B. Gaarde, K. J. Schafer, C. Erny, I. Sola, A. Zaïr, E. Constant, E. Cormier,

E. Mével, and A. L'Huillier, "Experimental studies of attosecond pulse trains," Laser Physics **15,** 888–898 (2005).

[180] F. Schäfers, H.-C. Mertins, F. Schmolla, I. Packe, N. N. Salashchenko, and E. A. Shamov, "Cr/Sc multilayers for the soft-x-ray range," Applied Optics **37,** 719–728 (1998).

[181] C. T. Horovitz, *Scandium: Its Occurrence, Chemistry Physics, Metallurgy, Biology and Technology* (Academic Press, London, 1975).

[182] M. Prasciolu, A. F. G. Leontowich, K. R. Beyerlein, and S. Bajt, "Thermal stability studies of short period Sc/Cr and Sc/B4C/Cr multilayers," Applied Optics **53,** 2126–2135 (2014).

[183] E. Ziegler, L. Peverini, N. Vaxelaire, A. Cordon-Rodriguez, A. Rommeveaux, I. V. Kozhevnikov, and J. Susini, "Evolution of surface roughness in silicon X-ray mirrors exposed to a low-energy ion beam," Nuclear Instruments and Methods in Physics Research Section A **616,** 188–192 (2010).

[184] N. N. Nagib, N. A. Mahmoud, L. Z. Ismail, M. A. Amer, and K. Abd-El-Sabour, "Effect of surface roughness on the optical constants of bulk polycrystalline gold samples," Optik **125,** 1085–1087 (2014).

[185] S. A. Yulin, T. Kuhlmann, T. Feigl, and N. Kaiser, "Thermal stability of Cr/Sc multilayers for the soft x-ray range," In *Proc. SPIE X-Ray Mirrors, Crystals, and Multilayers II*, **4782,** 285–291 (2002).

[186] R. Gavrila, A. Dinescu, and D. Mardare, "A power spectral density study of thin films morphology based on AFM profiling," Romanian Journal of Information Science and Technology **10,** 291–300 (2007).

[187] A. B. Gokhale and G. J. Abbaschian, "The Sc-Si (Scandium-Silicon) system," Bulletin of Alloy Phase Diagrams **7,** 333–336 (1986).

[188] E. I. Gladyshevskii and E. I. Émes-Misenko, "Crystal structures of silicon-rich scandium and yttrium silicides," Journal of Structural Chemistry **4,** 793–795 (1963).

[189] U. Kleineberg, "New routes towards even shorter attosecond soft X-ray pulses," Annalen der Physik **525,** A188–A190 (2013).

[190] J. Goldstein, *Scanning Electron Microscopy and X-ray Microanalysis* (Springer US, 2003).

[191] M. Zürch, J. Rothhardt, S. Hädrich, S. Demmler, M. Krebs, J. Limpert, A. Tünnermann, A. Guggenmos, U. Kleineberg, and C. Spielmann, "Real-time and Sub-wavelength Ultrafast Coherent Diffraction Imaging in the Extreme Ultraviolet," Scientific Reports **4,** 7356 (2014).

[192] J. Miao, T. Ishikawa, E. H. Anderson, and K. O. Hodgson, "Phase retrieval of diffraction patterns from noncrystalline samples using the oversampling method," Physical Review B **67,** 174104 (2003).

[193] J. Rothhardt, S. Hädrich, H. Carstens, N. Herrick, S. Demmler, J. Limpert, and A. Tünnermann, "1 MHz repetition rate hollow fiber pulse compression to sub-100-fs duration at 100 W average power," Optics Letters **36,** 4605 (2011).

[194] A. R. Maier, Ph.D. thesis, Universität Hamburg, Hamburg, 2012.

[195] T. Eichner, F. Grüner, S. Becker, M. Fuchs, D. Habs, R. Weingartner, U. Schramm, H. Backe, P. Kunz, and W. Lauth, "Miniature magnetic devices for laser-based, table-top free-electron lasers," Physical Review Special Topics - Accelerators and Beams **10,** 082401 (2007).

[196] M. Schultze, K. Ramasesha, C. D. Pemmaraju, S. A. Sato, D. Whitmore, A. Gandman, J. S. Prell, L. J. Borja, D. Prendergast, K. Yabana, D. M. Neumark, and S. R. Leone, "Attosecond band-gap dynamics in silicon," Science **346,** 1348–1352 (2014).

[197] W. Schweinberger, A. Sommer, E. Bothschafter, J. Li, F. Krausz, R. Kienberger, and M. Schultze, "Waveform-controlled near-single-cycle milli-joule laser pulses generate sub-10 nm extreme ultraviolet continua," Optics Letters **37,** 3573–3575 (2012).

[198] C. Montcalm, B. T. Sullivan, S. Duguay, M. Ranger, W. Steffens, H. Pépin, and M. Chaker, "In situ reflectance measurements of soft-x-ray/extreme-ultraviolet Mo/Y multilayer mirrors," Optics Letters **20,** 1450–1452 (1995).

[199] R. Soufli, E. Spiller, D. L. Windt, J. C. Robinson, E. M. Gullikson, L. Rodriguez-de Marcos, M. Fernandez-Perea, S. L. Baker, A. L. Aquila, F. J. Dollar, J. A. Méndez, J. I. Larruquert, L. Golub, and P. Boerner, "In-band and out-of-band reflectance calibrations of the EUV multilayer mirrors of the atmospheric imaging assembly instrument aboard the Solar Dynamics Observatory," In *Proc. SPIE, Space Telescopes and Instrumentation 2012: Ultraviolet to Gamma Ray*, **8443,** 84433C (2012).

[200] S. Bajt, "Molybdenum-ruthenium/beryllium multilayer coatings," Journal of Vacuum Science & Technology A **18,** 557–559 (2000).

[201] B. Sae-Lao and C. Montcalm, "Molybdenum-strontium multilayer mirrors for the 8-12-nm extreme-ultraviolet wavelength region," Optics Letters **26,** 468–470 (2001).

[202] C. Montcalm, P. A. Kearney, J. M. Slaughter, B. T. Sullivan, M. Chaker, H. Pépin, and C. M. Falco, "Survey of Ti-, B-, and Y-based soft x-ray-extreme

ultraviolet multilayer mirrors for the 2- to 12-nm wavelength region," Applied Optics **35,** 5134–5147 (1996).

[203] E. A. Pronin, A. F. Starace, and L.-Y. Peng, "Perturbation-theory analysis of ionization by a chirped few-cycle attosecond pulse," Physical Review A **84,** 013417 (2011).

Acronyms

List of abbreviations used throughout this thesis:

Al	aluminum
Al_2O_3	aluminum oxide
ALS	Advanced Light Source in Berkeley, USA
APT	attosecond pulse train(s)
Ar	argon
as	attosecond
ATI	above threshold ionization
B	boron
B_4C	boron carbide
Ba	barium
Be	beryllium
BS	beamstop
BESSY	Berliner Elektronenspeicherring-Gesellschaft für Synchrotronstrahlung
C	carbon
Ca	calcium
CCD	charge-coupled device
CDI	coherent diffractive imaging
CE	carrier-envelop
CEP	carrier-envelop phase
cm	centimeter
Co	cobalt
CPA	chirped pulse amplification
Cr	chromium
Cr_2O_3	chromium(III) oxide
ct	count(s)
Cu	copper (from latin: cuprum)
CXRO	Center for X-Ray Optics in Berkely, USA
DCM	dielectric chirped mirrors
EASE	easy-to-use acquisition/analyses software for spectroscopic ellipsometry (software by J. A. Woollam Co., Inc.)
EDX	energy dispersive x-ray spectroscopy
e.g.	for example (from latin: exempli gratia)

EUVL	extreme ultraviolet lithography
eV	electronvolt
Fe	iron (from latin: ferrum)
FEL	free electron laser
FL	Fourier limit
FLASH	Free electron laser in Hamburg
FROG/CRAB	frequency-resolved optical gating for complete reconstruction of attosecond bursts
fs	femtosecond(s)
FWHM	full width at half maximum
GD	group delay
GDD	group delay dispersion
Ge	germanium
GIXR	grazing incidence x-ray reflectometry
GV	gigavolt
h	hour(s)
HAADF	high angle annular dark field
HHG	high harmonic generation
i.e.	that is (from latin: id est)
IR	infrared
keV	kiloelectronvolt
kHz	kilohertz
Kr	krypton
kV	kilo volt
La	lanthanum
LAP	laboratory for attosecond physics
LCLS	Linac Coherent Light Source in Stanford, USA
LMU	Ludwig-Maximilians-Universität München
LPP	laser produced plasma
LVDT	linear variable differential transformer
LWFA	laser wakefield acceleration
m	meter
mA	milliampere
MAP	Munich-Centre for Advanced Photonics
MATLAB	MATrix LABoratory (software by Mathworks)
mbar	millibar
MeV	megaelectronvolt
meV	millielectronvolt
MF	merit function
Mg	magnesium
min	minute(s)
mJ	millijoule
ML	multilayer

mm	millimeter
Mo	molybdenum
MPQ	Max-Planck-Institute of Quantum Optics
ms	millisecond(s)
μJ	mikrojoule
μm	mikrometer
Ne	neon
Ni	nickel
NIR	near-infrared
nm	nanometer
O	oxygen
PBN	plasma bridge neutralizer
pC	picocoulomb(s)
Pd	palladium
pdf	portable document format (developed by Adobe Systems)
PMMA	polymethylmethacrylat
PSD	power spectral density
PTB	Physikalisch-Technische Bundesanstalt in Berlin
R	reflectivity or radius (depending on the context)
RABBITT	Reconstruction of Attosecond harmonic Beating By Interference of Two-photon Transitions
RF	radio frequency
RGB	red-green-blue color space
Rh	rhodium
rms	root mean square
ROC	radius of curvature
rpm	rotations per minute
Ru	ruthenium
s	second(s)
SASE	self amplified spontaneous emission
Sc	scandium
Sc_2O_3	scandium(III) oxide
SD	standard deviation or sputter design (depending on context)
Si	silicon
Si_3N_4	silicon nitride
SiO_2	silicon dioxide
Sr	Strontium
SRIM	the stopping and range of ions in matter
STEM	scanning transmission electron microscopy
TEM	transmission electron microscopy
Ti	titanium
TOD	third order dispersion
UHH	Universität Hamburg

UV	ultraviolet
V	vanadium or volt (depending on context)
VIS	visible
W	tungsten or watt (depending on the context)
Xe	xenon
XMCD	XUV/x-ray magnetic circular dichroism
XRR	x-ray reflectometry
XUV	(also EUV) extreme ultraviolet
Y	yttrium
Zr	zirconium

Danksagung

An dieser Stelle möchte ich mich bei allen bedanken, die zum Gelingen dieser Doktorarbeit beigetragen haben. Mein besonderer Dank gilt hierbei:

Prof. Dr. Ulf Kleineberg und Prof. Dr. Ferenc Krausz, die mir die Möglichkeit gaben in dieser einzigartigen Forschungsgruppe, unter besten Forschungsbedingungen, diese Doktorarbeit durchzuführen. Sie standen mir mit ihrem Wissen, Ideen und Anregungen in jedem Bereich dieser Arbeit zur Seite. Ich konnte selbständige Arbeitsweisen im Forschungsbereich entwickeln und durfte Verantwortung für die Betreuung von Bachelor und Master Studenten übernehmen. Die Koordination der Übungen sowie das Erstellen von Übungsaufgaben und Klausuren für Vorlesungen, gab mir zusätzlich die Möglichkeit am Lehrangebot der Universität mitzuwirken. Die Unterstützung für zahlreiche Konferenzen erlaubte es mir zudem, zahlreiche Wissenschaftler weltweit kennenzulernen und Einblick in aktuelle Forschungsergebnisse von zahlreichen führenden Forschungsgruppen zu bekommen. Die Infrastruktur und enge Zusammenarbeit in der gesamten LAP-Gruppe, speziell mit den Wissenschaftlern bei den einzelnen Attosekunden Experimenten, erlaubte die kontinuierliche Anwendung von weiterentwickelten hoch präzisen Spiegeloptiken und ermöglichte aufgrund der gewonnenen Daten zahlreiche Rückschlüsse auf den aktuellen Stand der Forschung. Dies war die Grundvoraussetzung für die Umsetzung von immer besseren maßgeschneiderten Spiegeloptiken für die Attosekundenphysik und war im Endeffekt ausschlaggebend für zahlreiche Ergebnisse dieser Arbeit.

Meinem Vorgänger Michael Hofstetter, der mich in diesen Forschungsbereich eingeführt hat und mir mit zahlreichen Einblicken in die Beschichtung und verschiedenen Messtechniken die Umsetzung dieser Arbeit sehr erleichtert hat. Mit seiner netten, freundschaftlichen und immer hilfsbereiten Art hat er sehr zum Gelingen dieser Arbeit beigetragen.

Meinen Kollegen Jürgen Schmidt, Christian Späth, Soo Hoon Chew, Kellie Pearce, Stephan Heinrich, Pan Huaihai und Anika Spreen für zahlreiche aufschlussreiche Diskussionen und auch für einige private Stunden außerhalb der Arbeitszeit.

Roman Rauhut und Stefan Radünz, die ich für ihren Bachelor- sowie Masterabschluss betreuen durfte. Ihr unentwegter Einsatz für die Weiterentwicklung der Optiken hat zu zahlreichen Ergebnissen geführt, welche in verschiedenen Journalen wissenschaftlich veröffentlicht werden konnten.

Georg Brandl, der mich in sämtlichen technischen, verwaltungstechnischen oder persönlichen Anliegen immer unterstützt hat und immer für eine Lösung gesorgt hat.
PD Bert Nickel für das Übernehmen des Zweitgutachtens und seiner Gruppe an der LMU in der Innenstadt, insbesondere Samira Hertrich, Stefan Fischer, Philip Böhm und Simon Noever für ihren Einsatz bei den Röntgenreflektometriemessungen.
Der Gruppe von Prof. Dr. Christine Scheu an der LMU in Großhadern, speziell Sriram Venkatesan und Angela Wochnik, für die Zusammenarbeit bei den TEM Aufnahmen.
Ein weiterer Dank geht nach Goßhadern an Prof. Dr. Wolfgang Schnick und Markus Seibald für die zahlreichen und aufschlussreichen EDX Messungen um die Verunreinigungen der Spiegel zu verringern.
Eric Gullikson und Sunling Yang für die Reflektometriemessungen an der ALS in Berkeley.
Prof. Dr. Spielmann und Michael Zürch aus Jena für die Zusammenarbeit bei den CDI Messungen und HHG Untersuchungen.
Prof. Dr. Reinhard Kienberger, Michael Jobst, Marcus Ossiander, Johann Riemensberger, Martin Schäffer, Ayman Akil, Clemens Jakubeit für ihre Unterstützung bei der ersten Anwendung von Cr/Sc Spiegeln für Attosekundenpulse.
Der Gruppe von Prof. Dr. Florian Grüner, speziell Andreas Richard Maier, und der Gruppe von Prof. Dr. Stefan Karsch für die Zusammenarbeit beim Undulatorexperiment.
Michael Rogg, Thomas Strobl und der gesamten MPQ Werkstatt, die jegliche Reparatur oder Maßanfertigung immer äußerst präzise und zeitnah ermöglichten.
Dem MAP/MPQ-Verwaltungsteam für schnelle Hilfen bei Dienstreisen, Einkäufen oder anderweitigen Anliegen.
Allen anderen vom MAP/MPQ-team, die bislang namentlich nicht erwähnt wurden, für die schöne Zeit und erfolgreiche Zusammenarbeit.

Geomayra für das Korrekturlesen dieser Arbeit.
Meinen Eltern und meinen Geschwistern für die großartige Unterstützung meines Studiums und der Doktorarbeit.
Meiner Frau Erika und meinen Kindern für die aufopferungsvolle Geduld bei sämtlichen Anliegen die während dieser Arbeit aufgetreten sind.